

---

Dépôt Institutionnel de l'Université libre de Bruxelles /  
Université libre de Bruxelles Institutional Repository  
**Thèse de doctorat/ PhD Thesis**

**Citation APA:**

Tóth, B. (2008). *Two-phase flow investigation in a cold-gas solid rocket motor model through the study of the slag accumulation process* (Unpublished doctoral dissertation). Université libre de Bruxelles, Faculté des sciences appliquées – Mécanique, Bruxelles.

**Disponible à / Available at permalink :** <https://dipot.ulb.ac.be/dspace/bitstream/2013/210575/4/19bfdc2f-8583-456a-83cb-356ef94e5460.txt>

---

(English version below)

Cette thèse de doctorat a été numérisée par l'Université libre de Bruxelles. L'auteur qui s'opposerait à sa mise en ligne dans DI-fusion est invité à prendre contact avec l'Université (di-fusion@ulb.be).

**Dans le cas où une version électronique native de la thèse existe, l'Université ne peut garantir que la présente version numérisée soit identique à la version électronique native, ni qu'elle soit la version officielle définitive de la thèse.**

DI-fusion, le Dépôt Institutionnel de l'Université libre de Bruxelles, recueille la production scientifique de l'Université, mise à disposition en libre accès autant que possible. Les œuvres accessibles dans DI-fusion sont protégées par la législation belge relative aux droits d'auteur et aux droits voisins. Toute personne peut, sans avoir à demander l'autorisation de l'auteur ou de l'ayant-droit, à des fins d'usage privé ou à des fins d'illustration de l'enseignement ou de recherche scientifique, dans la mesure justifiée par le but non lucratif poursuivi, lire, télécharger ou reproduire sur papier ou sur tout autre support, les articles ou des fragments d'autres œuvres, disponibles dans DI-fusion, pour autant que :

- Le nom des auteurs, le titre et la référence bibliographique complète soient cités;
- L'identifiant unique attribué aux métadonnées dans DI-fusion (permalink) soit indiqué;
- Le contenu ne soit pas modifié.

L'œuvre ne peut être stockée dans une autre base de données dans le but d'y donner accès ; l'identifiant unique (permalink) indiqué ci-dessus doit toujours être utilisé pour donner accès à l'œuvre. Toute autre utilisation non mentionnée ci-dessus nécessite l'autorisation de l'auteur de l'œuvre ou de l'ayant droit.

----- **English Version** -----

This Ph.D. thesis has been digitized by Université libre de Bruxelles. The author who would disagree on its online availability in DI-fusion is invited to contact the University (di-fusion@ulb.be).

**If a native electronic version of the thesis exists, the University can guarantee neither that the present digitized version is identical to the native electronic version, nor that it is the definitive official version of the thesis.**

DI-fusion is the Institutional Repository of Université libre de Bruxelles; it collects the research output of the University, available on open access as much as possible. The works included in DI-fusion are protected by the Belgian legislation relating to authors' rights and neighbouring rights. Any user may, without prior permission from the authors or copyright owners, for private usage or for educational or scientific research purposes, to the extent justified by the non-profit activity, read, download or reproduce on paper or on any other media, the articles or fragments of other works, available in DI-fusion, provided:

- The authors, title and full bibliographic details are credited in any copy;
- The unique identifier (permalink) for the original metadata page in DI-fusion is indicated;
- The content is not changed in any way.

It is not permitted to store the work in another database in order to provide access to it; the unique identifier (permalink) indicated above must always be used to provide access to the work. Any other use not mentioned above requires the authors' or copyright owners' permission.

---

**D 03536**

THÈSE DE DOCTORAT DE L'UNIVERSITÉ  
LIBRE DE BRUXELLES

FACULTÉ DES SCIENCES APPLIQUÉES

présentée par Balázs TÓTH

pour obtenir le grade de Docteur en Sciences Appliquées  
de l'Université Libre de Bruxelles

**Two-phase flow investigation in a cold-gas  
solid rocket motor model through the study  
of the slag accumulation process**

Pour être soutenue le 21 Janvier 2008

devant un jury composé de:

M. G. Degrez, Professeur, Université Libre de Bruxelles  
M. J.-M. Buchlin, Professeur, Université Libre de Bruxelles/IVK  
M. B. Leduc, Professeur, Université Libre de Bruxelles  
M. J. Anthoine, Professeur, Institut von Karman  
M. M.L. Riethmuller, Professeur, Institut von Karman  
M. J. Steelant, Docteur Ingénieur, ESTEC-ESA  
M. J-F. Guéry, Ingénieur, SNPE  
M. M. Prévost, Ingénieur, ONERA

Président du jury  
Directeur de thèse  
Examineur  
Examineur  
Examineur  
Examineur  
Examineur  
Examineur

Universite Libre de Bruxelles



003366881

6

*to my wife, Krisztina*

# Contents

<b>Abstract</b>	<b>xvii</b>
<b>Acknowledgement</b>	<b>xix</b>
<b>Nomenclature</b>	<b>xxi</b>
<b>The fundamentals of the study</b>	<b>3</b>
<b>1 Introduction</b>	<b>3</b>
1.1 Position of the problem . . . . .	3
1.2 Background . . . . .	6
1.2.1 Alumina formation . . . . .	7
1.2.2 Slag formation and modelling . . . . .	8
1.3 Existing experimental facilities . . . . .	12
1.3.1 Cold-gas facilities . . . . .	12
1.3.1.1 VECLA . . . . .	12
1.3.1.2 VALDO . . . . .	13
1.3.1.3 MICAT1 . . . . .	13
1.3.1.4 VIOLETTE . . . . .	14
1.3.1.5 VKI models . . . . .	15
1.3.2 Hot-gas facilities . . . . .	17
1.3.2.1 C1x . . . . .	17
1.3.2.2 SNPE 1/15, LP3 and LP6 . . . . .	17
1.3.2.3 LP9 and LP10 . . . . .	18
1.4 Objectives . . . . .	19
1.5 Methodology . . . . .	19
1.6 Overview . . . . .	20

<b>2</b>	<b>Modelling the phenomena</b>	<b>21</b>
2.1	The MPS P230 . . . . .	21
2.2	Main considerations . . . . .	24
2.3	Modelling and similarities . . . . .	25
2.3.1	The modelled geometry . . . . .	25
2.3.2	Flow conditions . . . . .	28
2.3.2.1	The flow velocity . . . . .	28
2.3.2.2	The droplet-phase . . . . .	28
2.4	The parameters of the experimental facility . . . . .	31
<b>I</b>	<b>Dedicated measurement techniques</b>	<b>33</b>
<b>3</b>	<b>The Level Detection and Recording technique</b>	<b>37</b>
3.1	About the conventional LeDaR technique . . . . .	37
3.2	The adapted LeDaR technique . . . . .	38
3.2.1	Adapting the measurement conditions . . . . .	38
3.2.2	Adapting the detection algorithm . . . . .	41
<b>4</b>	<b>The two-phase Particle Image Velocimetry technique</b>	<b>45</b>
4.1	Introduction . . . . .	45
4.1.1	The principle of PIV . . . . .	45
4.1.2	Difficulties in two-phase condition . . . . .	46
4.2	Choosing a two-phase PIV approach . . . . .	48
4.2.1	The preliminary technique . . . . .	49
4.2.1.1	The image recording . . . . .	49
4.2.1.2	The image processing algorithm . . . . .	49
4.2.2	The successive measurement technique . . . . .	52
4.2.2.1	The device generating fluorescent seeding . . . . .	52
4.2.2.2	Fluorescent tracer applicability . . . . .	53
4.2.2.3	Introducing the droplets . . . . .	55
4.2.3	The one-camera technique . . . . .	58
4.2.4	The UV technique . . . . .	59
4.2.5	Comparison between the different methods . . . . .	62
4.3	Developing the UV two-phase PIV method . . . . .	63

---

4.3.1	Adapting the experimental equipment for the UV technique . . . . .	63
4.3.2	Demonstrating the applicability of the UV technique . . . . .	66
4.4	The UV technique inside the test section . . . . .	69
4.4.1	Adapting the experimental conditions . . . . .	69
4.4.2	Image pre-processing . . . . .	73
<b>II</b>	<b>Liquid accumulation assessment</b>	<b>75</b>
<b>5</b>	<b>The investigated parameters of the liquid accumulation</b>	<b>79</b>
5.1	Experimental conditions . . . . .	79
5.2	Data processing . . . . .	84
5.3	Measurement parameters . . . . .	86
5.4	Liquid accumulation results . . . . .	87
5.4.1	The flow velocity . . . . .	87
5.4.2	The inhibitor size . . . . .	87
5.4.3	The inhibitor position . . . . .	87
5.4.4	The cavity width . . . . .	89
5.4.5	The nozzle throat opening . . . . .	89
5.4.6	Obstacle tip to nozzle tip distance . . . . .	90
5.5	Summary on the parameters of the accumulation rate . . . . .	91
<b>6</b>	<b>Statistical flow-field investigation</b>	<b>93</b>
6.1	Single-phase PIV experiments . . . . .	93
6.1.1	Experimental conditions . . . . .	93
6.1.2	Experimental results . . . . .	95
6.1.2.1	The statistical flow quantities . . . . .	95
6.1.2.2	Effect of the slag in the cavity . . . . .	98
6.2	Single-phase flow numerical simulations . . . . .	99
6.2.1	The numerical domain . . . . .	99
6.2.2	Validating the numerical data . . . . .	100
6.3	Two-phase flow numerical simulations . . . . .	103
6.3.1	The effect of the mono-disperse spray . . . . .	105
6.3.2	The effect of the poly-disperse spray . . . . .	106
6.3.3	Droplet size effect on the accumulation . . . . .	108

---

6.4	Two-phase flow PIV experiments . . . . .	111
6.4.1	The experimental configuration . . . . .	111
6.4.2	The resulting statistical flow fields . . . . .	114
6.4.3	The droplet-phase distribution . . . . .	118
6.4.4	About the mean relative motion between the two phases . . . . .	121
6.5	Summary on the statistical flow field properties . . . . .	122
<b>7</b>	<b>Instantaneous flow-field investigation</b>	<b>125</b>
7.1	The methodology of the vortex analysis . . . . .	125
7.2	Nominal speed investigation . . . . .	127
7.2.1	Single-phase flow configuration . . . . .	128
7.2.2	Two-phase flow numerical approach . . . . .	138
7.3	Two-phase PIV investigation . . . . .	140
7.4	Summary on the instantaneous flow behaviour . . . . .	145
<b>8</b>	<b>The understanding of the current accumulation process</b>	<b>147</b>
8.1	The dripping process . . . . .	147
8.1.1	Dripping visualization . . . . .	148
8.1.2	Liquid deposition with radial flow injection . . . . .	151
8.2	The entrapment process . . . . .	155
8.3	Summary on the accumulation process . . . . .	156
<b>9</b>	<b>Conclusions and future perspectives</b>	<b>159</b>
9.1	Conclusions . . . . .	159
9.2	Conclusions on the measurement techniques . . . . .	160
9.3	Conclusions on the slag accumulation process . . . . .	160
9.4	Future perspectives . . . . .	162
	<b>Appendices</b>	<b>175</b>
<b>A</b>	<b>The existing experimental tools</b>	<b>175</b>
A.1	The PIV technique . . . . .	175
A.2	The wavelet analysis based vortex detection . . . . .	179
A.2.1	The detection algorithm . . . . .	179
A.2.2	The detection criteria . . . . .	180

---

<b>B The design and characterization of the experimental facility</b>	<b>183</b>
B.1 Choosing the wind-tunnel . . . . .	183
B.1.1 General considerations and the Blockage effect . . . . .	183
B.1.2 Uniformity test with the original test section . . . . .	187
B.2 Facility design and adaptations . . . . .	189
B.2.1 The wind-tunnel . . . . .	190
B.2.2 The test section . . . . .	190
B.2.2.1 The test section geometry . . . . .	191
B.2.2.1.1 The sidewalls of the test section . . . . .	192
B.2.2.1.2 Inhibitors . . . . .	193
B.2.2.2 The cavity geometry . . . . .	194
B.3 Investigation of the Square and the Two-dimensional concept . . . . .	196
B.3.1 The in-plane investigation . . . . .	196
B.3.2 The out-of-plane investigation . . . . .	199
B.3.3 Deciding between the square and the two-dimensional design . . . . .	202
B.4 About the importance of the splitting plate . . . . .	206
B.4.1 The mean flow fields . . . . .	207
B.4.2 The vortical structures . . . . .	209
B.5 L-11 flow uniformity confirmation tests . . . . .	210
B.5.1 Inlet uniformity . . . . .	210
B.5.2 Flow symmetry . . . . .	215
B.5.3 Measuring the reference flow velocity . . . . .	217

# List of Figures

1.1	The Ariane 5 launcher. . . . .	4
1.2	Ariane 5 ECA launch on 11 August 2006 (photo from Arianespace). . . . .	4
1.3	Post-fire alumina deposition in the Titan IV SRMU nozzle cavity (from Salita (1995)). . . . .	6
1.4	Alumina formation (from Duterque (1996)). . . . .	7
1.5	Alumina droplet size distribution (from Delfour et al. (1998)). . . . .	8
1.6	The VECLA set-up (based on Guéry et al. (2000)). . . . .	12
1.7	The VALDO set-up (from Guéry et al. (2000)). . . . .	13
1.8	The MICAT1 set-up (from Guéry et al. (2000)). . . . .	14
1.9	The VIOLETTE set-up (from Guéry et al. (2000)). . . . .	15
1.10	The transparent VKI model (from Anthoine (2000)). . . . .	16
1.11	The VKI models (from Anthoine (2000)). . . . .	16
1.12	The C1x test bench (from Fabignon et al. (2000)). . . . .	17
1.13	The LP6 model (from Fabignon et al. (2000)). . . . .	18
1.14	The LP10 test bench (from Fabignon et al. (2000)). . . . .	18
2.1	The MPS P230. . . . .	22
2.2	Static- and unsteady pressure evolution in P230 during static test firing (Fabignon et al. (2003)). . . . .	22
2.3	The final geometrical parameters of the test section. . . . .	27
2.4	Different views of the final test section. . . . .	27
2.5	Particle-flow interaction. . . . .	30
2.6	The spray support system. . . . .	31
3.1	General LeDaR arrangement. . . . .	37
3.2	Sample frames of a video recording. . . . .	38
3.3	Droplets on the sidewall of the preliminary set-up. . . . .	39

3.4	Sample images of decreasing the DoF (without surface treatment).	40
3.5	Validating the adapted LeDaR measurement conditions.	41
3.6	Typical intensity variation in LeDaR images in the vicinity of the interface.	43
3.7	Comparing the different detection methods.	43
4.1	Raw image pair recorded during a PIV measurement.	46
4.2	Two-phase flow acquisition.	46
4.3	Arrangement using the preliminary technique.	49
4.4	The Mexican Hat mother wavelet.	50
4.5	The difference between the fields of view of the two cameras.	51
4.6	Test section configurations.	51
4.7	The seeding generator.	53
4.8	The seeding generator.	54
4.9	Sample image with fluorescent tracers.	55
4.10	Statistical flow field obtained with oil tracers.	55
4.11	Sample image with non-fluorescent droplets.	56
4.12	Verifying the dye content of the spray water.	57
4.13	The impact of the fluorescent tracer deposition.	58
4.14	Fluorescent tracers and droplets: black corresponds to $I = 78$ .	59
4.15	Two-phase flow measurement principle.	60
4.16	The principles of the proposed measurement technique.	60
4.17	The droplet size distribution of the spray device.	61
4.18	The UV test arrangement.	61
4.19	Visibility of the fluorescent droplets.	61
4.20	The $\lambda = 266$ nm laser-sheet passing through the quartz window.	63
4.21	Optical short-pass filter transmittance (obtained from Edmunds Optics (EO)).	64
4.22	Optical filter placement.	64
4.23	Pure water droplets visibility with $\lambda = 532$ nm illumination.	65
4.24	The visibility of the fluorescent tracers through the short-pass filter set.	65
4.25	The set-up of the simulated experiment.	66
4.26	Simultaneously recorded images.	67
4.27	Mean flow fields.	67
4.28	Spatial calibration of the simulated experiment (the unit of the axes and the contour variable are [pixels]).	68

4.29	Rhodamine B deposition in the test section. . . . .	70
4.30	Sample images of water droplets through the long-pass optical filter ( $I_{min} = 96$ , $I_{max} = 512$ , $\gamma = 2/3$ ). . . . .	70
4.31	Sample two-phase PIV images in the test section ( $I_{min} = 0$ , $I_{max} = 1024$ , $\gamma = 2/3$ ). . . . .	71
4.32	Sample background images ( $I_{min} = 0$ , $I_{max} = 1024$ , $\gamma = 2/3$ ). . . . .	73
4.33	Sample images after background subtraction ( $I_{min} = 0$ , $I_{max} = 1024$ , $\gamma = 2/3$ ). . . . .	74
4.34	Sample mean flow fields. . . . .	74
5.1	Experimental configuration. . . . .	80
5.2	Volumetric droplet size repartition of the poly-disperse spray. . . . .	80
5.3	The water supply system. . . . .	81
5.4	The calibration curve of the Venturi-based flow meter (the error bars represent the RMS of $U_{PT}$ ). . . . .	81
5.5	The effect of the inhibitor inclination on the flow ( $TI_V = v/U_0$ ). . . . .	82
5.6	The liquid extraction tube installed on the inhibitor. . . . .	82
5.7	Image recorded with the high-speed camera in the nominal configuration. . . . .	83
5.8	The camera trigger signal. . . . .	84
5.9	LeDaR data processing. . . . .	85
5.10	The difference between the LeDaR and the jug measurements. . . . .	85
5.11	Liquid accumulation results of different flow velocities and inhibitor sizes (the "X" symbols show the nominal configurations). . . . .	88
5.12	Liquid accumulation results of different inhibitor positions (the "X" symbols show the nominal configurations). . . . .	89
5.13	Liquid accumulation results of different cavity parameters (the "X" symbols show the nominal configurations). . . . .	90
5.14	The relative distance between the nozzle tip and the inhibitor tip ( $OT2NT$ ). . . . .	90
6.1	Experimental geometry. . . . .	93
6.2	Fields of view of the PIV measurements (the fields are slightly shifted transversally to facilitate the understanding). . . . .	94
6.3	Signal-to-noise ratio distribution of the PIV measurements. . . . .	95
6.4	Schematic of the main boundary elements and mean flow structures. . . . .	96
6.5	Results of the ensemble averaged PIV campaign in the symmetry plane. . . . .	97
6.6	Flow field by changing the medium in the bottom of the cavity. . . . .	98
6.7	Numerical domain geometry. . . . .	99
6.8	Inlet velocity distribution. . . . .	100

6.9	Some examples of the hybrid grid of the numerical domain. . . . .	100
6.10	Results of the time averaged LES simulation in the symmetry plane (single-phase). . . . .	101
6.11	Mid-span plane comparison between the experimental and the numerical longitudinal velocity components. . . . .	104
6.12	Mid-span plane comparison between the experimental and the numerical velocity fluctuation magnitudes. . . . .	105
6.13	Regions of numerical boundaries used for liquid accumulation record through droplet mass counting. . . . .	105
6.14	Results of the time averaged LES simulation in the symmetry plane using mono-disperse droplet size distribution (based on 3 FTs). . . . .	107
6.15	Instantaneous droplet-distributions. . . . .	108
6.16	Results of the time averaged LES simulation in the symmetry plane using poly-disperse droplet size distribution (based on 3 FTs). . . . .	109
6.17	Volumetric droplet size repartition of the poly-disperse spray during the droplet size assessment. . . . .	110
6.18	Instantaneous spatial droplet distributions. . . . .	111
6.19	The geometry of the test section and the FoVs during the two-phase PIV experiments. . . . .	112
6.20	Droplet size distribution of the spray device. . . . .	113
6.21	Measurement quality and mean flow field. . . . .	115
6.22	Velocity magnitude distribution. . . . .	116
6.23	Velocity magnitude profile ( $ \mathbf{U} $ ) at $Y/h = 2$ . . . . .	117
6.24	Transversal velocity component fluctuation. . . . .	118
6.25	Longitudinal velocity component fluctuation. . . . .	119
6.26	Determining the physical diameters of the detected droplets (using the data of FoV#2). . . . .	119
6.27	Mean droplet concentration. . . . .	120
6.28	Mean droplet diameter distribution. . . . .	120
6.29	Velocity component differences (air-droplets). . . . .	122
6.30	Velocity field differences (air-droplets). . . . .	122
6.31	Turbulence intensity differences (air-droplets). . . . .	123
7.1	The vortex analysis domain. . . . .	127
7.2	The distribution of the number of locally independent samples considering the $U$ velocity component of the 593 poly-dispersed CFD fields. . . . .	128
7.3	Spatial vortex distribution map at the nominal reference velocity. . . . .	129

---

7.4	Statistical properties of the identified coherent structures (concentration and vortex core diameter). . . . .	130
7.5	The estimated Kolmogorov scale distribution using the nominal speed PIV measurement data. . . . .	130
7.6	Normalized vortex diameter distributions (Nominal speed cases). . . . .	131
7.7	The effect of the flow field resolution on the vortex detection. . . . .	132
7.8	Statistical properties of the identified coherent structures (Oseen likeness). . . . .	134
7.9	Statistical properties of the identified coherent structures (Sign of rotation and circulation magnitude). . . . .	136
7.10	Turbulence spectrum estimation. . . . .	137
7.11	Normalized angular velocity distribution. . . . .	139
7.12	Normalized vortex diameter distributions (two-phase PIV). . . . .	141
7.13	Vortex concentration distribution obtained with the two-phase PIV experiments. . . . .	141
7.14	Mean core diameter distribution obtained with the two-phase PIV experiments. . . . .	142
7.15	Oseen likeness distribution obtained with the two-phase PIV experiments. . . . .	142
7.16	Vorticity peak distribution obtained with the two-phase PIV experiments. . . . .	143
7.17	Preferential direction of rotation with the two-phase PIV experiments. . . . .	143
7.18	Circulation magnitude distribution with the two-phase PIV experiments. . . . .	144
7.19	Normalized angular velocity distribution with the two-phase PIV experiments. . . . .	144
7.20	Turbulence spectrum estimation. . . . .	144
8.1	Dripping visualization arrangement. . . . .	148
8.2	Sample frames of the high-speed camera visualization of the dripping phenomenon. . . . .	149
8.3	Sample images of the CCD camera visualization of the dripping phenomenon. . . . .	150
8.4	Sample images of the upstream surface of the inhibitor with closed spray. . . . .	151
8.5	Instantaneous droplet distributions with quasi radial flow injection. . . . .	152
8.6	Instantaneous droplet distributions with radial flow injection in the axisymmetric domain (A common legend, shown in Figure 8.6(a) is applicable to all the sub-figures). . . . .	154
8.7	Instantaneous vortex-droplet distribution in FoV#2 of the two-phase PIV investigation. . . . .	156
8.8	Statistical vortex-droplet distribution in the two-phase PIV investigation. . . . .	156
A.1	A conventional PIV arrangement. . . . .	175
A.2	A conventional PIV arrangement. . . . .	177
A.3	The 2D Marr mother wavelet. . . . .	180

B.1	The initial arrangement of the VKI L-11 wind-tunnel. . . . .	184
B.2	Effect of using different blockages. . . . .	185
B.3	The square blockage installed on the test section of the wind-tunnel. . . . .	186
B.4	Speed test with the new blower of the L-11 wind-tunnel and with the square blockage. . . . .	187
B.5	The tubing between the blower and the wind-tunnel. . . . .	188
B.6	Preliminary flow inlet uniformity characterization location. . . . .	188
B.7	The applied hot-wire. . . . .	189
B.8	Mean velocity profiles of the inlet uniformity characterization. . . . .	189
B.9	The L-11 wind-tunnel installed vertically. . . . .	190
B.10	Test section concepts. . . . .	192
B.11	The main walls of the test section. . . . .	193
B.12	The position of the additional plates to fix the splitting plate. . . . .	193
B.13	The cavity at its position in the square configuration. . . . .	195
B.14	The cavity at its position in the square configuration. . . . .	195
B.15	Test section configurations. . . . .	197
B.16	Mean flow field (square configuration; in-plane). . . . .	197
B.17	Mean flow field (2D configurations; in-plane). . . . .	198
B.18	Velocity magnitude at $X = 8$ mm. . . . .	198
B.19	Velocity magnitude at $X = 80$ mm. . . . .	199
B.20	Test section configurations. . . . .	200
B.21	Measurement quality in the perpendicular planes. . . . .	201
B.22	Mean velocity field at $X = 8$ mm. . . . .	201
B.23	Mean velocity field at $X = 80$ mm. . . . .	202
B.24	$ V $ profiles at $X = 80$ mm (2D inhibitor; $h = 33.5$ mm). . . . .	203
B.25	Velocity magnitude and streamlines. . . . .	204
B.26	Absolute vorticity plot. . . . .	204
B.27	Negative Lambda distribution. . . . .	205
B.28	Mean flow field (square configuration; in-plane). . . . .	206
B.29	Resulting mean flow fields. . . . .	207
B.30	The location of the maximum velocity. . . . .	208
B.31	Flow acceleration in the vena contracta. . . . .	209
B.32	The evolution of mean vortex location. . . . .	210

---

B.33 PIV measurement planes. . . . .	211
B.34 The mean in-plane signal-to-noise ratio distribution. . . . .	211
B.35 The mean perpendicular plane signal-to-noise ratio distribution. . . . .	212
B.36 The mean in-plane flow field. . . . .	212
B.37 The mean perpendicular plane flow field. . . . .	213
B.38 The projection of the measured velocity vector. . . . .	213
B.39 The parallax effect on a uniform flow. . . . .	214
B.40 The measured mean flow field by correcting the parallax effect. . . . .	215
B.41 Symmetry verification geometry. . . . .	216
B.42 The incoming flow. . . . .	216
B.43 Longitudinal velocity component evolution at $x = -93.2\text{mm}$ . . . . .	217
B.44 The fluctuation of the longitudinal velocity component at $x = -93.2\text{mm}$ . . . . .	217
B.45 Velocity magnitude comparison inside the cavity. . . . .	218
B.46 Longitudinal velocity component evolution in the cavity at $x = 300\text{mm}$ . . . . .	218
B.47 Comparing the transversal velocity component fluctuation inside the cavity. . . . .	219
B.48 The fluctuation of the longitudinal velocity component in the cavity at $x = 300\text{mm}$ . . . . .	219
B.49 The pressure transducers of the wind-tunnel. . . . .	220
B.50 Typical Validyne calibration curve. . . . .	220

# List of Tables

1.1	Cold-flow experimental facilities (Guéry et al. (2000)). . . . .	12
1.2	Hot-gas experimental facilities. . . . .	17
2.1	Approximate P230 properties . . . . .	23
2.2	The ideal properties of the droplet-phase model . . . . .	30
2.3	The actual properties of the droplet-phase model . . . . .	31
4.1	Two-phase PIV technique comparison. . . . .	62
5.1	The main characteristics of the spray device for the nominal condition . . . . .	86
5.2	The experimental parameters and the obtained results . . . . .	88
6.1	Droplet size effect on the accumulation rate. . . . .	110
6.2	Two-phase PIV acquisition parameters. . . . .	112
6.3	Two-phase PIV processing parameters. . . . .	114
7.1	Database parameters for the vortex detection. . . . .	126
7.2	Number of detected vortices (at nominal speed). . . . .	128
7.3	Estimated turbulence dissipation rate (at nominal speed). . . . .	138
7.4	Two-phase PIV vortex detection results. . . . .	140
8.1	The importance of dripping . . . . .	155
B.1	Blockage geometries for the speed tests . . . . .	185
B.2	Determined inhibitor sizes . . . . .	194
B.3	The flow acceleration over the inhibitors . . . . .	207

# Abstract

The present research project is carried out at the von Karman Institute for Fluid Dynamics (Rhode-Saint-Gense, Belgium) with the financial support of the European Space Agency.

The first stage of spacecrafts (e.g. Ariane 5, Vega, Shuttle) generally consists of large *solid propellant rocket motors* (SRM), which often consist of segmented structure and incorporate a submerged nozzle. During the combustion, the regression of the solid propellant surrounding the nozzle integration part leads to the formation of a cavity around the nozzle lip. The propellant combustion generates liquefied alumina droplets coming from chemical reaction of the aluminum composing the propellant grain. The alumina droplets being carried away by the hot burnt gases are flowing towards the nozzle. Meanwhile the droplets may interact with the internal flow. As a consequence, some of the droplets are entrapped in the cavity forming an alumina puddle (slag) instead of being exhausted through the throat. This slag reduces the performances.

The aim of the present study is to characterize the slag accumulation process in a simplified model of the MPS P230 motor using primarily optical experimental techniques. Therefore, a 2D-like cold-gas model is designed, which represents the main geometrical features of the real motor (presence of an inhibitor, nozzle and cavity) and allows to approximate non-dimensional parameters of the internal two-phase flow (e.g. Stokes number, volume fraction). The model is attached to a wind-tunnel that provides quasi-axial flow (air) injection. A water spray device in the stagnation chamber realizes the models of the alumina droplets, which are accumulating in the aft-end cavity of the motor.

To be able to carry out experimental investigation, at first the the VKI *Level Detection and Recording*(LeDaR) and *Particle Image Velocimetry* (PIV) measurement techniques had to be adapted to the two-phase flow condition of the facility.

A parametric liquid accumulation assessment is performed experimentally using the LeDaR technique to identify the influence of various parameters on the liquid deposition rate. The *obstacle tip to nozzle tip distance* ( $OT2NT$ ) is identified to be the most relevant, which indicates how much a droplet passing just at the inhibitor tip should deviate transversally to leave through the nozzle and not to be entrapped in the cavity.

As LeDaR gives no indication of the driving mechanisms, the flow field is analysed experimentally, which is supported by numerical simulations to understand the main driving forces of the accumulation process. A single-phase PIV measurement campaign provides detailed information about the statistical and instantaneous flow structures. The flow quantities are successfully compared to an equivalent 3D unsteady LES numerical model.

Two-phase flow CFD simulations suggest the importance of the droplet diameter on the accumulation rate. This observation is confirmed by two-phase flow PIV experiments as well. Accordingly, the droplet entrapment process is described by two mechanisms. The smaller droplets (representing a short characteristic time) appear to follow closely the air-phase. Thus,

they may mix with the air-phase of the recirculation region downstream the inhibitor and can be carried into the cavity. On the other hand, the large droplets (representing a long characteristic time) are not able to follow the air-phase motion. Consequently, a large mean velocity difference is found between the droplets and the air-phase using the two-phase flow measurement data. Therefore, due to the inertia of the large droplets, they may fall into the cavity in function of the  $OT2NT$  and their velocity vector at the level of the inhibitor tip.

Finally, a third mechanism, dripping is identified as a contributor to the accumulation process. In the current quasi axial 2D-like set-up large drops are dripping from the inhibitor. In this configuration they are the main source of the accumulation process. Therefore, additional numerical simulations are performed to estimate the importance of dripping in more realistic configurations. The preliminary results suggest that dripping is not the main mechanism in the real slag accumulation process. However, it may still lead to a considerable contribution to the final amount of slag.

# Acknowledgement

Dear reader, before going any further, list everything by which *You* think, *You* made the completion of the present dissertation possible. I ask you to consider not only technical contribution, but also emotional support<sup>1</sup>. Please do not read any further before having a clear picture...

...now that you see *Your* contribution, believe me, you forgot at least a few things. However, I remember all those things as well and I am even more grateful to *You* than *You* think! If you know me, you jump now to the next chapter of your interest.

At first, I would like to thank the financial support of the European Space Agency. In particular, I am grateful to Johan Steelant from ESTEC, who dealt not only administratively with the present project, but provided his kind guidance as well.

Most importantly, I am glad that I had the opportunity to work under the supervision of Jérôme Anthoine, whose greatly valuable scientific experience, enthusiasm, dynamism and unprecedented patience gave a continuous inspiration and support throughout the years.

Furthermore, I am thankful to Professors Michel Riethmuller and Jean-Marie Buchlin for the numerous discussions, which helped to keep the path of my work on a consistent track.

I cannot forget the support of my former supervisor István Goricsán and Professor Mario Carbonaro, who made me possible to join the unique international environment of the *von Karman Institute for Fluid Dynamics*.

Additionally, the members of all the departments, especially the ones from the *Environmental and Applied Fluid Dynamics Department* are appreciated, for all their contribution, as practically each one of them made one thing or another move towards a better direction.

I wish to express my extinguished gratitude to all my students, who participated in the evolution of the present research. I prefer mentioning these highly inspiring people in the order of their arrival: Antonio De Lauretis, Andrew Simpson, Nicolas Tran, Patrick Flon, Roberta Di Biase, Michael Crichton, Erinc Erdem, Laurent Dessart, Juan García Martínez, Tamás Régert and Delphine Laboureur.

For the technical support, for the construction of numerous pieces required for the various experimental installations and for lending me all the necessary tools I wish to thank the help of Jacques Missart, Günther Cahay, Didier Welter, Guillaume Diquas, Fabien Bosthijs, Michel Bavier, Karl Colussa, Mohammed Rhamsoussi, Alain Goblet and the whole VKI workshop.

How could I have done anything without my colleagues and friends? Life would have been certainly worthless at the VKI without the presence of Anne and Marcos right from the beginning of my stay. I am glad that I know you and I can call you real friends! I always admired

---

<sup>1</sup>which is equally appreciated

the patience of Jérôme and Patrick with me in spite of your extremely busy time-table. The determination, the energy and the selfless humanity of Raf towards all sorts of challenges fills me with great wonder. Simply by seeing (and later remembering) the never decaying joy of Christophe and Thomas gave all the time new hope even in the most difficult periods. Only by recalling the optimism of e.g. Dilek, Delphine, Flora, Antonio, Nicolas, Tamás or Raimondo has always been sufficient to remind myself that *impossible* does not exist. I am also glad for the company of the core members of the *Hungarian community of the VKI*: Tamás, Gábor, Péter, János and Balázs. I am scared, because I am sure, I have not mentioned many others; if one of these victims were you, please forgive me; it is the present rush, which lead to this mistake!

Without repeating the above mentioned names again, I wish to thank the supportive company of all those, who could stand my presence in their vicinity, starting from Vicky until Mike, Julien and Hyun Woo.

Finally, my family deserves my greatest gratitude, who supported me even in the most difficult conditions during all these (and previous) long years. Being far from them is sometimes really difficult and thus all their support is even more appreciated.

Leaving to the end, but I say "above all", I consider myself infinitely lucky to have Kriszta, my wife on my side. In spite of the numerous lonely nights and weekends she supported me inexhaustibly and unconditionally. She is one of the key persons without whom the present achievements would not have been possible.

# Nomenclature

## Alphanumeric symbols

Symbol	Typical unit	Explanation
$a$	[m/s]	Speed of sound
$A$	[m <sup>2</sup> ; mm <sup>2</sup> ]	Area
$BR = S_{blockage}/S_{total}$	[-]	Blockage Ratio
$c_d$	[-]	Discharge coefficient
$c_{vc}$	[-]	Vena contracta coefficient
$d_{10}; D_{10}$	[μm]	Average droplet diameter
$d_{32}; D_{32}$	[μm]	Sauter mean droplet diameter
$D$	[m]	Motor internal diameter
$D_a$	[mm]	Aperture diameter of the camera lens
$D_i$	[pixel]	Droplet image size
$D_o$	[m]	Nozzle throat diameter
$D_p, d_p$	[μm]	Droplet diameter
$D_{pixel}$	[μm]	The physical dimension of one pixel of the CCD sensor
$D_v$	[mm]	Vortex core diameter
$Def_{p2p}$	[mm]	Peak-to-peak deformation of the liquid surface in the cavity
$Def_{p2pmean}$	[mm]	The mean peak-to-peak deformation of the liquid surface in the cavity
$E_{laser}$	[mJ]	Laser pulse energy
$f$	[Hz]	Frequency
$f_l$	[mm]	Focal length of the camera optics
$f\# = f_l/D_a$	[-]	Focal number (speed / stop number) of the camera optics
$f_d$	[Hz]	Dripping frequency (drops/seconds)
$FwStep$	[-]	Forward-step detection operator matrix
$h$	[mm]	Inhibitor height
$I$	[-]	Intensity level
$L_i$	[mm]	Longitudinal inhibitor location measured from the nozzle tip

$L_{cam}$	[mm]	Camera - laser-sheet distance
$M$	[-]	Magnification of the camera
$M_0 = U_0/a$	[-]	Mach number
$M_{PIV}$	[mm/pixel]	Magnification of the PIV camera
$o$	[mm]	Nozzle throat opening
$O2NR = L_i/h$	[-]	Obstacle-to-Nozzle Ratio
$OT2NT$	[mm]	Obstacle tip to nozzle tip distance
$\Delta p$	[Pa]	Pressure difference; pressure drop
$p_{air}$	[bar]	Spray air supply pressure
$P_{laser}$	[W]	Laser light power
$p_{water}$	[bar]	Spray water supply pressure
$p_{liq.}$	[bar]	Spray liquid supply pressure
$PR = S_{passage}/S_{total}$	[-]	Passage Ratio
$\dot{Q}_V; Q_V$	[m <sup>3</sup> /s]	Volumetric flow-rate
$\dot{Q}_{Vd}$	[l/min]	Volumetric droplet flow-rate
$\dot{Q}_{Vf}$	[m <sup>3</sup> /s]	Volumetric fluid flow-rate
$\dot{Q}_m; Q_m$	[kg/s]	Mass flow-rate
$Re_h$	[-]	Reynolds number based on $h$
$RH$	[%]	Relative Humidity
$ RMS  = \sqrt{RMS_U^2 + RMS_V^2}$	[m/s]	The magnitude of the in-plane (longitudinal and transversal) velocity fluctuation
$RMS_U, RMS_V, RMS_W$	[m/s]	The RMS of the longitudinal, transversal, span-wise velocity components
$S$	[m <sup>2</sup> ; mm <sup>2</sup> ]	Section
$\Delta \bar{s}$	[m; mm]	Displacement
$SN$	[-]	Signal-to-Noise ratio
$SobelY$	[-]	Sobel operator matrix
$St$	[-]	Stokes number
$\Delta t$	[ $\mu$ s]	Separation time of the PIV experiments
$T$	[K]	Temperature
$TI = RMS/U_0$	[%]	Turbulence intensity
$TI_U, TI_V, TI_W$	[%]	The turbulence intensity of the longitudinal, transversal, span-wise velocity components
$t$	[s]	Time
$t_{sp}$	[mm]	Splitting plate thickness
$t_{exp}$	[s]	Exposure time (acquisition time) during which the camera shutter is open
$ \bar{U} ,  \mathbf{U} $	[m/s]	Velocity magnitude
$U, V, W$	[m/s]	Longitudinal, transversal, span-wise velocity components
$u, v, w$	[m/s]	The RMS of the longitudinal, transversal, span-wise velocity components
$ \mathbf{U}  = \sqrt{U^2 + V^2}$	[m/s]	The magnitude of the in-plane (longitudinal and transversal) velocity components

$U_0$	[m/s]	Free stream (reference) flow velocity
$U_{PT}$	[V]	Pressure transducer raw voltage
$U_{inj.}$	[m/s]	Flow injection velocity
$U_{jet}$	[m/s]	Flow velocity in the <i>vena contracta</i>
$V_{acc}$	[l]	Accumulated liquid volume
$X, Y, Z (x, y, z)$	[mm]	Longitudinal, transversal, span-wise axes
$w$	[mm]	Cavity width
$We$	[-]	Weber number
$W_{ol}$	[%]	Window overlapping factor
$W_{ref}$	[-]	Number of window refinement steps (iterations)
$W_s$	[pixel <sup>2</sup> ]	Window size during PIV processing
$W_{s0}$	[pixel <sup>2</sup> ]	Initial window size during PIV processing

### Greek symbols

$\alpha_p$	[-]	Volume fraction
$\Gamma$	[m <sup>2</sup> /s]	Circulation
$\gamma$	[-]	Gamma correction parameter during non-linear image conversion ( $I_{out} = I_{in}^\gamma$ )
$\Delta$	[mm/cell]	Cell size, grid resolution
$\lambda$	[nm]	Light wavelength
$\lambda_2$	[1/s <sup>2</sup> ]	The second eigenvalue of the $S^2 + \Omega^2$ tensor ( $S$ and $\Omega$ being the symmetric and anti-symmetric part of the velocity gradient tensor respectively); used for vortex detection
$\rho$	[kg/m <sup>3</sup> ]	Density
$\rho_f$	[kg/m <sup>3</sup> ]	Fluid density
$\sigma$	[N/m]	Surface tension
$\tau_f$	[s]	Flow characteristic time
$\tau_p$	[s]	Particle/droplet characteristic time
$\omega$	[1/s]	Vorticity
$\omega_v$	[-]	Dimensionless angular velocity of a vortex

### Abbreviations

#	Number
AP	Ammonium perchlorate
ASSM	Aerodynamics of Segmented Solid Motors research and technology program
CCD	Charge-Coupled Device
CMOS	Complementary Metal-Oxide Semiconductor
CNES	Centre National d'Etudes Spatiales (French National Space Agency)

CVS		Corner (Angle) Vortex Shedding
DoF	[mm]	Depth-of-Field of the camera (the thickness of the field, which is in focus)
DTV		Droplet Tracking Velocimetry
EAP		Étage d'Acceleration à Poudre (the solid rocket motor of the Ariane 5 launcher)
FoV (FoVs)	[mm <sup>2</sup> ]	Field-of-view (Fields-of-view) of the camera
fps	[fps]	Frames-per-second (frame-rate)
fft; FFT		Fast Fourier Transform
FT (FTs)	[-]	Flow-through: the time required for a flow particle to travel through the whole numerical domain.
HPM		High-Power Motor (Space Shuttle Booster)
HTPB		Hydroxyl-terminated polybutadiene
LDA		Laser Doppler Anemometry
LES		Large Eddy Simulation
LeDaR		Level Detection and Recording
Meas.#		Measurement number
OVS		Obstacle Vortex Shedding
PIV		Particle Image Velocimetry
PSD		Power Spectral Density
PTV		Particle Tracking Velocimetry
RANS		Reynolds Averaged Navier-Stokes simulation
RSRM		Redesigned Solid Rocket Motor (Space Shuttle Booster)
Spray#		Spray number
SRM		Solid Rocket Motor
SRMU		Solid Rocket Motor Upgrade (the SRM of the Titan IV launcher)
SVS		Surface (Parietal) Vortex Shedding
TTL		Transistor-Transistor Logic
VKI		von Karman Institute

## **The fundamentals of the study**

# Chapter 1

## Introduction

### 1.1 Position of the problem

The utilization of civil-purpose rocket motors rapidly accelerated following the 1950s, when human became capable of launching objects to Earth orbit (starting with Sputnik-1) and into Space. This era of space exploration (studying Earth, the Solar System and the Universe) required larger and larger launcher vehicles for the ever increasing mass of spacecrafts and human missions.

During the decades, as Space became less distant thanks to the continuously developing vehicle technologies, the exploratory purpose started to shift towards commercial purposes. Various communication-, broadcasting-, meteorological-, positioning-, scientific-, etc. satellites need to be launched in constantly increasing number to altitudes varying between Low Earth Orbit (LEO) to Geostationary Earth Orbit (GEO).

In this market, the European Space Agency (ESA) is present with the Ariane 5 launcher, which appears to be one of the most competitive of the available vehicles (Isakowitz et al. (1999)). The current project is also associated to this vehicle. Its latest configuration, Ariane 5 ECA (shown in Figure 1.1(b) and 1.2) is capable of carrying 9.6 t payload to Geosynchronous Transfer Orbit (GTO), which is an elliptical orbit that allows to reach GEO. Furthermore, Ariane 5 is designed to have double launch capability to place two satellites simultaneously into orbit. The whole vehicle is 52 m tall and weights 780 t at lift-off. Its development is founded by ESA, managed by CNES (French National Space Agency) and operated by Arianespace. The launches take place at Europe's spaceport in Guiana Space Center, near Kourou, French Guiana.

Like most heavy launchers, Ariane 5 consists of several stages. The first stage comprises the Cryogenic main stage (EPC) with the Vulcain (more recently Vulcain 2) engine and two solid rocket motors (EAP) on either side.

Each EAP is 3 m in diameter and 31 m tall. Their casing is made of 8 mm thick steel, which can resist operating pressures above 60 bar. They weight 37 t each, when empty and they are filled with 238 t of solid propellant (therefore also called *MPS P230*), which are organized in three segments. Together, the EAPs provide about 11000 kN thrust during liftoff, which is about 92% of the total liftoff thrust. At tail-off, which occurs about 130 s after liftoff, the SRMs are jettisoned. By that time, the vehicle reaches an altitude of 60 km. After separation, the motors fall back to the Atlantic Ocean. They can be equipped with a parachute system, which allows recovery for examination purposes. The casing is never refurbished, like the Space Shuttle

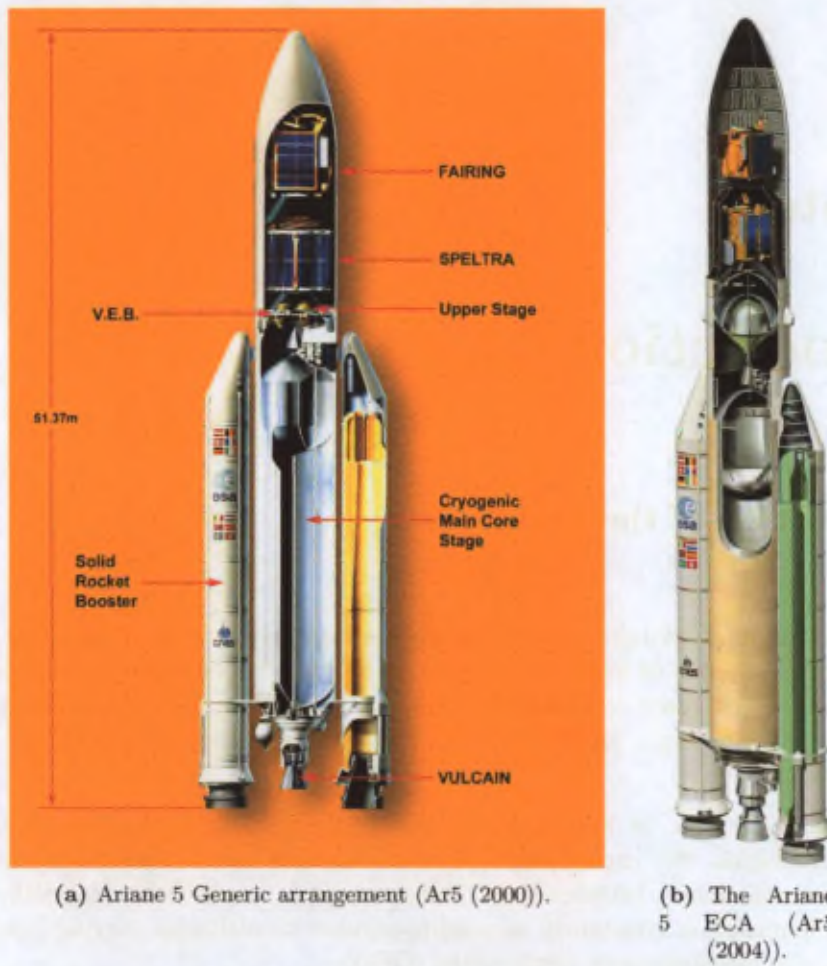


FIGURE 1.1 – *The Ariane 5 launcher.*



FIGURE 1.2 – *Ariane 5 ECA launch on 11 August 2006 (photo from Arianespace).*

Boosters.

As its name shows, overall the EPC provides the main thrust of the vehicle. It is about 5.4 m

in diameter and 31 m tall including the Vulcain (2) engine and two aluminium tanks for the 150 t liquid oxygen ( $\text{LO}_2$ ) and 25 t liquid hydrogen ( $\text{LH}_2$ ) fuel. In vacuum, it develops about 1350 kN thrust. The Vulcain engine is started about 9 seconds before EAP ignition (liftoff) to ensure and verify its proper functioning. From then, it operates during about 540 s, while the launcher reaches an altitude between 160 and 210 km depending on the mission objectives. After the On Board Computer (OBC) shuts down the EPC, it re-enters the atmosphere still above the Atlantic Ocean.

Above the EPC the Upper Stage can be found, which is encircled by the Vehicle Equipment Bay (VEB). The VEB contains all vehicle avionics: telemetry, guidance, stage sequencing and destruction systems. The inertial reference for the guidance is provided by two redundant laser gyroscopes.

The Upper Stage is used for the orbital injection and it can contain either the storable propellant upper stage (EPS, shown in Figure 1.1(a)) or the cryogenic upper stage (ESC-A, visible in Figure 1.1(b); or later the ESC-B Vinci engine). The reignitable EPS is mainly used for LEO missions, as it provides only 29 kN thrust and 321 s specific impulse. Ariane 5 ECA generally uses ESC-A, which contains 14 t of  $\text{LO}_2$  and ( $\text{LH}_2$ ). Powered by the HM7B engine of the Ariane 4 third stage, it delivers about 65 kN thrust in vacuum and 446 s specific impulse.

Finally, the payload fairing consists of two large composite half shells, which have acoustic absorbers on their interior to damp the noise generated at liftoff. The height of the fairing can be between 12.7 m and 17 m depending on the actual mission requirement. In case of a dual launch, the spacecraft compartment can be divided into two parts using either the SPELTRA (shown in Figure 1.1(a)) or the SYLDA5 (visible in Figure 1.1(b) module. SPELTRA is an external structure and therefore it has an external diameter of 5.4 m. SYLDA5 has a usable internal diameter of 4 m. Both structures surround the inner spacecraft and support the upper spacecraft. The fairing separates from the launcher already around 185 s after liftoff.

As it is shown from the above overview, Ariane 5 incorporates large solid rocket motors (SRMs). In these EAPs like in several other large SRMs (Space Shuttle Boosters, Titan IV Solid Rocket Motor Upgrade, etc.), the nozzle is submerged in the last segment of solid propellant to shorten the overall length. It means that the convergent, the sonic throat and a part of the divergent are surrounded by solid propellant. This integration allows orientation of the nozzle to provide adaptation of the rocket trajectory during the launch.

On the one hand, during the combustion, the regression of the solid propellant surrounding the nozzle integration part leads to the formation of a cavity around the nozzle lip (see Figure 2.1(c)).

On the other hand, the propellant combustion generates liquefied alumina droplets coming from chemical reaction of the aluminium composing the propellant grain. During the launch, some of these droplets are entrapped in the cavity instead of being exhausted through the throat. The droplet accumulation in the cavity generates an alumina puddle, also called slag (VKI (2002)). During the first static firings of the EAP, the average accumulated slag mass was equal to about 2070 kg for one motor (Peveigne and Le Helley (1998)).

The slag reduces the performances of the solid propellant motor simply due to momentum impulse loss and due to its dead weight absence of impulse generation and hence, it is undesirable. Therefore, this slag accumulation phenomenon is the object of the current investigation.

## 1.2 Background

Solid rocket motors contain conical propellant grains attached to their inner surface (for easier understanding see an example in Figure 2.1). The propellant grains are regressing radially during the combustion. Therefore, a flow is generated all along their surface (injected radially), which is then travelling towards the nozzle to leave the combustion chamber. As the combustion products (*mass*) escape at high velocity through the nozzle, a force is acting on the SRM (action-reaction), which is the thrust.

While the flow is travelling towards the nozzle, on the one hand it is constantly accelerating. On the other hand, instabilities may occur in the flow field causing e.g. vortex shedding (Vuillot (1995); Traineau et al. (1997)) or surface vortex generation (Lupoglazoff and Vuillot (1996)) as well. Concerning the topology of the flow, more details will be given in section 2.1.

In general, non-metalized solid propellants turn all their ingredients into gaseous phase during the combustion and therefore they do not produce slag. However, in order to increase the thrust, the enthalpy of the combustion is increased by adding aluminium to the propellant material (Geisler (2002)). As an example, the grains of the Ariane 5 EAPs contain 14% polybutadiene (HTPB) binder, 68% ammonium perchlorate (AP) oxidizer and 18% aluminium powder (altogether about 238 t solid fuel). This kind of propellants generate liquified alumina droplets ( $\text{Al}_2\text{O}_3$ ) as a residual of the combustion, which may accumulate in stagnant areas inside the motor (primarily in the nozzle cavity shown in Figure 1.3 and 2.1(c)) and generate alumina puddle, also called *slag*.

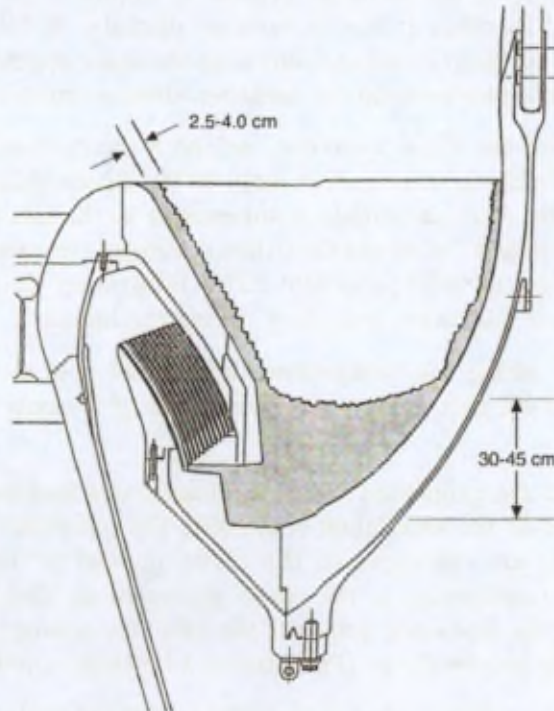


FIGURE 1.3 – Post-fire alumina deposition in the Titan IV SRMU nozzle cavity (from Salita (1995)).

In the followings, the life of alumina is shown: section 1.2.1 explains the formation of the alumina droplets and section 1.2.2 summarizes the history of investigations of the slag accumulation process.

### 1.2.1 Alumina formation

The formation of the alumina droplets is summarized by Duterque and Lambert (1998) and Jackson et al. (2005). Initially, the propellant (e.g. the grains of the EAP) contains spherical AP with a typical diameter of about  $200\ \mu\text{m}$ . The smaller aluminium particles (typically  $5$  to  $40\ \mu\text{m}$  diameter) are located in the pockets between the AP (please follow Figure 1.4). During the propellant regression, when the aluminium particles are exposed at the surface, two phenomena may occur:

- on the one hand, some of the aluminium is directly carried away by the flow. Later, a part of their material evaporates forming smoke and the remaining will form fine alumina droplets (up-to  $3$  to  $4\ \mu\text{m}$ ) during the combustion.
- on the other hand, aluminium particles may agglomerate on the propellant surface forming large globules. As the *pocket model* of Beckstead (1977) and Cohen (1983) describes, the size of the agglomerate is dependent on both the AP diameter and the initial aluminium particle size, since the AP diameter defines the size of the pockets available for the set of aluminium particles, which might form a globule.

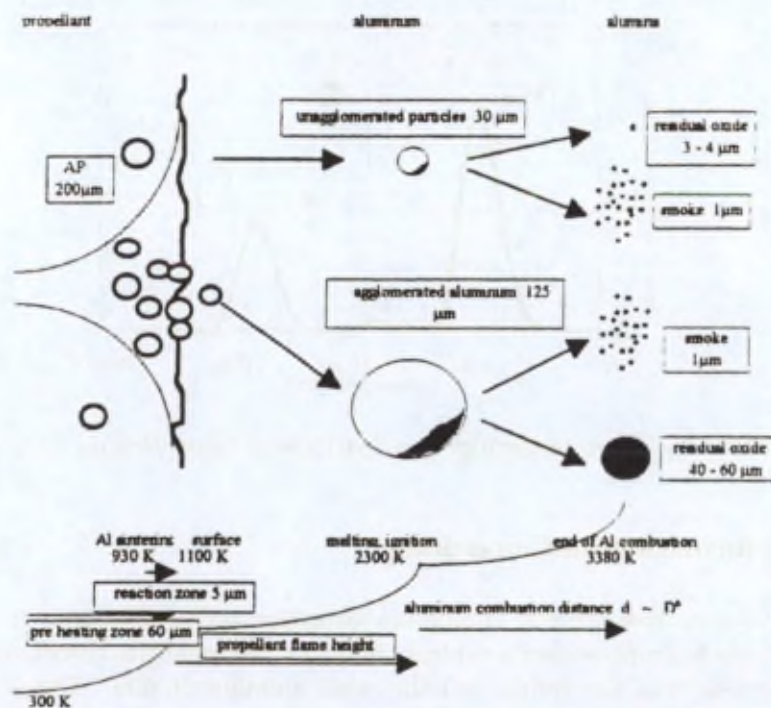


FIGURE 1.4 – Alumina formation (from Duterque (1996)).

As the agglomerate melts - still before the combustion -, an alumina cap is forming on its surface. In practice, the aluminium particles embedded in the propellant already contain a protective layer of alumina (Duterque (1996) assumes a thickness of  $5\ \text{nm}$ ). By burning propellant samples in a pressurized chamber, with optical methods Duterque (1996) found that the large agglomerates have a median diameter of about  $D_{05} = 125\ \mu\text{m}$  (with a mass fraction around  $35\%$  according to Duterque and Lambert (1998)). The cap of such an agglomerate can contain alumina equivalent to a  $15\ \mu\text{m}$  spherical particle.

The agglomeration process is further studied by Trubert (2000) confirming the applicability of the pocket model of Cohen (1983). Furthermore, using high-speed camera imaging, Trubert (2000) measured the ignition- and burning times of Al droplets as well. Furthermore, Legrand et al. (2000) studied the effect of  $\text{CO}_2$  and HCl gases on the combustion of levitating aluminium particles.

As it can be seen, the larger alumina particle formation is initiated by the agglomeration process prior to combustion. As the dilatation coefficient of aluminium and alumina differs by an order of magnitude, in the oxidizing environment containing large thermal gradients, the agglomerate surface is constantly renewing and thus the caps might even grow just before the combustion. Furthermore, according to Law (1973), some of the small particles can later retrodiffuse from the gas-phase as well. Naturally, due to evaporation, some of the material of the agglomerates forms smoke as well by the end of the combustion. The actual burning process and the burning rate are studied with optical technics by Melcher et al. (2002).

Considering only the remaining large agglomerates, a final alumina droplet size of typically 30 to 70  $\mu\text{m}$  is reported by Duterque (1996). Later, Duterque and Lambert (1998) obtain about 40 to 50  $\mu\text{m}$  final alumina droplets. Other authors find slightly different values (see e.g. the right-hand side lobe in Figure 1.5), but as a common consensus, the large alumina droplet sizes always fall within the range of 20 to 200  $\mu\text{m}$  with a mean diameter around 60 to 70  $\mu\text{m}$ .

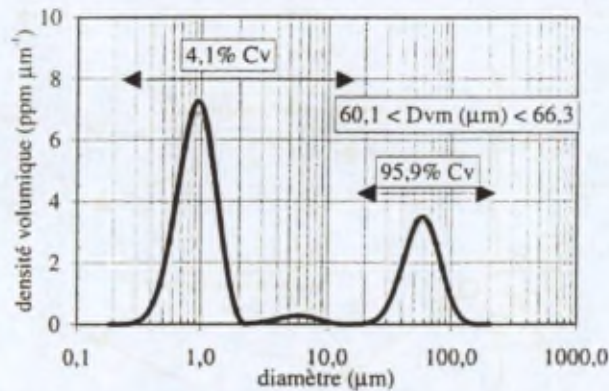


FIGURE 1.5 – Alumina droplet size distribution (from Delfour et al. (1998)).

### 1.2.2 Slag formation and modelling

As it can be seen from the way of alumina formation and qualitatively in Figure 1.5, finally the generated  $\text{Al}_2\text{O}_3$  droplets have a typical bimodal log-normal size distribution. The first lobe contains the sub-micron size smoke and the small alumina droplet. These are all sufficiently small to follow the flow streams and thus they do not contribute to the slag production (stated e.g. by Duterque (1996); Salita (1995), etc.).

However, the droplets of the second lobe (typically between  $d_p = 20$  and 200  $\mu\text{m}$ ) have a more important inertia, which prevents them following higher-frequency fluctuations of the gas-phase motion. Thus, they will have a time lag at each directional change or acceleration of the continuous-phase, making it more probable for these droplets to interact with the internal surfaces of the motor and may cause accumulation in the nozzle cavity indicated in Figure 1.3 and 2.1(c).

The P230 solid propellant motors of Ariane 5 are by far the largest solid rocket motors

that have ever been used in Europe. Therefore, to support its development, qualification and early servicing periods (approximately during a decade), a research and technology program, called *Aerodynamics of Segmented Solid Motors* (ASSM) was dedicated to the study of the internal phenomena (Fabignon et al. (2000)). The attention was turned mainly towards the flow stability, the internal structures (first of all the thermal protections), the fluid-structure coupling, the aluminium combustion and the slag accumulation phenomena.

Concerning the slag accumulation, the ASSM program started with the investigation of basic phenomena leading to the alumina droplet formation: agglomeration, aluminium combustion and droplet size distribution determination. The  $Al_2O_3$  formation process was described in section 1.2.1.

The alumina droplet size distribution of the EAP is characterized experimentally in the *rotating quench bomb* facility of SNPE and in the (LP2) *helium quench motor* of ONERA, where optical sizing is performed (Traineau et al. (1992)). The two experiments gave the same kind of droplet sizes. The mass fraction of the different alumina droplet sizes is measured by Delfour et al. (1998) in the LP2 facility. As mentioned in section 1.2.1, Duterque (1996) determined the agglomerate diameter distribution using the KL-12 dedicated visualization facility of ONERA. This data allowed later the modelling of the combustion process.

In order to determine the total slag accumulation in the EAP, a specific action is established, called MACADAM (Mini Action Concertée pour l'Analyse du Dépôt d'Alumine dans l'MPS – Mini action to study the alumina deposition in the EAP), where the alumina entrapment is estimated using computations of different droplet trajectories.

With a quasi-steady Eulerian-Lagrangian method, without simulating the combustion and the coupling between the phases, Cesco et al. (1997) identify the importance of the applied capture rules, the droplet diameter and the turbulence level.

Later, a great numerical effort is dedicated to model the effect of the flow field on the Al droplet combustion (Orlandi and Fabignon (2000); Lupoglazoff et al. (2000); Legrand et al. (2000)). Furthermore, Villedieu et al. (2000) take into account the coalescence of large droplets and therefore obtain larger droplet sizes numerically inside the SRM.

In order to help to establish appropriate capture rules during the droplet-wall interaction, various phenomena are defined upon the droplet impingement: rebound, deposition, spattering, splashing. These regimes are studied experimentally by Vardelle et al. (2000) using high-speed imaging of alumina droplets impinging on a hot plate and on liquid alumina film, and similar experiments were carried out in cold-flow condition as well using ethanol droplets. Furthermore, the droplet impingement on wall and liquid film is modelled numerically by Zaleski and Gueyffier (1998) using DNS simulations.

The first generation of slag modelling simulations (e.g. Pevergne and Le Helley (1998); Cesco et al. (1997)) are based on a RANS approach. Firstly the steady flow field and the turbulence levels are computed. Then, alumina droplets are injected at discrete locations along the propellant surfaces and tracked until they reach the nozzle and either escape or hit a surface. Upon an impact, according to the implemented capture rule the droplet is considered to be either accumulating in the slag pool or evacuated through the nozzle. By applying this method on several geometries (that correspond to different operational times of the motor), even the total accumulation estimate can be integrated over the whole launch.

However, unsteady simulations performed by Godfroy and Guéry (1997) showed that the shed vortices of the flow field could strongly influence the slag accumulation: due to the centrifugal forces acting on the droplets inside the core of a vortex, the larger droplets are pushed to the

periphery of the rotating structures and carried this way towards the nozzle, where a considerable amount deposits in the neighbouring cavity. As a result, e.g. Godfroy and Guéry (1997) - by performing the two-phase unsteady simulations with four different droplet diameters -, found that the accumulation is proportional to the square of the droplet diameter ( $D_p$ ).

Furthermore, in an unsteady simulation, Le Helley et al. (2000) reproduces the realistic pressure oscillation levels of the motor with an artificial excitation. Since the pressure oscillations affect the shed vortices, the phenomenon was found to be influential on the accumulation as well. Furthermore, due to the "suction effect" of the vortices, 23% of the accumulating droplets originate from the S2 segment, while with earlier steady simulations practically 100% of the accumulating droplets originated from the S3 segment. Finally, as a consequence of the periodic nature of the vortex shedding phenomenon, the accumulation is observed to be periodic as well.

Dupays (Dupays (2002); Dupays et al. (2000)) pointed out as well that the slag accumulation process and the instability of the internal flow field of the motor are dependent on each other. Thus, the investigation of the slag entrapment process should always take into account unsteadiness.

Concerning more recent numerical tool validations, Wirzberger et al. (2005) uses an Eulerian-Lagrangian approach with an in-house code (*FLDYNS*), which is still based on a steady approach. Similar e.g. to Pevergne and Le Helley (1998), at first the steady-state flow field is calculated using different motor geometries at each 5 s of the operation. Then, the alumina droplet models are injected and tracked from the propellant surface until the nozzle exit taking into account the drag forces and gravity. In order to represent a bimodal droplet size distribution, 1  $\mu\text{m}$  droplets model the alumina smoke and 100  $\mu\text{m}$  droplets model the larger droplets (Wirzberger and Yaniv (2005)). A simple *upper limit* capture rule is applied: all the droplets that do not leave through the nozzle exit plane are considered to be captured in the cavity. Finally, the accumulations observed in the different time instants are integrated to obtain the total accumulation evolution. As a consequence of the conservative capture rule, when comparing the results to static firing tests, the total slag mass appears to be highly over-estimated by the simulations. However, when comparing two different motor geometries, the accumulation tendencies are correctly predicted. Additionally, by analysing the droplet impact locations, using the same simulations a prediction of aft-end erosion is deduced, as described by Wirzberger and Yaniv (2005).

Lately, Najjar et al. (2006) demonstrates the actual version of a full-physics compressible multi-phase numerical tool through the 3D unsteady analysis of the AFRL 70-lb BATES motor and the RSRM Shuttle Booster. The simulations are Euler-type with no LES turbulence modelling. The droplets are followed in a Lagrangian way and the combustion process is modelled as well together with the alumina smoke (with Equilibrium-Eulerian treatment). Therefore, at the propellant surface the droplets contain 90% Al and 10%  $\text{Al}_2\text{O}_3$  as an initial cap. Later, the aluminium can evaporate, burn and the alumina can condense and solidify as well. Furthermore, the droplets may interact with the momentum of the gas-phase through a two-way coupling. Beside a 3D modelling of  $t = 0$  s, a 2D analysis of the RSRM at  $t = 100$  s of operation is shown. Here, recirculation zones are described in the head-end, in the cavity and around halfway between the nozzle head and the rearward inhibitor. Impacts of large droplets ( $d_p \geq 100 \mu\text{m}$ ) are reported on the nozzle cowl and impacts of smaller droplets ( $d_p \leq 25 \mu\text{m}$ ) on the nozzle exit cone. Unfortunately, the short integration time of the simulations prevents the detailed analysis of the droplet behaviour and thus the accumulation in the cavity.

Recently, those who perform numerical simulations all recommend 3D unsteady computations to model the internal flow of a SRM, especially in order to be able to capture the pressure

oscillation phenomenon (suggested e.g. by Anthoine et al. (2002) as well). However, using the experimental data provided by Anthoine et al. (2002), Telara et al. (2006a) presents a 2D axisymmetric simulation using a recent version of a commercial solver (Fluent<sup>TM</sup>), where the pressure oscillation frequencies and even the amplitudes are claimed to be well captured. Naturally, when the geometry (the thermal protection ring) is considered to be 3D, Telara et al. (2006b) models a 3D section of the domain as well.

Finally, once the slag is deposited in the cavity, its negative contribution to the launch does not finish. As it is liquid, on the one hand it may slosh inside the cavity (Meyer (1996)). On the other hand, if the aerodynamic forces are strong enough (and/or combined with the sloshing), slag may be ejected through the nozzle. However, even if it happens, although the on-board dead mass is decreasing, the momentum impulse loss of the motor can not be recovered. Furthermore, as Dotson et al. (1999) shows, depending on the amount of ejected slag, thrust oscillations may occur leading to control problems and possible vehicle instabilities. Another consequence of the slag ejection is that the total amount of actually accumulated alumina might be higher than what is observed after a firing or launch.

The droplets, which are not entrapped in the cavity are exhausted through the nozzle, where due to the large flow acceleration, they break up (Kovalev (2002); Sambamurthi (1996)).

Nevertheless, at the time of writing the present lines, only a very limited information is available concerning the observation of the slag accumulation process in a SRM. In the US, RTR movies (Real Time Radiography) are recorded of the aft dome (cavity) of the Titan IV SRMU and the SICBM during static test firings. The slag evolution is determined in the SRMU by Johnston et al. (1994) and in the SICBM by Frederick (1990). From Salita (1995) it is known that both evolutions exhibit a linear slag increase during the first part of the firing (up-to about 72% and 75% motor action time respectively) from which a plateau (no slag pool increase) is observed. Finally, at the end of the tail-off, due to slag boiling, the slag level increases (without changing effectively its mass). Since no slag ejection is expected, the cause of the plateau and the driving forces of the accumulation remained unknown.

Furthermore, as Salita (1995) shows, even the well-controlled static firings might result in a large scattering of slag accumulation rate using a given motor configuration (e.g. in the HPM version of the Shuttle Booster a factor of 7.2 was observed between the minimum and the maximum accumulation rate among 14 test firings), while other motors exhibit a more repeatable slag rate (e.g. 5 SRMU firing resulted a max/min factor of 1.1 and 6 RSRM Shuttle Booster firings gave a factor of 1.8).

However, in real flight condition the slag accumulation can be estimated only from the actual performance of the motor with respect to its nominal specifications and no reliable data is available. Although the SRMs are sometimes recovered and examined due to the liquid sloshing during the descent and the landing impact, probably a considerable amount of slag is lost. In Space Shuttle Boosters for instance, Boraas (1990) found a slag mass in a recovered motor being 3 times smaller than what is typically observed during static firings.

Concerning the accumulation process, beside the entrapment due to the gas-flow, Salita (1995) considers the contribution of streaming agglomerates on the propellant surface and on the case wall as well, which was effectively investigated in the simulation of a spinning motor by Meyer (1992).

As it can be seen, in spite of the fact that several aspects of the slag accumulation process have already been investigated, the phenomenon is not yet fully understood on global basis. Concerning the EAP of Ariane 5, after the ASSM program, the slag accumulation assessment

got a lower priority, as the problem of pressure oscillation-induced instabilities appeared to be associated with considerably higher risks for the launch safety. Thus, after many - predominantly - numerical investigations (Fabignon et al. (2000)) there is still a need of experimental observation of the complex slag accumulation phenomenon.

### 1.3 Existing experimental facilities

In order to give an idea about the experimental flow modelling of various aspects of the P230 motor, a few of the main test benches are summarized in the followings.

#### 1.3.1 Cold-gas facilities

Within the ASSM program, focusing mainly on the hydrodynamic instability, a number of cold-flow facilities are built to study certain fundamental phenomena present in the motor. A summary of the main set-ups is given in Table 1.1.

Table 1.1 – *Cold-flow experimental facilities (Guéry et al. (2000)).*

<i>Name</i>	<i>Geometry</i>	<i>Investigated phenomena</i>
VECLA	2D duct	SVS, turbulent transition
VALDO	axisymmetric duct	SVS, turbulent transition
MICAT1	2D with inhibitors	OVS, turbulence
VKI models	axisymmetric with inhibitors	cavity volume effect on pressure oscillations
VIOLETTE	axisymmetric	CVS, 2-phase flow dispersion

##### 1.3.1.1 VECLA

The VECLA set-up of ONERA is built in order to study the flow generated by wall injection (Taylor flow), similar to the radial flow injection in the SRMs. This flow may produce the *surface vortex shedding* (SVS) phenomenon, which was unknown prior to the ASSM program. The test section is a 2D duct, which is open to the ambient on one end (see Figure 1.6) and the flow is injected through a 581 mm long porous plate covering the bottom surface. The total length of the test section is 603 mm, its depth is 60 mm and its height can be fixed typically between 10 and 40 mm.

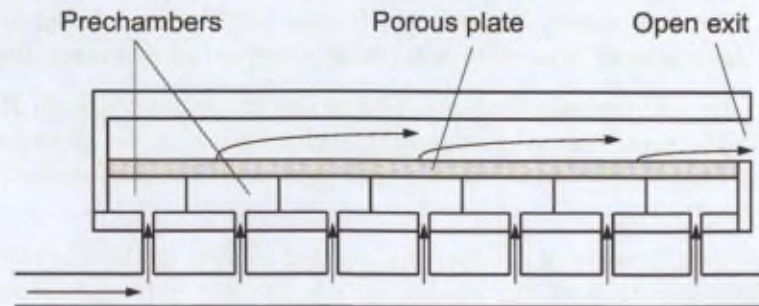


FIGURE 1.6 – *The VECLA set-up (based on Guéry et al. (2000)).*

The lateral walls are transparent in order to provide visual access. However, primarily split film anemometry and hot-wire measurements are performed in order to characterize the bending flow (called Taylor-flow) and the vortical structures generated by it. The injection velocity falls generally between 1 and 2 m/s. At the exit, the set-up can be equipped with a 2D nozzle if needed.

### 1.3.1.2 VALDO

Similarly to VECLA, the VALDO facility of ONERA is also built to study the SVS phenomenon and the eventual coupling between the SVS and acoustics, but this time in axisymmetric configuration, which is more representative for the SRM geometry. The set-up is based mainly on tubes made of porous material (see Figure 1.7), which ensures the radial flow injection. It is designed to use up-to four porous cylinders with  $\varnothing 60$  mm internal diameter and 168 mm length. Therefore, the total length of the model can be varied up-to 672 mm depending on the actually mounted cylinder combination.

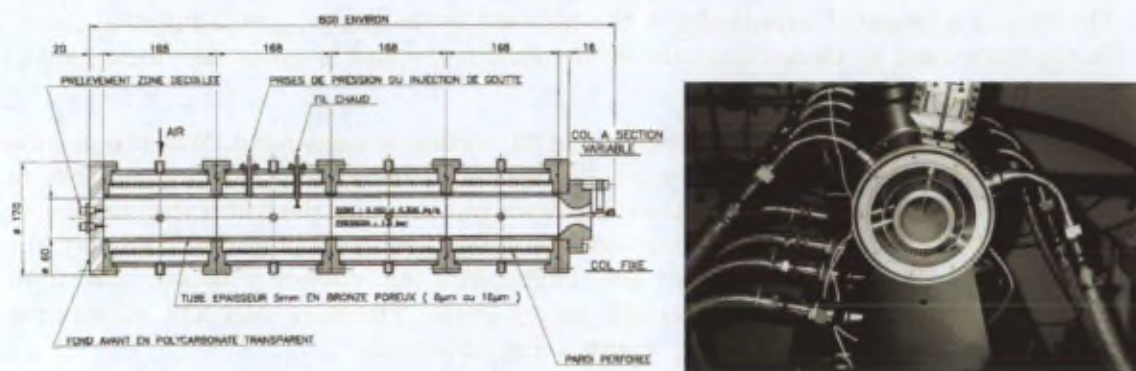


FIGURE 1.7 – The VALDO set-up (from Guéry et al. (2000)).

Similarly to VECLA, the channel is closed on one end and open to the ambient on the other end, where an axisymmetric nozzle can be mounted. In order to provide a good acoustic insulation, very fine poral material is chosen. Two sets of tubes:  $8\ \mu\text{m}$  and  $18\ \mu\text{m}$  are realized, which permits realizing different turbulence levels at the injection. The injection velocity is also of the order of 1 m/s.

Due to the porous tubes, there is no optical access to the test section. By design, hot-wires are used to measure the internal flow velocity distribution. The hot-wire can be inserted through a hole drilled in one of the porous cylinders.

### 1.3.1.3 MICAT1

The cold-gas model of ENSMA is a 2D duct, which represents the characteristic features of the P230 motor at a scale of 1/40. During the design the Mach number and the Strouhal number are respected in order to allow to investigate the hydrodynamic-acoustic coupling (primarily due to *obstacle vortex shedding* (OVS)). The air, representing the internal flow is injected quasi-radially through three segments of porous plates modelling the three segments of propellant grains (see also Figure 1.8). Due to the fact that in the real motor hydrodynamic instabilities occur at the time of the operation, when the first segment already burned out, in most of the test cases no flow is injected through the first porous plate.

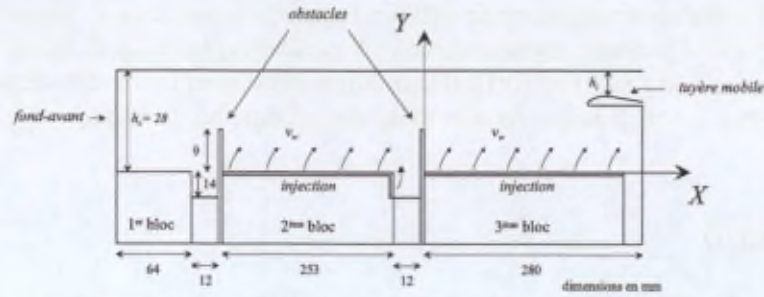


FIGURE 1.8 – The MICAT1 set-up (from Guéry et al. (2000)).

The set-up is equipped with a submerged nozzle model, where the throat opening (indicated by  $h_t$  in Figure 1.8) can be changed in order to control the characteristic Mach number inside the chamber. Finally, the thermal protection rings between S1 and S2 segments and between S2 and S3 segments are modelled by 2D obstacles to generate the vortices shed by the inhibitor (OVS). The interior is insulated acoustically on the one hand by the ( $2 \mu\text{m}$ ) porous injection plates and on the other hand by the sonic nozzle. In the facility, the flow is essentially investigated with hot-wire experiments.

In the wake of the inhibitor (between S2 and S3) vortices are generated. When these coherent structures are strong enough, they reach the rear-end (the nozzle). As they impinge on it, pressure waves are generated, which travel upstream and may tune the vortex shedding frequency and create therefore resonance. Furthermore, due to the quasi-radial injection, SVS phenomenon occurs as well. These wall vortices are later mixing with the coherent structures shed from the inhibitor, which may increase the acoustic energy levels. Therefore, MICAT1 allows to study the mixing effect of vortex shedding, acoustics and turbulence.

#### 1.3.1.4 VIOLETTE

The VIOLETTE (Vortex Internal Organization Leading to Experimental Turbulent Trajectory Evaluation) set-up of ONERA models the P230 motor at a scale of 1/30 as well. However, it respects the geometry at about 95 s after ignition (approximately 73% burn time). The facility (see Figure 1.9) serves the investigation of the *corner vortex shedding* (CVS) phenomenon, which - coupled with the first acoustic mode - can lead to aeroacoustic resonance as well. The main objective of VIOLETTE is to study the aeroacoustic coupling in two-phase flow condition.

The flow is injected through a porous cylinder. The downstream end of the cylinder is made to be conical in order to simulate a chamfered edge propellant grain and therefore realize the CVS phenomenon. A plexiglass channel is attached to this duct, where hot-wire and unsteady pressure probes can be inserted. Finally, a nozzle is mounted with a needle system by which one can regulate the flow-rate and hence the internal Mach number. The plexiglass cylinder is interchangeable. Thus, the acoustic mode of the channel and the distance between the shedding point and the nozzle can be modified and therefore the amplitude of the coupling can be tuned.

In order to generate two-phase flow, micronic oil droplets are injected through an annular chamber at the upper dome. Therefore, the effect of the droplet-phase on the flow-acoustic coupling could also be investigated in VIOLETTE.

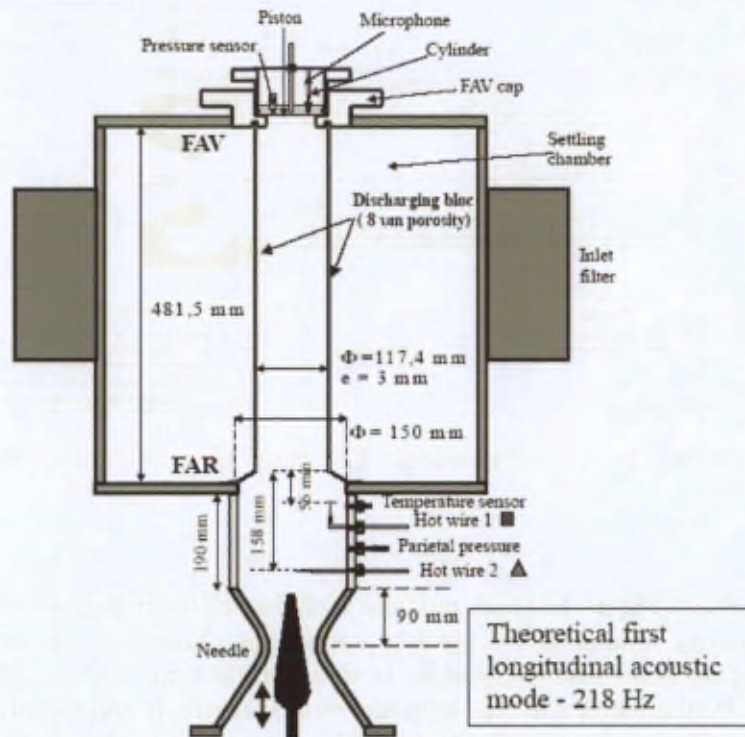


FIGURE 1.9 – The VIOLETTE set-up (from Guéry et al. (2000)).

### 1.3.1.5 VKI models

At the VKI one two-dimensional and three axisymmetric set-ups are available that allow studying the flow-acoustic coupling.

The two-dimensional model<sup>1</sup> is built to characterize the vortices created by wall flow injection, using whole-field optical measurement techniques, e.g. PIV (Laboureur (2007)). The seeded flow is injected through a 590 mm × 60 mm porous plate. The channel height is variable between 10 and 40 mm. The typical injection velocity is of the order of 1 to 2 m/s.

One of the axisymmetric models represents the P230 motor (when 50% of the propellant is burnt) at a scale of 1/15 and the two others at a scale of 1/30.

The 1/15 model is fed by axial flow injection (see Figure 1.10). The geometry of the set-up is similar to the real motor, except that the inhibitor, which models the emerging thermal protection between the S2 and S3 segments is placed closer to the nozzle in order to allow the shed vortices to reach the nozzle and interact with it in the absence of radial injection. In order to influence the vortex shedding phenomenon, the facility can be equipped with an acoustic active control system as well. During the investigation of Anthoine (2000) the nominal flow velocity is varied between 8 and 28 m/s without respecting the sonic condition at the nozzle.

The axial flow injection enables to apply transparent walls and thus the use of optical measurement techniques. The set-up is carefully designed to allow the best possible quality PIV experiments between the inhibitor and the cavity entrance. Thus, the 2D plane of the flow field is investigated considering both the statistical and the instantaneous (coherent structures) flow

<sup>1</sup>similar to VECLA, shown in section 1.3.1.1

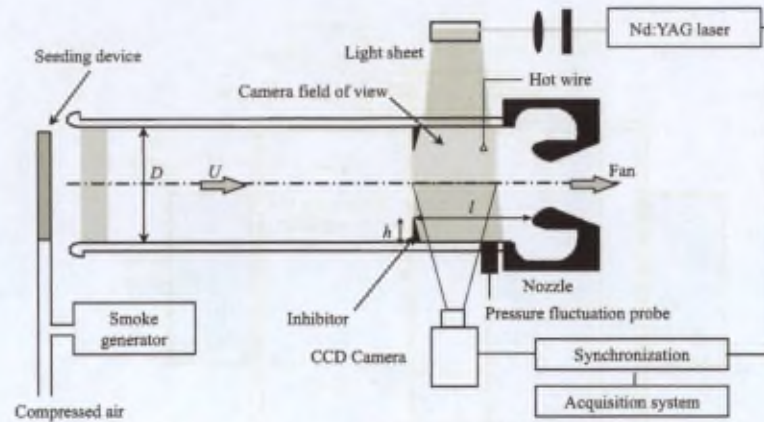


FIGURE 1.10 – The transparent VKI model (from Anthoine (2000)).

properties.

The 1/30 models (Figure 1.11) are modular facilities and their purpose is to study the effect of the aft-end cavity volume on the pressure oscillations. Therefore, the nozzle together with the surrounding cavity are interchangeable. In this case, the sonic flow condition at the nozzle is also respected. Furthermore, with the help of a moving needle in the throat, the internal Mach number can be varied as well. Similar to MICAT1, the interior of these models are acoustically insulated by the porous media at the injection and by the sonic condition at the nozzle throat.

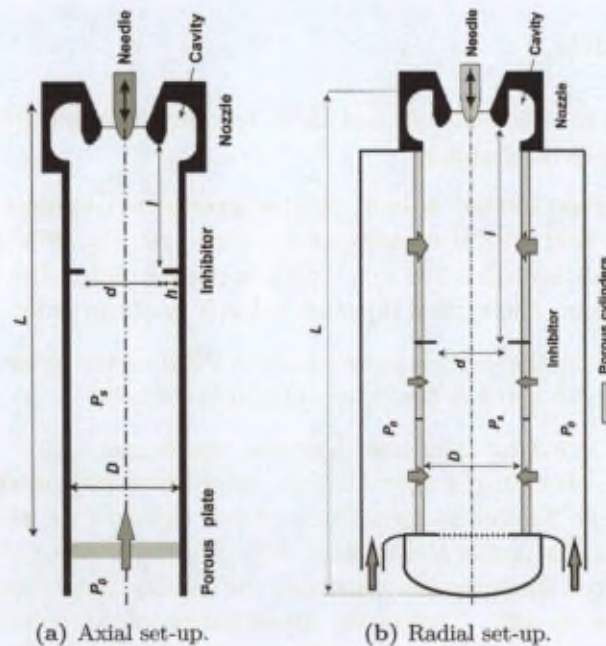


FIGURE 1.11 – The VKI models (from Anthoine (2000)).

The axial set-up (Figure 1.11(a)) reproduces the OVS phenomenon, while the radial injection set-up (Figure 1.11(b)) reproduces the SVS phenomenon as well.

In both of the facilities hot-wire and unsteady pressure measurements can be performed in order to characterize the flow field and the flow-acoustic coupling.

### 1.3.2 Hot-gas facilities

Within the ASSM program, a number of test benches are built, which take into account the combustion as well (Fabignon et al. (2000)). Some are modelling only specific phenomena of the EAP, others are a scaled model of the P230 motor. The models are built mostly by ONERA and the propellant is provided by SNPE. A few of the main set-ups are highlighted in Table 1.1 and detailed in the followings.

Table 1.2 – *Hot-gas experimental facilities.*

Name	Geometry	Investigated phenomena
C1x	planar / axisymmetric	vortex shedding
SNPE 1/15, LP3 and LP6	axisymmetric	1/15 P230
LP9 and LP10	axisymmetric	1/35 P230, SVS

#### 1.3.2.1 C1x

ONERA's C1x (also called as *whistling motor*) is among the first facilities, which model the operation of the P230 motor including combustion. It has an axisymmetric geometry (see Figure 1.12). This simplified model contains a chamfered edge propellant grain in order to provide an experimental database that can be used to validate numerical simulations (investigating turbulence models, propellant response, two-phase flow effects) of capturing the vortex shedding phenomenon. As it is shown in Figure 1.12, a simple converging-diverging nozzle is applied.

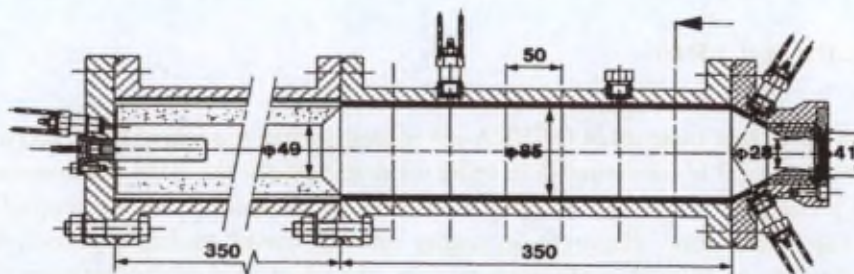


FIGURE 1.12 – *The C1x test bench (from Fabignon et al. (2000)).*

C1x served also during the first studies investigating the effect of particulate phase on the instabilities. Furthermore, in this test bench the applicability of the LDA (Laser Doppler Anemometry) technique is assessed, which provides a non-intrusive one-point unsteady velocity measurement.

#### 1.3.2.2 SNPE 1/15, LP3 and LP6

The SNPE 1/15 model and the LP3 (also called as *C2*) and LP6 (Figure 1.13) test benches of ONERA are all representative models of the P230 motor at a scale of 1/15. Therefore, in the nominal configuration they contain three propellant segments corresponding to S1, S2 and S3 of P230 (using the same composite propellant material), which are separated by proper inhibitor models.

With the help of these test benches, by modifying the propellant composition or the internal geometry, one can test the performances of alternative SRM designs.

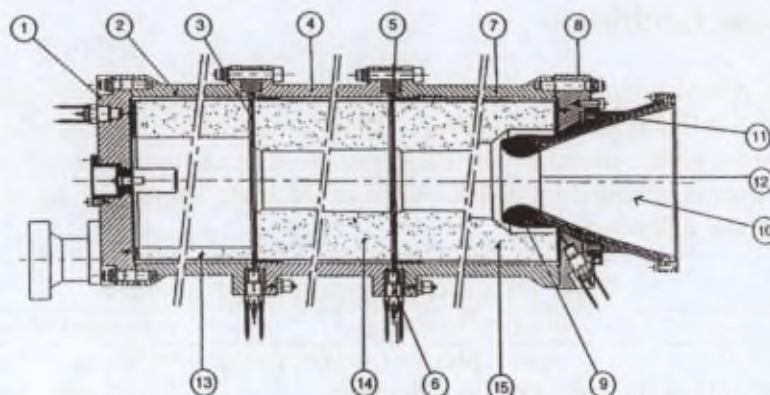


FIGURE 1.13 – The LP6 model (from Fabignon et al. (2000)).

These facilities provide typically static chamber pressure, temperature and unsteady pressure measurements. They are mainly used to investigate the flow-acoustic coupling driven instabilities. It was found e.g. in the LP3 and LP6 motors that instabilities might occur even in the absence of inhibitors, which initiated the analysis of the SVS phenomenon. Furthermore, one has the possibility to investigate the behaviour of thermal protections of various materials and shapes or analyse different nozzle geometries, etc.

### 1.3.2.3 LP9 and LP10

LP9 and LP10 test benches of ONERA are representative models of the P230 motor at a scale of 1/35. At first, LP9 is constructed in order to demonstrate the SVS phenomenon. Therefore, this set-up is designed to operate without inhibitors. It comports a single propellant segment to reproduce the Taylor-flow. However, in reality one can install multiple propellant segments as well to investigate additional configurations (e.g. the effect of a cavity between S2 and S3).

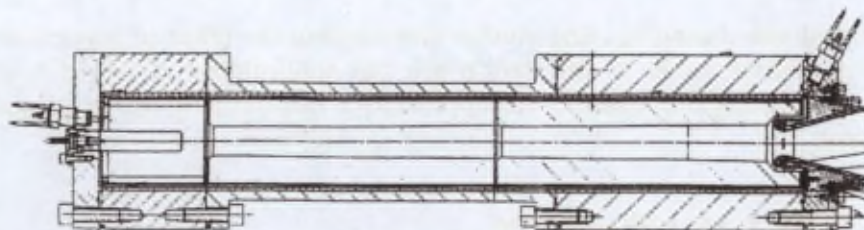


FIGURE 1.14 – The LP10 test bench (from Fabignon et al. (2000)).

LP10 (shown in Figure 1.14) is constructed with the aim to assess the scale effect. Therefore, nominally it is a 1/35 scale model of the P230 motor simulating all the three propellant segments, like e.g. LP6.

These test benches can be instrumented with the same kind of measurement devices as the 1/15 scale models.

## 1.4 Objectives

The main goal of the present investigation is to carry out a fundamental, mainly experimental study concerning the slag accumulation process in a stagnant area modelling the nozzle cavity of the EAP (MPS P230) of Ariane 5. For this purpose a scaled 2D-like cold-gas model is used in order to obtain a quantitative visualisation database, through which the liquid accumulation phenomenon could be better described.

To achieve this goal, a primarily optical experimental approach is followed. However, to extend the measurement data and observations, complementary Computational Fluid Dynamics (CFD) techniques are used as well.

In practice, the objectives are defined to be twofold:

- On a global basis one should first determine the main influential parameters of the slag accumulation process.
- The driving forces of the slag accumulation should be identified by studying the details of the internal flow field.

## 1.5 Methodology

Initially, no suitable facility existed at the VKI, which could be applied for the experimental approach of the present project. Therefore, an appropriate cold-gas SRM model should be designed and built at first.

In order to achieve the global objective, one should perform an experimental campaign, where by changing various geometrical- and flow parameters the most influential factor of the accumulation process can be identified. These measurements are carried out using the so-called *Level Detection and Recording* (LeDaR) technique developed at the VKI. LeDaR provides quantitative information about the accumulation, but it gives only a qualitative insight to the properties of the flow field in the vicinity of the accumulated liquid. Therefore, this campaign can provide only a database concerning the evolution of the magnitude of the accumulation in function of a large number of parameters. However, to understand the process itself, the internal flow field should be studied. Although the basis of LeDaR has existed, it needs to be modified considerably before its application in order to accommodate the actual conditions.

The investigation of the driving forces of the accumulation process is based a priori on the hypothesis that the slag accumulation is essentially governed by the vortex-droplet interaction of the two-phase flow. Therefore, one should be able to resolve experimentally (and numerically as well) the vortical structures of the flow. This means that one should favour optical whole-field measurement techniques (e.g. *Particle Image Velocimetry*, PIV) against intrusive (e.g. hot-wire) or optical (e.g. *Laser Doppler Velocimetry*) point measurement techniques, which do not provide quantitative information about the vortices of the flow.

Although PIV is a commonly used and well-established experimental technique, the basic technique is not operational in two-phase flow condition. Thus, an approach should be developed, which allows its application to two-phase flows as well. Therefore, from these experiments one should be able to determine the relative motion of the droplets with respect to the continuous-phase both on instantaneous and statistical basis. Furthermore, using the PIV database the vortices of the airflow can also be analyzed.

However, already the standard PIV technique is rather resource-consuming. Therefore, a complete parametric study can not be performed with it, especially not in two-phase flow condition. That is why the considerably lighter LeDaR experimental campaign is essential, because it allows to highlight the tendencies of the slag accumulation, which provides guidelines during the flow field investigation with the PIV technique so as to be able to explain better the physics of the slag accumulation process.

The primary goal of the present investigation is to perform LeDaR and PIV experiments and to derive a physical interpretation of the slag accumulation process. However, a CFD approach, based on 3D unsteady simulations are also carried out to be used in complement with the experimental database to understand better the liquid entrapment phenomenon.

## 1.6 Overview

Chapter 2 describes the experimental facility that was mostly used during the present study. The main parameters and the properties of that wind-tunnel are determined. The performed measurements concerning the crucial steps of its design concept evolution, characterization, etc. are detailed in appendix B.

From this point, the present thesis is divided into two main parts:

Part I explains the evolution and the development of the two main optical measurement techniques that are used during the experimental investigation: the Level Detection and Recording (chapter 3) and the two-phase Particle Image Velocimetry (chapter 4) techniques.

Being the core, part II is dedicated to the description of the current slag accumulation assessment. Chapter 5 shows the measurement campaign during which the main parameters of the liquid accumulation in the current facility are determined. In the followings, chapter 6 shows the analysis of the internal flow field on statistical basis both in single-phase and two-phase configuration. Here, besides the experiments, numerical simulations are mentioned as well, which are compared to the measurement data. Chapter 7 investigates the same data set, but on instantaneous bases by focusing on the vortical structures that are present in the flow. The purpose of chapter 8 is to summarize the slag accumulation assessment and describe the current understanding of the phenomenon.

Finally, concluding remarks are given and the future aspects are highlighted.

## Chapter 2

# Modelling the phenomena

Although the present research has a fundamental nature, when designing the parameters of the experimental facility, the parameters of the real motor are kept in mind, whenever it is possible. Therefore, at first the main conditions of the MPS P230 are overviewed. Then, a list is given about the necessary simplifications and another one about the parameters that should be respected. In the followings the determination of the nominal conditions of the current model is shown and finally the droplet-phase modelling is described.

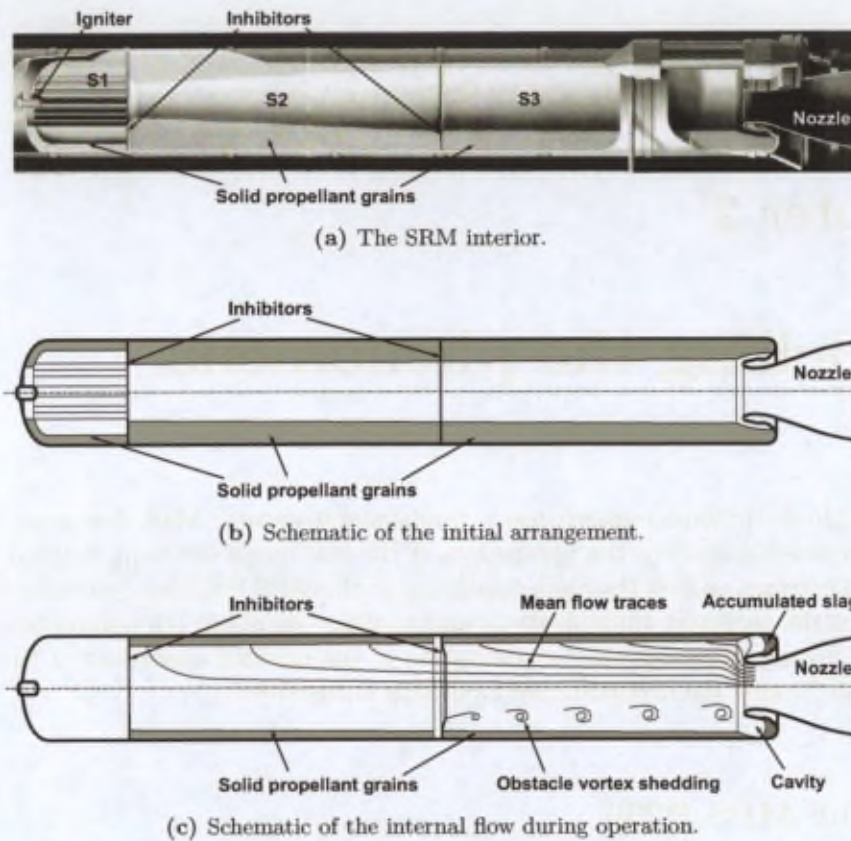
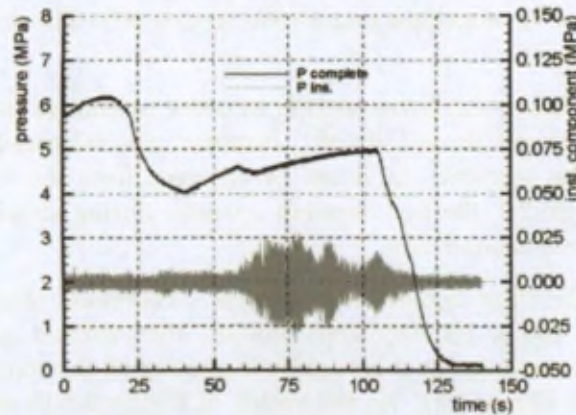
### 2.1 The MPS P230

A schematic of the EAP before firing is shown in Figure 2.1(a). As it can be seen, the motor contains three segments of propellant grains ( $S1$ ,  $S2$  and  $S3$ ). The propellant can be ignited by the igniter within 350 ms.

The first segment has a *star* cross-section in order to enlarge its surface and therefore to provide an increased thrust during lift-off. However, the increased burning rate leads to a quicker burn-out of this segment. As it can be observed from the corresponding higher static pressure levels in Figure 2.2, the first segment operates during about 25 s effectively, while its complete burnout occurs around 40 s.

The second and the third segments are conical. Therefore, they provide thrust from the ignition during about 130 s. As they burn radially, their surface increases. That is why the static pressure is not constant, but it is slightly increasing in the combustion chamber until the end of the launch (see Figure 2.2). As the sketch of Figure 2.1(b) shows, initially the aft end cavity around the submerged nozzle is also filled with propellant. As the solid fuel is consumed, the cavity is created.

The topology of the flow is shown schematically in Figure 2.1(c) after the burn-out of the first segment. The top half of the figure exhibits the topology of the mean flow, showing the radial injection and the streamlines, which are curved in order to be directed towards the nozzle. The bottom half of the figure shows the instantaneous events. As the flow which originates from  $S2$  is passing over the *thermal protection* inhibitor ring, vortex rings are shed. These are travelling towards the nozzle, while the bending flow of  $S3$  is probably maintaining their energy and therefore preventing them from early dissipation. Thus, these vortices are capable of reaching the nozzle head. As the vortices are travelling in front of the cavity entrance, they create small pressure fluctuations, which - coupled with acoustics - may lead to the instability phenomenon

FIGURE 2.1 - *The MPS P230.*FIGURE 2.2 - *Static- and unsteady pressure evolution in P230 during static test firing (Fabignon et al. (2003)).*

mentioned in section 1.2.

As it is mentioned earlier, the propellant material contains aluminium powder (about 18%) in order to increase the enthalpy of the combustion and therefore the thrust as well. Besides, it should also reduce the pressure oscillations. However, due to the aluminium content, liquified alumina ( $Al_2O_3$ ) droplets are formed, which should also travel towards the nozzle. On their way they might interact with the vortices shed by the inhibitor and modify their properties. Finally, most of them are evacuated through the nozzle, but - as it was mentioned in section 1.1 - around

2 t remains in the cavity around the nozzle by the end of the launch in each of the EAPs.

Summarizing the previous information, the most important phenomena of the EAP operation are:

- the obstacle vortex shedding,
- the presence of a two-phase flow,
- their interaction with a nozzle and its neighbouring stagnant area.

As a reference condition, the configuration of the launcher at about half of its operational time is taken (similarly to the already existing cold-gas axisymmetric VKI facilities, which are described in section 1.3.1.5). As mentioned before, by this time the first segment has already finished its combustion; only the second and the third segments represent the flow source. The main reference parameters are summarized in Table 2.1. The necessary information about the corresponding geometry and the flow properties of the P230 is gathered from the works described in chapter 1.2.

Table 2.1 – Approximate P230 properties

<i>Main geometrical parameters</i>			
Motor internal diameter	$D$	2.3	[m]
Nozzle throat diameter	$D_o$	0.9	[m]
Inhibitor section height	$h$	0.27	[m]
S2 inhibitor-nozzle distance	$L_i$	9.7	[m]
<i>Main flow parameters</i>			
Internal temperature	$T$	3400	[K]
Gas-phase viscosity	$\mu_f$	$4.7 \cdot 10^{-5}$	[kg/(m · s)]
Alumina density ( $3.11 - 9.54 \cdot 10^{-5} \cdot T$ from Sarou-Kanian et al. (2000))	$\rho_p$	2786	[kg/m <sup>3</sup> ]
Droplet diameter range	$d_p$	20..200	[ $\mu\text{m}$ ]
Internal mach number	$M$	0.1	[–]
Reference velocity	$U_0$	100	[m/s]
Total injection flow-rate	$\dot{Q}_m$	12	[kg/(s · m <sup>2</sup> )]
Alumina flow-rate	$\dot{Q}_{Vd}$	0.067	[m <sup>3</sup> /s]
Gas-phase flow-rate	$\dot{Q}_{Vf}$	408	[m <sup>3</sup> /s]

Concerning the droplet-phase, the size distribution of the alumina droplets of the motor internal flow is bimodal. The majority of the particles (80-90% in terms of mass fraction) have a sub-micron size. These particles are following the fluid. Therefore, they can be considered as part of the flow and it is not necessary to model them. The diameter distribution of the remaining alumina droplets ranges between 20 and 200  $\mu\text{m}$ . These particles should be modelled during the two-phase experiments. A mean diameter of about 70  $\mu\text{m}$  is chosen as a reference. Regarding the quantity of the particles, it is assumed that 85% of the total mass of the alumina forms the sub-micron size droplets and the remaining 15% forms the droplets that should be taken into account.

## 2.2 Main considerations

During the design of the experimental model, the main features of the Ariane 5 EAPs should be represented. However, due to the fundamental nature of the present study, several assumptions are made:

- Cold-gas model: at present no chemical reaction is modelled and no thermal similarities are respected. The gas-phase of the real SRM is modelled by air and the liquified alumina droplets mainly by water droplets.
- Axial flow injection: since only non-intrusive optical measurement techniques are planned to be used, the flow cannot be injected through the shell of the model. Due to the lack of the radially injected bending flow, no surface vortex shedding SVS phenomenon should exist. Furthermore, the lifetime of any vortical structure in the model is expected to be shorter than it would be with the radial flow injection.
- Two-dimensional design: on the one hand, two-phase PIV technique has not been used before. On the other hand, the LeDaR technique has not been applied in the presence of liquid droplets. Thus, the prospectively complex model is attempted to be simplified by defining a two-dimensional geometry.
- Subsonic operation: the sonic flow behaviour in the nozzle throat is not respected. However, the sonic throat is assumed to have no impact on the path of the droplets inside the combustion chamber and therefore on the rate of accumulation since the flow velocity inside the real motor is lower than  $M = 0.1$  up to the nozzle lip (see Table 2.1).
- Gravity = 1g: the acceleration ( $\sim 4$  to 4.5g) and the inclination angle of the motors are neglected in order to prevent the facility from being overcomplicated. Up-to 10g Johnston et al. (1994); Salita et al. (1990) found no effect of the acceleration on the particle trajectories.
- Rigid inhibitor: the inhibitors are to be made of rigid material and therefore no flexibility is respected compared to the real case.
- Rectangular cavity: As it is shown in Figure 2.1, the bottom and the top surfaces of the cavity are curved. In order to be able to make the dimension (and thus the volume) of the cavity parametric<sup>1</sup>, all the boundaries should be flat with sharp 90° corners between them.

Taking into account the above mentioned simplifications, during the design of the simplified model the following similarities should be respected:

- Presence of the main geometrical features: First of all, the main geometrical elements of the real motor should be represented (the inhibitor between the segments S2 and S3, the nozzle and the neighbouring cavity).
- Obstacle vortex shedding (OVS): due to the presence of an inhibitor, the OVS phenomenon is respected. However, as it is mentioned earlier, the lifetime of the shed vortices is expected to be shorter due to the lack of radial flow injection.

<sup>1</sup>to allow to investigate its relevance on the accumulation rate

- These vortices should however be able to reach the nozzle head after passing in front of the cavity opening.
- Flow acceleration: the flow acceleration features primarily at the inhibitor, but also at the nozzle should be modelled.
- Stagnant area: by modelling the presence of the cavity neighbouring the nozzle lip, the stagnant area exists, where the liquid accumulates.
- Flow regime: even if the sonic condition at the nozzle is not respected, the flow inside the model should be in the same regime (e.g. turbulent) as in the real case.
- Two-phase flow condition: as it is mentioned before, the two-phase behaviour of the flow should be respected (using mainly water for the droplet-phase).
- Two-phase coupling: in the model, the interaction between the two phases should fall in the same regime as in the real case in order to obtain similar effect of the droplets on the vortices.

Additional requirement: as only optical experimental techniques are intended to be used, optical access to the interior of the model is essential. Therefore, its boundaries should be made of transparent material.

The final experimental facility is not explained in details at this point. It will be shown later in section 2.4. Furthermore, a detailed description concerning its design and characterization is given in Appendix B.

## 2.3 Modelling and similarities

The design of the present experimental model should attempt to keep the geometrical parameters similar to the real configuration. It should also allow a parametric study, therefore most of its dimensions should be modifiable. The current section is focusing on the definition of the nominal dimensions of the set-up (including the droplet-phase properties as well), while section 2.4 will show the available ranges of parameters.

### 2.3.1 The modelled geometry

As it is mentioned in section 2.2, due to the frequent use of optical measurement techniques, the experimental model is based on a two-dimensional design consisting of planar walls. The geometrical similarity is planned to be based primarily on respecting the *passage ratios* ( $PR = \text{unblocked section}/\text{total section}$ ) of the various internal elements of the EAP.

Therefore, the model is similar to the MICAT1 facility (described in section 1.3.1.3), but using quasi-axial flow injection in order to facilitate the two-phase investigation.

The axial flow of the model is supplied by the VKI L-11 wind-tunnel (its choice and preliminary characterization are detailed in section B.1). Its outlet has a cross-section of  $200 \times 200 \text{ mm}^2$ . Therefore, the model should be based on these dimensions, which should correspond to the internal diameter ( $D = 2.3 \text{ m}$ ) of the EAP. Due to the square outlet of the wind-tunnel, one has the possibility of constructing either a two-dimensional model, or even a square one. The complete design of the two kinds of arrangements are described in section B.2.2.1. When modelling an

axisymmetric geometry, the advantage of the square concept over the two-dimensional geometry is that by respecting the passage ratios of the various elements (e.g. the  $PR$  of the inhibitor), the dimensions (e.g. the inhibitor height,  $h$ ) are scaled proportionally as well. In a two-dimensional design the blockage elements tend to become larger (e.g. at a given  $PR$ :  $h_{2D} > h_{square}$ ) and therefore e.g. the generated vortices would tend to be larger as well. However, as the detailed investigation of section B.3 proved, due to the strong corner effects the square design is not applicable.

Nevertheless, building a simple two-dimensional model from the square cross-section outlet of the wind-tunnel, could lead to strong three-dimensional flow disturbances developing along the two wall corners opposite to the inhibitor. To overcome this problem, one could increase the two-dimensional aspect ratio of the model by designing it to be symmetric and incorporating a pair of inhibitors and a pair of cavities symmetrically to the axis of the wind-tunnel. However, the vortex shedding from that symmetric arrangement would be probably alternating between the two inhibitors, while *annular* vortex rings are shed from the real thermal protections. In order to prevent the interaction between the two sides of the symmetric test section, a splitting plate should be installed along the wind-tunnel axis. It can dissociate the phenomena in the two sides and if its surface is smooth enough, its boundary layer should be negligible as well.

In order to install a splitting plate, first of all its thickness ( $t_{sp}$ ) should be defined. This investigation is detailed in section B.4. However, according to equation B.6 (which defines in a channel the flow acceleration in the so-called *vena contracta* downstream a protruding obstacle) one can see that the flow acceleration depends not only on the  $PR$  ( $PR = S_p/S$ ), but also on the *vena contracta coefficient* ( $c_{vc}$ ). The  $c_{vc}$  depends on the shape of the obstacle and - most importantly - on the proximity of the top-wall of the channel. Therefore, by modifying  $t_{sp}$  and the inhibitor height ( $h$ ), one should be capable of achieving similar flow accelerations downstream the inhibitor than in an axisymmetric case. That is why a study was initiated using PIV experiments (the details are shown in section B.4) to determine  $c_{vc}$  in various configurations and to compare it to the axisymmetric arrangement studied by Anthoine (2000). Furthermore, the instantaneous vortices are also identified and compared to the axisymmetric data. Finally, a  $t_{sp} = 5$  mm splitting plate and  $h = 33.5$  mm were selected to represent the nominal configuration.

In the followings the nozzle is defined. The geometry of its cross-section is taken directly from the first generation EAP nozzle. This shape is used by Anthoine (2000) as well in the cold-gas axisymmetric VKI models (shown in section 1.3.1.5). Its throat opening in the present model is simply defined in order to represent equal  $PR$  to the full-scale motor ( $PR = D_o/D$ , according to Table 2.1). Thus, a throat opening of  $o = 15.4$  mm is defined to be nominal.

Then, the cavity geometry needs to be defined. As it was mentioned in section 2.2, the cavity should have a rectangular design to allow easier parametrization. To define its width, simply the section ratios are taken once again. The section of the EAP cavity is considered to be a ring of  $1.77 \text{ m} < D_{cavity} < 3 \text{ m}$ . Therefore, by normalizing the section of this ring by the nozzle opening section (based on  $D_o$ ), a ratio of about  $S_{cavity}/S = 6.99$  should be respected. Thus, the nominal cavity width of the model should be  $w = 107$  mm.

Finally, the nominal inhibitor location is defined. In reality, during the combustion, the flow is injected radially. This radial injection may increase the energy and thus the lifetime of the vortices, as it is mentioned in section 2.1. Therefore, in spite of the large distance (approximately  $35h_{real}$ ) between the inhibitor and the nozzle head, the vortices can reach and interact with the nozzle. However, the present simplified model is mounted on a wind-tunnel, which provides only axial flow injection. In order to allow the vortices to reach the nozzle and mimic the vortex-nozzle interaction phenomenon in a model with axial injection, Stubos et al. (1999) found an

optimum distance of  $L_i = 8$  to  $10h$  and obtained no interaction beyond  $L_i > 12h$ . Therefore, in the present 2D model, the inhibitor is placed  $L_i = 9h$  far from the nozzle tip.

Thus, the main dimensions of the nominal parameters are defined. When the nominal configuration is modelled numerically, exactly these parameters are taken as well. A schematic of the final two-dimensional model can be seen in Figure 2.3.

Furthermore, as it is visible in Figure 2.4, most of the walls of the test section are made of plexiglass in order to provide optical access. Where the laser-sheet is intended to be introduced for the measurements, a glass window is embedded in a plexiglass frame. The second exception is the opposite wall, which is made of a polished stainless steel. These two elements are used to avoid light diffraction from the wall during the laser-sheet impact and improve the PIV measurement quality in the vicinity of these surfaces by allowing only full reflection of the sheet on itself.

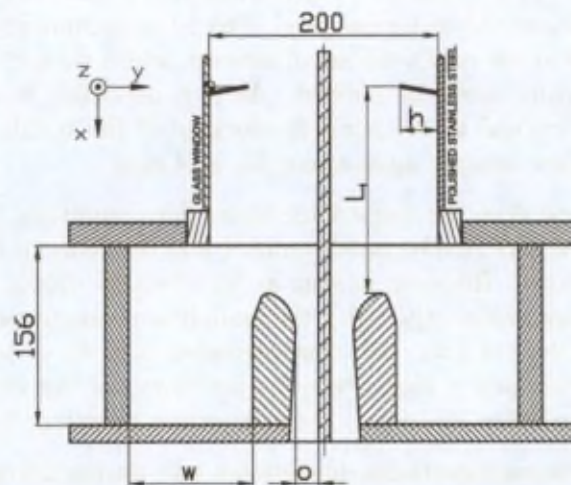


FIGURE 2.3 – The final geometrical parameters of the test section.

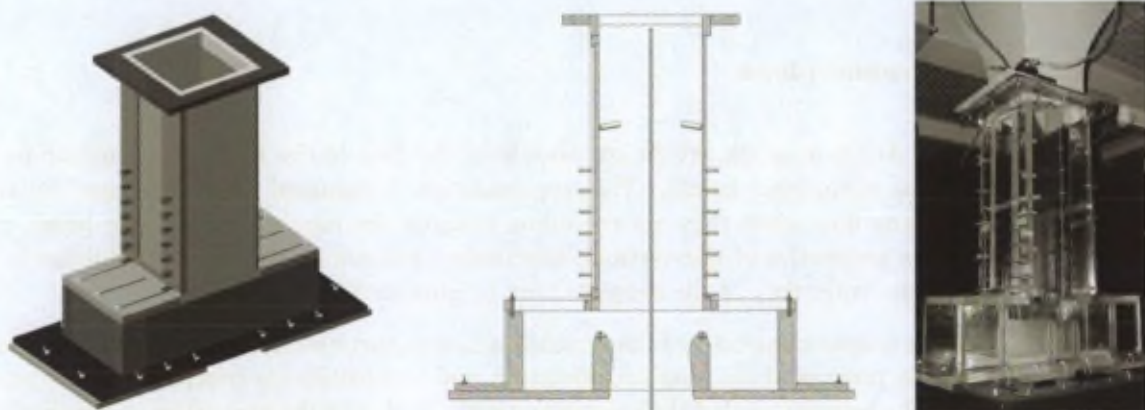


FIGURE 2.4 – Different views of the final test section.

Since the final model is based on a symmetric design, the actual flow symmetry has to be verified. All the details of this investigation are described in section B.5. Thanks to the satisfactory results, one can use either side of the model to characterize the internal phenomena.

### 2.3.2 Flow conditions

The previous section showed the similarity considerations concerning the geometry of the facility. The current section describes the main flow similarity parameters, which include the reference flow velocity and the models of the alumina droplets.

#### 2.3.2.1 The flow velocity

To respect the Mach number of the full-scale motor ( $M_0 = U_0/a$ , where  $U_0$  is the mean velocity in the cross-section just upstream the nozzle tip), an axial flow velocity of the order of  $U_0 = 30$  m/s should be applied. However, as mentioned in section 2.2, the sonic condition at the nozzle throat is not attempted to be modelled. From the accumulation point of view only the flow characteristics up to the nozzle tip are of interest, which do not imply any compressibility. Therefore, lower velocities could be applied. As it is described in section B.1.1, by using a blockage that is proportional to the nominal blockage of the nozzle, the blower of the wind-tunnel can provide a flow velocity up-to about  $U_0 = 14$  m/s.

However, even if one does not respect the exact flow condition, the flow regime has to be kept similar. In the real EAP, the Reynolds number is of the order of  $Re \sim 10^7$ , which cannot be matched in a scaled model. However, as long as the viscosity effects are kept insignificant (the Reynolds number is kept sufficiently high), the main flow characteristics should remain similar. A Reynolds number ( $Re_h$ ) of  $2.51 \cdot 10^4$ , that corresponds to  $U_0 = 10$  m/s is acceptable. This flow velocity can be sustained in longer term by the blower of the wind-tunnel and is therefore chosen to be the nominal flow velocity in the test section upstream the inhibitor.

However, as it will be explained later (in section 4.4.1), during the two-phase PIV experiments the reference velocity has to be reduced to  $U_0 = 2$  m/s. This velocity represents a Reynolds number of  $Re_h = 5025$ , which should still represent a turbulent regime.

#### 2.3.2.2 The droplet-phase

The liquefied  $Al_2O_3$  droplets, which are present in the flow of the EAPs, accumulate in the cavity next to the submerged nozzle. This accumulation is assumed to be governed by their interaction with the flow while they are travelling towards the nozzle. On the one hand, they may influence the properties of the vortical structures (that are shed from the inhibitor). On the other hand, the trajectory of the droplets may be governed by the gas-flow.

Modelling the proper behaviour of the liquified alumina particles during the tests is essential to understand the process of the slag accumulation and to identify its controlling parameters, which represent the primary goal of the present project. To choose the properties of the droplets, first of all the particle-flow interaction is taken into account. The turbulence modulation by liquid droplets in a plane mixing layer is studied at the VKI by Suda (2000) using PIV measurements in a vertical twin-jet wind-tunnel. The dimensionless parameters suggested to be used to characterize the interaction between the two phases of the flow are the Stokes number ( $St$ ) and the volume fraction ( $\alpha_p$ ). The Stokes number is defined by the ratio between the characteristic response time of the droplets ( $\tau_p$ ) and the characteristic turbulent time scale of the flow ( $\tau_f$ ), as

indicated in equation 2.1.

$$St = \frac{\tau_p}{\tau_f} = \frac{\rho_p d_p^2 U_0}{18\mu_f L_0} \quad (2.1)$$

where

$$\tau_p = \frac{\rho_p d_p^2}{18\mu_f} \quad (2.2)$$

and

$$\tau_f = \frac{L_0}{U_0} \quad (2.3)$$

In equation 2.2  $\rho_p$  is the density of the droplet phase,  $d_p$  is the typical diameter of the droplets,  $\mu_f$  is the dynamic viscosity of the fluid phase. Therefore, one can see that the determination of the characteristic time associated to the droplet-phase ( $\tau_p$ ) is rather straightforward. However, the characteristic time of the flow ( $\tau_f$  in equation 2.3) is less definite. It involves a reference velocity ( $U_0$ ) and a reference dimension ( $L_0$ ). Since these quantities are difficult to be defined without knowing the exact properties of the flow field, at this stage  $U_0$  is chosen to be the nominal reference velocity of the flow (e.g. the average velocity upstream the nozzle tip) and  $L_0$  is chosen to be the diameter of the largest shed vortices, which is assumed to be proportional to the height of the inhibitor ( $L_0 = h$  is defined).

The volume fraction is defined by equation 2.4.

$$\alpha_p = \frac{\dot{Q}_{Vd}}{\dot{Q}_{Vf} + \dot{Q}_{Vd}} \quad (2.4)$$

Based on the Stokes number and the volume fraction one can estimate the interaction between the phases of the two-phase flow (Gore and Crowe (1989) and Elghobashi (1994)). The analogy to Elghobashi (1994) can be seen in Figure 2.5. In the figure it is shown that the interaction between the phases depends first of all on the volume fraction ( $\alpha_p$ ). If the quantity of the particulate phase is too low ( $\alpha_p < 10^{-6}$ ), it does not have any effect on the fluid flow. If the quantity of the particulate phase is high ( $\alpha_p > 10^{-3}$ ), the so-called four-way coupling occurs, where beside the particle-fluid interaction, also particle-particle interaction (e.g. frequent particle collision) is present. Between these regions ( $10^{-6} < \alpha_p < 10^{-3}$ ) the two-way coupling takes place, where the presence of the particles may modify the turbulence and the flow may act on the particle motion as well. Based on the graph, the nature of the modification in presence of two-way coupling depends on the Stokes number.

If it is possible, the two-phase flow of the present model should represent in the best possible way the internal two-phase flow of the motor. Therefore, the Stokes number ( $St$ ) and the volume fraction ( $\alpha_p$ ) are the most important parameters that should be respected. First of all, the Stokes number and the volume fraction of the real case should be determined. Then, the models of the particles can be chosen.

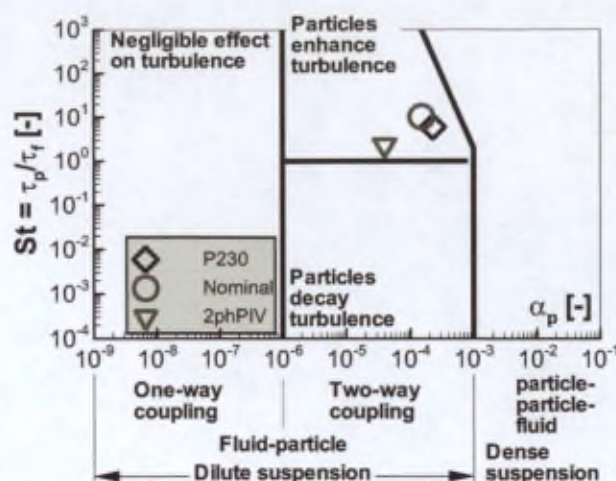


FIGURE 2.5 – Particle-flow interaction.

Using the reference values of the full-scale P230 shown in section 2.1, the resulting Stokes number is  $St = 6.01$  and the volume fraction is  $\alpha_p = 2.2 \cdot 10^{-4}$ . Therefore, these values are to be respected when determining the properties of the desired droplet-phase model.

Since the main purpose of the project is to study the driving parameters of the alumina entrapment and accumulation in the cavity next to the submerged nozzle, the model of the droplet-phase should be liquid as well. For safety and simplicity, water is chosen, which can be sprayed easily to form droplets. Thus, the mean droplet diameter ( $d_p$ ) and the volumetric water flow-rate ( $Q_{V,d}$ ) of the ideal spray device can be calculated and are summarized in Table 2.2.

Table 2.2 – The ideal properties of the droplet-phase model

	Nominal condition	During 2-phase PIV
$St$ [-]	6.01	6.01
$\alpha_p$ [-]	$2.2 \cdot 10^{-4}$	$2.2 \cdot 10^{-4}$
$L_0$ [mm]	33.5	33.5
$U_0$ [m/s]	10	2
$d_p$ [ $\mu\text{m}$ ]	<b>76.1</b>	<b>170.3</b>
$Q_{V,d}$ [ $\text{m}^3/\text{s}$ ]	$8.8 \cdot 10^{-5}$	$1.8 \cdot 10^{-5}$
	[l/min]	5.31
		1.06

However, in reality an exact match cannot be found. The idea is to find a spray available on the market, which has properties as close as possible to the ideal spray. For the nominal configuration finally, a Lechler 502.548 series spray is chosen, which operates with pressurized water. This model provides droplets with a mean Sauter diameter of about  $d_{32} = 100 \mu\text{m}$  at a volumetric flow-rate of  $Q_{V,d} = 5.8 \cdot 10^{-5} \text{ m}^3/\text{s}$  (about 3.5 l/min). As it is indicated in Figure 2.5 and Table 2.3, the operating conditions of this atomizer represent quite well the estimated conditions of the full-scale motor.

During the two-phase PIV experiments a Lechler 156.000.17.13 series pneumatic atomizer is chosen. The mean Sauter diameter of water droplets generated by this device is about  $d_{32} = 106.2 \mu\text{m}$  (the actual droplet size distribution will be shown in Figure 6.20 in section 6.4.1) at a

volumetric flow-rate of  $Q_{Vd} = 0.31 \cdot 10^{-5} \text{ m}^3/\text{s}$  (about 0.19 l/min). As it is visible in Figure 2.5 (and quantified in Table 2.3), although the operating conditions of this atomizer are different, theoretically it should still represent a similar regime to the estimated conditions of the full-scale motor.

Table 2.3 – *The actual properties of the droplet-phase model*

		Nominal condition	During 2-phase PIV
$L_0$	[mm]	33.5	33.5
$U_0$	[m/s]	10	2
$d_p$	[ $\mu\text{m}$ ]	100	106.2
$Q_{Vd}$	[ $\text{m}^3/\text{s}$ ]	$5.8 \cdot 10^{-5}$	$0.31 \cdot 10^{-5}$
	[l/min]	3.5	0.19
$St$	[-]	<b>10.36</b>	<b>2.33</b>
$\alpha_p$	[-]	$1.5 \cdot 10^{-4}$	$0.4 \cdot 10^{-4}$

The actually used spray can be installed at a constant level in the stagnation chamber of the wind-tunnel to achieve a good mixing. In order to reduce the change of disturbance of the spray regardless the actual device, a tubing system is designed. Since the wind-tunnel is based on a square build-up, a cross of tubes is installed in the stagnation chamber and the spray can be mounted inside the one, which has an axis normal to the splitting plate. Therefore, if necessary, the position of the spray normal to the splitting plate can be modified as well. The system is shown in Figure 2.6 without any of the atomizers.

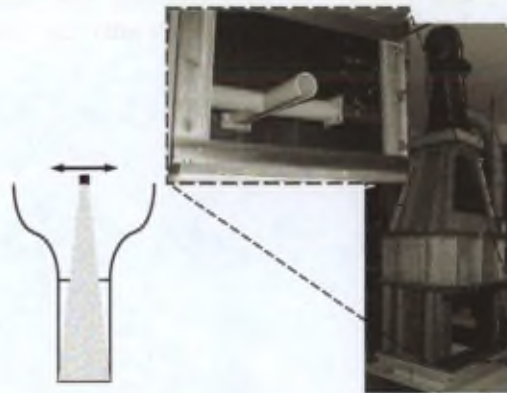


FIGURE 2.6 – *The spray support system.*

The choice of the spray devices finalizes the definition of the nominal configuration of the new facility.

## 2.4 The parameters of the experimental facility

As it is mentioned in section 2.3.1, the model has a  $200 \times 200 \text{ mm}^2$  cross-section, which is divided into two channels by a splitting plate, which has a final thickness of  $t_{sp} = 5 \text{ mm}$ . Furthermore, the longitudinal dimension of the cavity is fixed as well (156 mm). However, the rest of the main geometrical dimensions shown in Figure 2.3 are parametric.

The inhibitors are easily interchangeable and therefore any values of  $h$  can be realized (typically, inhibitor heights between  $h = 13.5$  to  $41$  mm are used). As it will be explained in section 5.1, the obstacles are all inclined by  $10^\circ$  upstream. This arrangement allows to control better the accumulating water droplets on the top of the inhibitors, while the sprays are operating. A suction system is installed in the upstream corner of these obstacles close to the sidewalls, which extracts the accumulated liquid directly through the wall. Otherwise, the water would be taken away from the inhibitors by the airflow in forms of large droplets (several millimetres in diameter) and deteriorate the quality of the slag accumulation (LeDaR) investigations.

The inhibitors can be fixed only at discrete locations. Positions between  $L_i = 110$  to  $310$  mm from the nozzle head are available in  $40$  mm increment. This allows to realize obstacle-to-nozzle ratios in the range of  $O2NR = 2.7$  to  $23$ , when considering inhibitor height ranging from  $h = 13.5$  mm to  $h = 41$  mm.

Furthermore, the opening of the nozzle (nozzle throat) can be varied continuously between  $o = 15.4$  and  $45.4$  mm. This allows to study the blockage effect of the nozzle and the relative position of the nozzle tip with respect to the inhibitor tip.

The final available geometrical parameter is the width of the cavity. It can vary between  $w = 44$  and  $140$  mm continuously. By modifying the width of the cavity, different cavity volumes can be realized.

It should be noted that the width of the cavity ( $w$ ) and the nozzle opening ( $o$ ) are two independent parameters, i.e. they can be modified separately.

Concerning the flow parameters, as it is shown in section B.1.1, the reference velocity can be varied between  $U_0 = 0$  to  $14$  m/s continuously. The actual velocity is determined with a calibrated Validyne pressure transducer by measuring the pressure difference between the stagnation chamber and the test section. Further details are given concerning the reference velocity measurement in section B.5.3.

## Part I

# Dedicated measurement techniques



The present part is focusing on the optical measurement techniques, which are to be applied during the experimental campaigns, namely the so-called LeDaR and the PIV techniques. Although both of them are in use at the VKI, the flow conditions in the actual facility are not appropriate for the direct application of either of these tools. As it will be shown, primarily the presence of the droplets in the experimental domain are responsible for the limitation. Therefore, both of the techniques have to be adapted/extended to make them applicable.

Chapter 4 is explaining the LeDaR technique, which should be applied to perform the parametric investigation and determine the relevant parameters of the slag accumulation, while chapter 4 is dealing with the PIV technique and its adaptation to two-phase flow condition.

The first part of the chapter discusses the importance of the...  
The second part of the chapter discusses the importance of the...  
The third part of the chapter discusses the importance of the...  
The fourth part of the chapter discusses the importance of the...  
The fifth part of the chapter discusses the importance of the...  
The sixth part of the chapter discusses the importance of the...  
The seventh part of the chapter discusses the importance of the...  
The eighth part of the chapter discusses the importance of the...  
The ninth part of the chapter discusses the importance of the...  
The tenth part of the chapter discusses the importance of the...

## Chapter 3

# The Level Detection and Recording technique

### 3.1 About the conventional LeDaR technique

*Level Detection and Recording (LeDaR)* is a VKI home-made non-intrusive optical measurement technique that detects the gas-liquid interface in a plane of a tank. The principle and performances of the original version are described by Bouchez et al. (2000); Planquart et al. (2002). By choosing an optical method for the liquid surface detection, apart from the volume measurement, one has the possibility to investigate the shape of the surface as well.

Therefore, during the LeDaR measurement, one requires a transparent reservoir to allow optical access. During the two-phase flow experiments, the reservoir is filled with some liquid (in the present case water) (see Figure 3.1). The instantaneous position of this water surface is the subject of the investigation.

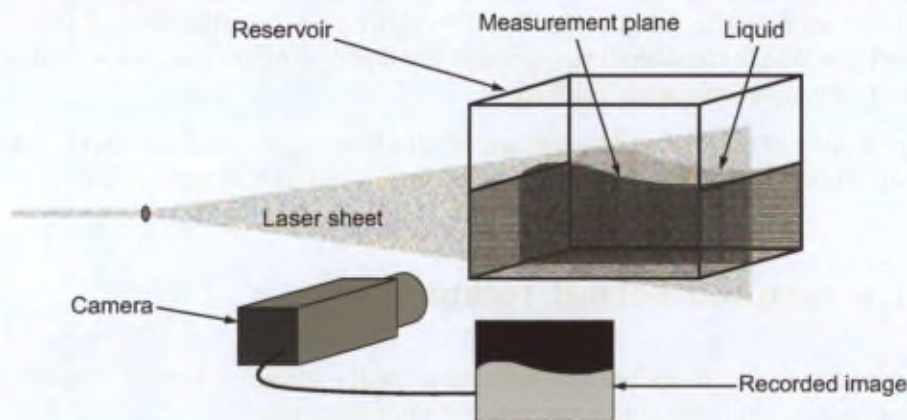


FIGURE 3.1 – General LeDaR arrangement.

By generating a laser-sheet (using a continuous laser source), the plane of interest is illuminated. The surface detection is limited to the illuminated region.

When the investigated liquid does not diffuse effectively the light - as for water -, one should dissolve some fluorescent dye in the liquid. Thus, the laser-sheet is exciting the fluorescent dye and the fluorescent light emission visualizes the plane.

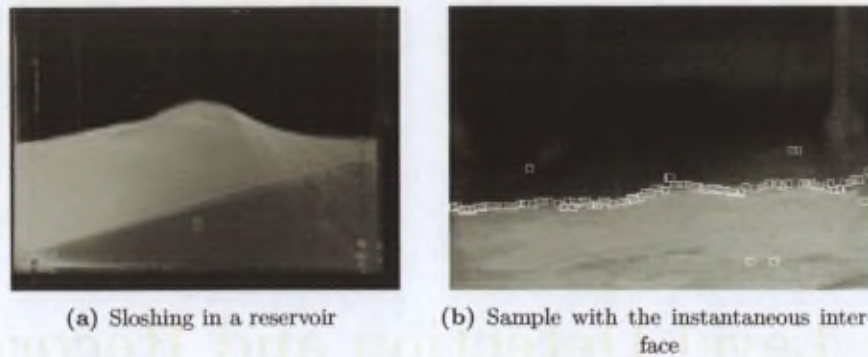


FIGURE 3.2 – Sample frames of a video recording.

From the illuminated plane, a colour video stream can be recorded with a camera. Typical frames are shown in Figure 3.2. The stream is analysed in real time by the LeDaR algorithm.

The LeDaR algorithm is basically an image processing tool using Microsoft DirectX and relying on the so-called *Sobel edge-detection transformation filter*. In practice, it scans the selected region of each frame pixel column by pixel column from top to bottom. At each pixel location it computes the convolution of the local intensity distribution with the  $3 \times 3$  Sobel operator matrix (see Eq. (3.1)).

$$\mathit{Sobel}Y = \begin{bmatrix} -1 & -2 & -1 \\ 0 & 0 & 0 \\ 1 & 2 & 1 \end{bmatrix} \quad (3.1)$$

As it can be seen, the filter is sensitive to vertical dark-to-bright gradients. At each location, the coefficient of the filter (Sobel coefficient) is determined and compared to a user-defined threshold. As soon as the value of the Sobel coefficient reaches the value of this threshold, the actual pixel position is considered to represent the liquid interface and the scanning of the lower positions of that pixel column is skipped.

The ensemble of the detected positions in all of the pixel columns draws the whole liquid surface corresponding to the plane of the laser-sheet (similar to Figure 3.2(b)).

## 3.2 The adapted LeDaR technique

The present section describes the limitations of the classical LeDaR technique within the present application and introduces the realized improvements.

### 3.2.1 Adapting the measurement conditions

Within the present study the operation of the EAPs of the Ariane 5 launcher is investigated. A water spray installed in the stagnation chamber simulates the alumina formation. Furthermore, the main geometrical elements (inhibitor, nozzle, cavity) are modelled. With the LeDaR technique the goal is to determine the governing parameters of the slag accumulation process.

A preliminary assessment was carried out with the help of Tran (2004) and some serious limitations of the classical LeDaR technique were shown, which prevent reliable measurements.

Although the set-up is built to be 2D-like, the motion of the airflow inside the cavity shows three-dimensional behaviour. As a consequence, the waves of the accumulated water surface (induced by the airflow) are three-dimensional as well. The laser-sheet (the plane of the investigation) is positioned in the mid-span plane of the test section (as it is also done during the PIV measurements). Therefore, if the camera is placed normally to the laser-sheet, the three-dimensional waves may block the view and inhibit acquiring images from the middle plane. To overcome this problem, the camera should simply be inclined (looking slightly from above). During the data processing, one can easily take into account this perspective effect.



FIGURE 3.3 – *Droplets on the sidewall of the preliminary set-up.*

Furthermore, as it was already described by Tran (2004), the main source of the constraints is due to the water droplets that stick to the plexiglas through which the camera is looking at the field (a sample frame is shown in Figure 3.3). These droplets restrict the optical access. They may deviate the light rays travelling towards the camera. Furthermore, if they are close to the "depth of field" of the camera (the portion of space that is in focus and appears sharp in the images), they may represent intensity gradients that affect the level detection. In practice, these droplet images are detected instead of the real liquid surface. The conclusion of Tran (2004) is that the measurements performed within this condition have a very large ambiguity. In order to reduce the visibility of these droplets, two main solutions are found:

- Surface treatment of the cavity wall;
- Modification of the imaging properties of the droplet images.

The first solution consists of using a special transparent surface treatment that makes the surface hydrophobic, i.e. avoiding the droplets to stick to the sidewall through which the camera observes the middle plane. Unfortunately, it is experienced that none of the tested materials provide noticeable improvement on plexiglas surfaces. However, treating the surface of glass results in a considerable modification. Therefore, the inner surface of the cavity wall through which the camera records images is covered by a 2 mm thick glass sheet. The glass is treated with a silicon-based spray, which was found to be the most effective.

With this treatment, the surface would not remain dry while the spray is operating. Water droplets are still depositing. However, the size of the droplets remains smaller (the bigger ones are not able to stay on the vertical surface), which reduces their optical effect.

The second solution to reduce the visibility of the wall droplets is to modify the imaging properties of the droplet images. The main goal of this approach is to have the blurriest possible images during the measurements from these droplets, while the plane of the laser-sheet is still sharp. By blurring the droplet images, most importantly their contour would represent lower gradients. Furthermore, their intensity would reduce, as their size in the image increases (compared to the sharp droplet image size). The distance between the laser-sheet and the sidewall is fixed, therefore the only parameter that could be modified is the optical properties of the lens system of the camera.

Apart from a few exceptions, all of the image recording systems have a property called the *depth-of-field* (DoF). The DoF stands for the depth (the dimension along the optical axis of the image recording system) of a brick-shaped space portion. By placing any object within this space portion, the recorded image would be absolutely sharp. In other words, this is the region, which is in focus. The size of the DoF depends mainly on two parameters: the focal number ( $f\#$ ; aperture) of the camera optics and the size of the recording medium (film or CCD/CMOS sensor). The smaller the recording medium is, the larger the DoF would become. Obviously, changing the size e.g. of a CCD-chip is not a common task. Therefore, one should consider the focal number. The larger the focal number is, the larger the DoF is. In order to limit the sharpness of the droplets on the wall, the narrowest possible DoF should be chosen, which can be achieved by opening the aperture and thus using the minimum available focal number.

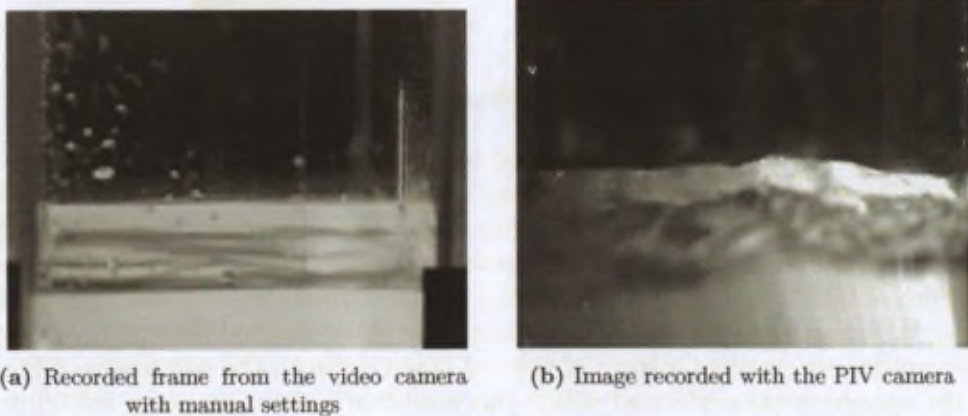


FIGURE 3.4 – Sample images of decreasing the DoF (without surface treatment).

Therefore, during the preliminary tests manual focusing (to the laser-sheet) is used with the video camera and the aperture is set to the lowest available value ( $f\# = 2.8$ ). In spite of all the efforts spent using the video camera, no better image quality could be achieved than what is shown in Figure 3.4(a). Unfortunately, the visible droplets are not blurred enough and the detection algorithm identifies them as the liquid surface.

That is why the tests with the video camera are not continued. Instead, the applicability of a CCD camera that is used for PIV measurements (PCO 12-bit SensiCam) is investigated. Installing a  $f_l = 50$  mm Nikkor lens ( $f\#_{min} = 1.8$ ) on this camera, rather promising images (a sample is shown in Figure 3.4(b)) could be recorded in the preliminary set-up even without surface treatment.

The preliminary tests are performed using one side of the VKI L-6 vertical twin-jet wind tunnel<sup>1</sup> with a simplified test section. A sketch of the set-up can be seen in Figure 3.5(a). A

<sup>1</sup>a detailed description of the L-6 wind-tunnel is given by Suda (2000)

water spray installed in the stagnation chamber provides the liquid-phase. For further details regarding the conditions, refer to Tran (2004).

As it can be seen in Figure 3.5(a), a balance supports the simplified cavity model (it is not fixed to the test section). Simultaneously with the LeDaR acquisitions (using the PCO PIV camera inclined by  $10^\circ$  and no wall treatment), the instantaneous mass of the cavity (including the accumulated liquid) is recorded regularly from the display of the balance (at  $U_0 = 7$  m/s). During the same recording, the water spray fills the cavity at first and then the cavity is drained through a tube installed in one of its corners.

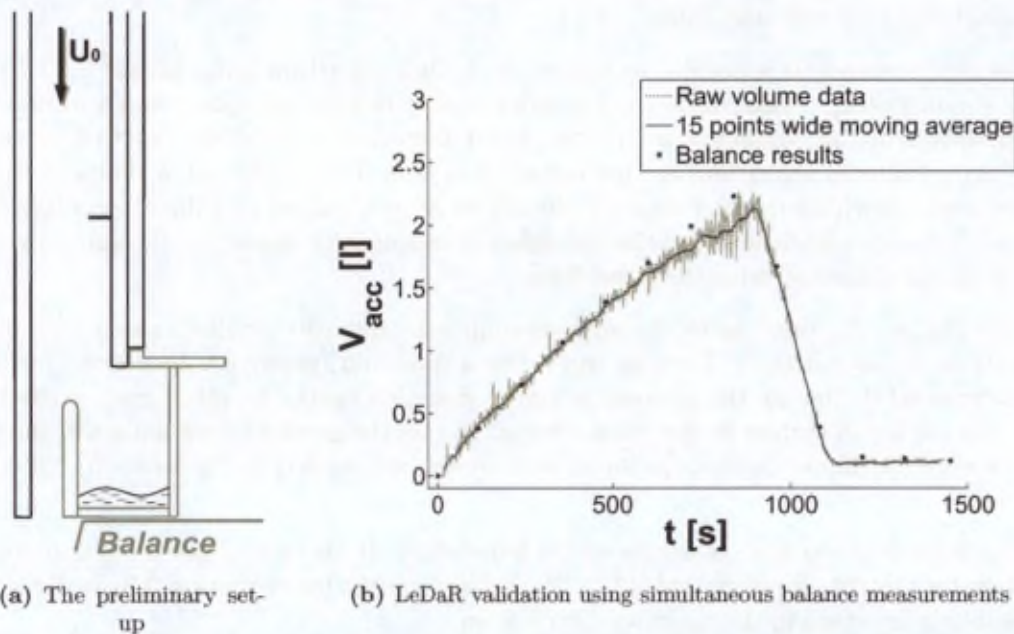


FIGURE 3.5 – Validating the adapted LeDaR measurement conditions.

The evolution of the water volume in time measured by LeDaR and simultaneously by the balance is plotted in Figure 3.5(b). One can observe a good agreement between the two measurements up to a volume of about 1.3 litres. Above this value, the LeDaR measurements under predict the real volume. The reason originates most probably from the  $10^\circ$  viewing angle of the camera. At higher water levels it does not seem to be sufficient and the three-dimensional waves together with the splashes of the arriving droplets are biasing the measurements.

To sum up, a CCD or CMOS camera should be used for the image recording with the lowest possible focal number. The camera should be inclined more than  $10^\circ$  with respect to its horizontal position. Furthermore, the final liquid volumes should be always validated.

### 3.2.2 Adapting the detection algorithm

As already mentioned, the classical LeDaR program is a DirectX filter designed to analyse colour video streams. Fluoresceine is emitting essentially green light with a low amount of yellow content. In the digital RGB (red-green-blue) domain these colours cover therefore primarily the green layer and secondarily the red as well. However, at locally brighter regions (which is the case near the air-liquid interface) the yellow is more dominant. This means more pronounced intensity gradients in the red component at the surface. Hence, the filter is detecting the surface using only the red layer of each frame (the green and the blue layers are not taken into account).

On the other hand, it is suggested to apply a CCD or a CMOS camera instead of a video camera to reduce the effect of the droplets that are depositing on the wall of the test section. However, current scientific CCD cameras involve greyscale sensors (do not apply e.g. any *Bayer Colour Filter Array*, *Foveon-type sensor* or other technique to colorize the images) and thus output greyscale still images. Although, formally it is possible to convert a series of greyscale images into a colour video format - since the red, the green and the blue layers would contain identical information -, the particularity of the red component is lost. Furthermore, the classical LeDaR program processes the video files in the same way as the real-time video signal. Thus, in function of the CPU speed it may skip several frames of the video stream, which makes the resulting time evolution unreliable.

As a consequence, it is decided to rewrite the LeDaR algorithm using *Matlab's GUI* (Graphical User Interface). This version reads series of still images and analyses them one-by-one. Furthermore, in the Matlab-based version apart from the Sobel edge-detection filter (equation 3.1), additional algorithms are implemented as well. Two of these new methods that seem to be promising within the current study are the *Positive Gradient* and the *Forward Step* filters. Both of these new algorithms scan the user-selected area of the images (pixel) column-by-column, like the original method with the Sobel-filter.

The Positive Gradient method computes simply the intensity gradient along each pixel column (from top to bottom). The user can define a threshold (positive values stand for dark-to-bright gradients). In case the gradient is higher than this value, the given pixel is identified to represent the liquid surface at the given column. In case the gradient does not reach the value of the threshold within a column, the liquid level would be declared to the location of the highest gradient.

The Forward Step filter is similar to the Sobel-filter. It also computes the convolution with an operator matrix. However, this  $[21 \times 3]$  operator matrix (see equation 3.2) is not detecting edges, but more steps in the intensity distribution.

$$FwStep = \begin{bmatrix} -1 & -2 & -1 \\ \vdots & \vdots & \vdots \\ -1 & -2 & -1 \\ 0 & -1 & 0 \\ 0 & 0 & 0 \\ 0 & 1 & 0 \\ 1 & 2 & 1 \\ \vdots & \vdots & \vdots \\ 1 & 2 & 1 \end{bmatrix} \quad (3.2)$$

In Figure 3.6(a) a  $200 \times 200$  pixels<sup>2</sup> sample of a LeDaR image can be seen. Along the vertical inverted pixel column, the intensity profile is extracted and shown in Figure 3.6(b). Along the profile, one can observe a sharp peak at  $Y = 77$  pixels, which represents a small droplet image. Furthermore, a step is visible around  $Y = 150$  pixels, which corresponds to the liquid interface.

As it can be seen, the intensity gradient of the droplet image is even steeper than the gradient of the water surface. Therefore, the Positive Gradient method would identify the liquid interface around the droplet. Since the Sobel-filter also detects a local gradient, it would predict the liquid interface around the droplet as well. However, the Forward Step filter is sensitive to intensity steps similar to the raising edge of an electric TTL signal thanks to its operator matrix. It

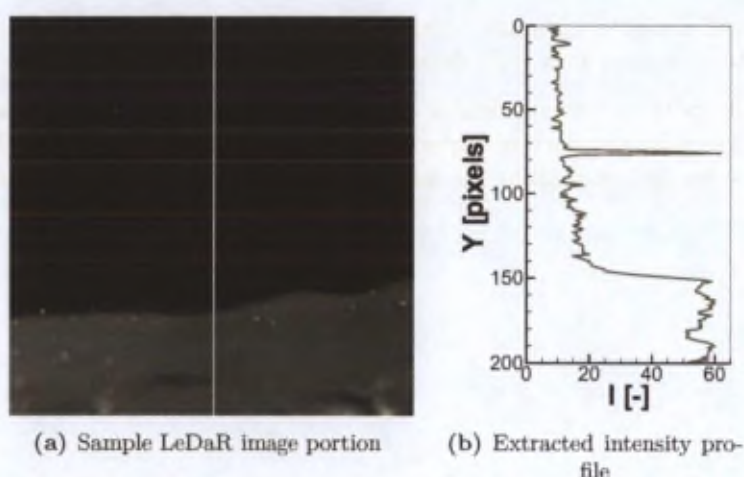


FIGURE 3.6 – Typical intensity variation in LeDaR images in the vicinity of the interface.

would have higher coefficient value around (positive) gradients, where the preceding pixels have uniformly low values and the following pixels have uniformly high values.

The coefficient of the Forward Step filter is also compared to a user-defined threshold. The location where the coefficient reaches the value of the threshold is associated to the liquid interface.

The Forward Step filter can follow very well the shape of the surface. However, its drawback is that it is difficult to find a global threshold, which gives an accurate  $Y$  position of the water surface in the whole analysed image. The method is too sensitive to the uniformity of the illumination of the water. At regions where the illumination is stronger, it over-predicts the surface; while at weaker illumination regions it is not able to find the surface.

To make the detection more robust, an additional criterion is implemented. Similarly to the Positive Gradient method, in case the coefficient does not reach the user-defined threshold within one pixel column of the detection region, the position with the maximum coefficient value is distinguished to be the local position of the liquid level. The filter with this extension is called *Maximum Forward Step filter*.

This automatic method appears to be more robust than the previously described filters. Furthermore, it detects generally more precisely the water level than the basic Forward Step filter.

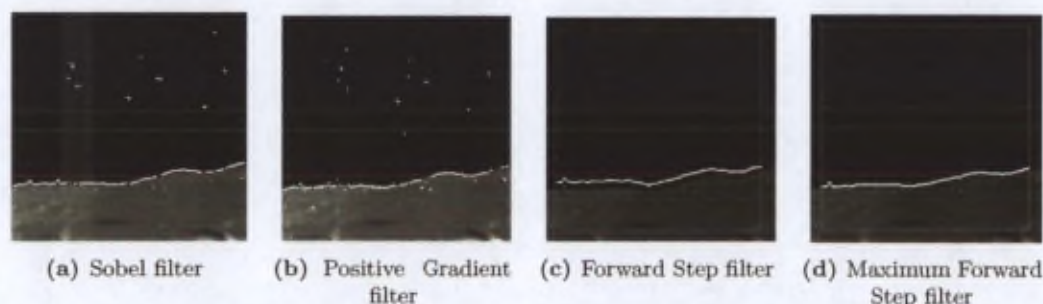


FIGURE 3.7 – Comparing the different detection methods.

A comparison of the filtering performances of the above-described techniques is shown in

Figure 3.7 using the given sample image. However, it is important to emphasize that the optimal detection method may vary depending on the actual image quality.

Thus, finally both the experimental conditions and the surface detection algorithm should be capable of handling the current experimental conditions and therefore the LeDaR technique is considered to be operational for the foreseen parametric accumulation investigation.



## Chapter 4

# The two-phase Particle Image Velocimetry technique

In order to be able to perform PIV experiments in two-phase flow (air + liquid droplets) condition, first an appropriate technique should be established. The present chapter explains the evolution and the principle of the currently developed approach.

As an introduction, a description is given about the main difficulties concerning the two-phase PIV technique. After defining the main goals, several methods are proposed which could be followed to achieve the objectives. The advantages and disadvantages of all these solutions are investigated.

Finally, the proposed technique is further developed, and all the aspects of its applicability are verified and demonstrated as well.

### 4.1 Introduction

#### 4.1.1 The principle of PIV

*Particle Image Velocimetry* (PIV) is a whole-field non-intrusive optical measurement technique whose aim is to determine the instantaneous velocity field of a flow.

In single-phase flow condition, small (investigating air:  $\sim 1 \mu\text{m}$  diameter oil) tracer particles are injected to the fluid. The tracers are following the motion of the fluid without disturbing it. The region of interest is illuminated by a light-sheet (in general, using a laser-source). The tracers inside the sheet are scattering light, from which two successive images with a known *separation time* ( $\Delta t$ ) are recorded with the help of a - generally digital - camera (a sample is shown in Figure 4.1). Therefore, by determining the displacement of the tracer images ( $\Delta \bar{s}$ ), the velocity of the flow can be easily obtained ( $\bar{v} = \Delta \bar{s} / \Delta t$ ).

In practice, the image pairs are divided into smaller regions, called interrogation windows. In each window pair, the mean displacement of the tracer images is determined using basically the cross-correlation function. In the PIV algorithm of the VKI (WiDIM), more elaborate methods (e.g. iterative window refinement, window overlapping, validation procedure, etc.) ensure a more precise displacement determination. More details about the conventional PIV technique itself and on the algorithm can be found in Appendix A.1, Scarano and Riethmuller (1999b;a); Scarano (2000).

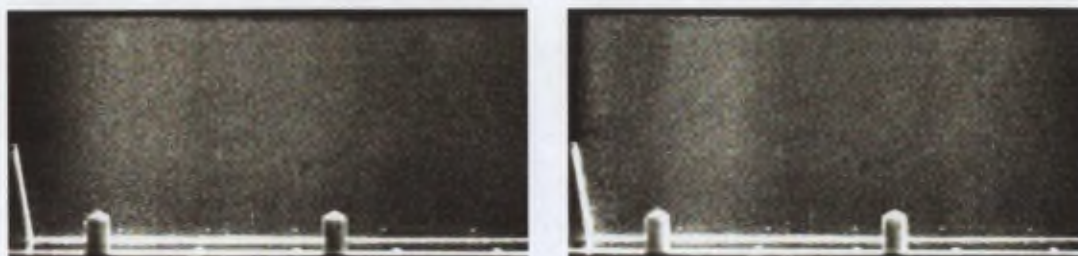


FIGURE 4.1 – Raw image pair recorded during a PIV measurement.

#### 4.1.2 Difficulties in two-phase condition

Nowadays, the PIV technique in single-phase condition is widely used in most laboratories. However, by introducing a second phase (liquid droplets, solid particles or gas bubbles) in the fluid, the application of the PIV technique is not obvious anymore. In the present case, liquid droplets should simulate the liquified alumina particles of the SRM.

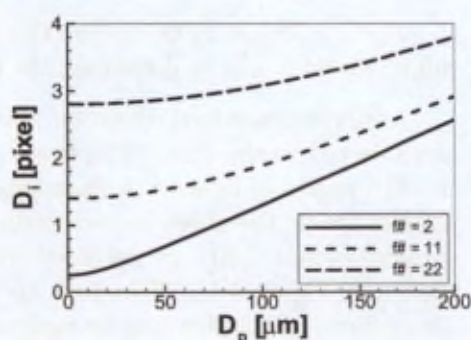
In two-phase flow configuration the objective of PIV is to simultaneously measure the velocity of each phase.

By recording images using the above-described method, one would obtain images similar to Figure 4.2(a). Here, the droplets belonging to both of the phases appear. However, as the second-phase droplets are at least one order of magnitude larger than the tracers, they are not able to follow the motion of the continuous-phase. In addition, they may even modify the gas flow field. The investigation of this interaction is one of the objectives of the present study. By analysing these kind of images directly with the PIV algorithm, the displacement of the droplets could bias the correlation and therefore the velocity field of the gas-phase and thus the corresponding gas-droplet interaction cannot be safely determined.

As a consequence, the images of the two phases have to be separated. This is the key point of all the multi-phase PIV measurements. Once succeeded, the conventional PIV algorithm could be used to determine on the one hand the velocity field of the continuous-phase and on the other hand the displacement of the second phase droplets.



(a) Sample image in two-phase condition (air + water droplets)



(b) Theoretical droplet image sizes

FIGURE 4.2 – Two-phase flow acquisition.

As the difference in size between the tracers and the droplets is at least one order of magnitude, it seems to be straightforward that by measuring the sizes of their images, they could be sorted out. However, these objects have a diameter close to the wavelength of the illuminat-

ing light ( $\lambda = 532$  nm in case of the 2nd harmonic of a YAG laser). In this domain the laws of geometrical optics are not valid; instead, the Mie scattering theory is describing the image formation:

$$D_i = \frac{\sqrt{(M \cdot D_p)^2 + (2.44 \cdot f_{\#} \cdot \lambda \cdot (M + 1))^2}}{D_{pixel}} \quad (4.1)$$

The droplet image size ( $D_i$ ) is computed using equation 4.1 in function of the physical droplet size ( $D_p$ ) using a typical magnification ( $M = 0.15 : 1$ ) and three different focal numbers ( $f_{\#}$ ). According to the results (shown in Figure 4.2(b)) it is visible that computing the real droplet size based on the images (in pixels), the uncertainty can be very large up-to several tens of  $\mu\text{m}$ . Therefore, distinguishing the tracers from the smallest droplets based only on their diameter in the images is practically impossible.

In order to overcome the difficulties and allow two-phase flow PIV measurements, several solutions are proposed by researchers. Among the recent investigations, Khalitov and Longmire (2002) demonstrated a phase separation technique using solid glass particles in a turbulent channel flow. The glass particles are quasi mono-dispersed. During the experiments only one camera is used and the identified images of the two phases are discriminated with a relatively complex algorithm based on the intensity and the diameter of the appearing objects.

However, as soon as the second phase particles are truly poly-dispersed, additional information has to be found. The simplest excess information is related to the colour of the objects. Therefore, most of the researchers apply fluorescent dyes in either of the phases.

The flow around growing bubbles was studied by Dias Pereira (1999); Dias Pereira and Riethmuller (1998). An Argon-Ion laser illuminates the plane of interest. With the help of fluorescent tracers and a long-pass optical filter the PIV camera is not affected by the laser reflections occurring at the bubble surface. A second camera equipped with the same kind of long-pass filter acquires the bubble shadow contour with white back-illumination. Therefore, the discrete-phase (bubble) contours and the tracer particle images are separated.

Lindken and Merzkirch (2002) studied also a bubbly liquid flow. They applied a green ( $\lambda = 532$  nm) laser-sheet with fluorescent tracers (which emits light close to red) and a red back-illumination. Thus, in the images of the single camera - that is equipped with an optical long-pass filter to cut the laser light - the bubbles show shadows and the tracers have higher intensity compared to the background. Therefore, the images of the different phases are identified and masked based on their intensity level.

The shadow technique was used by Nogueira et al. (2004) as well in order to detect the contours of large bubbles travelling in a vertical tube and to investigate the liquid motion upstream and downstream the bubble and the liquid film between the bubble and the tube wall with PIV.

Considering the air-droplet flows, several approaches are proposed. Boëdec and Simoëns (2001) doped their droplets with fluorescent dye. One camera records Mie scattering images ( $\lambda = 532$  nm) from the ensemble field (tracers and droplets) and a second camera equipped with an optical long-pass filter records fluorescent droplet image pairs. To separate the two phases, the droplet images are identified and subtracted from the ensemble flow field.

The realized method of Towers et al. (1999) implies a green ( $\lambda = 532$  nm) laser pulse corresponding to the first images of the PIV couples and a red ( $\lambda = 610$  nm) laser pulse

corresponding to the second images. The tracer particles are fluorescent. A home-made quasi-colour camera grabs single images from the green layer and the red layer of the field-of-view. That allows on the one hand to separate the temporal information and on the other hand to discriminate between the fluorescent and non-fluorescent objects which correspond to the first laser pulse.

The applicability of fluorescent tracers in the presence of a dense spray was demonstrated by Rottenkolber et al. (1999). Rottenkolber et al. (2002) shows two techniques: the masking and the peak separation. The masking technique involves fluorescent tracers and one camera, which is equipped with a carefully chosen optical long-pass filter that reduces the Mie scattering intensity levels to the levels of the fluorescent emission. Later, the images of the tracers and the droplets are digitally separated based on delicate intensity thresholding. In case the local displacement of the two phases are sufficiently different, the peak separation technique can be applied as well. This separates the displacement information of the two phases according to the properties of the correlation peaks.

Grünfeld et al. (2000) combines PIV with *Laser Induced Fluorescence* (LIF). A gaseous tracer (NO) is excited by a UV ( $\lambda = 266$  nm) laser-sheet from which fluorescent images are recorded. A second laser-sheet illuminates the field quasi-simultaneously. This light is scattered by the droplets, which can be recorded with a second camera. Thus, the images of the two phases are separated optically.

Fluorescent tracers excited by  $\lambda = 355$  nm are used by Driscoll et al. (2003). A second laser-sheet produces  $\lambda = 532$  nm illumination used for the visualization of the droplets. However, the illuminations are not simultaneous. The separation time of the double pulses corresponding to the different wavelengths are adapted according to the velocity magnitudes of the different phases. A camera equipped with a bandpass filter acquires image pairs of the tracers and a second camera equipped with an interference filter acquires Mie scattering images at  $\lambda = 532$  nm. As the number of droplets in the spray region is substantially higher than the number of tracers and since the droplets are considerably larger, the authors claim no need of additional phase separation.

The most appealing technique - presented by Kosiwczuk (2006) - uses a laser-sheet of  $\lambda = 355$  nm and different fluorescent dyes in the two phases. Using two cameras and proper optical filters, the Mie scattered light is cut and the images of the phases are separated optically. Some further details on this method will be given later in section 4.2.4.

Similarly to most of these techniques, the approaches that are described in the following sections also differentiate between the objects of the two phases using an additional information based on fluorescent wavelength shift.

## 4.2 Choosing a two-phase PIV approach

In the present section various candidate tools are proposed for the two-phase PIV experiments. Both the potential and the limitations of each of them are described based on which finally a selection is made.

### 4.2.1 The preliminary technique

The first technique that allows two-phase (gas + liquid droplets) PIV measurements is also developed within this research work. Details of its basic principle are given by Tóth and Anthoine (2003); here only a summary is outlined together with a discussion concerning its performance.

#### 4.2.1.1 The image recording

The technique itself is very similar to the one used by Boëdec and Simoëns (2001).

The method utilizes fluorescent dye (Rhodamine 6G) which is dissolved in the droplet-phase (represented by water droplets). In general, the molecules of a fluorescent paint absorb the photons of the illumination and use their energy to emit light at a higher wavelength. At the illuminating  $\lambda = 532$  nm wavelength Rhodamine 6G has a high absorbance, high efficiency and its emission band has a peak around 566 nm (e.g. according to Brackmann (2000)). Thus, on the one hand the droplets emit light in the yellow-orange range of the visible spectrum. On the other hand, on the surface of the droplets light reflection still occurs. Therefore, droplet images can be acquired at the fluorescent emission wavelength and/or at the illumination (laser) wavelength.

Within the present technique (see also Figure 4.3) two PIV cameras are used to record simultaneous image pairs. One of the cameras records image pairs from both of the phases (entire flow field images, similar to Figure 4.2(a)). The second camera is equipped with an optical long-pass filter that cuts the 532 nm illumination wavelength (and all the shorter ones as well) and lets only the emitted fluorescent light pass through. As a result, the second camera records simultaneous image pairs containing only droplet images. In the followings, an image processing algorithm is separating the two phases.

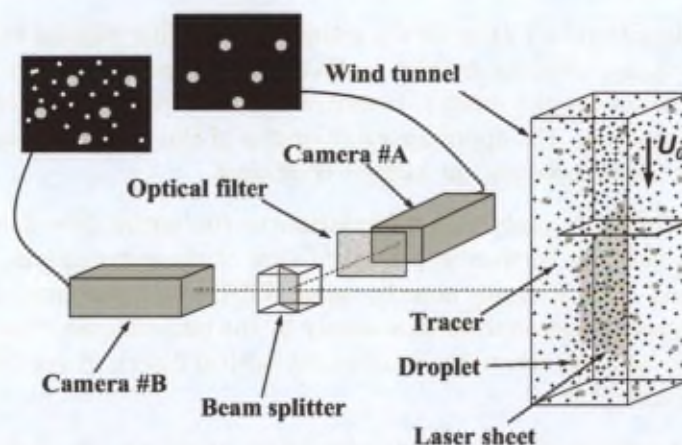


FIGURE 4.3 – Arrangement using the preliminary technique.

#### 4.2.1.2 The image processing algorithm

Here, only the latest version of the algorithm is described, which differs at some points from the one shown by Tóth and Anthoine (2003).

The main idea of the process is to create a mask that hides the images of the droplets in

the instantaneous entire flow field image pairs. Once accomplished, the separate image pairs containing only tracer images and only droplet images are available.

At first the droplet images from *Camera #A* are analysed. After filtering the image (to reduce noise and sharpen the images of the objects), the algorithm performs a wavelet analysis (for details, concerning the similar vortex-detection wavelet technique, please refer to Schram et al. (2004)) in order to detect the location and the size of each droplet image.

The images of the droplets represent an Airy pattern, which can be well approximated by a Gaussian distribution (shown e.g. by Adrian and Yao (1983) and Scarano (2000) as well). Therefore, using the two-dimensional *Marr* (Mexican hat) mother wavelet, the Gaussian droplets can be well localized. The shape of the mother wavelet is shown in Figure 4.4. In the detection algorithm typically  $n_{scales} = 12$  different scales (diameters) of this function are considered. The smallest scale is typically 2 pixels in radius; the largest scale is of the order of the largest droplet radius observed visually in the images (around 7 pixels).

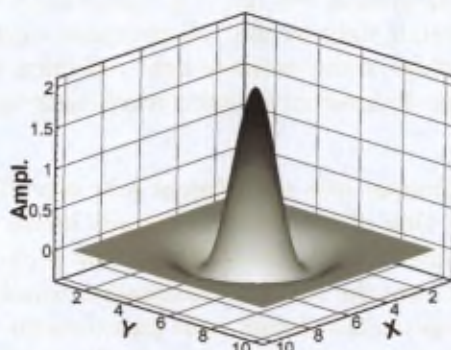


FIGURE 4.4 – *The Mexican Hat mother wavelet.*

The wavelet algorithm correlates all the scales of the mother wavelet function with the whole image. From the  $n_{scales}$  resulting wavelet coefficient fields local peaks are detected. These ones give the locations of the droplet images. Investigating the wavelet coefficients at a given position among the different scales, the approximate diameter of the droplet image can be obtained by choosing the scale that represents the highest coefficient.

In order to be able to apply this information to the entire flow field images (of *Camera #B*), the transfer function between the fields of view of the two cameras has to be determined (spatial calibration). This is simply done by using WiDIM on instantaneous single-phase images (containing only tracers) acquired simultaneously by the two cameras (these images are obtained from a separate preliminary recording without any optical filter). A typical transformation field can be found in Figure 4.5.

Using the transformation field, the droplet image locations obtained by the wavelet-based algorithm can be transferred from the droplet-phase image (*Camera #A*) to the ensemble flow field image (*Camera #B*). During the preliminary tests it was discovered that a small misalignment (up-to a few pixels) can occur in the droplet image location due to the uncertainty of the spatial calibration. Thus, the transformed droplet image location in the entire flow field image has to be tuned. For this purpose a small (the size of the detected radius of the droplet) search area is defined, where a new wavelet analysis is carried out using only three scales close to the predicted droplet image diameter.

However, in practice the lenses of the two cameras do not use the same aperture ( $f\#$ ) and do not receive the same light. Therefore, different image diameters will be projected from each

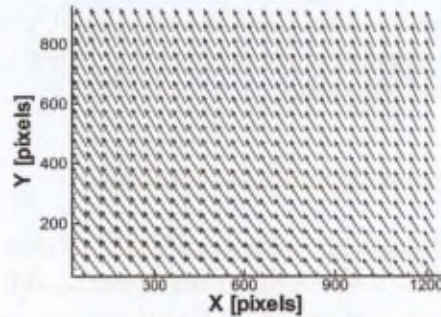


FIGURE 4.5 – *The difference between the fields of view of the two cameras.*

droplet according to Figure 4.2(b). Thus, once the real droplet image position is determined, its diameter needs to be recomputed as well. In order to reduce the computational time and still remain accurate, in this last step the wavelet algorithm using several scales is avoided. Instead, starting from the centre of the droplet image, the intensity gradient is investigated along a vertical and a horizontal profile. The location, where the gradient changes sign (the intensity values stop decreasing) is considered to be the border of the droplet image along each profile. Finally, these values are averaged to obtain the final droplet diameter.

This process is repeated with all the droplet images. As a result, one owns a map of the exact droplets' image location together with their sizes. Therefore, all the droplet images can be masked now in the same way as it is described by Tóth and Anthoine (2003), namely by defining zero intensity value in the area corresponding to a droplet. In Figure 4.6(a) an example of a masked image is shown.



(a) Gas-phase PIV (tracers) image sample after masking



(b) Droplet-phase image sample

FIGURE 4.6 – *Test section configurations.*

As a result, one has image pairs containing only tracer images (Figure 4.6(a)) and image pairs containing only droplet images (Figure 4.6(b)). Therefore, the conventional PIV algorithm (WiDIM) can be applied to obtain the gas-phase velocity field. Furthermore, the droplet properties can also be determined using the droplet-image pairs, as it was presented in Tóth and Anthoine (2003).

As shown by Régert (2004), using this method, the masks that practically displace together with the droplet images may still bias the gas-phase velocity field since they do not follow the gas-phase as the tracers but will be taken into account during the cross-correlation operation (as pointed out by Gui et al. (2003) as well). Furthermore, it was found (Régert (2004)) that the amount of scattered light from particularly large droplets could reach beyond the limit the

CCD sensor of the camera can sustain (for *Camera #B*). This may lead to the damage of the PIV camera. Therefore, this technique can not be used. However, using various elements of this method, other approaches are proposed.

#### 4.2.2 The successive measurement technique

From the camera safety point of view, it is essential that no light should arrive in any camera at the wavelength of the laser, as direct light reflections from large droplets could contain dangerously high energy. Thus, the camera(s) should be protected by optical filters. Therefore, in order to be able to record images of objects, the use of fluorescent dye is inevitable (to realize a wavelength shift compared to the laser emission). As the fluorescent emission is isotropic, no direct reflection can occur at this wavelength.

However, one needs to differentiate between the two phases. By using 532 nm green light as an illumination (the 2nd harmonic of the YAG laser), unfortunately there is not enough space in the visible spectrum to use two different dyes in the two phases and separate them properly via optical filters. The applicability of a technique of this kind is investigated by Kosiwczuk et al. (2005).

Therefore, according to the first proposed technique, the images are not recorded simultaneously. At first, a given type of fluorescent dye (e.g. Rhodamine B) is dissolved in the tracers. Image pairs are recorded using one camera, which is equipped with a long-pass optical filter that cuts the wavelength of the laser. Then, the same fluorescent dye is dissolved only in the droplets and another series of image pairs is acquired with the same camera through the same filter.

In other words, the same test is repeated twice. In both cases, the droplets are physically present in the test section. However, they become visible to the camera only when they contain fluorescent dye. When the droplets are not doped, fluorescent tracers are injected in the gas-phase.

Thus, in theory one should have separate image pairs containing only tracer images (the gas-phase) and separate image pairs containing only droplet images. Since they are recorded in different time instants, only the statistical properties of the two phases can be correlated.

##### 4.2.2.1 The device generating fluorescent seeding

Fluorescent droplets have already been generated using the preliminary technique without any problem. However, fluorescent tracers have not been generated yet. The traditional seeding generators of the VKI evaporate oil by spraying it on a heated (approx. 170 °C) plate. These devices produce particles of the order of 1 to 2  $\mu\text{m}$ . Unfortunately, the fluorescent dye intended to be used (Rhodamine B) can not be dissolved in oil. Furthermore, by applying a fluorescent material, one does not want to heat up the tracers so as not to change the properties of the dye. The only available device producing fine droplets without heating is a Laskin nozzle at the VKI (Moraitis (1987)). However, the generated tracer diameter turned out to be too small<sup>1</sup> to emit sufficient fluorescent light, which could be detected by the camera. Therefore, a new seeding generator, a nebulizer is built.

The sketch and some pictures of the device are shown in Figure 4.7. During operation, sonic air is injected through a vertical tube. A feed pipe which originates from the bottom of the reservoir is attached to the horizontal liquid tube. At the injection, the sonic air is passing in

<sup>1</sup>it produces sub-micron size droplets

front of the exit of this horizontal tube and creates a considerable pressure decrease. Therefore, the liquid from the reservoir is sucked up through the liquid feed pipe and immediately atomized by the airflow. The final unit contains four identical nozzles to be able to produce a large amount of seeding particles.

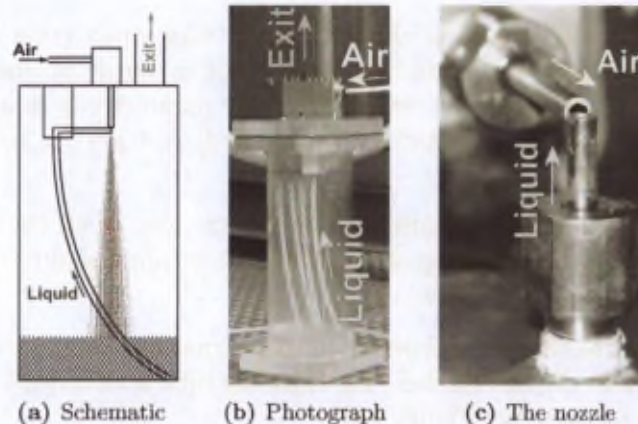


FIGURE 4.7 – The seeding generator.

The exit of the device is located on the top cover. As the atomized particles are travelling with the flow from top to bottom, they need to turn  $180^\circ$  to reach the exit. Therefore, the large particles (representing a Stokes-number closer to unity), which are not capable of following the motion of the air-flow will fall back into the liquid bath. Thus, the arrangement itself plays the role of an impactor entrapping the particles that are too large to be tracers.

Using this device one can generate droplets with a mean diameter of  $d_{32} = 1.5 \mu\text{m}$ . Finally, glycerine is applied as the base of the tracers' material in which Rhodamine B can be dissolved effectively.

#### 4.2.2.2 Fluorescent tracer applicability

In order to verify the applicability of the generated tracer particles, a single-phase PIV measurement is carried out in the VKI L-11 wind-tunnel by installing an inhibitor of  $h = 27 \text{ mm}$  and without installing the nozzle cavity to allow easy access to the test section for frequent cleaning.

The fact that the acquired light is fluorescent emission (and not simple reflection) does not bias the PIV measurements. This was already confirmed e.g. by Kosiwczuk et al. (2005). However, working with fluorescent material, the particles should still be small enough to follow the airflow, but they should be large enough to contain sufficient dye molecules that could emit enough light from the laser excitation to be detected by the camera.

Unfortunately, in the fluorescent domain, the amount of emitted light is not necessarily proportional to the amount of dissolved dye. In practice, by increasing the concentration, at first the emitted light intensity increases. However, beyond a given concentration one falls in the region of *self-quenching*. It means that the dye molecules are so close to each-other that the probability of an emitted photon hitting another dye molecule is very high. When this photon hits a molecule, it will be re-absorbed. As the efficiency of the dye molecules is well below 100% (in case of Rhodamine B the efficiency peak is around 29%), it means that the amount of emitted light from a tracer decreases again beyond a given concentration.

Concerning the illuminating light intensity, a non-linear behaviour can be observed as well. As the light energy is increased, more-and-more photons are absorbed by the dye molecules. However, the molecules have a given recovery time, therefore by exciting them with higher intensity would not produce more light emission. On the contrary, by applying too high illumination energy, the molecules might be burnt.

Therefore, as one can see, since the tracers are very small (they are comparable to the illuminating wavelength) there should be a size limit in terms of diameter below which the droplets would not be visible to the camera whatever parameter is changed (dye concentration or laser energy). This limit was found to be around  $d_p = 4 \mu\text{m}$  by Towers et al. (1999) using saturated Rhodamine 640 solution.

Thus, during the present verification measurement, first of all the visibility of the tracers should be checked. The secondary goal is to verify their applicability from the dynamic point of view (whether they follow the flow).

During the tests, the tracers are injected in the stagnation chamber to allow sufficient mixing before the air arrives at the test section. The injecting tube is installed on the top of the existing cross-shaped spray support (see Figure 4.8).

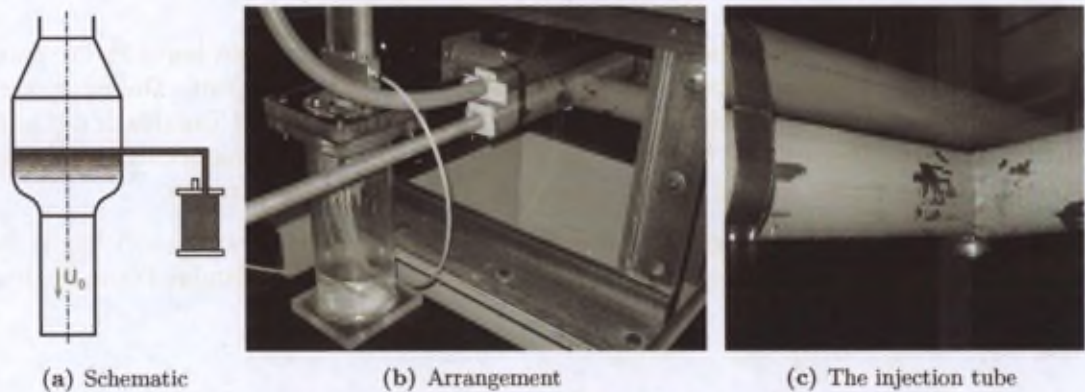


FIGURE 4.8 - *The seeding generator.*

In the test section, the laser-sheet is generated in a classical way in the mid-span of the test section just downstream the inhibitor. One 12-bit PCO SensiCam PIV camera is recording images through a long-pass optical filter (cutting around  $\lambda = 580 \text{ nm}$ ) in order to eliminate the wavelength of the laser. The filter is working effectively: without fluorescent dye dissolved, no tracer is visible.

The concentration of the fluorescent dye is increased gradually and the image quality is always verified. A peak in the number of visible tracers is found around the concentration of 7.5 g/l. Therefore, this concentration is considered to be optimal for the present application. It should be noted that looking visually at the actual number of tracers in the test section, only a few percent of the tracers produce sufficient light that can be captured by the camera.

Since the brightness of a tracer is proportional roughly to its volume, a slight change in its diameter results in a considerable change in its intensity in the image. Thus, the tracers that reach above the noise level of the images (which is around  $I = 60$  to 70) cover a wide range of intensities. They reach up-to  $I = 500$ . The maximum intensity level that can be recorded by the 12-bit camera is 4096.

The sample image that is shown in Figure 4.9 was acquired by using a  $f_l = 50 \text{ mm}$  lens at an

aperture corresponding to  $f\# = 1.8$ . Furthermore, the black pixels correspond to an intensity level of  $I = 78$  and the white pixels correspond to  $I = 135$  of the 12-bit information. The grey levels in between are converted linearly.



FIGURE 4.9 – Sample image with fluorescent tracers.

The image of Figure 4.9 is recorded at a free stream velocity of  $U_0 = 2$  m/s (the inhibitor is in the bottom left corner of the image and the flow is moving from left to right). As one can see, the amount of visible fluorescent tracers can be just sufficient to perform a PIV analysis. Therefore, 300 image pairs are recorded and analysed. The mean flow field represented by velocity profiles is shown in Figure 4.10(a). The contour plot shows the velocity magnitude normalized by  $U_0$ .

The results are compared to an earlier single-phase measurement (presented in Tóth and Anthoine (2003)), which was carried out using the same inhibitor height and similar free stream velocity. The earlier result is shown in Figure 4.10(b) using the same quantities.

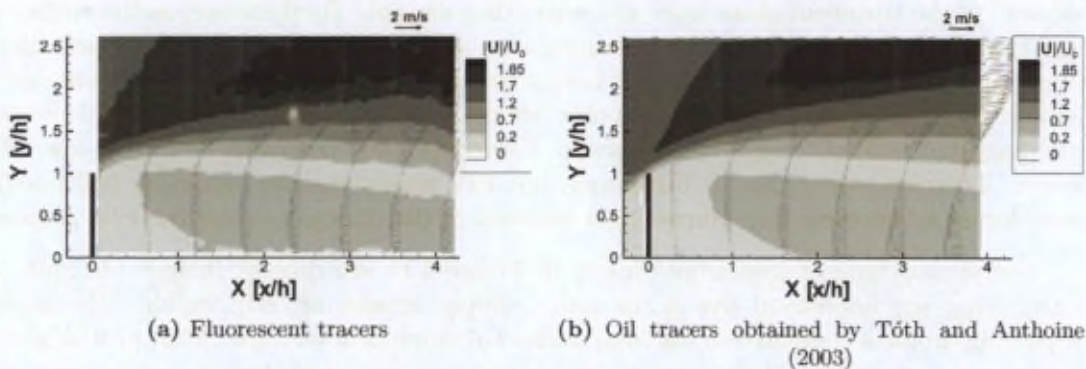


FIGURE 4.10 – Statistical flow field obtained with oil tracers.

As it can be seen the data obtained with the fluorescent tracers shows a good agreement with the classical oil tracers. Therefore, the present tracers are considered to be applicable with flows at lower volumetric flow-rate (up-to 2 m/s in the present test section).

#### 4.2.2.3 Introducing the droplets

Once the applicability of the fluorescent tracers is confirmed, one should investigate the droplet-phase. As it is demonstrated in section 4.2.1, one can record images only of the droplet-phase, while it contains fluorescent dye using the preliminary technique. However, in two-phase

flow condition the non-coloured droplets should be present in the test section, while they should not appear in the tracer images.

Therefore, a test is performed by injecting only water droplets in the test section (without tracers). Before the test, the spraying system and its supply were cleaned carefully to remove all possible earlier fluorescent dye remains. The optical properties of the camera are kept unchanged; therefore it is still equipped with the long-pass optical filter.

During the test, by running the water spray and the YAG laser (at the same energy level as during the fluorescent tracer-test), images similar to Figure 4.11 are recorded. In the sample apart from the contours of the test section two kinds of objects are visible.

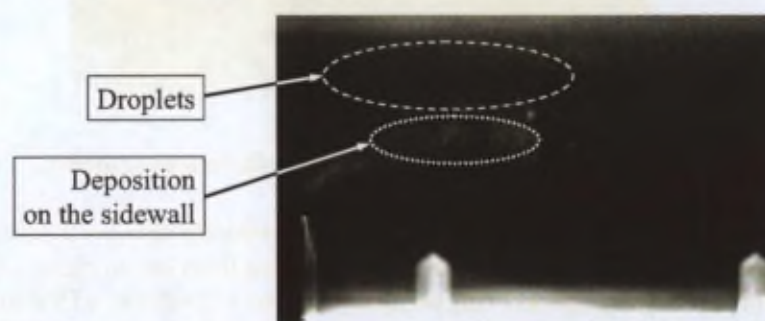


FIGURE 4.11 - Sample image with non-fluorescent droplets.

First of all, a fog-like object appears shortly after starting up the experiment, which originates roughly from the tip of the injector and visually it diverges following the streamlines of the flow. However, this object is not located in the plane of the laser-sheet, but on the lateral wall through which the camera records the images. In practice, as some of the droplets hit the sidewall in the turbulent shear layer and wake, they deposit. Furthermore, as the surface of the wall contains some fluorescent dye remaining even after careful cleaning, the droplets dissolve a small amount of fluorescent material and using the energy of the laser light reflections, they emit light at the fluorescent wavelength. As they are not located in the depth of field of the camera, the deposited droplet images are not sharp. Generally, they represent uniformly low intensity levels. Therefore, they may be disturbing, but PIV measurements should be still possible by considering this non-moving blurred light emission in the background for the PIV processing.

The second type of appearing objects in Figure 4.11 are droplet images. In spite of not introducing any fluorescent dye in the water, droplet images are still visible. The number of appearing droplets compared to the total number of droplets is very low. Most probably only the largest ones are visible. Their intensity level is very low, but since they are not uniform objects, they may disturb the gas-phase PIV measurements. Therefore, the source of their presence is attempted to be identified.

First of all their fluorescence content is checked. To find it out, a laser-beam reflection from one of the optical elements is directed roughly vertically into a small cap, which contains first normal tap water from the same source from which the water of the spray is taken. The image in Figure 4.12(a) is recorded with the camera using a given setting. Here, the laser-beam is slightly visible.

Then, the tap water is directed through the spray supply system (reservoir and tubes), but not the spray itself to see how much dye the water picks up, if any. As it is visible in Figure 4.12(b), the water already contains a very small amount of fluorescent material (the laser-beam appears brighter with the same camera setting).

Finally, the water is directed through the whole spraying system (through the spray as well) and as it can be seen in Figure 4.12(c), the water dissolves even more dye (the fluorescent emission is so strong that the whole liquid surface saturates the image).

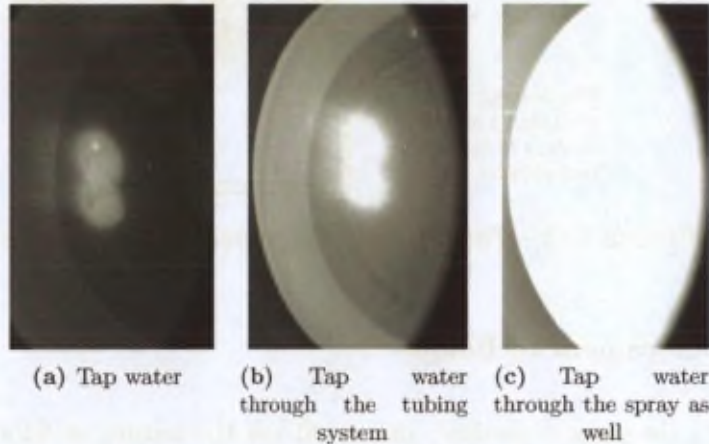


FIGURE 4.12 – *Verifying the dye content of the spray water.*

In fact, the current spray device was used extensively to investigate fluorescent droplets and materials earlier. Before the current tests it was dismantled, cleaned carefully, kept in methanol bath and it was operated with clean water during an extensive period of time. As it is experienced, in spite of all the cleaning processes, a small amount of dye can be still picked up by the water. The concentration should be practically zero and inside the limited volume of the droplets the amount of dye itself might not be sufficient to make the droplets visible. However, this can contribute to the visibility of the water droplets in the camera images (at the time of the tests there was no spray of similar type available, which would have never been used with fluorescent dye).

To analyse further the droplet visibility problem, the possible impact of the tracers is considered. By running only the water spray (the same, cleaned device) and adjusting the camera and the laser properties roughly to the same settings, the droplets were considerably less visible in the images. Tests outside the test section also confirm that the dye content of the droplets is not sufficient to make them visible.

That is why the contribution of the fluorescent tracers is suspected. Although, the tracers travel with the flow, time-to-time some tracers may touch the wall, which are then accumulating on the surfaces of the test section covering it with rather high-concentration fluorescent dye. In the regions where the laser-sheet enters the test section, the fluorescent dye is excited with very high energy. As it forms a very thin film, self-quenching does not play an important role, thus all the emitted light will illuminate the test section (see also Figure 4.13) and therefore the illuminating light-sheet already contains fluorescent wavelengths. As this light is reflected by the droplets towards the camera, the droplet images are appearing in the acquisitions.

If the test section is cleaned carefully, this effect is low, but during the investigation, the more tracers deposit on the surface, the more serious this problem may become. Therefore, during the future measurements short experiments and frequent cleaning should take place. Furthermore, the spraying system should contain preferably elements, which never had any contact with the fluorescent dye of the tracer-phase.

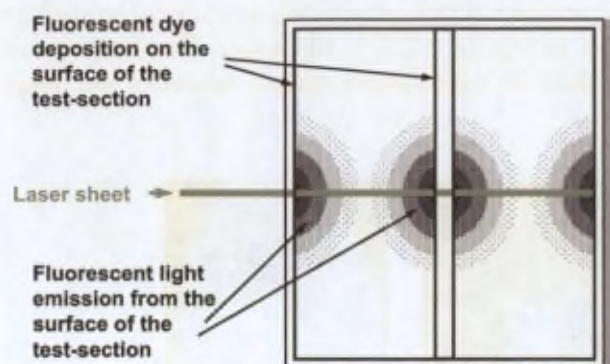


FIGURE 4.13 – *The impact of the fluorescent tracer deposition.*

### 4.2.3 The one-camera technique

According to the present method, one could use the nature of fluorescent light emission during the measurements.

When using a technique based on light scattering, one can not distinguish the tracer images from the (smaller) droplet images by measuring their diameter, as shown in Figure 4.2(b). Their intensity can not be used either.

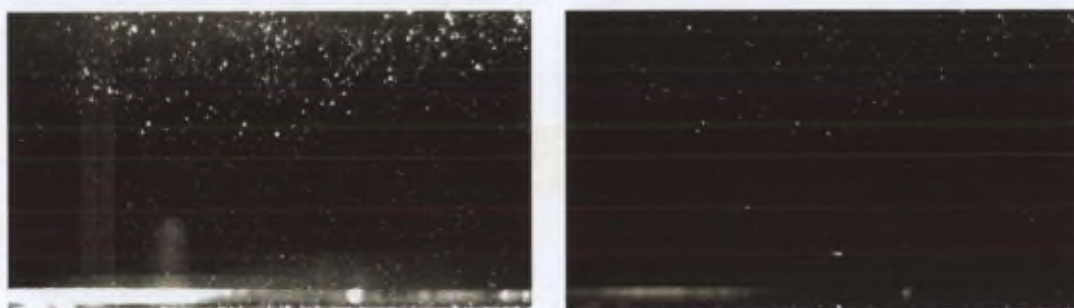
Furthermore, an optical filter has to be used to protect the camera sensor from light arriving at the wavelength of the laser and therefore one has to use fluorescent dye to visualize the droplets and the tracers.

When using a technique based on light emission, the intensity of the fluorescent light (assuming a constant illumination) depends on the number of excited molecules, as already detailed in section 4.2.2.2. Therefore, assuming a given dye concentration, the emitted light is proportional to the volume of the droplet and thus to the cube of its diameter.

In the present case, the droplets are at least one order of magnitude larger than the tracers. Thus, assuming the same dye concentration and applying the same image recording conditions, the tracers' images can just reach an intensity level of  $I = 500$ , while the droplets' images are all saturated ( $I = 4095$ ).

Naturally, by optimizing the dye concentration in the liquid of the droplet-phase, the saturation could be avoided, while the brightness of the two kinds of objects could remain distinct. Therefore, although the tracers and the droplets would both appear in one image, they could be distinguished from each other using their intensity and size information. To measure their properties, the droplet detection algorithm described in section 4.2.1.2 could be applied, which could give directly the required properties. In the followings, a discrimination criterion based on the object size and intensity could be implemented (similar to the one described by Khalitov and Longmire (2002)).

A sample image is shown with two different grey-level conversions in Figure 4.14. The sample is recorded by using the 7.5 g/l Rhodamine B in glycerine to generate the tracers and 0.015 g/l Rhodamine B in water that forms the droplet-phase. The latter concentration is not an optimized value. In the figure it can be seen that more dye could have been used in the droplet-phase. Thus, the intensity levels of the two phases are slightly overlapping, but the potential of the technique can already be seen.

(a) white corresponds to  $I = 135$ (b) white corresponds to  $I = 512$ FIGURE 4.14 – *Fluorescent tracers and droplets: black corresponds to  $I = 78$ .*

Concerning its performance, on the one hand the experiments would simplify. Only one camera is sufficient for the image recording and the problem related to the fluorescent dye deposition on the walls (described in section 4.2.2.3) would probably have a negligible effect.

On the other hand however, the phase separation should be done by image processing. This process would be very time consuming, which could be a serious limitation, when considering some thousand image pairs. Furthermore, the seeding concentration could become even coarser in the region of the images, where high number of droplets are present.

#### 4.2.4 The UV technique

The last proposed technique uses a modified laser wavelength ( $\lambda = 266$  nm) compared to the classical PIV application ( $\lambda = 532$  nm). Performing two-phase PIV experiments with the use of the third harmonics of a YAG laser ( $\lambda = 355$  nm) has already been performed by Kosiwczuk et al. (2005). In this case, the illuminating wavelength is sufficiently short so that using two different fluorescent dyes in the two phases, the dyes will emit light at two rather distinct bands of the visible spectrum. Thus, using two cameras equipped with proper optical filters, the images of the two phases can be separated optically. Therefore, two images can be recorded simultaneously, which contain only one of the phases each. However, Kosiwczuk et al. (2003) showed that the optical separation is not perfect as some residual light remains in one of the images originates from the other phase.

In the present proposition, keeping the idea of separating the two phases optically (see Figure 4.15), the quality of the separation is attempted to be improved. Therefore, two different fluorescent dyes are dissolved in the two phases (droplets and tracers). However, these dyes would be excited simultaneously by different wavelengths.

A schematic of the principle of the proposed technique can be seen in Figure 4.16. As an illumination source, a YAG laser would be applied that is capable of producing pulses at the 2nd harmonic (532 nm) and the 4th harmonic (266 nm) simultaneously. The idea is that the two pulses are exciting fluorescent dyes, which have high absorbance at only one of the wavelengths (Rhodamine B at  $\lambda = 532$  nm and Butyl PBD at  $\lambda = 266$  nm). Therefore, the two phases would emit light at very distinct bands of the spectrum. Finally, by using two cameras equipped with proper optical filters only the light of the fluorescent emissions would be recorded.

The applicability of fluorescent tracer particles containing Rhodamine B was verified in chapter 4.2.2.2. In the present technique they would be excited with the same,  $\lambda = 532$  nm

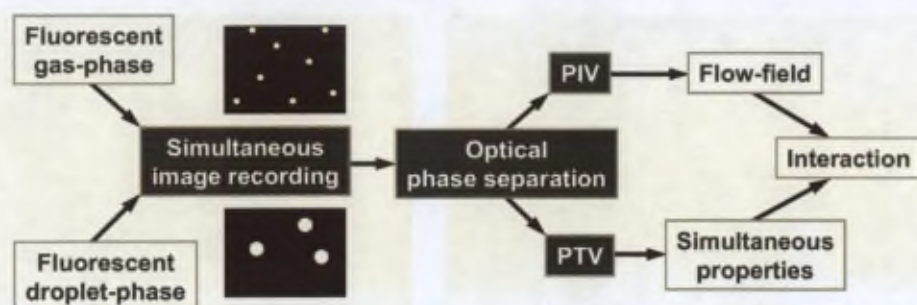


FIGURE 4.15 – Two-phase flow measurement principle.

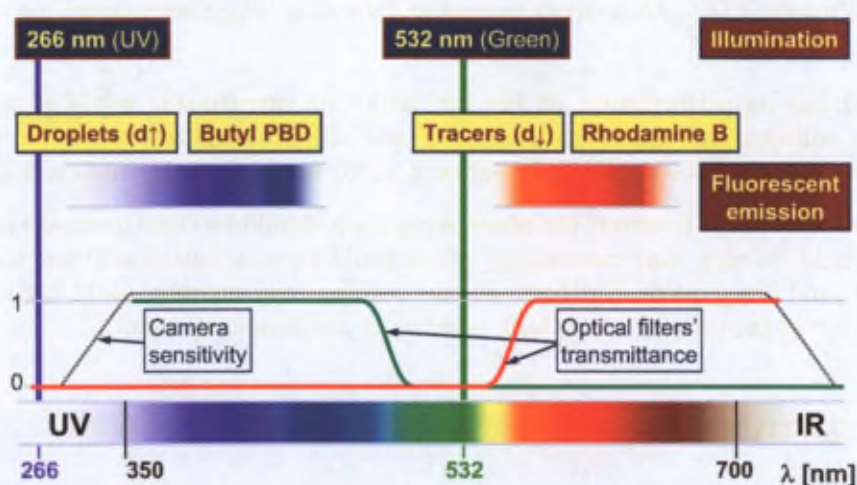


FIGURE 4.16 – The principles of the proposed measurement technique.

wavelength. Therefore, their applicability is not questioned.

However, the image recording capabilities using the current fluorescent droplets (containing Butyl PBD) has to be verified. The results of the preliminary tests are shown in the followings. As a laser source, a "Quantel Twins Ultra 180" MiniYAG laser with simultaneous UV ( $\lambda = 266$  nm) capabilities is used.

The droplet-phase is generated by a spray device. The spray produces small -  $d_p = 10$  to  $50$   $\mu\text{m}$  droplets (its droplet size distribution is shown in Figure 4.17). The liquid used for the atomization is methanol containing Butyl-PBD fluorescent dye. Butyl-PBD absorbs the 266 nm UV light of the laser and emits light around a peak of 365 nm (according to Brackmann (2000)). Since the efficiency of the dye is low, visualizing relatively small droplets should be challenging.

In order to verify the applicability of the UV illumination and the UV fluorescent dye, the spray is installed in a tube to limit the dispersion of liquid droplets. A schematic of the test arrangement can be seen in Figure 4.18. A dichroic mirror separates the two wavelengths of the laser-beam; currently only the 266 nm beam is utilized. Since BK7 lenses are not transparent for the 266 nm UV light and there was no other lens available during the period of the tests, simply the laser-beam was applied for the illumination and no sheet was generated. In practice, if a laser-sheet does not diverge considerably, the light energy per unit area is in the same order of magnitude as in the beam.

The fluorescent droplets are falling through the laser-beam and the fluorescent light emission

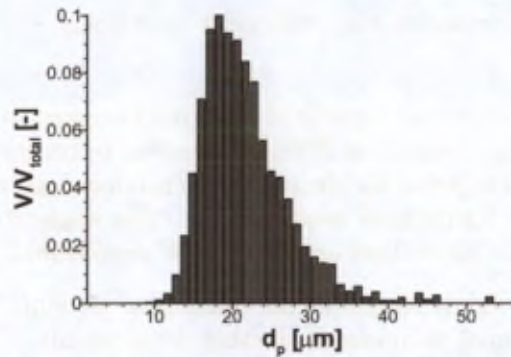


FIGURE 4.17 – *The droplet size distribution of the spray device.*

is recorded with the 12-bit PCO SensiCam camera. In order to increase its sensitivity,  $2 \times 2$  pixels<sup>2</sup> binning is applied. The sensor of the camera is blind below 280 nm wavelength. Thus, no optical filter is needed.

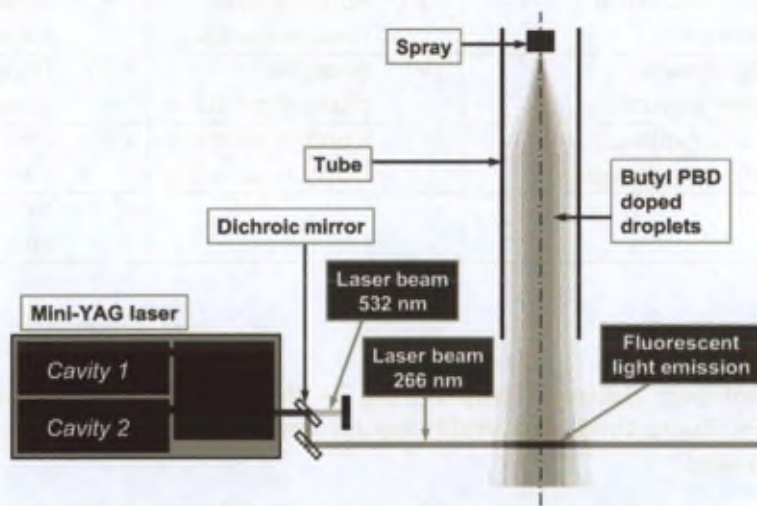


FIGURE 4.18 – *The UV test arrangement.*

A sample image can be seen in Figure 4.19(a). The number of droplets can be counted in the instantaneous acquisitions. Then, scattering images are recorded with  $\lambda = 532$  nm illumination (see Figure 4.19(b)), where a similar number of droplet images can be seen. Thus, the  $\lambda = 266$  nm illumination appears to be applicable.



(a) Sample image using fluorescent droplets



(b) Sample image using 532 nm scattered light

FIGURE 4.19 – *Visibility of the fluorescent droplets.*

Finally, it was also verified that the Rhodamine B doped tracers do not emit detectable light with the 266 nm excitation and the Butyl-PBD doped droplets do not emit detectable light with the 532 nm excitation.

#### 4.2.5 Comparison between the different methods

Currently, three approaches are presented that could be used as the replacement of the originally developed preliminary two-phase PIV measurement technique. The preliminary technique cannot be used, as it is dangerous for the camera. Therefore, one of the latter three techniques should be chosen for the future final measurements. The applicability of the three methods is investigated and in theory all of them appeared to be operational.

The advantages and disadvantages of the techniques are summarized in Table 4.1 in order to help choosing the optimal technique for further development.

Table 4.1 - *Two-phase PIV technique comparison.*

Successive measurements	One-camera	UV-technique
(+) Only one camera is needed	(+) Only one camera is needed	(-) Need of two cameras
(-) Only statistical analysis	(+) Simultaneous measurements	(+) Simultaneous measurements
(+) High-quality phase separation	(-) Sensitive phase separation	(+) High-quality phase separation
(+) Quick (optical) phase separation	(-) Computationally heavy separation	(+) Quick (optical) phase separation
		(-) Need of special optical elements

The fact that only statistical property can be obtained with the successive measurement technique makes this method considerably less favourable. Therefore, the two remaining should be further evaluated.

Using only one camera at a time is obviously easier during the measurements, but it was already demonstrated by Tóth and Anthoine (2003) that two cameras can be synchronized and handled during an experimental campaign. Therefore, this disadvantage of the UV technique is far from being critical.

A huge advantage of the UV-technique is that it is separating the images of the two phases optically with the use of optical filters in front of the cameras. Optical separation is not only quicker (it requires no additional computation), but once it is established, the images of the droplets and tracers all fit smoothly in the image background. Therefore, during the PIV processing no moving intensity steps would be present, which might bias the correlation algorithm (mentioned in section 4.2.1.2).

In case of the UV technique, the cost of the optical phase separation is the need of special optical elements and a special laser source. Furthermore, beyond the financial aspects, during the imaging of both of the phases one has to balance right at the edge of the laws of physics and the current capabilities of the experimental equipment.

Considering all the presently known advantages and disadvantages and the experience gathered during the techniques assessments, the UV technique appears to be the most appealing. Therefore, this was made to function in the experimental facility.

### 4.3 Developing the UV two-phase PIV method

#### 4.3.1 Adapting the experimental equipment for the UV technique

Concerning the ability to apply the UV technique in the facility, the most important obstacle is the  $\lambda = 266$  nm light, because the transparent-like materials applied at the construction of the test section (glass and plexiglass) and the laser sheet optics (BK7 glass) are only transparent to the visible light rays, starting from around  $\lambda = 300$  nm.

In order to be able to generate the laser-sheet, the applied optical elements have to be exchanged as well. For this purpose, a quartz cylindrical lens of  $f = -50$  mm and two quartz spherical lenses of  $f = 150$  mm and  $f = 300$  mm respective focal lengths are purchased.

Furthermore, to be able to allow the  $\lambda = 266$  nm light to enter the test section of the wind-tunnel, the glass window of the detachable plexiglass wall is replaced by quartz as well. However, before building a new frame, the transmittance of the quartz piece is verified qualitatively. Thus, the  $\lambda = 266$  nm laser-beam is separated from the  $\lambda = 532$  nm using the dichroic mirror and a laser-sheet is generated from the  $\lambda = 266$  nm component. This light sheet is impinging on a conventional white A4 paper. Whitened papers often contain sufficient fluorescent material, to be able to visualize the UV laser light. Thus, before the sheet would impinge on the paper, a part of it is passing through the quartz window and the remaining part is passing next to it.

An image is recorded from the fluorescent emission (see Figure 4.20). No intensity change is observed in the region corresponding to the part of the laser-sheet which passes through the quartz window. Therefore, according to the preliminary specifications, the presently available quartz material is transparent to the  $\lambda = 266$  nm light. Thus, both of the wavelengths of the laser-sheet can illuminate the test section up-to the glass splitting plate.

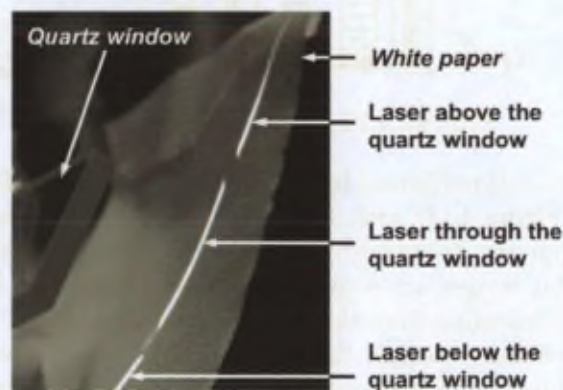


FIGURE 4.20 – The  $\lambda = 266$  nm laser-sheet passing through the quartz window.

The final optical elements needed to make the technique operational are the optical filters of the cameras. On the one hand, the long-pass filter of the tracer-phase camera already existed at the VKI and was used during the earlier tests (see e.g. section 4.2.2.2). However, on the other hand the short-pass filters of the droplet-phase camera have to be chosen.

It is known that the short-pass filter should cut effectively the green laser wavelength ( $\lambda = 512$  nm) and the fluorescent tracer light, but it should have a maximum transmittance below  $\lambda = 400$  nm allowing the fluorescent droplet imaging. As it was mentioned earlier, the camera is not sensitive to the  $\lambda = 266$  nm illumination either. Therefore, no precaution should be taken against it. Typical characteristics of the optical short-pass filters is shown in Figure 4.21(a). Although

cutting the green laser light is not difficult, the absorption of the fluorescent tracer wavelength could be more problematic due to the local transmittance peaks at longer wavelengths.

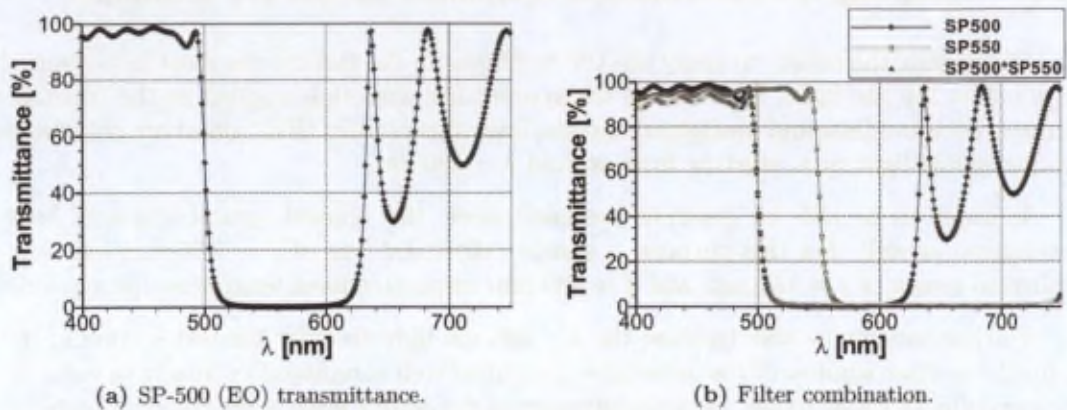


FIGURE 4.21 – Optical short-pass filter transmittance (obtained from Edmunds Optics (EO)).

Therefore, two kinds of short-pass filter should be combined during the experiments. For this purpose, one SP-500 and one SP-550 Melles-Griot (MG) filters are selected, which are placed in front of the camera lens (see Figure 4.22). These have a cut-off wavelength of 500 nm and 550 nm respectively.

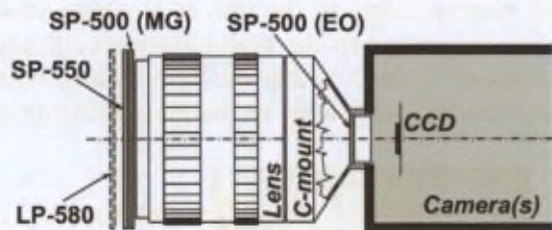


FIGURE 4.22 – Optical filter placement.

A visibility verification is performed in the ambient using water droplets (with the same size distribution shown in Figure 4.17) with  $\lambda = 532$  nm illumination and the MG SP-500 filter in front of the camera (applying  $2 \times 2$  pixels<sup>2</sup> binning). The intensity values between  $I_{min} = 78$  and  $I_{max} = 135$  of the 12-bit images are converted into 8-bit format to highlight the low-intensity objects, which are just emerging from the noise level of the camera (the noise level is close to  $I = 78$ ). As shown in Figure 4.23(a), the water droplets are still visible behind the MG SP-500 filter even in the presence of monochromatic light ( $\lambda = 532$  nm). Thus, a second SP-500 filter from Edmunds Optics (EO) is installed between the camera and its lens (see Figure 4.22). Finally, this configuration of two SP-500 filters already ensured the proper attenuation of the  $\lambda = 532$  nm wavelength of the laser, as the droplets are no longer visible in the images (an example is shown in Figure 4.23(b)).

One has to add that these tests are rather conservative as these filters should block primarily the reflected light from the tracers, which are about one order of magnitude smaller in diameter than the presently investigated water droplets. Since the relatively large water droplets are not visible in the highlighted camera images, the scattered light from the tracers should not appear in the final droplet images either.

However, one should verify that by applying the three short-pass filters ( $2 \times$ SP-500 and SP-550) together the fluorescent tracer images are not visible to the camera, which is supposed to

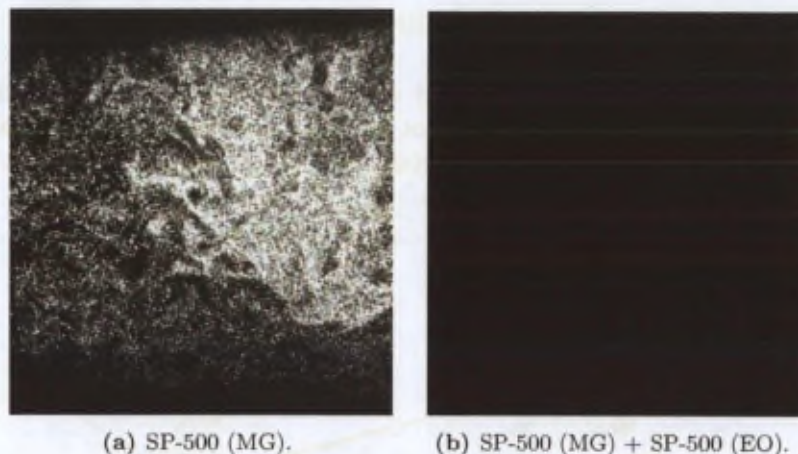


FIGURE 4.23 – *Pure water droplets visibility with  $\lambda = 532$  nm illumination.*

record images only of the droplet-phase. Therefore, the outlet of the seeding generator is placed a few cm from the laser-sheet (containing only  $\lambda = 532$  nm). The camera, equipped with the previously mentioned three short-pass filters, records the area where the tracers are crossing the sheet. The tracers are composed of glycerine and 7.5 g/l Rhodamine B. This concentration is intended to be used during the experiments, as mentioned in section 4.2.2.2.

An example of the recorded images is shown in Figure 4.24. As before, the intensity values between  $I_{min} = 78$  and  $I_{max} = 135$  of the 12-bit images are converted into 8-bit format to highlight the low-intensity objects. No tracer particle is visible in the acquisition, which proves the proper cut-off feature of the present short-pass filter set. The tube visible in the sample image is the outlet of the seeding generator, which is dimly illuminated by the parasitic light entering the darkroom.



FIGURE 4.24 – *The visibility of the fluorescent tracers through the short-pass filter set.*

Therefore, the fluorescent droplet-phase is considered to be applicable with the chosen optical filter set. The fluorescent tracer-phase and the long-pass filter were successfully investigated in section 4.2.2.2. Thus, at the present status the UV technique is assumed to be practically operational.

### 4.3.2 Demonstrating the applicability of the UV technique

In order to demonstrate the applicability of the whole UV two-phase PIV technique a simulated experiment is performed in the ambient (outside the test section of the wind tunnel). The measurement is performed in the tube installation which was used during the test described through Figure 4.18.

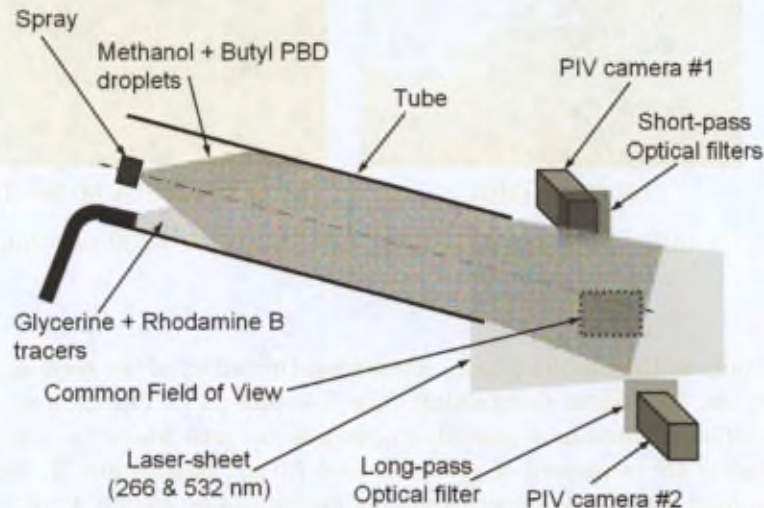


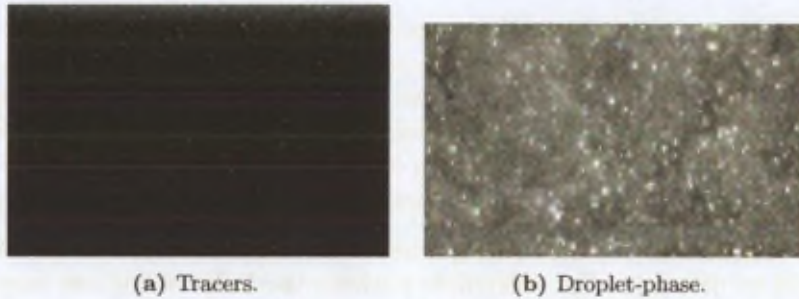
FIGURE 4.25 – The set-up of the simulated experiment.

The present arrangement is shown in Figure 4.25. The spray device that produces a droplet size distribution of Figure 4.17 is installed on the axis of the tube ( $\varnothing 135 \times 620$  mm). The flow inside the tube is induced mainly by the droplet injection. The droplets are produced from 2.67 g/l Butyl PBD - Methanol solution. To visualize the air-phase the above-described tracers of 7.5 g/l Rhodamine B - Glycerine solution are generated with the nebulizer. The seeding is injected close to the shell of the tube. Within the length of the tube the tracers are mixing properly. Furthermore, the airflow from the nebulizer also contributes to the induction of the flow inside the tube.

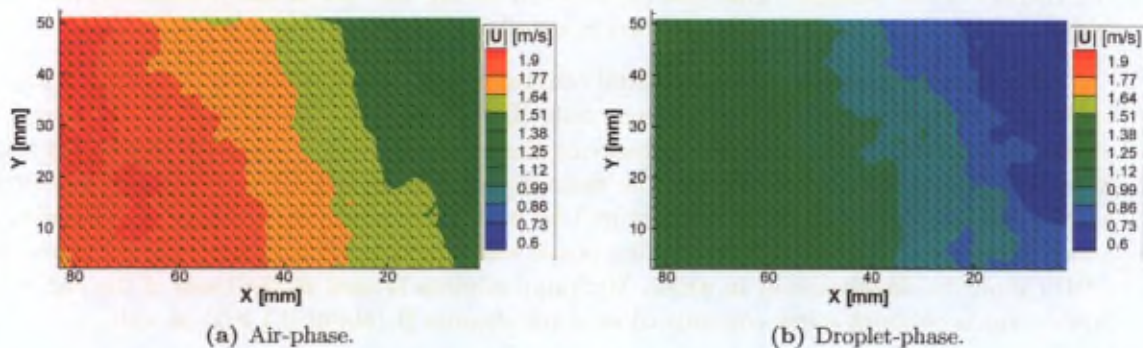
The laser-sheet is generated downstream the exit of the tube. With the help of the fourth harmonic generator crystal the laser source contains approximately 30 mJ  $\lambda = 266$  nm light and about 100 mJ residual  $\lambda = 532$  nm light according to the specifications. The cameras equipped with the corresponding long-pass filter and short-pass filters are placed perpendicularly on either side of the sheet. They acquire images from the same, about  $80 \times 50$  mm field of view (FoV). To ensure a good overlapping between the two FoVs, each camera is placed in a way that the opposite camera appears in the middle of the images. The focal length of the camera lenses is  $f = 50$  mm and their aperture is set to  $f\# = 1.8$ . In agreement with the preliminary tests  $2 \times 2$  pixels<sup>2</sup> binning is applied to increase the sensitivity of the cameras. Therefore, the final resolution of the tracer images becomes  $640 \times 432$  pixels<sup>2</sup> and the droplet images  $640 \times 416$  pixels<sup>2</sup>. The separation time between the image pairs is set to  $\Delta t = 125 \mu\text{s}$ . Altogether 530 image pairs are acquired by each camera.

A sample of the simultaneously recorded images are shown in Figure 4.26. No crosstalk can be noticed visually between the two phases (no objects are visible from the opposite phase).

During the processing of both of the phases, an initial window size of  $96 \times 96$  pixels<sup>2</sup> and two refinement steps are defined with 75% window overlapping. Using all the available instantaneous

FIGURE 4.26 – *Simultaneously recorded images.*

velocity fields, the mean flow fields of the two phases are determined.

FIGURE 4.27 – *Mean flow fields.*

The statistical fields are indicated in Figure 4.27. The vectors of the figures represent the mean velocities and the contour-plots show the mean velocity magnitudes. In Figure 4.27(a) and 4.27(b) different flow fields are visible. The droplets appear to respond quicker to gravity, as their velocity vectors tend to be closer to vertical direction. Furthermore, the mean velocity magnitude of the air-phase appears to be 40 to 60% higher than that of the droplet-phase. The overall momentum of the air-phase originates from the pneumatic atomizer and the seeding injection together. Therefore, the visible velocity difference is acceptable. The observed deviations in the mean velocity fields prove once again that the images of the two phases are properly separated optically.

A last aspect to be demonstrated is the spatial calibration of the FoVs of the cameras. Even if one takes a great care positioning the cameras to look at the same FoV, the two fields would never coincide. However, they can be matched easily by recording an image of an object, which lies exactly in the laser-sheet.

For this purpose one could use a transparency, which contains a random pattern. The same pattern could be seen by both of the cameras and by simple correlation of the images the difference of the FoVs could be determined. For calibration purposes and to determine various distortions this kind of technique is widely used in the literature. However, one has to ensure that the transparency is perfectly planar and lies perfectly in the laser-sheet. Furthermore, the laser-sheet has a given thickness ( $\sim 1$  mm), which is considerably larger than the thickness of a transparency. Therefore, the placement of the calibration sheet becomes more difficult. Considering that the magnification of the PIV images are of the order of 0.1 mm/pixel, it is obvious that with the calibration of this type one can easily end up with an error of 4–5 pixels.

To avoid it, one should use the laser-sheet itself to define the calibration plane. Thus, one could consider a calibration grid of e.g. wires, where thin wires are perpendicularly crossing the measurement plane. Therefore, they are illuminated by the laser-sheet and the eventually recorded images could be correlated to determine the difference between the two FoVs. However, here the difficulty could be the construction of the grid support, which should represent exactly the same optical distortion towards the cameras placed on either side of the measurement plane.

In order to minimize all these ambiguities, it was finally decided to use the laser-sheet and the flow itself to determine the differences between the FoVs of the two cameras. During the measurements with the two phases, the cameras are equipped with optical filters to record images from distinctive bands of the visible spectrum. Furthermore, none of the cameras can see any of the wavelengths of the laser source. In practice, one could remove the optical filters from the cameras for the spatial calibration. However, by doing so, the ray-tracing of the whole optical system is modified and one would again obtain about 3 to 5 pixels of error especially close to the corners of the images. This was experienced during the use of the preliminary technique (mentioned in section 4.2.1 and described in details by Tóth and Anthoine (2003)).

Thus, the only possibility for the spatial calibration is to keep the optical filters. This imposes to use the two associated fluorescent materials (Butyl PBD and Rhodamine B). However, one should be sure that both cameras are observing the same objects. This is guaranteed only if both fluorescent materials are dissolved in the same liquid. The generated droplets are then excited by the two laser wavelengths to be captured by both cameras simultaneously. Considering the lower efficiency of Butyl PBD the droplet-phase was chosen to carry the two dyes. Since Butyl PBD cannot be dissolved e.g. in water, Methanol solution is used as the basis of the calibration liquid, which contains a low concentration of Rhodamine B (about 0.1 g/l) as well.

Therefore, by operating the spray of the calibration liquid, simultaneous images are recorded by both of the cameras. Then, pairs are composed from the simultaneous acquisitions, which are simply correlated using *WiDIM*. An example of the resulting calibration field is shown in Figure 4.28. This one corresponds to the demonstration experiment just previously described.

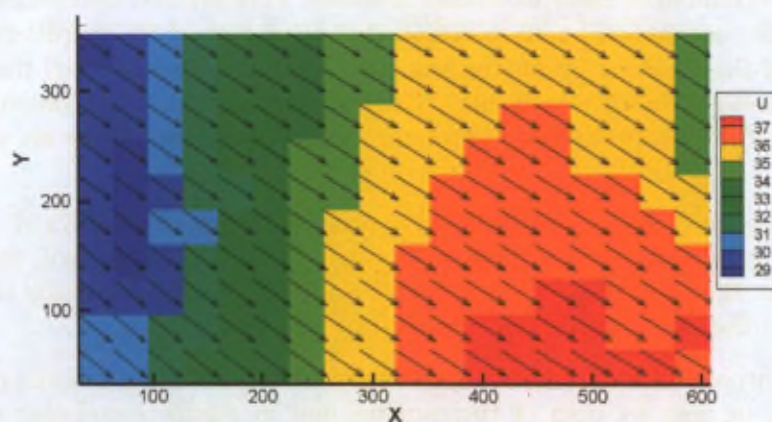


FIGURE 4.28 – Spatial calibration of the simulated experiment (the unit of the axes and the contour variable are [pixels]).

The spatial calibration completes the UV two-phase PIV technique, which should be applied now in the SRM model.

## 4.4 The UV technique inside the test section

Once the various aspects of the UV technique itself are clarified and its applicability is demonstrated in the ambient, the technique should be made operational inside the present specific test section as well.

### 4.4.1 Adapting the experimental conditions

First of all, one should note that UV two-phase PIV measurements can only be performed in the side of the test section which contains the quartz window through which the laser-sheet enters. The laser-sheet passing through the glass splitting plate contains only the  $\lambda = 532$  nm wavelength as the  $\lambda = 266$  nm UV light is blocked by glass.

Unfortunately, the successful demonstration of the UV technique does not guarantee its direct applicability inside the test section. The most important concern is the liquid deposition of the two phases on the walls of the test section.

The effect of Rhodamine deposition was already mentioned through Figure 4.13. In order to avoid the Rhodamine B deposition on the splitting plate a stripe of black tape is glued to the surface illuminated by the laser-sheet. The tape is relatively easily replaceable and thus the surface can be kept free of Rhodamine B in longer term. Furthermore, by avoiding the multiple reflections of the  $\lambda = 532$  nm light between the quartz window, the splitting plate and the polished stainless steel surface, the excitation of the deposited dye is reduced as well.

However, as it is discovered, the most important Rhodamine B deposition is not the one on the quartz window and on the central part of the splitting plate, but in the corners of the splitting plate, where the glass splitting plate is glued to the sidewalls with silicone. As the Rhodamine B doped tracers are depositing on the surface of silicone, Rhodamine B is diffusing probably in the surface roughness of silicone. This penetration makes any cleaning ineffective. As the laser-sheet goes through the quartz window (see Figure 4.29), light is scattered inside the test section illuminating the corners as well.

Due to the considerable amount of fluorescent dye already deposited in the corners, the scattered light produces sufficient fluorescent emission, which is able to visualize at least the larger droplets with the sensitive camera. Even if the tracer camera is equipped with an optical long-pass filter, since the illumination occurs at the emission wavelength of the tracers, the droplets may become visible in the tracer-images. Although the corner emission illuminates practically all the droplets in the test section quasi-equally, not all of them are visible; only the ones which are within the few mm thick depth-of-field (DoF) of the imaging system (the ones which are sharp) will appear in the acquisitions. However, the DoF is typically larger than the laser-sheet thickness.

In order to block the fluorescent corner illumination, these two glued corners are painted black and the painting is regularly renewed after almost each measurement session. An example of the tracer camera image is shown in Figure 4.30 before and after the corner treatment, while only water droplets are injected in the test section. As it can be seen, the parasitic illumination from the splitting plate corners could be reduced effectively.

However, performing optical two-phase experiments in a confined test section is known to be difficult. As it was shown by Tóth et al. (2006), during the LeDaR experiments in the cavity, water droplet deposition on the wall through which the camera acquires the images causes serious difficulties. On the one hand, it is known from the accumulation data that only a few percent

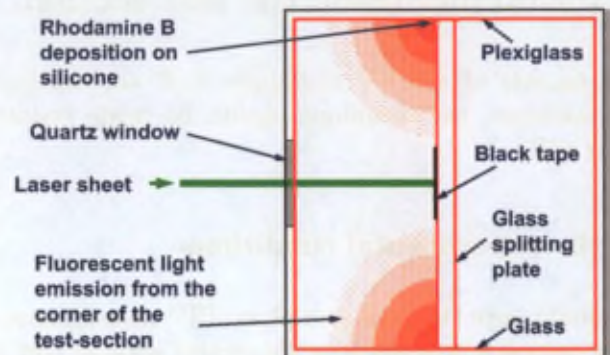


FIGURE 4.29 – Rhodamine B deposition in the test section.

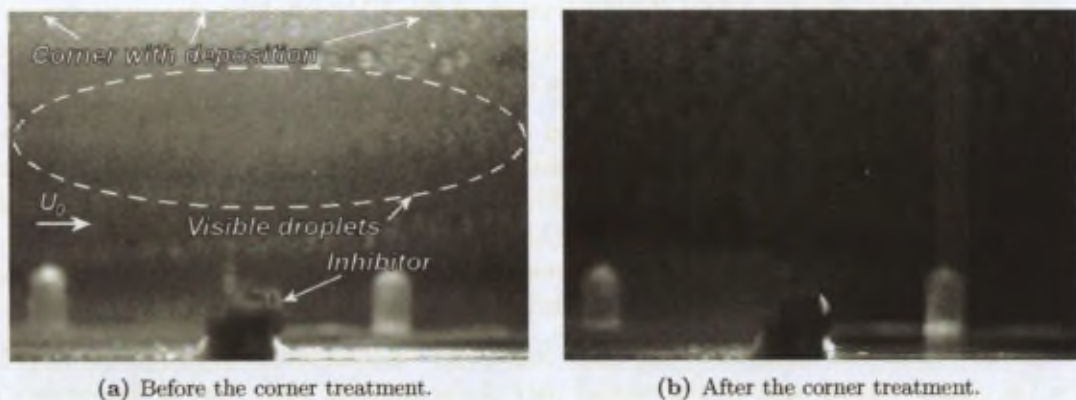


FIGURE 4.30 – Sample images of water droplets through the long-pass optical filter ( $I_{min} = 96$ ,  $I_{max} = 512$ ,  $\gamma = 2/3$ ).

of the droplets enter in the cavity. On the other hand, in the wake of the inhibitor a larger turbulence is present than inside the cavity, as it is described by Lema et al. (2006) and Tóth et al. (2005). As a consequence, in the region of the present interest (downstream the inhibitor) an even more intense droplet deposition is expected. These expectations are indeed confirmed by preliminary tests. Therefore, a strategy should be established to minimize the deposition as much as possible and to minimize its effect during the data processing.

First of all, in order to limit the amount of liquid interacting with the surface, the chosen spray device has only about  $20^\circ$  cone angle. Within the measurement conditions this is still sufficient to provide a rather uniform mass loading throughout the cross-section of the test section.

In order to minimize the deposition, surface treatment is applied to make the sidewalls hydrophobic, similarly to the LeDaR experiments. Thus, the inner surfaces of the plexiglass and the glass sidewalls (see Figure 4.29) are treated with *Rain-X*. Earlier, a silicone-based product was used, but as it performs similarly to *Rain-X*, the choice is made on availability-basis. Although *Rain-X* is also less effective on plexiglass, no glass layer is fixed on the plexiglass surface, like during the LeDaR investigation, because it would further complicate the optical access due to its fixation.

Making the surface hydrophobic does not mean that no droplet deposits on it, but the size of the depositing droplets are strongly limited. Only very small droplets (e.g.  $d_p < 1$  mm) would

be able to stick to and accumulate on the surface. As soon as any of the droplets would grow larger (due to agglomeration), it would quickly flow down the surface by gravity and the flow. Having a fine layer of droplets of  $d_p < 1$  mm on the window through which the camera records images, the acquisition is still possible as soon as the deposition is sufficiently far from the DoF of the camera optics (the image of the deposited liquid is sufficiently blurred).

As the deposition on the foreground window is more critical (it may hide tracer/droplet images) than the one in the background, its blur disk is attempted to be increased by choosing a short focal length camera lens<sup>2</sup>. Therefore,  $f = 35$  mm,  $f\# = 2$  Nikkor lenses are chosen for both cameras. This allows to reduce the distance between the sidewall and the camera (approximately to 300 mm, with respect to the 200 mm test section width), while the FoV is kept reasonably large ( $> 100$  mm). Thus, by applying the thinnest possible DoF, which is provided at  $f\# = 2$ , the image recording conditions are optimized. A sample of the final image quality is shown in Figure 4.31 from both of the phases, when the surface liquid deposition already became quasi-steady.

The way of reducing the effect of the remaining surface wetting will be described in section 4.4.2.

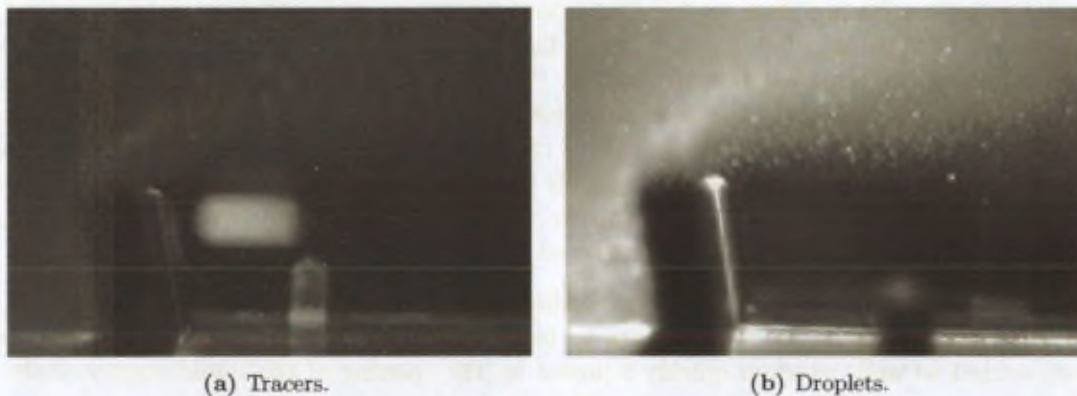


FIGURE 4.31 – Sample two-phase PIV images in the test section ( $I_{min} = 0$ ,  $I_{max} = 1024$ ,  $\gamma = 2/3$ ).

The liquid-phase is based on Methanol, in which Butyl PBD is dissolved. However, when the solution is sprayed, a solid material deposition is observed at the high flow velocity (low pressure) regions inside the pneumatic atomizer. The deposition is so intense that it allows to acquire only a few dozens of images (at 3 fps) before the liquid supply of the spray is completely blocked. In order to extend the experimental period, the solution is modified. It was found that by adding water to the solution, the deposition can be slowed down. Although the resulting mixture is not stable, it can be used within one day before the fluorescent dye recrystallizes.

Thus, the final solution representing the liquid-phase is created volumetrically from 1/5 part Methanol (in which all the necessary Butyl PBD is dissolved) and 4/5 part demineralized water. This way the spray device can work practically unchanged, while at least 100 to 150 images are acquired and the fluorescent properties of the fresh liquid remain identical to the pure Methanol solution.

Concerning the adaptation of the experimental conditions, one should consider safety factors as well. Liquid containing Methanol is sprayed in the stagnation chamber of the wind-tunnel and

<sup>2</sup>at short subject distances - such as in the present case - the influence of the focal length ( $f$ ) on the DoF is negligible using a given magnification

once it is mixed with water, its flammability is reduced. However, Methanol itself is still toxic, like Rhodamine B. Therefore, one should be sure that the flow extraction system downstream the test section is effective. Unfortunately, currently this is not the case at high velocities. Furthermore, apart from the toxicity, the liquid-phase is not stable, which prevents storing larger quantities of it. In addition, larger liquid flow-rate injection would result larger liquid deposition on the lateral walls. Together with the difficulty that the spray is frequently blocked by the mixture, at the present status lower liquid flow-rates are preferred. Furthermore, a more effective seeding generator is built (same type as described in section 4.2.2.1). Although it provides a larger seeding concentration, this increase should be used purely to increase the quality of the experiments, which is further degraded by the liquid deposition on the lateral walls. Finally, considering all the above-mentioned reasons, it is decided not to respect anymore the nominal condition of the previous investigations ( $U_0 = 10$  m/s). Instead, by keeping the geometry unchanged, the flow velocity is defined to be  $U_0 = 2$  m/s. Therefore, the Reynolds number is reduced from  $Re_h = 2.51 \cdot 10^4$  to  $Re_h = 5025$ .

To sum up, the experimental procedure is the following. First of all, Butyl PBD is dissolved in Methanol in 5 times the desired concentration at least one week prior to the experiments due to the weak dissolving characteristics. The corners of the test section between the lateral walls and the splitting plate are black-painted and a clean stripe of black tape is placed in the centre of the splitting plate the day before the experiments. Before the wind-tunnel is started, the lateral walls are treated with Rain-X. Once the wind-tunnel ran at least 30 minutes at  $U_0 = 2$  m/s (to stabilize), the laser is switched on to heat up the fourth harmonic generator crystal, which requires about 5 minutes to reach its effective operation. During this time 1/5 Methanol solution is put in the spray supply reservoir and 4/5 demineralized water is added to it. Finally, the air-supply of the pneumatic atomizer is opened (however, the liquid supply is kept closed so that no droplets are generated at this moment).

When everything is prepared, the seeding generator is started to produce the gas-phase tracers and when the seeding appears to be visually steady, the acquisition of the cameras are started as well, which is quickly followed by the opening of the liquid supply of the spray device to generate the droplet-phase. The acquired images of both phases are continuously and simultaneously monitored. The image recording is stopped, when a decrease in droplet concentration is observed in the images, or at very latest 200 image pairs after the first droplets appeared.

Then, the liquid supply of the spray and the seeding generator are switched off and the test section is dismantled. From the walls the deposited liquid and fluorescent dye are cleaned. Furthermore, after a few cycles the surface treatment is renewed as well. Once the test section is assembled, the stagnation chamber of the wind-tunnel is opened and the spray device is removed and dismantled for a complete cleaning of its internal channels. Furthermore, the seeding injection elements are always cleaned as well, to prevent the agglomeration and the eventual dripping of large glycerine droplets with very high concentration Rhodamine B, which could seriously contaminate the test section. After the cleaning process, the spray and the seeding injection are re-installed and the stagnation chamber is closed again. When needed, the liquid reservoir of the spray is refilled with a new mixture. Finally, a new series of images is acquired.

This process is repeated 10 to 15 times in each FoV of each configuration. Once the simultaneous two-phase image pairs are acquired, the set-up is once more cleaned (including the spray device) and a series of 1500 images are recorded with the tracer-camera exactly in the same condition as the previous measurements, except that no liquid is supplied to the spray device. These image pairs therefore represent the single-phase flow configuration.

Finally, the spatial calibration is performed by the above-mentioned calibration spray, which contains both fluorescent dyes. At the very end, an absolute spatial calibration is performed with the help of a ruler to be able to locate each FoV with respect to the inhibitor tip.

#### 4.4.2 Image pre-processing

The fact that the liquid deposition on the lateral walls is reduced and its effect is limited as much as possible by optimizing the DoF of the camera optics does not mean that the images could be free of their presence (see Figure 4.31). Even if their image is blurred, on the one hand they simply reduce the signal-to-noise ratio of the images of the tracers and droplets. On the other hand, they may influence directly the velocity determination of either of the phases at low seeding (or droplet) concentration regions. Therefore, their presence in the images is attempted to be reduced.

In general, to improve the signal-to-noise ratio of PIV experiments, it is a widely applied technique to subtract the background intensity distribution of the images. This could be determined by using either the actual PIV images or separately recorded background images (without seeding). In either case, generally the mean intensity of all the pixel locations are determined together with the RMS of the local intensity value. Later, the background can be defined with various combinations of the mean and RMS intensity distribution. Others define the background image by taking the minimum intensity value over the whole set of images in every pixel location. In any case, the resulting background image can be subtracted from each PIV image and therefore one can obtain an image of only the tracers, which is ideally free of any reflection or other artifacts that might be caused by the investigated geometry.

However, in the present case, recording background images (without tracers and droplets respectively) is pointless, because the depositing droplets to be masked are changing almost from one image to the other. For the same reason, one cannot use the measurement images, because the statistical analysis would not give any indication of the temporal change of deposition.

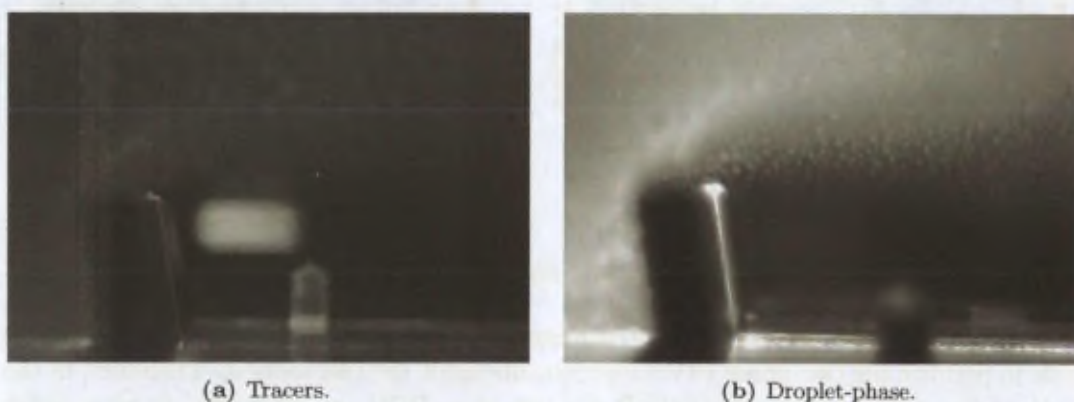


FIGURE 4.32 – Sample background images ( $I_{min} = 0$ ,  $I_{max} = 1024$ ,  $\gamma = 2/3$ ).

Therefore, a masking technique is defined, where an individual background image is determined for each instantaneous recording. Namely, at each acquisition the actual image and the four preceding recordings are analysed and in every pixel location the minimum intensity is determined (a pair of examples is shown in Figure 4.32). Thus, with a high probability, in each pixel location an intensity value is recorded that is not associated to a tracer (or droplet) located inside the laser-sheet, but to the locally deposited liquid on any of the lateral walls. Later, each

unique background image is subtracted from the corresponding acquisition. An example of the resulting images is shown in Figure 4.33.

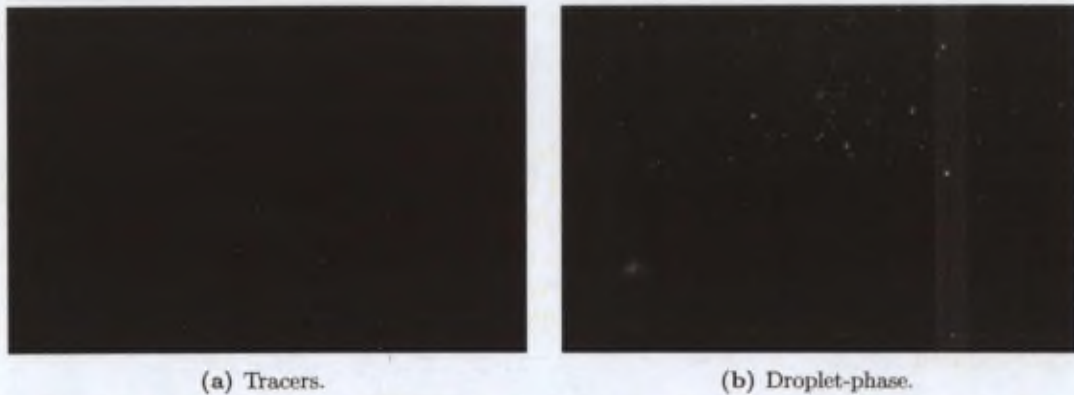


FIGURE 4.33 – Sample images after background subtraction ( $I_{min} = 0$ ,  $I_{max} = 1024$ ,  $\gamma = 2/3$ ).

In order to demonstrate the impact of the present background subtraction method, a series of 1500 images is recorded, while the spray device is producing water droplets and only the tracer-camera is acquiring images of the fluorescent tracers of the air-phase. Basically, this is the method called *successive measurement technique* described in section 4.2.2. From here, only the mean flow field is shown in Figure 4.34 without and with the local background subtraction. It can be seen easily that without applying the background subtraction even the largest mean flow structures can not be resolved, while with the local background subtraction these mean structures are appearing in the flow.

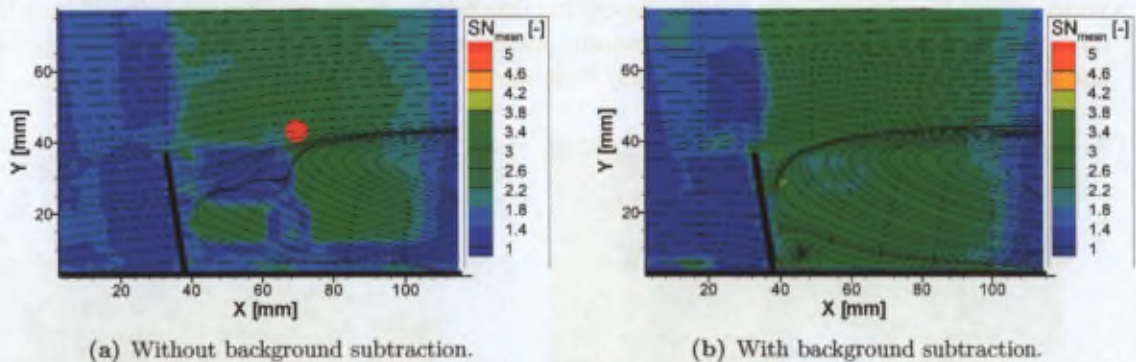


FIGURE 4.34 – Sample mean flow fields.

Thus, the overall quality of the experiments meets the requirements that are needed to be able to perform the two-phase PIV measurements inside the test section. Therefore, at this point both of the optical techniques (LeDaR and two-phase PIV) are considered to be applicable and the development of the dedicated experimental tools is finished.

**Part II**

**Liquid accumulation assessment**

1901

Journal of the American Medical Association

---

Following the methodology described in chapter 1.5, the investigation of the slag accumulation process in the current 2D cold-gas model begins by the measurement of the liquid deposition in the cavity using the LeDaR technique. The influence of all the available parameters on the liquid accumulation are assessed by this technique and the most important ones are identified. However, LeDaR gives only the tendencies of the accumulation, but it is not capable of explaining the driving forces of it.

Therefore, after the LeDaR measurements, the flow-field should be analyzed as well. For this purpose both experimental and numerical (CFD) tools can be used. However, before considering any of the numerical data, the relevance of the simulations have to be verified. The validation can be performed relatively easily in single-phase flow configuration e.g. by performing classical PIV experiments and numerical simulations in the nominal condition of the LeDaR investigation. Once validated, the numerical data can be used to extract additional properties of the flow supporting the experimental database.

During the experimental flow investigation, besides the single-phase flow characterization, two-phase PIV experiments should be performed as well.

Concerning the flow field analysis, at first the statistical quantities should be extracted and the main mean flow structures should be investigated together with the distribution of the velocity fluctuations. To see the effect of the presence of the droplets on the mean gas-phase, the single-phase and the two-phase flow quantities can be compared.

However, the accumulation process is very probably driven by forces, which could not be described through statistical quantities. Therefore, the instantaneous structures of the flow field should be analyzed as well, which means primarily the vortices of the gas-phase. The goal is to reveal the global mechanism of the droplet transport via the vortical structures.

Following the above-described steps, by the end of the current part a better understanding should be gathered concerning the accumulation process.



## Chapter 5

# The investigated parameters of the liquid accumulation

The present chapter is explaining the parametric investigation carried out using the LeDaR technique in order to determine the relevant parameters of the slag accumulation, the forces behind that process being investigated in the following chapters.

Following the LeDaR technique adaptation, the parametric investigation of the liquid accumulation is depicted starting with the measurement conditions. Later, the various measurement parameters and the main results are introduced as well.

### 5.1 Experimental conditions

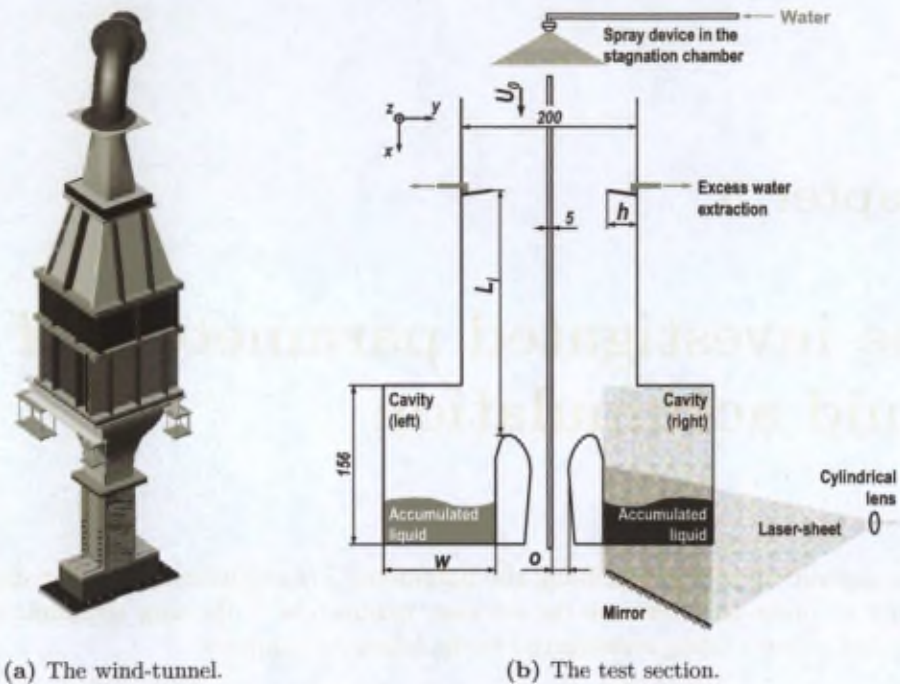
The LeDaR investigation is carried out in the VKI L-11 wind-tunnel (Figure 5.1(a)), which is described in section 2.4 and Appendix B. The LeDaR configuration of the test section is shown in Figure 5.1(b).

Most of the test section walls are made of transparent material, which allows optical access. Furthermore, different geometrical parameters ( $h$ ,  $L_i$ ,  $\alpha$ ,  $w$ ) can be varied to see their effect on the accumulation. Due to the symmetric flow condition (its verification is shown in section B.5.2), the measurements are carried out using only one side of the test section.

The experiments are carried out at room temperature using air to model the gas-phase of the internal fluid of the SRM and using water droplets generated by a spray device (the droplet size repartition is shown in Figure 5.2) to model the alumina droplets. The water spray is mounted in the middle of the stagnation chamber of the wind tunnel in order to allow a proper mixing of the water droplets with the air-phase before reaching the test section. For more details concerning the flow similarity parameters and the spray device, please refer to section 2.3.

In the current study, the rate of liquid accumulation in the cavity should be compared to the initial flow-rate of the spray to determine the portion of the entrapped liquid. Therefore, the supplying water flow-rate of the sprays needs to be measured. Furthermore, one should apply similar flow-rates, while studying the effect of different parameters. In order to have a direct, more precise measure of the flow-rate, a flow meter is installed in the water supply system.

The water supply system of the spray consists of (see Figure 5.3) a 200 l tank, which stocks water with 10 mg/l Fluoresceine. This concentration ensures the visibility of the water in



(a) The wind-tunnel.

(b) The test section.

FIGURE 5.1 – Experimental configuration.

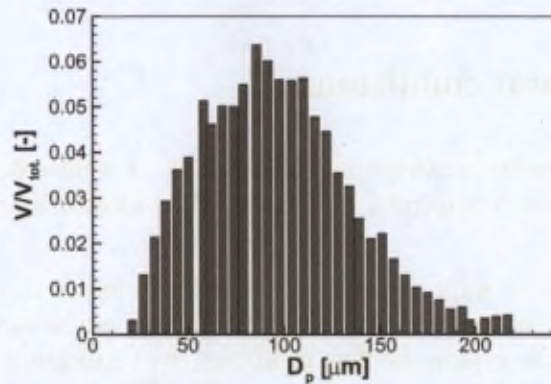


FIGURE 5.2 – Volumetric droplet size repartition of the poly-disperse spray.

the measurement plane, while the fluorescent dye does not absorb a considerable amount of light, which would prevent from having a uniform illumination. A pump provides the required water supply to the spray device. Its flow-rate can be regulated with a by-pass. A pressure-difference transducer connected to a Venturi tube yields an electric signal (proportional to the instantaneous water flow-rate), which is recorded with an acquisition computer.

A direct flow-rate vs. voltage calibration is made. By operating the spray outside the wind-tunnel, the water droplets are collected during 2 minutes in a reservoir. Simultaneously, the computer acquires the output voltage of the transducer at an acquisition frequency of 270 Hz. During 2 minutes 32400 samples are taken. The flow-rate can be determined from the volume of the accumulated water and by computing the mean of the recorded samples the corresponding voltage value can be obtained as well.

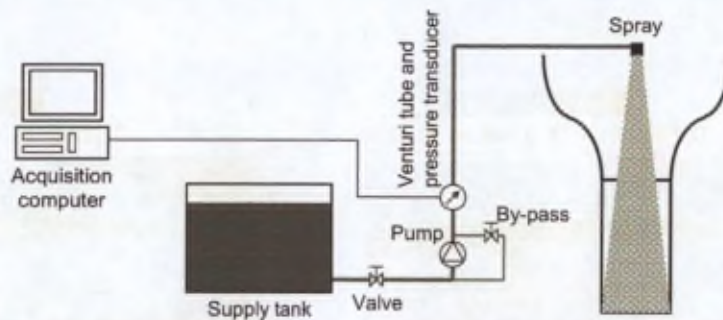
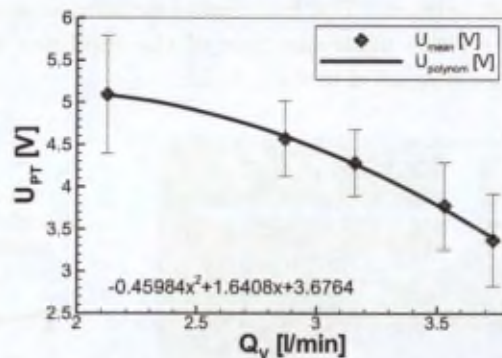


FIGURE 5.3 – The water supply system.

By applying different settings in the by-pass, the voltage corresponding to several flow-rates can be determined. Finally, the calibration curve (shown in Figure 5.4) can be obtained by fitting a polynomial on the measurement points. Since the output voltage of the pressure transducer is linearly proportional to the pressure difference and the pressure difference has a second order relationship with the flow-rate, the fitted polynomial should be second order as well.

FIGURE 5.4 – The calibration curve of the Venturi-based flow meter (the error bars represent the RMS of  $U_{PT}$ ).

In Figure 5.4, beside the mean of the recorded voltage quantities, their fluctuation (RMS) is indicated as well. One can see that the electric signal has a very large fluctuation, which prevents setting precisely the flow-rate of the water by using the instantaneous reading of the output voltage. However, the mean value of a long-term voltage recording (e.g. simultaneous recording during the LeDaR measurements) can give the real flow-rate accurately.

Furthermore, within the measurement condition, a considerable amount of water droplets is hitting the inhibitor. As a result, this liquid is accumulating on the upstream side of the obstacle and as it reaches a critical amount, it is carried away by the airflow in the form of large droplets (several millimeters in diameter). Due to gravity, the main part of this water is dripping into the cavity creating large splashes, which degrade the surface detection of LeDaR.

In order to limit its effect, the depositing liquid is evacuated from the obstacle. To achieve this, the inhibitor is inclined by  $10^\circ$  upstream (see Figure 5.1(b)). To verify the influence of this inclination on the flow field, PIV experiment is carried out at  $U_0 = 7$  m/s using an  $h = 25$  mm obstacle (straight and inclined successively). The field downstream the inhibitor is divided into two *fields of view* (FoVs). In each FoV 400 image pairs are acquired to obtain statistical quantities. As it is shown in Figure 5.5, no critical effect of the inclination is found on the flow

field downstream the inhibitor.

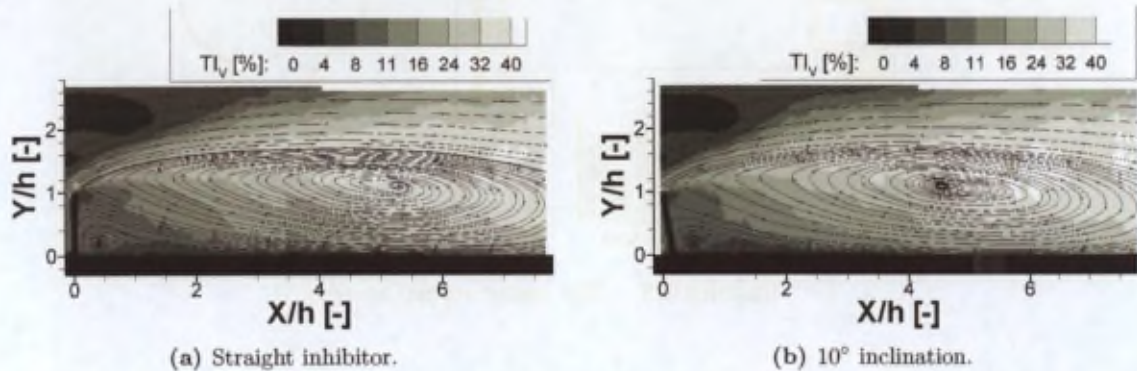


FIGURE 5.5 – The effect of the inhibitor inclination on the flow ( $TI_V = v/U_0$ ).

On the upstream side of the obstacle the accumulating liquid is pushed (by gravity and by the airflow) towards the base of the inhibitor. With the help of a pump (set to an adequate flow-rate) and a small tubing system (the airflow should not be modified) the excess water can be evacuated from the test section. The final liquid extraction system is shown in Figure 5.6. The liquid accumulation on the upstream face of the inhibitor and the associated dripping phenomenon will be further discussed in section 8.1.

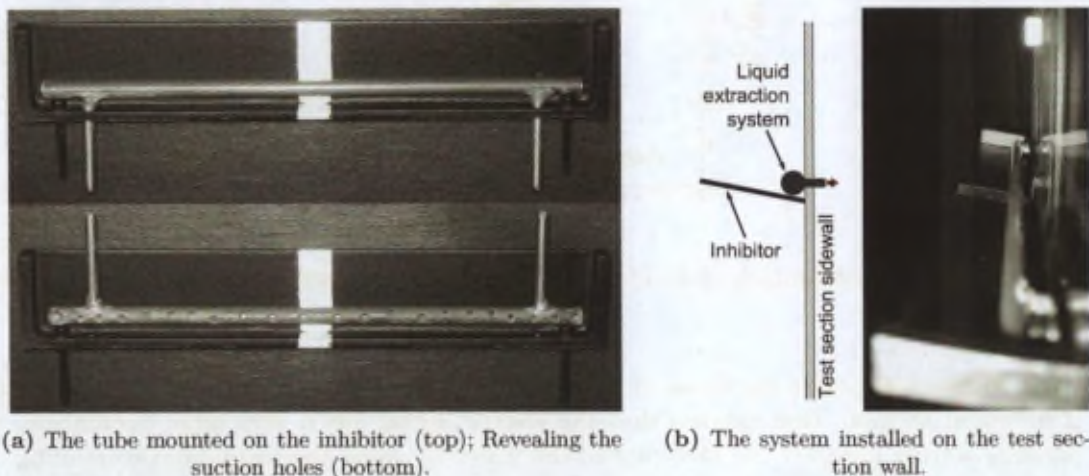


FIGURE 5.6 – The liquid extraction tube installed on the inhibitor.

During all the LeDaR measurements the light-sheet is generated in the mid-span plane of the cavity using an Argon Ion continuous laser and a cylindrical lens (see Figure 5.1(b)). The laser-beam diameter is of the order of 1 mm. Therefore, the laser-sheet has the same thickness. On the one hand, the most energetic part of the light plane is directed towards a mirror placed below the investigated cavity. This mirror reflects the sheet and illuminates the region of interest from below. On the other hand, the rest of the laser-sheet goes through the sidewall of the cavity. Due to the construction of the set-up, from the side one can not illuminate the bottom 20 mm of the cavity. This is the main reason why the most energetic part of the light plane is directed towards the mirror.

The energy of the continuous laser is always adjusted according to the actual image quality. In most of the cases  $P_{laser} = 0.4$  to  $0.6$  W is used.

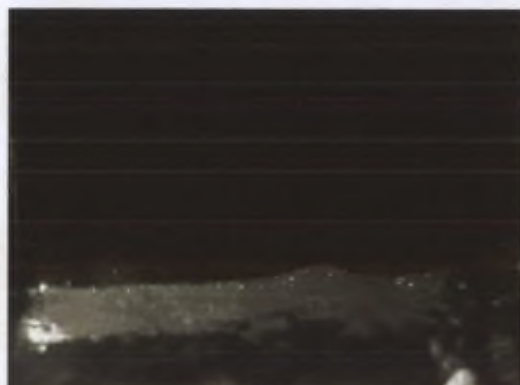


FIGURE 5.7 – Image recorded with the high-speed camera in the nominal configuration.

During the present experiments a Phantom v7.1 high-speed CMOS camera is used. The exposure time of the camera is chosen to be  $t_{exp} = 0.5$  ms, which is sufficiently short to freeze the motion of the liquid surface. However, the flow and thus the accumulated water do not have a strict two-dimensional behaviour inside the cavity. In agreement with the preliminary investigation, to ensure a clear view in the presence of three-dimensional waves, the camera is inclined by about  $15^\circ$  and the spray is working only until the accumulated water reaches roughly the middle of the recorded images. However, when the spray is stopped, the acquisition goes on until the camera buffer is full.

The camera is equipped with a  $f = 35$  mm AF Nikkor lens. As explained in section 4.4.1, the advantage of the short focal length is the larger blur disk of the objects (i.e. liquid droplets) depositing on the window through which the camera records images. To realize the shallowest possible DoF<sup>1</sup> the widest available aperture ( $f\# = 2.0$ ) is used. The thin glass sheet through which the images are acquired is also treated with the silicon-based product to prevent the deposition of large droplets. The final image quality is shown in Figure 5.7.

The high-speed camera has a maximal spatial resolution of  $800 \times 600$  pixels<sup>2</sup> and 1 GB on-board memory. The size of this memory determines the maximum number of recordable images and thus the length of the series of acquisitions. Therefore, the image size is reduced to  $640 \times 480$  pixels<sup>2</sup>, at which a maximum of 2289 acquisitions can be taken in each series.

The camera is capable of recording images with the maximum resolution even at 4000 *frames-per-second* (fps). However, during the LeDaR measurements this high frame-rate is not required. With the internal triggering of the camera, the lowest applicable recording speed is 100 fps. At this frame-rate 2289 images are taken in only 22.88 seconds.

With most of the parameters, a very low amount of accumulation is expected during 22.88 s, which could be measured only with a high uncertainty. In order to increase the recording time, the overall frame-rate should be reduced, which can only be realized by triggering the camera with an external signal.

For the LeDaR measurements, the motion of the flow or the liquid surface should not be followed in time. The only criterion from the point of the accumulation is that the images (samples) should be taken at known instants. Although currently it is not a goal to follow the deformation of the water surface in time during the accumulation, the chance should be kept for this investigation, as it might appear to be important in the future. Therefore, a burst recording (triggering signal) is designed (for easier understanding see Figure 5.8). It is decided to acquire

<sup>1</sup>Depth of Field

a sequence of 10 samples in each 4 seconds. These 10 images are recorded at a frame-rate of 100 Hz, which allows to resolve locally the motion of the liquid interface. Furthermore, at the period time of 4 seconds it is still possible to follow the volume increase with sufficient resolution.

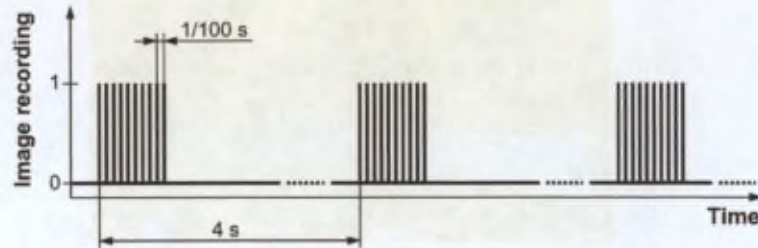


FIGURE 5.8 – *The camera trigger signal.*

Applying this image recording method, it takes about 908 seconds to record 2289 images and fill the on-board memory of the camera.

Although the LeDaR measurement technique was validated earlier, at the end of each experiment the water is drained from both of the cavities into a jug and the volumes are recorded to verify in-situ the LeDaR experiments. Furthermore, due to the fact that the spray device does not operate perfectly symmetrically, determining the difference of accumulated liquid in the two cavities, the non-symmetric behaviour of the spray can be corrected.

## 5.2 Data processing

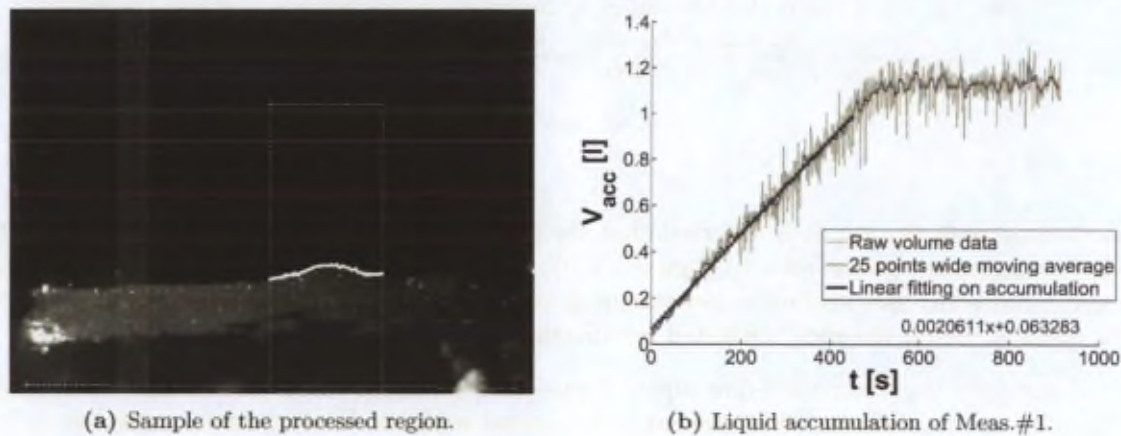
In order to determine the increase of the water volume in the cavity, the recorded series of images are processed first with LeDaR using always the optimal detection method.

Within the present study, the evolution of the shape of the liquid interface during the accumulation is out of interest<sup>2</sup>, the surface is detected only in a small zone of the images. This zone is defined in each series separately based on the mean image quality distribution. Since the acquisitions have occasionally some disturbances, while the spray is operating (e.g. splashes of droplets falling from the inhibitor, reflections from the 3D waves, etc.) and the illumination is not ideally uniform (it is influenced by the liquid surface movement and the volume increase as well), choosing an optimal region of processing is necessary. However, one can always find a narrow (at least 100 pixels wide) zone, within which the intensity distribution does not change significantly and it is not disturbed frequently by droplets or waves (a sample is shown in Figure 5.9(a)). In this way, the analysis is more reliable and the processing time can be reduced as well. By investigating only a part of the images, the fluctuation of the volume in time would be artificially larger (due to the waves of long wavelength). However, having sufficiently large number of samples, the mean rate of entrapment remains unaffected.

The LeDaR output data containing the instantaneous liquid surface shapes are post-processed by an algorithm which is analysing and correcting the eventual discontinuities in the detected surface.

Finally, the instantaneous water volume is calculated knowing the mean actual water level (assumed along the whole width of the cavity), the position of the bottom of the cavity, the

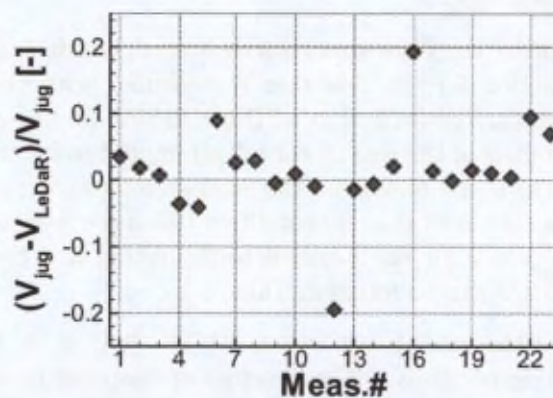
<sup>2</sup>using the presently acquired images, the liquid surface shape and motion characteristics are analysed by Myrillas (2006); Tóth et al. (2006)

FIGURE 5.9 – *LeDaR* data processing.

magnification of the images (the length corresponding to one pixel) and the inclination angle of the camera.

Plotting the liquid volume evolution in time, graphs similar to the one shown in Figure 5.9(b) can be obtained. As one can see, the raw volume increase shows increasing fluctuation as the volume of the liquid increases. However, by computing the moving average (averages of 25 local volume points) the evolution already shows a more stable mean increase.

Focusing on the part of the plot which corresponds to the time while the spray is not operating (in the example of Figure 5.9(b), for  $t > 580$  s), the mean final volume can be determined. The mean final volumes are compared to the values that are measured with the jug after each test. This comparison shows a good agreement in most of the cases (the result is shown in Figure 5.10).

FIGURE 5.10 – *The difference between the LeDaR and the jug measurements.*

Focusing on the part of the plot which corresponds to the time while the spray is operating, a linear volume increase can be observed for all the 23 tested configurations. In order to determine the rate of liquid accumulation, a first-order polynomial is fitted on the time-series in the corresponding range. The slope of this linear fitting (the relationship of Meas.#1 is shown in Figure 5.9(b)) gives directly the rate of accumulation.

Finally, the portion of the accumulated droplets should be determined with respect to the total amount generated by the spray. However, from the post-experimental volume measurements

Table 5.1 – The main characteristics of the spray device for the nominal condition

Config.	$p_w$ [bar]	$d_{32}$ [ $\mu\text{m}$ ]	$Q_{V_d}$ [l/min]	$St$ [-]	$\alpha_p \times 10^{-4}$ [-]
Spray	5	100	3.5	10.36	1.5
MPS P230				6.01	2.2

performed with the jug, it is observed that the rate of entrapment in the left cavity (regarding the arrangement, please refer to Figure 5.1(b)) is not equal to the one measured in the right cavity. Since the flow inside the test section is verified to be symmetric, the entrapment should be equal as well if the spray operated symmetrically.

Therefore, the water mass-flow injected into each half of the test section is defined by re-partitioning the total mass-flow of the spray (measured with the Venturi tube) using the ratio of the accumulated liquid in the two cavities obtained by the post-experimental jug measurement.

### 5.3 Measurement parameters

Within the present experiments the main objective is to study the effect of the available parameters on the liquid deposition. Altogether 23 configurations are chosen. The parameters are summarized in Table 5.2. The measurement results in terms of accumulation rate are indicated as well in the table, but they will be discussed only later.

As it is defined in section 2.3, the present configuration #1 (Meas.#1) is considered to be the nominal condition. The measurements with this configuration are taken twice (see Meas.#1 $r$ ) in order to verify the repeatability of the tests. In most of the other configurations only one parameter is modified compared to this nominal setting (in Table 5.2 the modified parameters are shown with bold characters).

For all the configurations the same spray device is used, which works with pressurized water. As it is described in section 5.1, its flow-rate is measured with the help of a Venturi tube. Although the present tests are performed in a 2D-like facility in cold-gas condition, the dynamic characteristics of the droplets of the real motor are attempted to be modelled. By respecting the volume fraction ( $\alpha_p$ ) of the liquid-phase and the Stokes number ( $St$ ), the interaction between the two phases should be similar as in the real condition (for more details refer to section 2.3). The properties of the spray device for the nominal configuration and the corresponding similarity parameters of the real SRM can be found in Table 5.1.

At first, the effect of the free stream velocity is studied. 6, 8, 12 and 14 m/s are chosen within Meas.#2 to #5 respectively. These values correspond to a Stokes number of  $St = [6.22; 8.29; 12.44; 14.51]$  and a volume fraction of  $\alpha_p = [2.5; 1.9; 1.2; 1.1] \cdot 10^{-4}$  respectively.

In the followings the effect of the inhibitor is measured. Within Meas.#6 to #8, the nominal inhibitor is moved closer to the nozzle to realize smaller Obstacle-to-Nozzle Ratios ( $O2NR$ ,  $L_i/h$ ). Furthermore, Meas.#8, #9, #10 and #12 represent roughly similar  $O2NR$ s, where the inhibitor size and position are modified simultaneously. Finally, inhibitors with different sizes are installed to the nominal position (Meas.#11 to #13) to cover a wide range of  $O2NR$ , but keeping the same physical location. Using Meas.#6 to #13 and Meas.#1, it is possible to analyse the effect of the inhibitors keeping constant either its height, its position or the  $O2NR$ s, by modifying the two other parameters. The  $h = [13.5..50]$  mm inhibitors represent a range of Stokes numbers of  $St = [25.72..6.94]$ .

Additionally, two special arrangements are defined related to the obstacle. In Meas.#14 no inhibitor is installed in the test section. In contrary, in case of Meas.#15 two inhibitors are mounted. The first inhibitor is the nominal one at its nominal position. The additional inhibitor is the smallest available obstacle, which is placed to the closest available position to the nozzle.

Within Meas.#16 to #18, different cavity widths ( $w$ ) are taken keeping the nozzle at the same position. Thus, the volume of the cavity is modified.

The final parameter is the size of the nozzle throat ( $o$ ) within Meas.#19 to #23. By keeping the volume of the cavity constant, the importance of the distance between the inhibitor tip and the nozzle tip along the  $y$  axis (please, refer to Figure 5.1(b)) could be seen at a given  $O2NR$ . In case of Meas.#20 ( $o = 42$  mm), the tip of the obstacle is aligned with the tip of the nozzle. Furthermore,  $o = 67$  mm is the largest dimension that could be set with the present facility. Finally, according to continuity, with  $o = 25.4$  mm the flow velocity in the nozzle throat should be the same as at  $U_0 = 6$  m/s.

## 5.4 Liquid accumulation results

The rate of liquid accumulation in percentage of the total amount generated by the atomizer and corrected for the non-symmetry of the spray is summarized in Table 5.2 for every configuration. In the followings, the rate of accumulation is also plotted in function of the main parameters. In each plot, the nominal configurations (Meas.#1 and #1 $r$ ) are highlighted. The corresponding descriptions only list the observations. Here no detailed physical explanation is given; it will be included in chapter 8.

### 5.4.1 The flow velocity

In Figure 5.11(a) the accumulation rate is plotted in function of the free stream air velocity ( $U_0$ ). By increasing  $U_0$  with a factor of 2.3, the accumulation decreases by a factor of 3.4. Therefore, the flow velocity is considered to be one of the influential parameters.

### 5.4.2 The inhibitor size

The liquid accumulation with respect to the height of the inhibitor ( $h$ ) is shown in Figure 5.11(b). By changing  $h$  between 0 and 50 mm, the rate of accumulation ranges from 25.0 % down to 5.5 % respectively with a relationship that appears to be close to linear. Therefore,  $h$  should be one of the most relevant parameters.

Focusing on the  $h = 33.5$  mm inhibitor, in Figure 5.11(b) below the nominal conditions the configuration with two inhibitors can be seen. Thus, by installing a small additional obstacle between the main inhibitor and the nozzle, the entrapment rate appears to be reduced from an average of 8.2% to 4.9%.

### 5.4.3 The inhibitor position

Figure 5.12(a) shows the rate of accumulation in function of the physical distance between the nozzle tip and the inhibitor ( $L_i$ ). In the plot, the  $h = 0$  mm case (Meas.#14; without inhibitor) is indicated as  $L_i = 0$  mm.

Table 5.2 - The experimental parameters and the obtained results

Meas.#	$U_0$ [m/s]	$h$ [mm]	$L_i$ [mm]	O2NR [-]	$w$ [mm]	$o$ [mm]	Accumulation [%]
1	10	33.5	310	9.25	107.2	15.4	8.6
1'	10	33.5	310	9.25	107.2	15.4	7.8
2	<b>6</b>	33.5	310	9.25	107.2	15.4	10.0
3	<b>8</b>	33.5	310	9.25	107.2	15.4	7.3
4	<b>12</b>	33.5	310	9.25	107.2	15.4	6.1
5	<b>14</b>	33.5	310	9.25	107.2	15.4	2.9
6	10	33.5	<b>70</b>	2.09	107.2	15.4	7.6
7	10	33.5	<b>150</b>	4.48	107.2	15.4	6.8
8	10	33.5	<b>230</b>	6.87	107.2	15.4	10.2
9	10	<b>41</b>	<b>270</b>	6.59	107.2	15.4	6.2
10	10	<b>23.5</b>	<b>150</b>	6.38	107.2	15.4	14.1
11	10	<b>23.5</b>	310	13.19	107.2	15.4	10.0
12	10	<b>50</b>	310	6.20	107.2	15.4	5.5
13	10	<b>13.5</b>	310	22.96	107.2	15.4	17.1
14	10	<b>0</b>	<b>(0)</b>	<b>0</b>	107.2	15.4	25.0
15	10	<b>33.5/13.5</b>	<b>310/110</b>	9.25/8.15	107.2	15.4	4.9
16	10	33.5	310	9.25	<b>45.2</b>	15.4	3.8
17	10	33.5	310	9.25	<b>76.2</b>	15.4	8.4
18	10	33.5	310	9.25	<b>139</b>	15.4	6.5
19	10	33.5	310	9.25	107.2	<b>25.4</b>	4.5
20	10	33.5	310	9.25	107.2	<b>42</b>	4.6
21	10	33.5	310	9.25	107.2	<b>47</b>	3.1
22	10	33.5	310	9.25	107.2	<b>52</b>	6.8
23	10	33.5	310	9.25	107.2	<b>67</b>	5.4

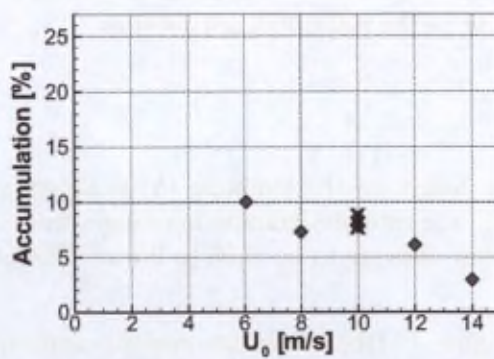
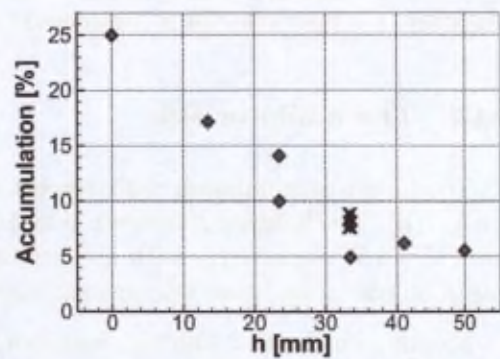
(a) The flow velocity ( $U_0$ ).(b) The inhibitor height ( $h$ ).

FIGURE 5.11 - Liquid accumulation results of different flow velocities and inhibitor sizes (the "X" symbols show the nominal configurations).

Considering the ensemble of all the indicated measurement points, one can not define a tendency in function of  $L_i$ . One can however observe that the accumulation rate is the highest for the smallest inhibitor height ( $h = 0$  and  $h = 13.5$  mm), as already indicated in the previous section.

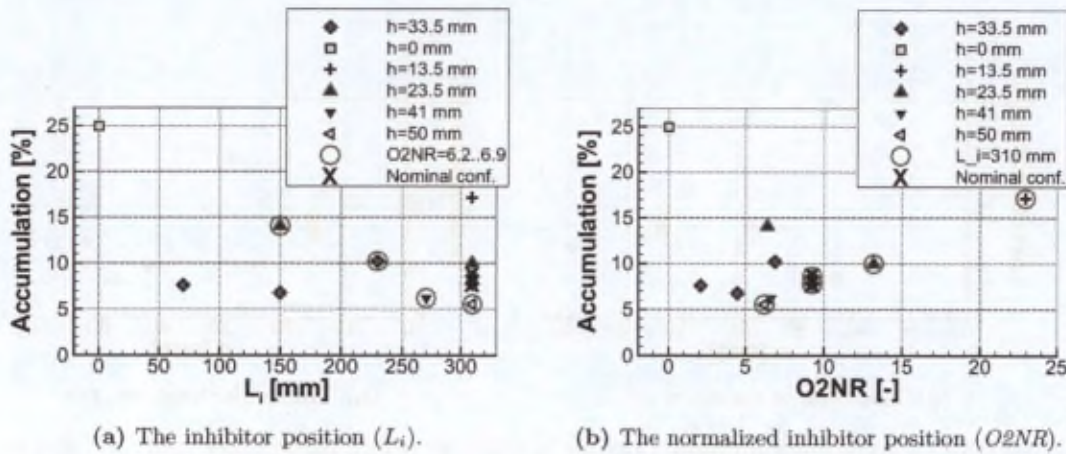


FIGURE 5.12 – Liquid accumulation results of different inhibitor positions (the "X" symbols show the nominal configurations).

Focusing on the data with constant inhibitor size (e.g.  $h = 33.5$  mm), the accumulation does not change considerably by varying the position; between the minimum and the maximum value one can find a factor of 1.5.

Focusing on the data that represent a roughly constant *Obstacle-to-Nozzle Ratio* ( $O2NR = 6.20..6.87$ ), the accumulation shows a roughly linear decrease in function of increasing  $L_i$ . However, the increase of  $L_i$  is also associated to an increase of  $h$  since  $O2NR$  is constant. Thus, the relevant parameter is again the inhibitor size and not its position.

Furthermore, in Figure 5.12(b) the accumulation in function of  $O2NR$  is shown. Now focusing on the measurements, where inhibitors with different heights are mounted to the same position ( $L_i = 310$  mm), a clearly linear increase can be observed in the accumulation in function of increasing  $O2NR$ , which proves once again that the relevant parameter is neither  $L_i$  nor  $O2NR$ , but  $h$ .

#### 5.4.4 The cavity width

The accumulation in function of the cavity width ( $w$ ) is shown in Figure 5.13(a). By keeping the nozzle ( $o$ ) at a given position, the width of the cavity is modified. Within the investigated range, a concave behaviour is discovered. The maximum droplet entrapment rate appears around  $w = 100$  mm (64% of the height of the cavity).

Although the accumulation rate changes by a factor of two within the examined range, the width of the cavity does not appear to be the most influential parameter since the accumulation changes in a smaller range compared to  $h$ , for instance.

#### 5.4.5 The nozzle throat opening

The effect of the nozzle opening ( $o$ ) on the droplet entrapment rate is shown in Figure 5.13(b). According to the plot, one can conclude that in the investigated range, the nozzle throat opening does not have a direct impact on the liquid accumulation.

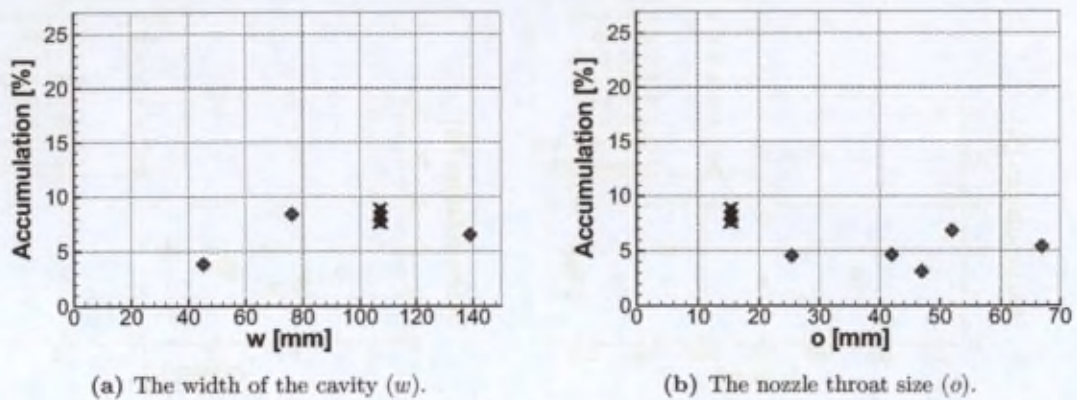


FIGURE 5.13 – Liquid accumulation results of different cavity parameters (the "X" symbols show the nominal configurations).

#### 5.4.6 Obstacle tip to nozzle tip distance

The *Obstacle tip to nozzle tip distance* ( $OT2NT$ ) is defined by the distance between the tip of the inhibitor and the tip of the nozzle along the  $y$  (transversal) axis (see Figure 5.14(b)). The component of the distance along the  $x$  (longitudinal) axis is not taken into account. Therefore, the  $OT2NT$  gives the distance by which a droplet - passing near the tip of the inhibitor - has to be deviated by the flow in order to escape through the nozzle and not to be trapped in the cavity.

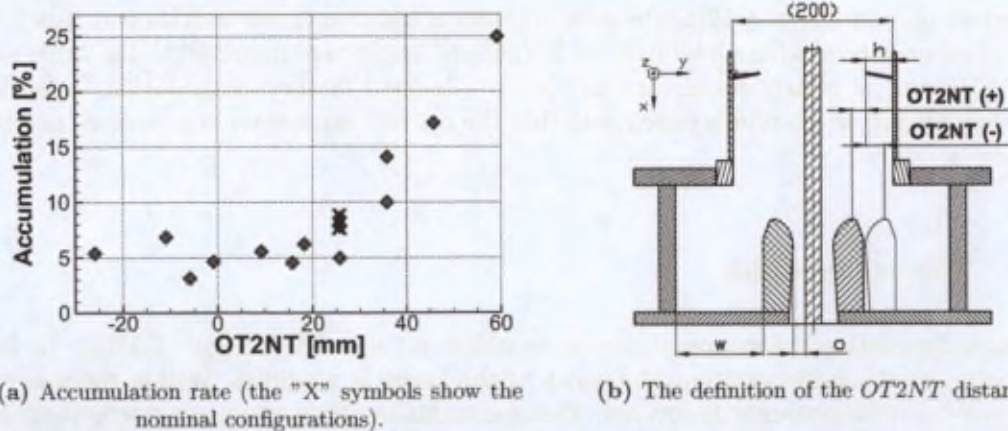


FIGURE 5.14 – The relative distance between the nozzle tip and the inhibitor tip ( $OT2NT$ ).

In Figure 5.14(a), the liquid accumulation rate is plotted in function of the  $OT2NT$  distance.

At first sight, by increasing this distance, the accumulation is not affected up to about  $OT2NT = 20$  mm. Further increasing  $OT2NT$  the liquid entrapment increases gradually.

According to Figure 5.14(a), regardless to the position of the nozzle, a minimal accumulation rate is present.

This accumulation may represent on the one hand the droplets, which are hitting the wall in the recirculation region downstream the inhibitor. As soon as a droplet hits the wall, most probably it does not enter the flow anymore, but it slides into the cavity.

On the other hand, droplets may be entrapped due to the vortex-nozzle interaction. This process is assumed to be quasi-periodic, controlled by the vortex shedding frequency downstream the inhibitor. Therefore, it could contribute by a constant amount of liquid.

However, by modifying the size (and the position) of the inhibitor, one may change considerably the instantaneous and the mean topology of the internal flow field. Therefore, this modification could also have a considerable impact on the amount of accumulated liquid.

One has to add that while  $o$  is changed,  $U_0$  is kept constant. Therefore, the velocity magnitudes and thus the flow dynamics around the nozzle lip are changing considerably as well.

To sum up, the  $OT2NT$  distance - which comprises  $o$  and  $h$  as well - is found to be a relevant parameter in the droplet entrapment process.

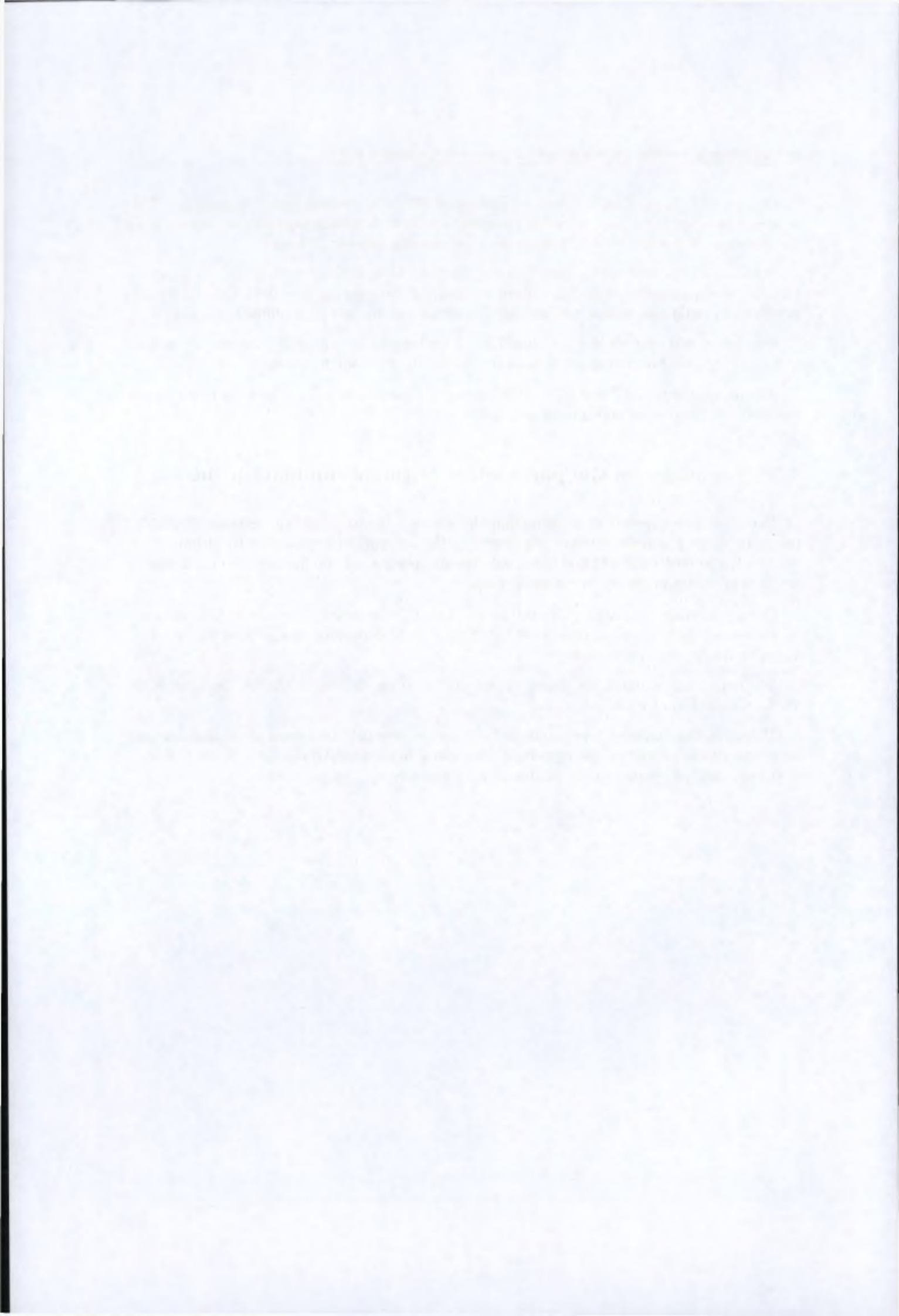
## 5.5 Summary on the parameters of the accumulation rate

From the above described investigation the obstacle tip to nozzle tip distance ( $OT2NT$ ) turns out to be the most relevant parameter in the accumulation process. By definition, it involves the inhibitor size ( $h$ ) and the nozzle throat opening ( $o$ ). From these two the inhibitor height is predominant in the investigated range.

One can identify the cavity width ( $w$ ) and  $U_0$  being the secondary parameters that drive the accumulation. As it was seen, they could modify the liquid deposition rate at least with a factor of two in the investigated ranges.

The remaining inhibitor position ( $L_i$ ) and obstacle-to-nozzle ratio ( $O2NR$ ) parameters do not have a significant influence.

Therefore, the following investigations focus on the flow field by means of single-phase and two-phase PIV experiments and numerical simulations to reveal the main mechanisms that lead to the primary importance of the inhibitor and the nozzle tip.



## Chapter 6

# Statistical flow-field investigation

Concerning the investigation of the flow field inside the present 2D cold-gas SRM model, the present chapter provides the analysis of the statistical quantities. At first, a detailed single-phase PIV experiment and the corresponding results are described. This case is mainly used for the validation of numerical tools, which is shown in the followings. Later, droplets are injected in the numerical domain and their effect on the statistical flow quantities are highlighted. Finally, the (statistical) data obtained with the new two-phase PIV technique are shown.

### 6.1 Single-phase PIV experiments

Since the main purpose of the present experimental data is to validate numerical tools, only one geometrical arrangement is chosen, which is then entirely characterized in the mid-span plane with the highest possible resolution and in the best possible way.

#### 6.1.1 Experimental conditions

The geometry of the experimental model is shown in Figure 6.1. This is the configuration which is considered to be nominal in the current facility.

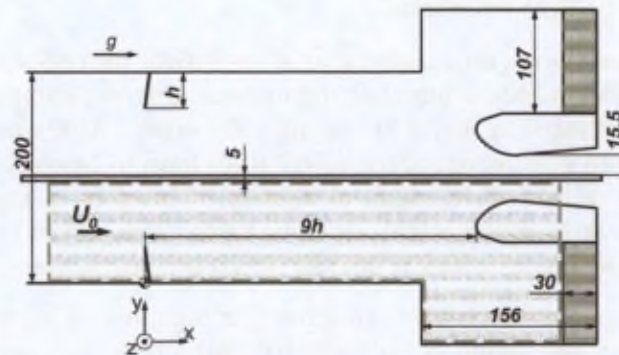


FIGURE 6.1 – *Experimental geometry.*

The height of the inhibitor is  $h = 33.5$  mm. The presence of this fence induces the *obstacle vortex shedding* (OVS). In order to allow the vortices to reach the nozzle and reproduce the

vortex-nozzle interaction phenomenon in the 2D model, the inhibitor is placed at  $L_i = 9h$  from the nozzle.

At the bottom of the cavity a 30 mm thick plexiglass piece is modelling the accumulated liquid. Later, the plexiglass piece is replaced by the same amount of water to see the importance of having liquid interface with respect to the solid wall.

The nominal free stream velocity of  $U_0 = 10$  m/s is chosen, which results  $Re_h = 2.51 \times 10^4$ .

To characterize the single-phase internal flow field of the 2D-like simplified model of the SRM, the PIV technique is used (the principle of the technique is introduced in section 4.1.1). The laser-sheet representing the measurement plane is generated in the mid-span plane of the test section perpendicularly to the splitting plate. The tracers are oil particles of the order of 1 to 2  $\mu\text{m}$  in diameter. A camera with  $1280 \times 864$  pixels<sup>2</sup> effective resolution - placed perpendicularly to the laser-sheet - is recording the measurement image pairs.

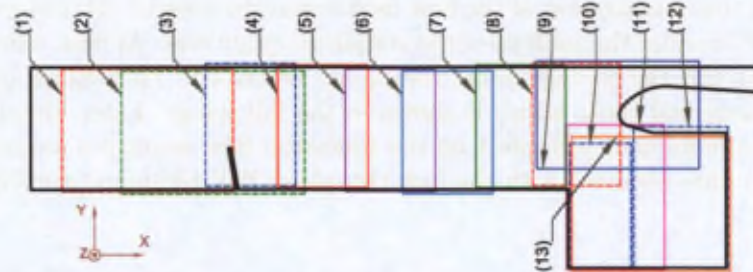


FIGURE 6.2 – Fields of view of the PIV measurements (the fields are slightly shifted transversally to facilitate the understanding).

Currently, the region of interest covers the whole mid-span plane of the test section from the inhibitor until the nozzle throat, including the cavity. All this area should be covered by the PIV experiments in order to be able to compare the data to the numerical simulations. Furthermore, since from these measurements (later on) the vortices should be identified and their properties should be extracted, the measurements should have high enough resolution. Hence, the magnification of the images is limited to about 0.081 mm/pixel between the inhibitor and the nozzle and about 0.09 mm/pixel inside the cavity. The low magnification has a good contribution to the measurement quality near the walls of the section; this reduces the area of regions affected by the light reflections.

In order to achieve the required higher spatial resolution, the region of interest is divided into 12 fields-of-view (FoV), which means that the measurement is performed by using 12 different camera positions (indicated in Fig. 6.2) one after the other. After the PIV analysis, once the mean flow field of each FoV is computed, the 12 fields have to be combined in order to retrieve the mean flow field of the whole region of interest. Therefore, a special care of the spatial calibration (position and magnification) has to be taken. The 13<sup>th</sup> FoV shown in Fig. 6.2 covers the whole cavity. However, this field is not taken into account in the combined view.

Furthermore, a special care is taken to achieve as high overall *signal-to-noise ratio* ( $SN$ ) as possible. Focusing on the region of the expected path of the vortices, the settings are tuned until the  $SN$  reaches mostly above 5.

The separation time ( $\Delta t$ ) between the PIV images is optimized in each FoV according to the actual magnification and the local flow conditions. In each FoV 1000 image pairs are recorded which allow to determine reliable turbulence quantities beside the mean velocity vectors. As

it was mentioned before, all the plots of the different FoVs are combined and presented as one single field.

### 6.1.2 Experimental results

During the PIV processing of each FoV (by using *WiDIM* PIV software developed by Scarano (2000)), the optimal initial window size and the number of window refinement iterations are determined according to the actual image quality. The switched-on window-distortion algorithm and the 75% window overlapping are common parameters of the data processing. As a result, e.g. in the region between the inhibitor and the nozzle, the resolution of the velocity field is 1.4 to 2.5 vectors/mm by keeping a high mean *signal-to-noise ratio* (SN) (see Figure 6.3).

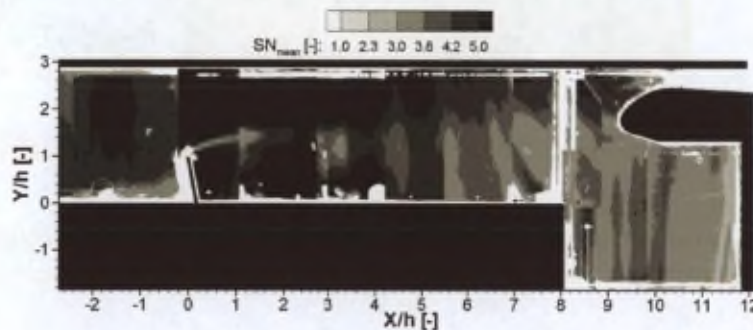


FIGURE 6.3 – *Signal-to-noise ratio distribution of the PIV measurements.*

While the statistical quantities are computed from the instantaneous flow fields, a validation process is carried out in every cell of each field. Where  $SN_{mean}$  does not reach a value of 2.3, the measurement is considered to be unacceptable. An indicator of this effect is e.g. when streamlines enter in the wall. In the contour plots these ambiguous areas appear in white (without value) which indicates that locally the measurement quality is low and the mean velocity vectors may not represent physical behaviour.

#### 6.1.2.1 The statistical flow quantities

During the analysis of the obtained statistical flow structures the plane of interest and the boundaries are divided into several zones. The most frequently used terms (in chapter 6, 7 and 8) are summarized in Figure 6.4.

After combining the 12 FoVs recorded in the symmetry plane of the test section, the streamlines of the mean flow are shown in Figure 6.5(a). It can be observed that in the mean, a flow particle, following the streamline which originates roughly from the tip of the inhibitor ( $X/h = 0$ ;  $Y/h = 1$ ), arrives at the nozzle head and escapes from the model through the throat. The flow particles placed at higher  $Y/h$  positions than this streamline are directly escaping as well.

As no radial flow injection occurs perpendicular to the side wall, a complex circulating region can be seen below this streamline (at lower  $Y/h$  values). This area is governed mainly by two mean rotating structures. One of them is located in the cavity, centered at ( $X/h = 9.82$ ;  $Y/h = -0.11$ ), and the other one extends from the tip of the inhibitor until the entrance of the cavity; its center is at ( $X/h = 4.04$ ;  $Y/h = 0.89$ ). At the downstream corner of the inhibitor and just upstream from the entrance of the cavity, smaller counter-rotating mean structures are

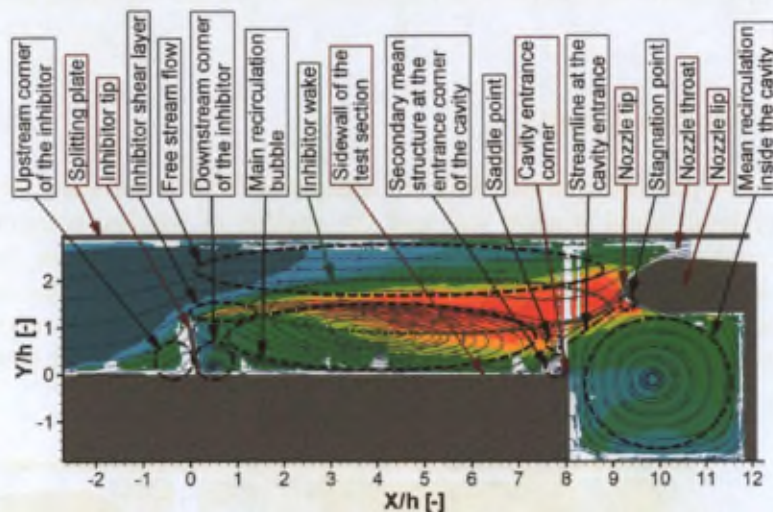


FIGURE 6.4 – Schematic of the main boundary elements and mean flow structures.

formed. Due to local light reflection and image quality problems, the counter-rotating mean structures at the upstream corner of the inhibitor and in the three corners of the cavity could not be captured.

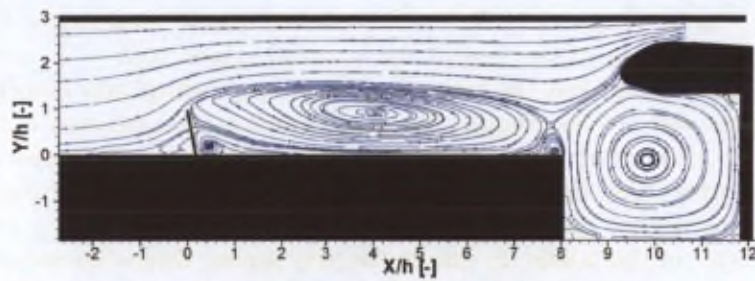
In the contour of Figure 6.5(b) the mean in-plane velocity magnitudes can be seen. It can be observed that the flow is accelerating as it passes over the inhibitor. The magnitude of the velocity reaches slightly above 21 m/s in the *vena contracta*. Then, the free stream flow slows down below 20 m/s. As it approaches the nozzle, it accelerates again and in the nozzle throat it reaches a velocity magnitude higher than 50 m/s. Unfortunately, this latter value could not be captured more precisely.

Considering the fluctuations, Figures 6.5(c) and 6.5(d) show the RMS of the stream-wise ( $U$ ) and of the transversal ( $V$ ) velocity components respectively.  $RMS_U$  increases abruptly above 3.6 m/s at the tip of the obstacle, due to the presence of a shear layer at the separation. The area from the inhibitor to the nozzle head may be divided roughly into two zones. In the first one, from  $X/h = 0$  to  $X/h = 4.2$  (corresponding approximately to the center of the main recirculation structure), the value of this fluctuation component is increasing and spreading gradually, reaching a value of about 50% of the initial free stream velocity ( $U_0$ ). In the second zone, from the center of the recirculation region to the nozzle head, the iso-contours of this fluctuation component keep a constant width together with a constant maximum value of  $RMS_U$  at about 50% of  $U_0$ .

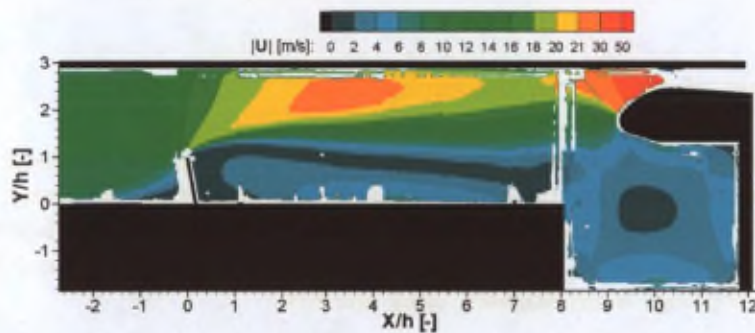
$RMS_V$  shows a similar evolution to  $RMS_U$ , with a maximum value above 35% of  $U_0$ . However, in the second region, in front of the nozzle head one may notice values above 45% of  $U_0$ , due to the local acceleration of the flow and turbulence production by the flow impingement on the nozzle wall.

In practice, the main fluctuations are driven by the shear layer attached to the inhibitor tip. Close to the obstacle tip it is very stable, representing mainly longitudinal fluctuation. Therefore, in a narrow band high  $RMS_U$  values appear immediately. However, shortly after the obstacle the shear layer starts flapping and breaks up into vortices, which make the transversal fluctuations ( $RMS_V$ ) increase gradually.

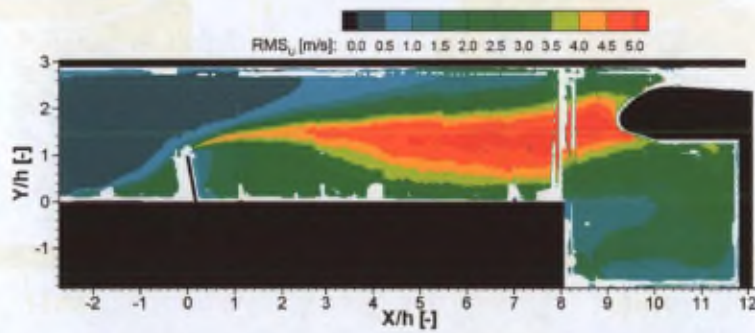
From the numerical simulations that will be introduced in section 6.2, some instantaneous



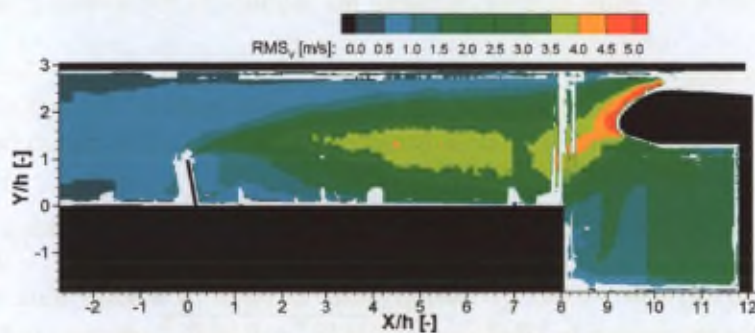
(a) Streamlines of the mean flow field.



(b) Mean velocity magnitude distribution.



(c) Fluctuation of the longitudinal velocity component.



(d) Fluctuation of the transversal velocity component.

FIGURE 6.5 – Results of the ensemble averaged PIV campaign in the symmetry plane.

fields are extracted by Lema et al. (2005). In those fields it can be seen that the vortices are formed around  $X/h = 1.5$  to 2 and a first pairing takes place already around  $X/h = 3$  to 4. Until here, the coherent structures are growing, thus the fluctuations are spreading transversally. A

second pairing can be observed at  $X/h = 4$  to 6, but due to dissipation, this does not result in a considerable increase of the size of the vortices. From  $X/h = 8$  until the nozzle tip a second shear layer is present at the entrance of the cavity, which may deform and elongate the vortical structures and increase slightly the level of fluctuations (as seen e.g. in Figure 6.5(d)). At the nozzle tip, depending on the transversal vortex position with respect to the stagnation point, the structures either escape through the throat or enter in the circulation zone inside the cavity. Inside the cavity, they initiate the fluctuations. However, they break up already in the boundary layer of the nozzle lip due to the very strong three-dimensional effects and they dissipate. Therefore, by the time the flow makes a  $270^\circ$  turn and arrives back to the entrance of the cavity, the fluctuations decay (also visible in Figure 6.5(c)).

### 6.1.2.2 Effect of the slag in the cavity

The statistical flow quantities described in section 6.1.2.1 are obtained by performing the experiments, while a 30 mm thick plexiglass sheet is placed in the cavity, which models the accumulated liquid. In the present section the influence of the rigid surface with respect to the deformable liquid interface is assessed. Therefore, 30 mm water is poured into the cavity and the mean flow topology is investigated using one FoV.

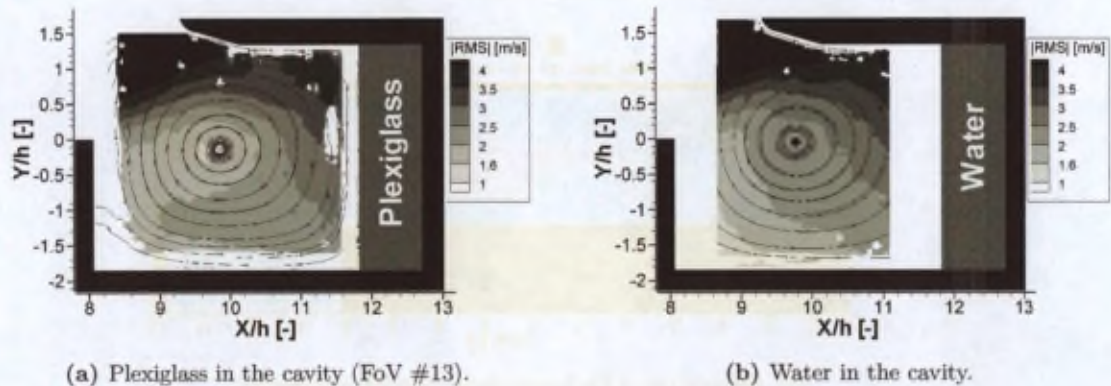


FIGURE 6.6 - Flow field by changing the medium in the bottom of the cavity.

The comparison of the two cases can be seen in Figure 6.6. Due to the presence of waves, high-energy laser light reflections occur above the water surface. To protect the camera from dangerous reflections, the interface area is not characterized (white region between  $X/h = 11.1$  and  $11.8$  in Figure 6.6(b)).

Some differences can be observed between the two plots. At first, looking at the streamlines, the center of the mean recirculating structure shifts slightly from  $(X/h = 9.82; Y/h = -0.11)$  to  $(X/h = 9.76; Y/h = -0.04)$  by having water in place of a solid wall. Secondly, defining absolute velocity fluctuation by  $|RMS| = \sqrt{RMS_U^2 + RMS_V^2}$ , one may notice that the highest values appear at the cavity entrance and along the nozzle wall in both cases (Figure 6.6). Most probably, these high values are associated with the entering of the vortical structures in the cavity together with the generation of a shear layer at the cavity opening. However, investigating the lower  $|RMS|$  values, one can see the minimum value of this absolute fluctuation near the centre of the main mean recirculating structure by having plexiglass in the cavity. On the contrary, a similar minimum value area is not visible, when water is present in the bottom of the cavity. The recirculation area appears to be globally less stable than with solid wall.

This is due to the presence of waves already observed on the liquid interface during the liquid accumulation investigation performed in chapter 5. Therefore, while the mean flow field does not seem to be strongly affected by the presence of the liquid interface, the velocity fluctuation appears to be influenced by the waves of the water surface.

## 6.2 Single-phase flow numerical simulations

The slag reduction in the SRM could be achieved by intensive numerical campaign. Nevertheless, the validation of both the methodology and the commercial solver is mandatory. In the present section the validation of the single-phase condition is shown.

The numerical investigation that is discussed in section 6.2 and 6.3 (except 6.3.3) was entirely carried out by M. R. Lema and P. Rambaud from the preparation of the simulations until their statistical analysis. Therefore, only the main aspects are shown here, which are necessary to understand better section 6.3.3, the instantaneous flow assessment (chapter 7) and the discussion of the accumulation process (chapter 8). More details on this numerical study and further results are given by Lema et al. (2005; 2007).

### 6.2.1 The numerical domain

The numerical simulations are performed with *CFD-ACE+* commercial solver using LES turbulence modelling. The computations are based on the experimental conditions. Accordingly, the numerical domain is three-dimensional with 200 mm span-wise dimension. The irrelevance of two-dimensional simulations was proven by Lema (2005) and Lema et al. (2005). As it is shown in Figure 6.7, the geometry corresponds to one half of the test section, up-to the splitting plate (see Figure 6.1). Furthermore, the properties of room-temperature air are given to the fluid.

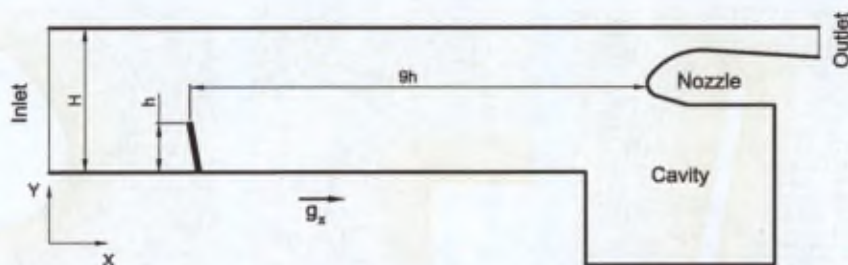


FIGURE 6.7 – Numerical domain geometry.

The boundary conditions are taken to reproduce the measured flow. The inlet of the numerical domain is located at  $X/h = -2.8$ . For this boundary, a two-dimensional mean velocity distribution is created by using two experimental velocity profiles. The first profile is taken from the  $xy$  plane of the previous PIV experiments. The second profile is measured with PIV in a plane parallel to the splitting plate ( $xz$ ) in the middle of the test section. Based on these measurements, the inlet velocity distribution is generated as shown in Figure 6.8. The RMS value of each velocity component is also measured experimentally. Even though this value is not constant along the profiles, a constant typical value is defined in the numerical simulation:  $RMS_U = 0.3$  m/s,  $RMS_V = 0.5$  m/s and  $RMS_W = 0.5$  m/s.

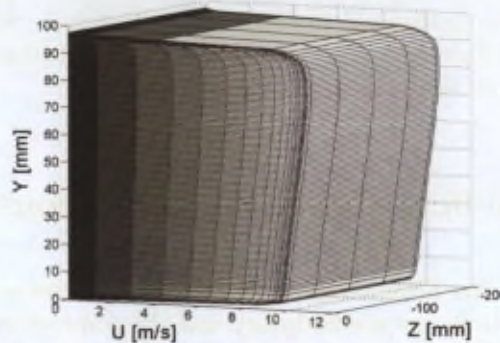


FIGURE 6.8 – Inlet velocity distribution.

The applied numerical methods to discretize the equations are second order in time (Crank-Nicolson method) and second order limited in space. The linear equations of velocity and pressure correction are solved with the Algebraic Multi-Grid (AMG) numerical solver. The convergence criterion of the iterative unsteady solver is set to a minimum residual of  $10^{-3}$  or a maximum of 20 iterations in each time step. The sub-grid stress tensor is modelled with a dynamic version of the Smagorinsky model.

The grid must be generated to be fine enough to approximate the details of the flow, while trying to reduce the computational effort to reach a converged solution. For this purpose, a hybrid mesh is created (some enlargements are shown in Figure 6.9): a structured grid near the solid walls and the inhibitor to approximate the high gradient boundary layer, and an unstructured quadrilateral mesh in the rest of the domain. The number of mesh points is  $20786 \times 50$  (by having 50 cells in the  $z$  direction), which corresponds to more than one million cells. The size of the smallest cell is as fine as  $\Delta_{min}/H = 4.25 \cdot 10^{-5}$ . The auto time step option is used so as not to exceed a  $CFL$  number of 0.425. During the simulation the flow field at every 20th time step is saved.

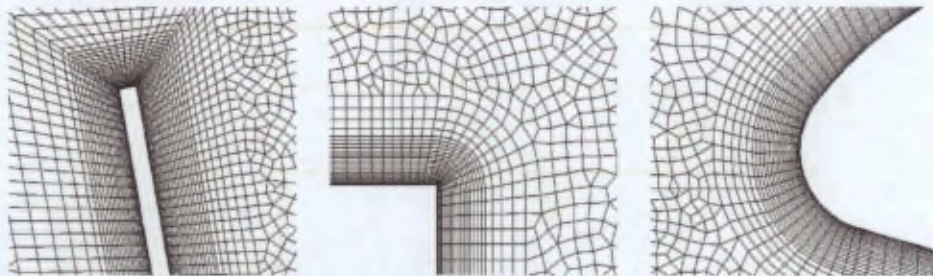
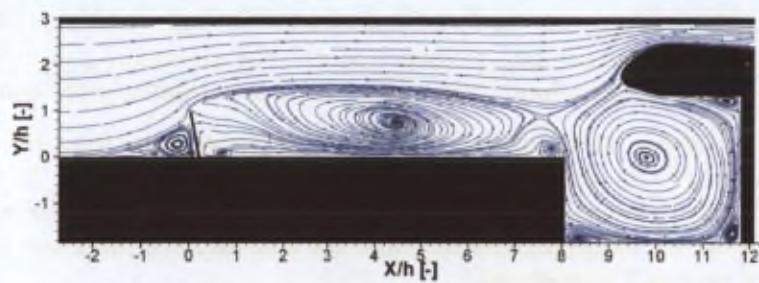


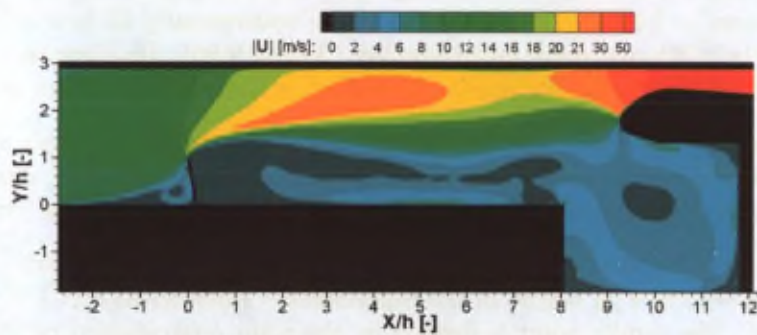
FIGURE 6.9 – Some examples of the hybrid grid of the numerical domain.

### 6.2.2 Validating the numerical data

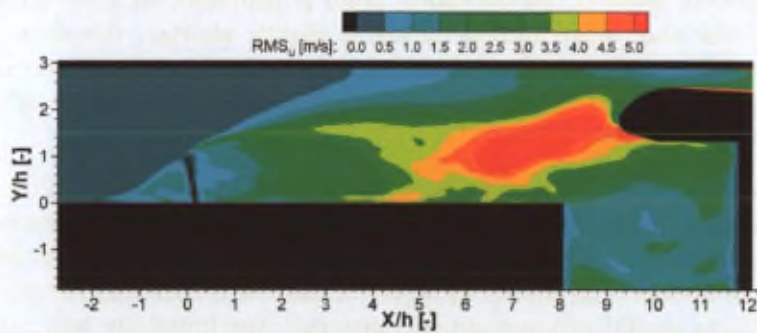
In order to compare the unsteady numerical data to the statistical experimental results, first of all the simulation was calculated during more than three *flow-throughs* (FTs). One FT stands for the time required for a flow particle to travel through the computational domain at bulk velocity. Later, all the stored flow fields of the 3 FTs are averaged. Finally, from the mid-span plane of the 3D numerical domain (defined by the laser-sheet position of the experiments) the in-plane components of the data are extracted and presented.



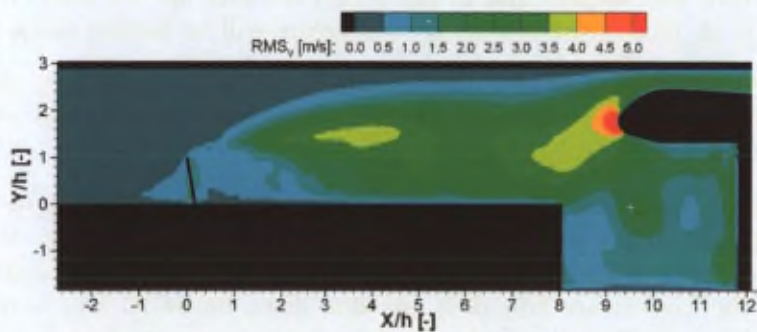
(a) Streamlines of the mean flow field.



(b) Mean velocity magnitude distribution.



(c) Fluctuation of the longitudinal velocity component.



(d) Fluctuation of the transversal velocity component.

FIGURE 6.10 – Results of the time averaged LES simulation in the symmetry plane (single-phase).

In Figure 6.10 one can see the distribution of the same quantities as those presented in Figure 6.5 related to the experimental investigation.

Concerning the topology of the mean flow fields, the numerical field (Figure 6.10(a)) resembles well the experimental data (Figure 6.5(a)). The streamlines visualize the same mean circulating structures. Furthermore, these mean zones have similar sizes and locations.

A large recirculating bubble downstream the inhibitor extends from the tip of the obstacle until the entrance of the cavity. Its centre is located at  $X/h = 4.45$ ;  $Y/h = 0.75$ , which is about 10% more downstream and  $0.14h$  (approximately 19%) closer to the sidewall than in the experiments. However, its height and therefore the dimension of the *vena contracta* of the free stream flow are very well reproduced.

The mean flow rotation inside the cavity appears to be convincing as well. The position of its centre appears to be  $0.11h$  closer to the nozzle transversally (it is located at  $Y/h = 0.00$ ) and shifted only  $0.02h$  upstream longitudinally ( $X/h = 9.80$ ). Its dimension is defined mainly by the three cavity walls and the nozzle. Therefore, no deviation is discovered here.

Concerning the secondary circulating mean flow structures, they all appear in the time averaged numerical results even those that were not obtained from PIV due to light reflection problems. Mostly, their location and dimension match very well with the experimental data.

One of the aspects worth mentioning is the saddle point. This hyperbolic point - which is located at  $X/h = 7.78$ ;  $Y/h = 0.65$  in the experiments - shifts to  $X/h = 7.57$ ;  $Y/h = 0.87$  in the numerical plot. The saddle point is defined by the main recirculation bubble downstream the inhibitor, the shear layer at the entrance of the cavity, the free stream flow and the small mean circulating structure below it. As the saddle point is displaced, all these structures are modified as well. Thus, the main recirculation bubble is slightly shorter, the shear layer of the cavity entrance is less steep, the streamlines of the free stream flow are less curved as the flow begins its acceleration towards the nozzle, and the secondary circulating structure at the entrance corner of the cavity is considerably larger.

Finally, the smaller circulating structure at the downstream corner of the inhibitor, together with the beginning of the main recirculating bubble show some differences with respect to the experimental results. Visually, the small structure looks to be less developed, or highly affected by three-dimensional effects. However, if the flow is correctly simulated, even the three-dimensional effects should produce similar patterns experimentally and numerically. For this reason, and considering that the numerical mean flow field is constructed using only 3 FTs<sup>1</sup>, Lema et al. (2005) also suspect that in this region the data are not fully converged. Using the data of Lema et al. (2005), the statistical convergence will be further assessed in section 7.2.

As it can be expected from the good agreement of the flow topology, globally the in-plane velocity magnitude plots (see Figure 6.5(b) and Figure 6.10(b)) also show very similar patterns and well matching velocity magnitudes.

However, a slight difference can be seen in the acceleration of the flow in the *vena contracta*. Concentrating only to the local velocity maxima, while experimentally the 21 m/s value is reached farther downstream ( $X/h > 2$ ), numerically this value appears already at  $X/h < 1$ . Furthermore, the free stream flow does not slow down below 20 m/s numerically before the second acceleration towards the nozzle, which is clearly due to the higher saddle point position.

In the recirculation region, the velocity amplitudes appear to be well represented; both the magnitudes in the main recirculation bubble and the rotational speed of the mean vortex in the cavity are well matching. However, the pattern of the numerical plot (Figure 6.10(b)) does not appear to be as regular as the experimental plot (Figure 6.5(b)) in the same regions. This is

<sup>1</sup>Flow-throughs, 1 FT is the time during which a flow particle travels through the numerical domain at bulk velocity

suspected to be caused simply by the lack of full convergence.

Concerning the velocity fluctuations, as it can be seen in Figure 6.10(c) and 6.10(d), the statistical convergence issue arises once again. By analysing the plots, the field can be divided again into two main regions: 1)  $X/h \leq 4.5$ ; 2)  $X/h > 4.5$ .

In the first region - practically until the centre of the main recirculating structure downstream the inhibitor - the standard deviation of both velocity components exhibit lower values than those ones which were observed during the experiments (shown in Figure 6.5(c) and 6.5(d)). This underestimation originates from the definition of the random inlet turbulence, which neither represents spatial nor temporal correlation. However, in spite of the incorrect prediction until the region of the inhibitor, further downstream a rather correct turbulence content is retrieved. As it can be seen in the second zone, at  $X/h > 4.5$  the levels of the fluctuation components are accurate; at some places they are even slightly over-predicted. The phenomenon is due to the natural unsteadiness of the shear layer attached to the inhibitor, which is producing a shedding of coherent structures seeding the flow with the necessary perturbations.

In order to be able to compare more precisely the actual matching and deviation of the experimental and numerical data, profiles of the longitudinal velocity component and the velocity fluctuation magnitudes are also extracted at four  $X/h$  positions (Figures 6.11 and 6.12).

One profile is taken at  $X/h = 0$ , which corresponds to the tip of the inhibitor. The second profile is taken (according to the experimental data) approximately at the position of the center of the main mean recirculating structure ( $X/h = 4$ ), which originates from the tip of the inhibitor and extends until the cavity. The third profile is desired to be extracted from the corner of the beginning of the cavity. However, in this region (due to the structure of the set-up) the PIV measurements have locally low quality (see Figure 6.5). Hence, the position of the third profile is defined to be at  $X/h = 7.6$ . The fourth profile is defined at  $X/h = 10$ . This location is close to the center of the main mean swirling structure inside the cavity (according to the experimental data).

All the above-mentioned observations driven from the contour plots can be seen locally more precisely in Figures 6.11 and 6.12.

Finally, the extracted profiles and the previous contour plots also show a good agreement between the time-averaged numerical data and the ensemble averaged experimental results.

### 6.3 Two-phase flow numerical simulations

As for section 6.2, the achievements described in the current section (6.3) (except 6.3.3) are also performed by M. R. Lema and P. Rambaud. Therefore, only the main aspects are shown and commented here. Further details can be found in Lema et al. (2005; 2007; 2006).

After the satisfactory single-phase flow validation, the second phase is injected in the numerical domain. The Lagrangian water-droplets may act on the air-phase through a two-way coupling source term. In practice, two simulations were performed. One with droplets of constant diameter ( $d_p = 100 \mu\text{m}$ ) and one using the same (poly-disperse) droplet size distribution as during the LeDaR experiments (see Figure 5.2). The water flow-rate is the same in both cases as during the nominal condition of the LeDaR measurements (Table 5.1).

The amount of liquid accumulation is attempted to be determined numerically as well. Therefore, a capture rule has to be defined. Cesco (1997) studied the droplet-wall interaction,

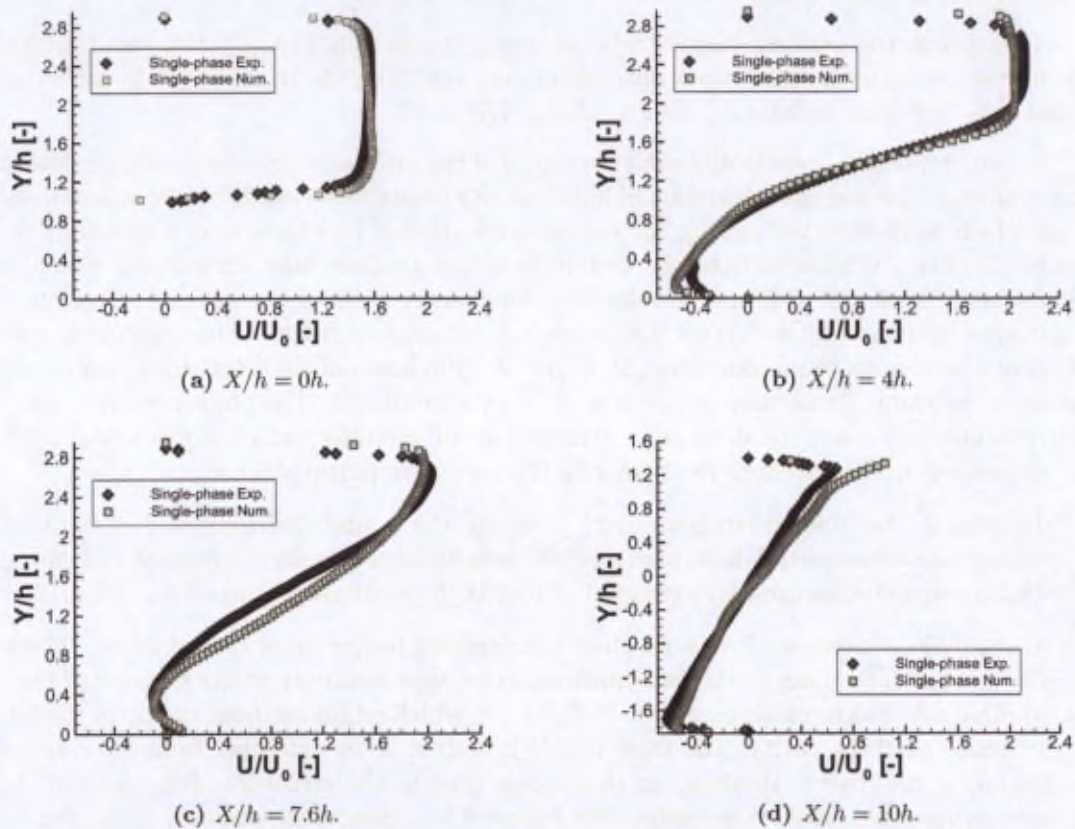


FIGURE 6.11 – Mid-span plane comparison between the experimental and the numerical longitudinal velocity components.

where various phenomena are considered during the collision: rebound, deposition, spattering and splashing. These phenomena can be distinguished and modelled reasonably well in the presence of a dry surface. However, in the presence of a wet surface (e.g. liquid alumina film on the nozzle lip), without simulating directly each collision, the uncertainty on the type of the actual phenomenon is very large. Therefore, in the final simulations Cesco (1997) counted every droplet hitting the wet nozzle lip depositing and contributing to the liquid film.

Since in the present case all the internal walls of the test section are wet during the spray operation, the same criterion is used to estimate the accumulation. Various zones are defined to cover all the boundaries of the numerical domain (see Figure 6.13): the *topwall* region from which the droplets are escaping through the nozzle, the *cavity* region extending from the downstream face of the inhibitor until about the stagnation point of the airflow on the nozzle lip (see Figure 6.10(a)) and the *obstacle* zone where droplets deposit on the inhibitor which are extracted by the experimental water extraction system.

At the walls of the numerical domain vanishing droplet condition is applied, but through a user subroutine the mass of the droplets hitting any of the walls of the above-described three regions is counted in each time-step. In particular, the droplets hitting any of the walls of the cavity region as defined above (from the inhibitor to the nozzle lip) are considered to end up finally in the pool of the cavity. In this way, the water accumulation in the cavity can be determined numerically.

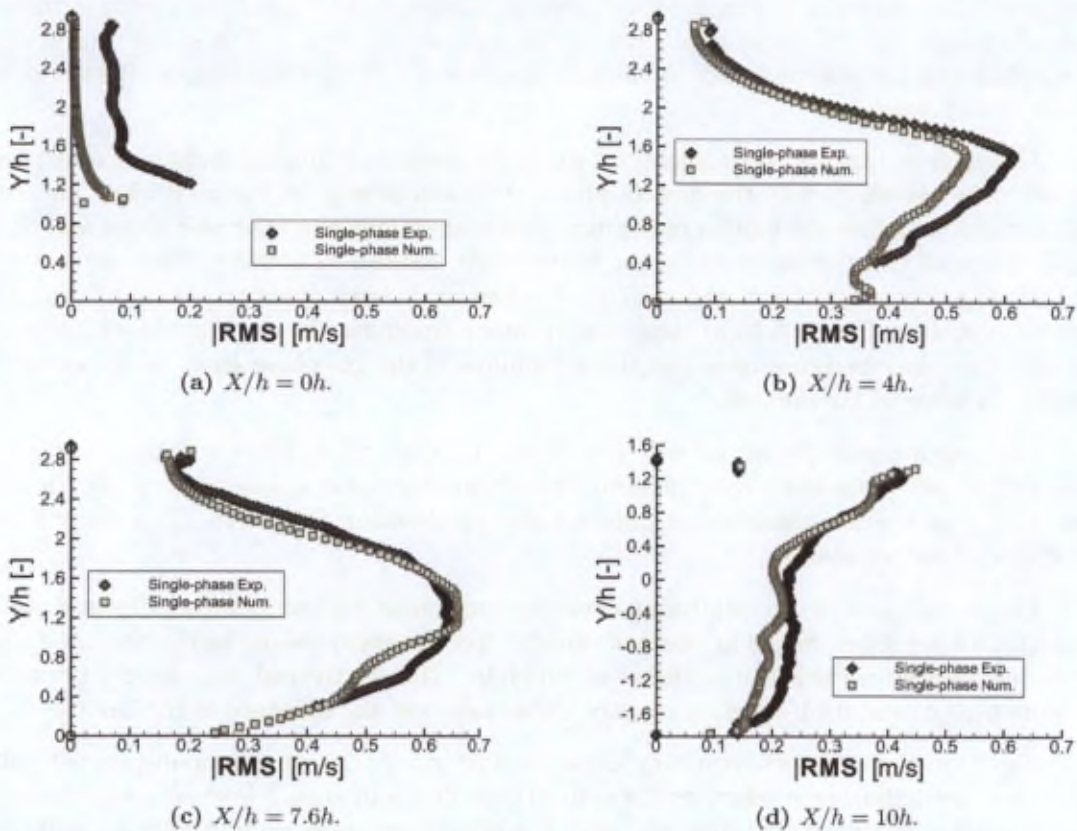


FIGURE 6.12 – *Mid-span plane comparison between the experimental and the numerical velocity fluctuation magnitudes.*

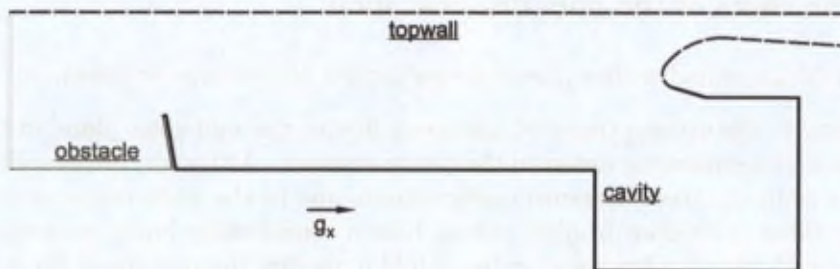


FIGURE 6.13 – *Regions of numerical boundaries used for liquid accumulation record through droplet mass counting.*

### 6.3.1 The effect of the mono-disperse spray

The statistical two-phase flow LES results including the action of the mono-disperse droplets are presented in Figure 6.14. In the followings, a comparison between the single-phase flow numerical results and two-phase flow is given.

The impact of the mono-disperse droplets is clearly visible already from the stream-traces of the mean flow, especially at the entrance of the cavity and inside of it. In the single-phase flow configuration (see Figure 6.10(a)) the cavity is closed by a streamline that points to the stagnation point on the nozzle head (i.e. no streamline enters in the cavity). In the mono-

disperse case (shown in Figure 6.14(a)) there is no streamline closing the cavity entrance and therefore some stream-traces even enter in the area located at  $9 < X/h < 9.4$ . Naturally, this behaviour can be observed only in the mid-span plane. Three-dimensional effects ensure the mass conservation.

Although it appears to be slightly flatter, the main recirculation bubble downstream the inhibitor is less affected by the droplet phase. As it can be seen in Figure 6.15(a), the droplets are not able to follow the motion of the flow (due to their long characteristic time) and therefore only a few of them enter in the main recirculation bubble. Therefore, they are not able to modify the flow properties at about  $Y/h < 1$ . However, a large quantity of droplets enter in the cavity (visible in Figure 6.15(a)) and due to their momentum they act on the air-phase. That is why the cavity becomes *open* and the streamlines of the gas-phase enter in the cavity in the mid-span plane of the domain.

The magnitude of the air velocity (see Figure 6.10(b) and 6.14(b)) is slightly weaker in the free stream above the main recirculation. This shows that the droplets react to the flow but not as quickly as a phase composed of pure tracers (representing  $St \ll 1$ ). This delay induces a decrease of the air velocity.

The distribution of the longitudinal velocity component fluctuations (see Figure 6.10(c) and 6.14(c)) shows lower values in the free stream, but increased values inside the cavity, at the location associated with the intrusion of droplets. The transversal velocity fluctuations (see Figure 6.10(d) and 6.14(d)) show slightly higher values at the entrance of the cavity.

Based on these results, one may conclude that  $d_p = 100 \mu\text{m}$  mono-disperse droplets at this volumetric flow-rate affect significantly the air flow and should lead to a significant water accumulation in the cavity. However, with the help of the mass counter user subroutine, only 0.5% of the injected droplet mass is effectively accumulating in the cavity.

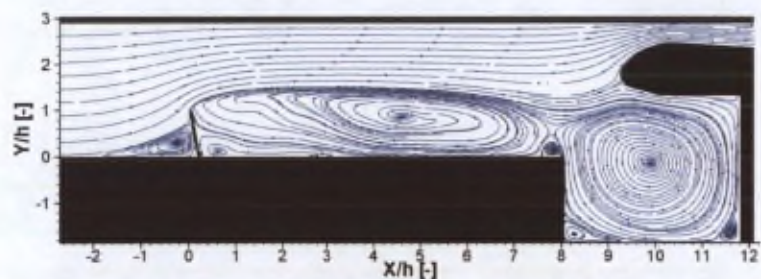
### 6.3.2 The effect of the poly-disperse spray

The result associated with a poly-disperse droplet distribution is presented in Figure 6.16.

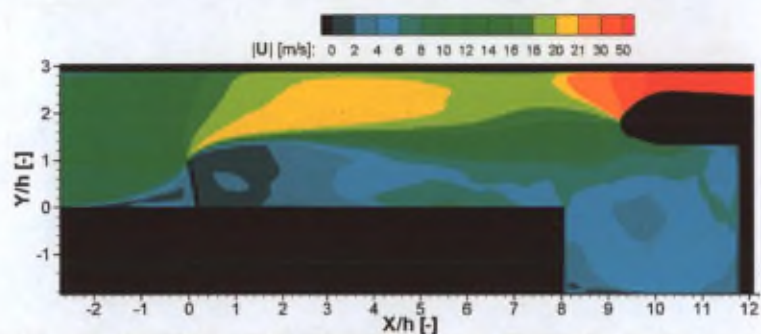
According to the stream-traces of the mean flow in the mid-span plane of the domain (see Figure 6.16(a)) no streamline enters in the cavity anymore. Although, the overall water flow-rate is the same as in the mono-disperse configuration, due to the wide range of droplet sizes and the large number of smaller droplets (which have a considerably lower momentum and shorter relaxation time), the droplets seem to be unable to modify the pattern of the mean flow at the cavity entrance.

The global arrangement of streamlines is also very similar to a flow free of droplets (see also Figure 6.10(a)). Nevertheless, some small differences have to be noticed. First of all, the downstream half of the main recirculation bubble ( $4 < X/h < 8$ ) appears clearly to be flatter in the poly-disperse configuration. Furthermore, the secondary circulating structure at the downstream corner of the inhibitor ( $0.2 < X/h < 1.5$ ) looks to be smaller and more pronounced as well. These indicate that more droplets enter in the main recirculation zone, which is confirmed also by an instantaneous snapshot of the droplets distribution (shown in Figure 6.15(b)). In this plot a wide range of Stokes number may be found from  $St < 1$  to  $St > 1$ . Although in this distribution the droplets of about  $d_p = 100 \mu\text{m}$  are still included, they represent only a low part of the total amount of droplets.

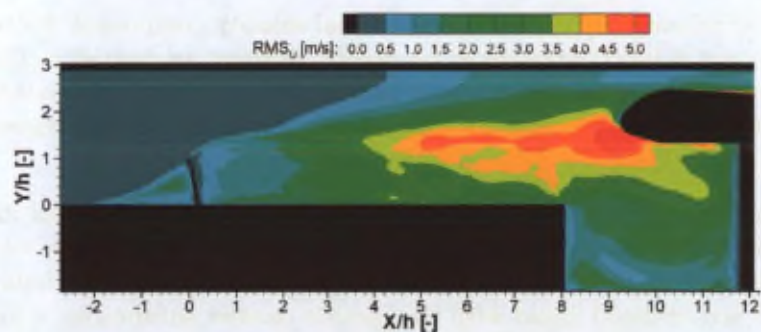
Looking at the overall results, the poly-disperse droplets seem to have a weaker influence on the mean flow than the mono-disperse droplets. This is probably due to the lower volume



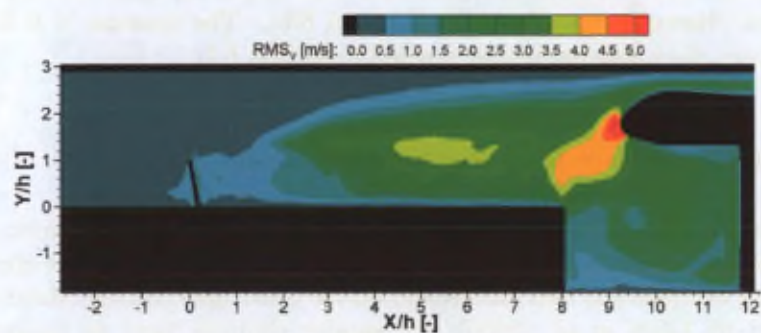
(a) Streamlines of the mean flow field.



(b) Mean velocity magnitude distribution.



(c) Fluctuation of the longitudinal velocity component.



(d) Fluctuation of the transversal velocity component.

FIGURE 6.14 – Results of the time averaged LES simulation in the symmetry plane using mono-disperse droplet size distribution (based on 3 FTs).

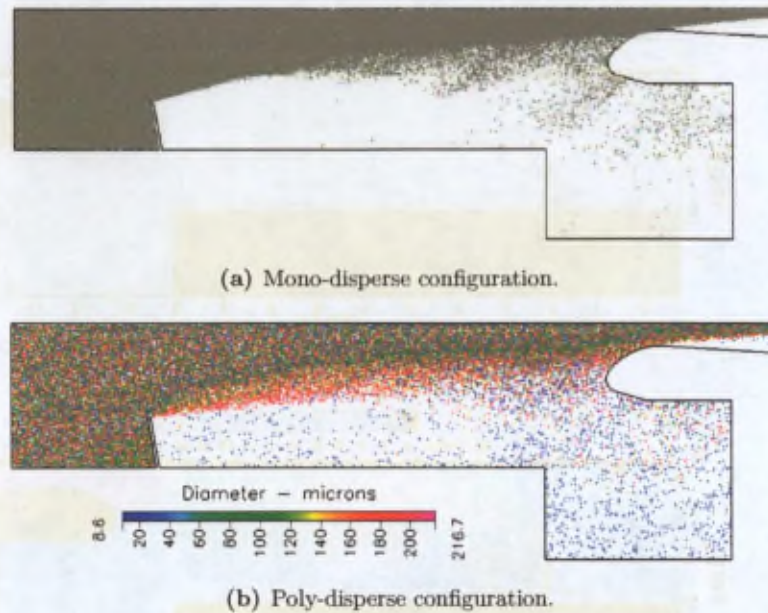


FIGURE 6.15 – *Instantaneous droplet-distributions.*

fraction having an active diameter (i.e. sufficiently large diameter and high mass flow-rate to perturb the air-flow).

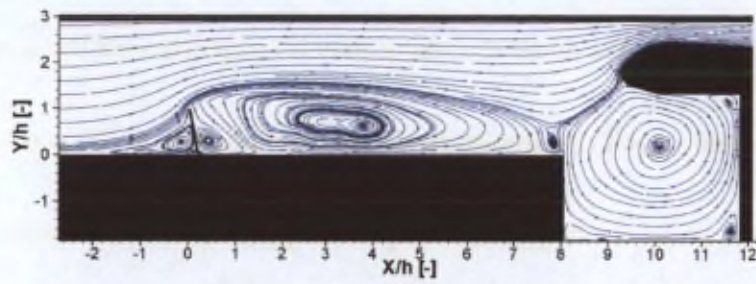
The high-turbulence region of the longitudinal velocity component fluctuation pattern (see Figure 6.10(c) and 6.16(c)) appears to be slightly different compared to the single-phase flow results. However, judging the differences is knowing that the results are not fully converged statistically. Furthermore, the transversal velocity component fluctuations (shown in Figure 6.10(d) and 6.16(d)) exhibit lower peak values in general.

On the one hand, it appears that even if the distribution of droplets induces less changes in the statistical air-phase properties, a larger number of droplets may be carried inside the cavity (see Figure 6.15(b) compared to Figure 6.15(a)). On the other hand, when estimating the amount of accumulated liquid with the particle counter subroutine, a higher rate (0.7%) is observed with the poly-disperse distribution than with the mono-disperse droplets. However, these numerically observed accumulation rates show about an order of magnitude lower values than what was observed experimentally (around 8%). The reasons of this deviation are not investigated here, they will be further studied in section 8.1.

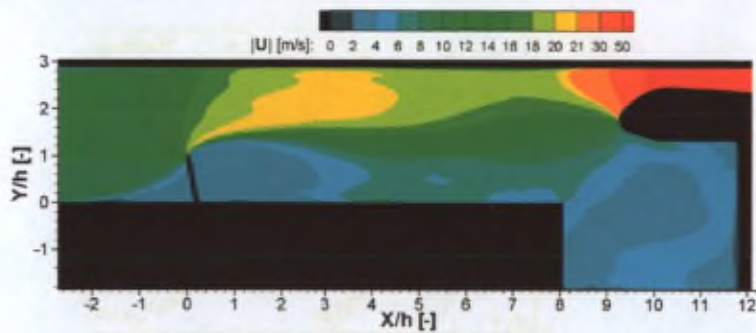
### 6.3.3 Droplet size effect on the accumulation

As it could be seen from the comparison between the simulations with the mono-disperse and poly-disperse droplet-distributions, the droplet size has an important effect on the one hand on the coupling between the two phases and on the other hand on the amount of accumulation. As it is found by Lema et al. (2006), the smaller droplets tend to provide a larger rate of accumulation.

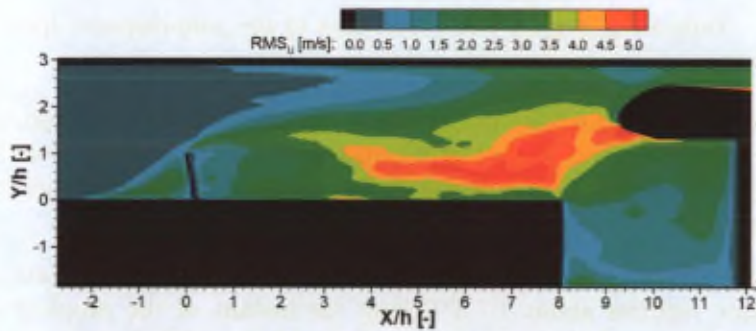
In order to verify this observation, taking it from its final time step, the simulation of Lema et al. (2007) is modified. First of all, the injected liquid mass is set to  $1 \cdot 10^{-15}$  kg/s (quasi zero). The computation is run in this way during 2.9 *flow-throughs* (FTs) in order to evacuate the droplets from the domain. Then, the liquid flow-rate is increased again to the nominal level



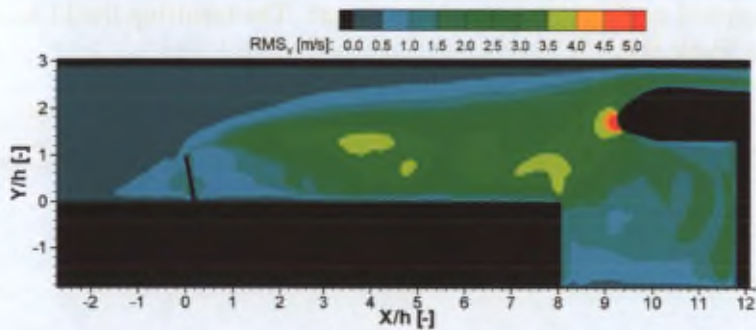
(a) Streamlines of the mean flow field.



(b) Mean velocity magnitude distribution.



(c) Fluctuation of the longitudinal velocity component.



(d) Fluctuation of the transversal velocity component.

FIGURE 6.16 – Results of the time averaged LES simulation in the symmetry plane using poly-disperse droplet size distribution (based on 3 FTs).

and three different simulations representing different droplet size distributions are performed:

- In the first thread the nominal configuration is computed with the nominal droplet size distribution;
- In the second thread the droplet diameters corresponding to the nominal distribution are halved;
- In the last thread the droplet diameters corresponding to the nominal distribution are doubled;

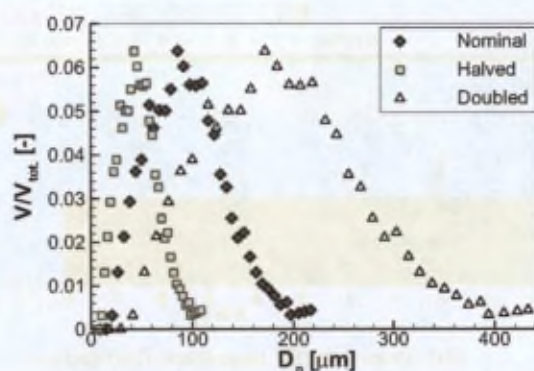


FIGURE 6.17 – Volumetric droplet size repartition of the poly-disperse spray during the droplet size assessment.

The volumetric repartition of the resulting distributions is indicated in Figure 6.17. By running these simulations, at first they fill up the numerical domain with liquid droplets and consequently provide liquid accumulation in the cavity, which is monitored with the dedicated user subroutine.

As the accumulation rate re-establishes, a quasi linear deposition rate can be observed in time. This state requires about 1.7 FT from the instant of the droplets injection. Starting from this instant the simulations are run for about 1.3 more FT during which the accumulation in the cavity is recorded. Finally, the average droplet entrapment rate is determined with a linear fitting applied on this last *accumulation* part. The resulting liquid accumulation rates are summarized in Table 6.1.

Table 6.1 – Droplet size effect on the accumulation rate.

Simulation	Accumulation rate [%]
with <i>nominal</i> droplet size distribution	0.55
with <i>halved</i> droplet size distribution	2.18
with <i>doubled</i> droplet size distribution	1.47

As it can be seen, the entrapment rate in the nominal configuration is slightly underestimated with respect to Lema et al. (2007) (0.55% vs. 0.7%). This is probably due to the relatively short (1.3 FT) integration time of the accumulation phenomenon.

With respect to the nominal configuration about 4-times higher accumulation rate is observed in the presence of the *halved* droplet size distribution. Indeed, an increasing tendency is

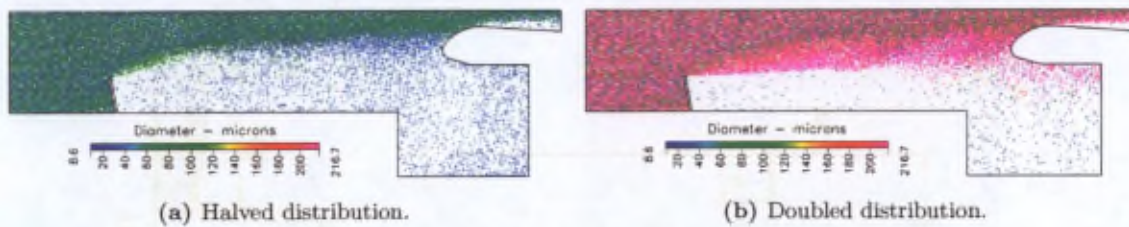


FIGURE 6.18 – *Instantaneous spatial droplet distributions.*

expected, because the smaller droplets have a shorter associated characteristic time-scale, which allows them to respond better to the air-phase fluctuations and therefore to be entrained in the recirculation zone and into the cavity. Accordingly, Figure 6.18(a) shows a large number of small droplets in the recirculation zone. Although they are relatively small, they still do not satisfy the  $St \ll 1$  criterion and thus they are not able to follow perfectly the continuous phase. This means that as soon as they approach a wall (e.g. in the cavity), they are likely to hit it and therefore contribute to the accumulation.

Applying the same analogy to the doubled droplet size distribution, one should expect a lower entrapment rate, while the computations show more than 2.6-times higher accumulation. In this case, the entrapment is governed primarily by the larger droplets as only a few amount of small droplets are injected in the domain. To the present large droplets a longer characteristic time should be associated, which means that they are even less sensitive to the surrounding air-phase motion. They are less likely to be affected by the flow acceleration in the vena contracta or by the generated turbulent structures. Therefore, the importance of the momentum of these droplets is superior to the entrainment phenomenon. Accordingly, in Figure 6.18(b) almost no mixing of large droplets can be observed. As a consequence, the liquid entrapment should be lead by the  $OT2NT$  parameter<sup>2</sup> (see its definition in Figure 5.14(b)). If  $OT2NT > 0$ , the large droplets passing just in front of the inhibitor tip might not be deviated sufficiently by the flow field in order to allow them to escape through the nozzle.

Due to the short computational time after the droplets' re-establishment, unfortunately no statistical quantities can be derived from the flow properties.

## 6.4 Two-phase flow PIV experiments

With the help of the two-phase PIV technique described in chapter 4, the flow field in the presence of the droplets is studied as well. From the gathered database the statistical quantities are shown in the present section.

### 6.4.1 The experimental configuration

The present experimental campaign is the first with the UV two-phase PIV technique. As it can be seen in section 4.4, applying this method in the 2D SRM model is rather challenging. Furthermore, the flow to be investigated is rather complex as well. Therefore, no parametric study is carried out. Thus, the attention is turned towards the nominal geometrical configuration

<sup>2</sup>The *Obstacle Tip to Nozzle Tip distance* shows how much a droplet passing at the inhibitor tip needs to travel transversally (along the  $Y/h$  axis) to be able to escape through the nozzle and to avoid being entrapped in the cavity.

(see Figure 6.19, where  $h = 33.5$  mm).

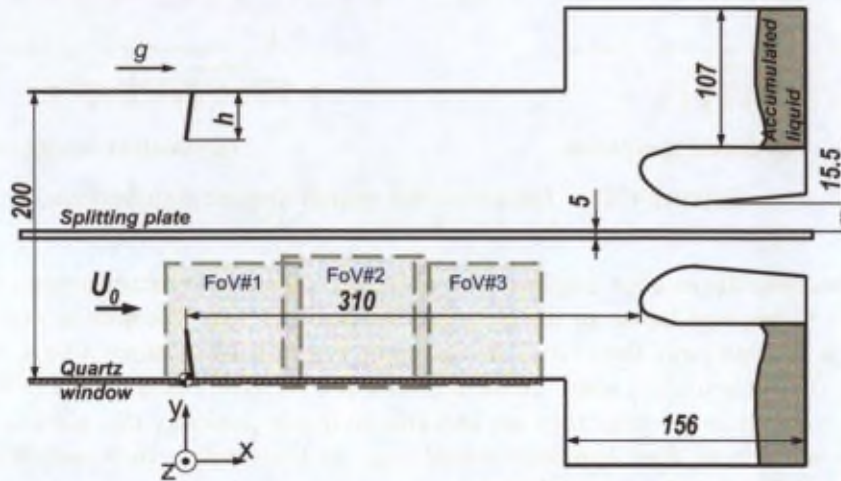


FIGURE 6.19 – The geometry of the test section and the FoVs during the two-phase PIV experiments.

Altogether three FoVs are defined (as indicated in Figure 6.19). At first, the region of the inhibitor is to be investigated. The third FoV is defined to be as close as possible to the cavity entrance. Since experiment can only be performed through the quartz window, even FoV#3 cannot reach up-to the corner of the cavity entrance. Finally, the second FoV is chosen to overlap with #1 and #3 covering the space between them.

As mentioned in section 4.4.1, the flow velocity has to be  $U_0 = 2$  m/s. Thus, the Reynolds number based on  $h$  and  $U_0$  becomes  $Re_h = 5025$ .

The separation time ( $\Delta t$ ) during the image recording is adjusted to have approximately a maximum of 5 to 7 pixels displacement in single-phase flow configuration. The actual separation times are indicated in Table 6.2 together with the approximate magnification of the PIV cameras.

Table 6.2 – Two-phase PIV acquisition parameters.

FoV	$\Delta t$ [ $\mu$ s]	$M_{PIV}$ [mm/pixel]
FoV#1	330	0.184
FoV#2	330	0.192
FoV#3	330	0.187

The illuminating YAG laser is operating at 9.22 Hz. However, in order to ensure a simultaneous image recording, the two cameras acquire an image pair only at every third laser double pulse. This results in an acquisition rate of about 3.07 Hz. Among the settings of the cameras  $2 \times 2$  pixels<sup>2</sup> binning is selected in agreement with the preliminary technique assessment (section 4.3.2). Therefore, both of the image pairs have  $640 \times 432$  pixels<sup>2</sup> resolution.

The droplet-phase is generated by a Lechler 156.000.17.13 spray device, which is supplied by  $p_{liq.} = 0.8$  bar and  $p_{air} = 1.25$  bar. With these parameters it provides a flow-rate of about  $\dot{Q}_{Vd} = 0.133$  l/min. The generated droplet size distribution is characterized by PDPA measurements using water. The actual distribution is shown in Figure 6.20, where the mean Sauter droplet diameter is  $d_{32} = 106.2 \mu\text{m}$ .<sup>3</sup>

<sup>3</sup>During the two-phase PIV experiments lower reference velocity has to be used than in the nominal configu-

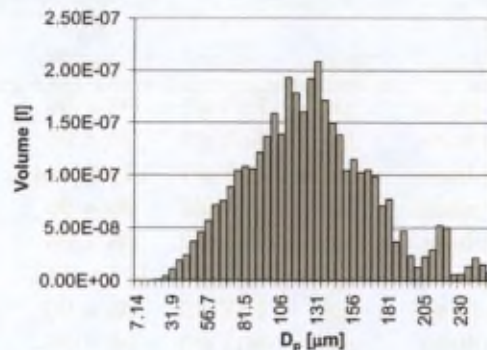


FIGURE 6.20 – Droplet size distribution of the spray device.

The experiments are performed according to the procedure described in section 4.4.1. This means that at each FoV, when all the series of two-phase acquisitions are finished, 1500 to 1800 image pairs are recorded in single-phase flow condition, while everything is operating in the same way as during the two-phase flow condition (except the liquid supply of the spray is closed). This can give a reference single-phase flow field.

Before the PIV processing the local background is subtracted from all the images using the method described in section 4.4.2.

As one can see in Figure 4.33(b), the droplet images contain a rather high droplet concentration, which is comparable to the current seeding density (see Figure 4.33(a)), while the droplets have typically higher intensity and larger size in the images. Therefore, the droplet images seem to be even better candidates for PIV processing than the tracers. Although they represent poly-disperse size distribution, the current goal is to obtain statistical information from the flow (investigate the mean flow field). Therefore, all the recordings - including the droplet images - are processed by the PIV algorithm, *WiDIM*.

During the analysis, the processing parameters are adapted to the current image conditions. The actually applied initial window size combinations, number of iterations and the final window overlapping factors are summarized in Table 6.3.

Once the instantaneous flow fields are available, a statistical analysis is performed. At first, the droplet-phase data are taken, where in all the series of every FoV the first image, where the spray is already established is determined. Starting from this instant altogether 100 flow fields are extracted from each series, which result 1200, 1700 and 1200 instantaneous droplet-phase fields in the three FoVs respectively. The same time instants are extracted from the simultaneously acquired tracer-phase fields (two-phase flow condition). Finally, from the single-phase flow recordings the same total number of instantaneous fields are taken. All these data are analysed statistically in order to obtain the mean flow field and turbulence information.

---

ration of the LeDaR investigation and in the numerical simulations. As explained in section 2.3.2.2, to limit the modification of the characteristic non-dimensional parameters ( $St$ ,  $\alpha_p$ ), a different spray device has to be chosen for the present measurements.

Table 6.3 - Two-phase PIV processing parameters.

Flow condition	Phase	FoV	$W_{s0}$ [pixel <sup>2</sup> ]	$W_{ref}$ [-]	$W_{ol}$ [%]
Single-phase	air	FoV#1	96 × 96	2	75
Two-phase	air	FoV#1	96 × 96	2	75
Two-phase	droplet	FoV#1	144 × 144	2	75
Single-phase	air	FoV#2	96 × 96	2	75
Two-phase	air	FoV#2	96 × 96	2	75
Two-phase	droplet	FoV#2	144 × 144	2	75
Single-phase	air	FoV#3	96 × 96	2	75
Two-phase	air	FoV#3	96 × 96	2	75
Two-phase	droplet	FoV#3	144 × 144	2	75

### 6.4.2 The resulting statistical flow fields

In the current section the statistical flow fields are shown and analysed. Here, no comparison of the two-phase flow data is given with respect to earlier single-phase flow measurements, because the eventual observations might not be relevant due to the different reference velocity. However, the two-phase flow information can be compared to the new available complementary single-phase flow data. Furthermore, within the two-phase flow case at each FoV simultaneous air-phase and droplet-phase fields are obtained. Therefore, in the following figures, when plotting any of the statistical quantities, at first the single-phase flow condition is shown, which is followed by the gas-phase of the two-phase flow configuration and finally the droplet-phase information can be seen.

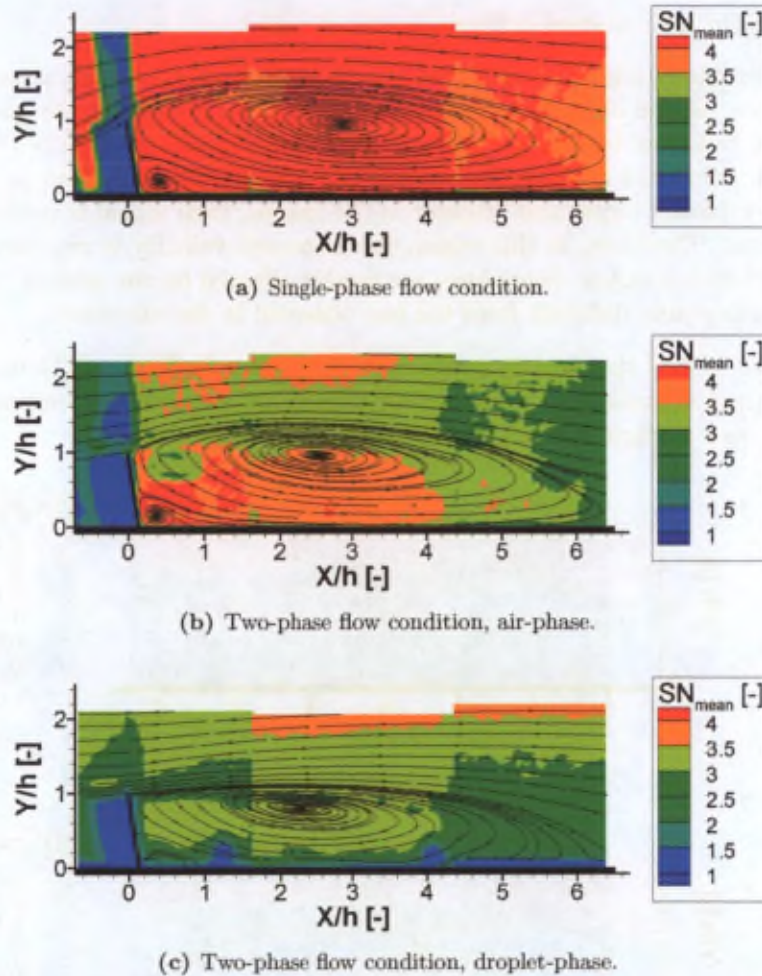
First of all, the distribution of the measurement quality is shown in Figure 6.21 together with the stream-traces of the flow. Later, when drawing any conclusion, the regions where  $SN_{mean} < 2$  should be handled with great care, as the observed information might have no physical content due to the low measurement quality.

Focusing on the flow fields represented by the stream-traces of the air-phase, a similar recirculation region is revealed downstream the inhibitor, as previously e.g. in section 6.1 or 6.3.2. A main circulating structure is created by the separating flow, which extends from the inhibitor tip. Unfortunately, its downstream end falls outside the investigatable area, therefore it is not known whether the flow reattaches before the cavity entrance. By analysing the captured part of the recirculation, the main bubble appears to be flatter in the two-phase flow case (see Figure 6.21(b)) than in the single-phase flow case (shown in Figure 6.21(a)). As it was already discussed in section 6.3.2, with the poly-disperse spray distribution, the primary effect of the droplets on the mean flow field is also the flatter main recirculation bubble, which is pronounced primarily in the downstream half of it (see Figure 6.10(a) and 6.16(a)).

Furthermore, the centre of the main recirculation bubble shifts about  $0.3h$  upstream in the two-phase flow condition (Figure 6.21(b)) with respect to the single-phase flow case (Figure 6.21(a)). As the main bubble is compressed, the secondary counter-rotating mean structure at the downstream corner of the inhibitor becomes smaller as well.

As it was mentioned above, the droplet-phase image pairs are analysed by WiDIM as well. This result is shown in Figure 6.21(c). However, when inspecting the indicated flow field, the plot should be divided into two regions: the free stream and the recirculation region.

As it can be seen in the plot, the droplets (especially the larger ones) are not able to follow

FIGURE 6.21 – *Measurement quality and mean flow field.*

the curvature of the airflow as it is accelerating in the vena contracta. From the tip of the inhibitor, the droplets seem to be unaffected by the flow as their trajectory remains parallel to the sidewall. On the other hand, since the liquid volume fraction is sufficiently high, the droplets are acting on the air-phase by making the main mean structure flatter.

Before analysing the droplet-phase in the recirculation zone, one should investigate their behaviour upstream the inhibitor. The droplets are generated by the spray device in the stagnation chamber. Then, they enter in the test section. During this time, they fall probably straight as their motion is dominated by gravity and the uniformly accelerating airflow. As the air approaches the inhibitor, it accelerates rapidly and it creates a mean rotating structure, which extends about  $1h$  upstream the obstacle (see Figure 6.5(a)). However, as the droplets have a large momentum and long characteristic time, they are not able to follow this abrupt change and most of the droplets, which were travelling towards the inhibitor are impinging on it and accumulate. This process means that downstream the inhibitor (at  $Y/h < 1$ ) no large droplet should be present, because they are filtered out by the obstacle.

However, due to the mixing in the shear layer, the smaller droplets might tend to enter in the recirculation region. Their behaviour is more similar to the tracers: they follow better the motion of the flow. Although their concentration is quite low, it seems to be still sufficient to

visualize the main recirculation bubble.

Thus, by summarizing the droplet-phase motion, on the one hand a mean pattern similar to the air-phase can be observed at about  $Y/h < 1$ , which is drawn by the smaller droplets, which are able to follow better the airflow. On the other hand, at  $Y/h > 1$  the whole range of the injected droplet sizes are present, including the larger droplets. Due to the fact that these are appearing typically larger and brighter in the images, their signal is predominant during the cross-correlation. Therefore, in this region the measured velocity is representing primarily the motion of the larger droplets. Since they are weakly effected by the airflow, the velocity field at  $Y/h > 1$  is considerably different from the one observed in the air-phase.

The contour plot of the velocity magnitudes are shown in Figure 6.22. In the regions where the measurements are reliable, only slight differences can be observed between the single-phase and the two-phase configurations.

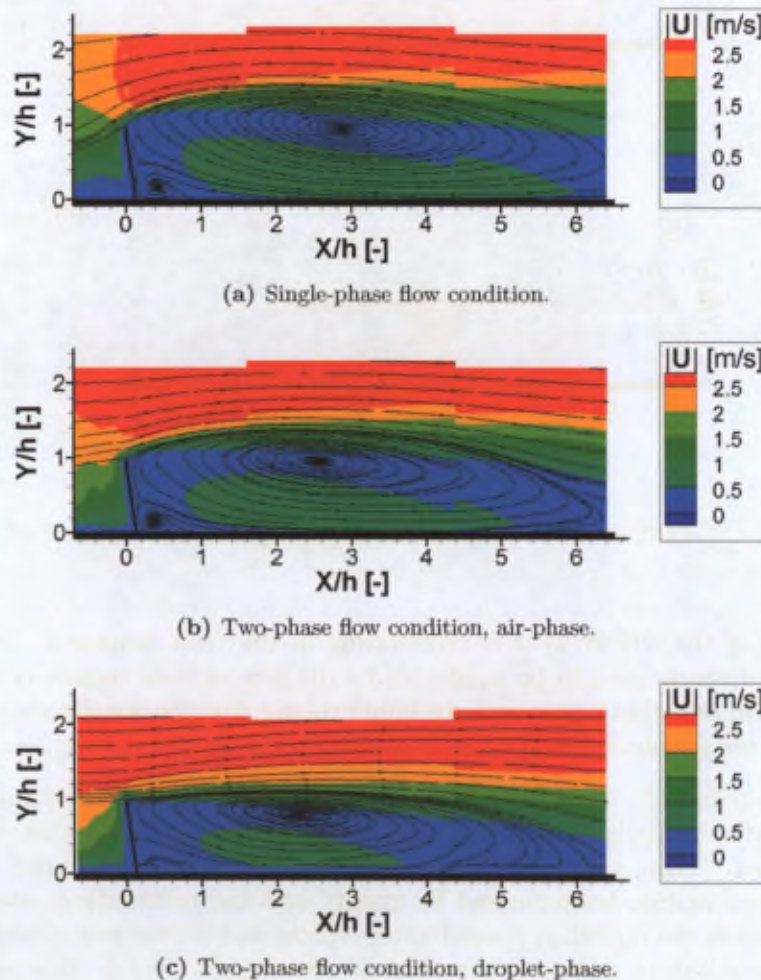


FIGURE 6.22 – Velocity magnitude distribution.

In the figures, the edges of the FoVs are visualized by the discontinuity of the contour plot. It is the most pronounced between FoV#2 and #3. In FoV#3 the air velocity appears to be substantially higher than in FoV#2. The differences originate from the fact that the nominal flow velocity is rather low ( $U_0 = 2$  m/s), which is difficult to measure accurately with the Validyne (described in section 2.4). In order to quantify the velocity mismatch, a  $|U|$  profile

is extracted along  $Y/h = 2$  (in the free stream). The profile is shown in Figure 6.23, where a difference of about 17% is measured at the discontinuity between FoV#2 and #3, and 2% between FoV#1 and #2. Therefore, the reference velocity could be considered to be affected roughly by the same amount.

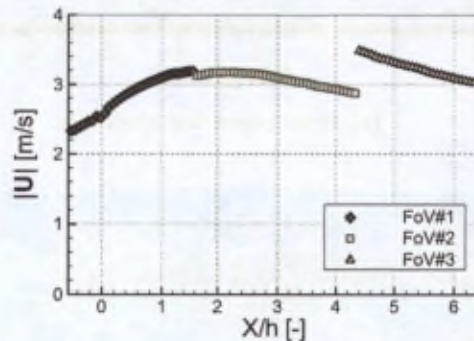


FIGURE 6.23 – Velocity magnitude profile ( $|U|$ ) at  $Y/h = 2$ .

In the followings, the turbulence intensity (TI) of the velocity components are determined.  $TI_U$  and  $TI_V$  are obtained by normalizing the RMS of the corresponding velocity component by the free stream velocity,  $U_0$ .

Concerning the transversal fluctuations of the continuous phase, a slight turbulence decay (around 20% smaller values) can be observed in the two-phase flow configuration with respect to the single-phase flow results (see Figure 6.24(a) and 6.24(b)).

However, looking at Figure 6.24(c), in the droplet-phase motion considerably lower fluctuation can be seen compared to the  $TI_V$  levels of the corresponding air motion (around 50% smaller). These observations seem again to be in good agreement with the longer characteristic time of the droplets, which are not able to follow the large-frequency changes of the air-phase and therefore, they might damp the fluctuations of the air as well.

Furthermore, one should note that the meaning of the droplet-phase fluctuation is not entirely analogous to the carrier-phase fluctuations. Especially below the inhibitor shear layer, where the free stream flow separates and creates a low-velocity recirculation, large droplets travel at considerably higher velocity, as they are unable to adapt rapidly to the low-velocity fluctuations. On the other hand, the smaller droplets may adapt quicker to the local low-speed conditions and to the continuous-phase fluctuations as well. Therefore, in the droplet-phase images different velocity information may be present at the same location depending on the actual droplet diameter, which may also increase the local velocity fluctuation during the statistical analysis.

The patterns of the fluctuations of the longitudinal velocity component ( $TI_U$ ) seem to be even more similar in general between Figures 6.25(a) and 6.25(b). However, in the shear layer region (between  $0 < X/h < 2.5$ ) the turbulence appears to be slightly higher and more spread in the two-phase flow condition. This might be explained by the fact that while the air-phase is accelerating in the vena contracta, the droplets are not able to adapt the flow change. Since the droplets are randomly distributed in the domain, when the local droplet-concentration is higher, they may slow down the acceleration of the air; when the local droplet concentration is lower, the air could be able to accelerate freely. Finally, at any point around and in the shear layer, due to the temporal variation of the droplet concentration, lower and higher air velocities are expected, which obviously increase the  $TI$  of the longitudinal component.

Unlike to the transversal turbulence intensity, the longitudinal velocity fluctuation of the

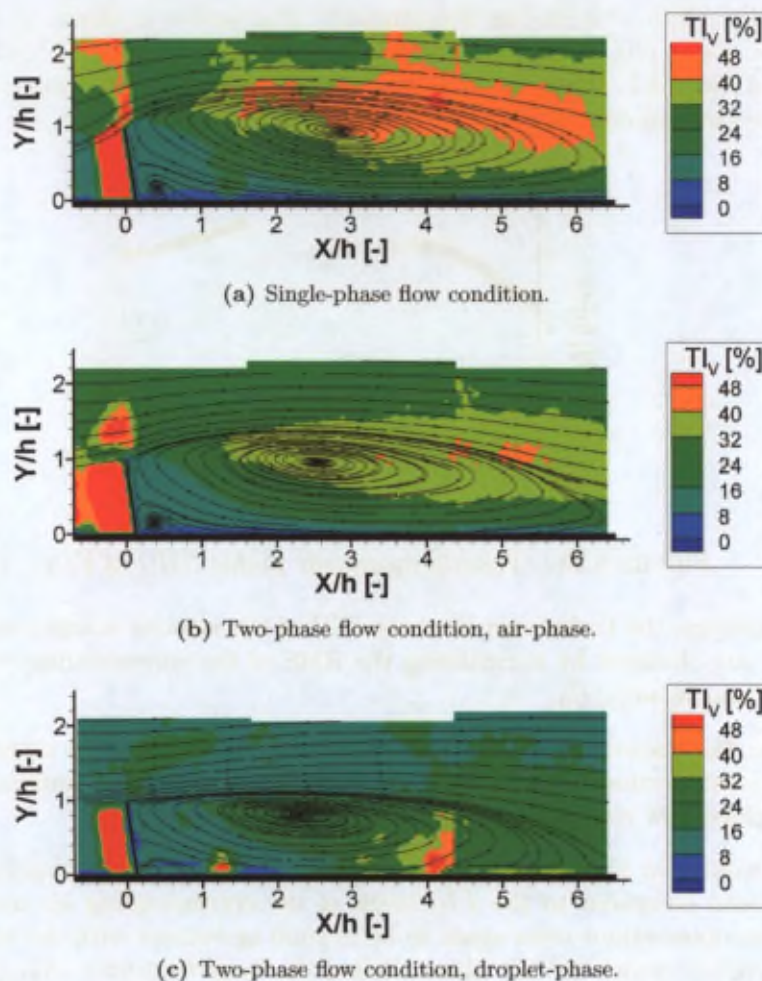


FIGURE 6.24 – Transversal velocity component fluctuation.

droplets shows similar levels (see Figure 6.25(c)) as that of the continuous-phase. However, although the levels are similar, the pattern is still differing from the air-phase. Here, the high-fluctuation area is following approximately  $Y/h = 1$ , instead of the curvature of the vena contracta. This pattern could show the mixing region, where the smaller droplets could start entering the recirculation region.

### 6.4.3 The droplet-phase distribution

In order to separate the motion of droplets of various sizes, the acquisitions are further analysed. A droplet image detection algorithm is developed based on the one explained in section 4.2.1.2, which identifies the location and the diameter of particle images using wavelet analysis. Then, the droplet image diameters are assumed to be proportional to the real diameter. Considering droplets ranging from some tens of  $\mu\text{m}$  to a few hundreds  $\mu\text{m}$ , during the image formation the Mie scattering law is gradually overtaken by the laws of geometrical optics. In this latter domain, the larger an object is, the larger its image becomes. In addition, the droplet images are acquired from the fluorescent light emitted by the droplets. Thus, by assuming a constant illumination energy and uniform fluorescent dye concentration, the intensity of the fluorescent light is proportional to the volume of the droplets (therefore,  $\sim D_p^3$ ). Due to the

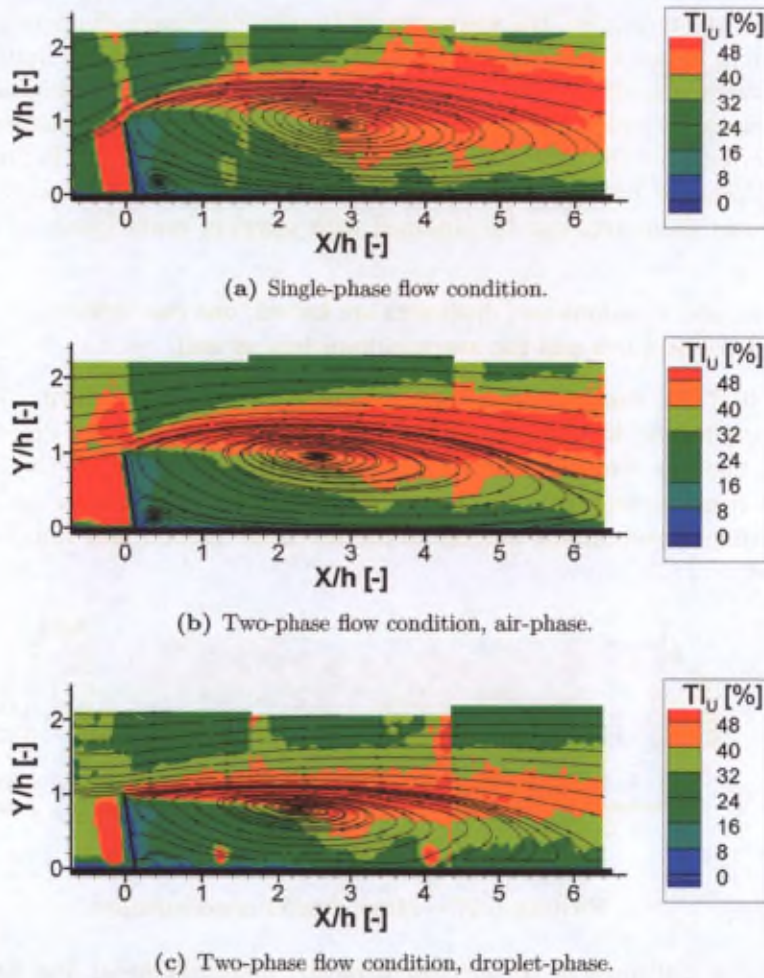
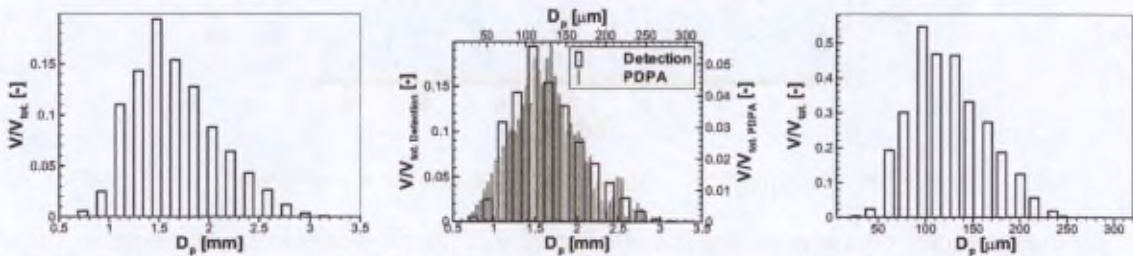


FIGURE 6.25 – Longitudinal velocity component fluctuation.

fact that the wind-tunnel walls are wet, a halo is appearing around each droplet image, which makes the droplets look even larger in diameter (see e.g. Figure 4.33(b)). The intensity of the halo depends on the intensity of the light source: the droplet. Thus, if a larger droplet image is detected, with a high probability it should represent a droplet, which is of the larger kind physically.



(a) The arbitrary diameter distribution. (b) Relating the arbitrary distribution to the physical quantities. (c) The resulting physical droplet diameters.

FIGURE 6.26 – Determining the physical diameters of the detected droplets (using the data of  $FoV\#2$ ).

Hence, after the detection, the histogram of the droplet image diameters is plotted. An example is shown in Figure 6.26(a). Although, here the dimension of  $D_p$  is indicated to be [mm], it is still an arbitrary magnitude; the [pixel] diameter value is simply multiplied by the magnification of the camera. In order to determine the physical quantity, a one-dimensional wavelet-like algorithm is looking for the best match (the superposition is shown in Figure 6.26(b)) between the arbitrary diameter histogram and the one obtained from PDPA experiments (Figure 6.20). Thus, the droplet diameters can be obtained with physical units ( $\mu\text{m}$ ), as it is shown in Figure 6.26(c).

Once the droplet locations and diameters are known, one can investigate the spatial concentration map of the droplets and the average diameters as well.

In Figure 6.27 the mean droplet concentration distribution is shown. As it is expected, in the recirculation region downstream the inhibitor about 4-times lower droplet concentration is found than in the free stream flow. As it is explained in section 6.3.3 the inhibitor is filtering out the larger droplets and in the recirculation region typically smaller droplets can be found, which are capable of responding quicker to the air-phase motion and thus being carried by the flow structures.

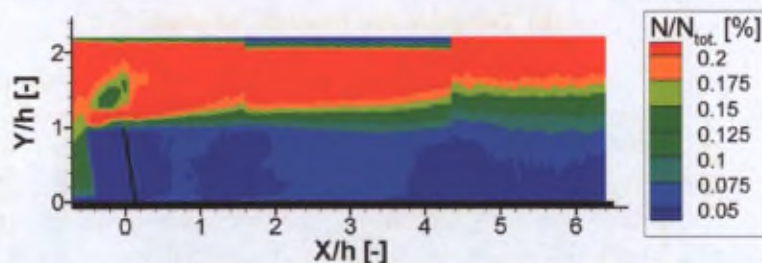


FIGURE 6.27 – Mean droplet concentration.

This theory is confirmed by the arithmetic mean droplet diameter distribution of the current experiments as well (see Figure 6.28). In the recirculation region a considerably lower mean droplet diameter is found than in the free stream. Furthermore, as the smaller particles are entering in the recirculation zone, in the wake of the shear layer the mean droplet diameter increases and therefore this region may exhibit even slightly larger average sizes than the free stream region.

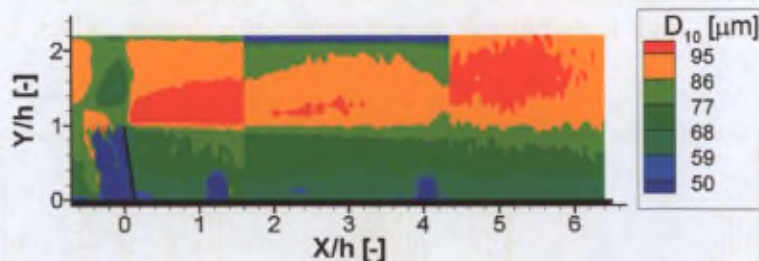


FIGURE 6.28 – Mean droplet diameter distribution.

Furthermore, one may notice that in Figure 6.27 in the zones corresponding to the three FoVs, the centre region always suggests a slightly higher local droplet concentration. However, this should not be considered to be physical. The phenomenon should be the consequence of the non-uniform laser-sheet thickness. During the laser-sheet generation the laser-beam is stretched to form a sheet. Therefore, the centre region of the laser-sheet is always thicker than the extremities and thus in the centre more droplets are illuminated.

Looking at the zone corresponding to FoV#3 in Figure 6.27, one can see that the droplets seem to be pushed even closer to the splitting plate than in FoV#2. Considering the fact that in this zone the reference velocity is higher than in the preceding zones (as it is described earlier in section 6.4.2), this observation is probably physical.

Finally, the average droplet diameter in the region of FoV#2 appears to be about 10% lower than in the two neighbouring regions. The mismatch is certainly not caused by the flow, but the source is not yet identified. In any case, the figure still represents well the tendencies of the droplet diameter distribution.

#### 6.4.4 About the mean relative motion between the two phases

From the previous sections, it is clear that noticing the differences between the mean air-phase motion and the mean droplet-phase motion are not always obvious. In order to be able to highlight them better, the above-described two-phase flow plots are interpolated to a common rectangular grid (containing  $150 \times 50$  elements) and all the droplet-phase quantities are subtracted from the air-phase quantities. These new variables are indicated by an "a-d"<sup>4</sup> index.

Concerning the mean velocity differences between the continuous-phase and the droplets, on the one hand the transversal component (see Figure 6.29(b)) shows a low-amplitude deviation, which is caused mainly by the lack of vena contracta in the droplet-phase mean flow field. On the other hand, the pattern of the longitudinal velocity component difference (see Figure 6.29(a)) visualizes clearly that in the region where the mixing of the droplets should take place, the air-phase has a substantially lower velocity, especially close to the tip of the inhibitor (in the top part of the main recirculation bubble). Since the mean longitudinal velocity component difference is more important than the transversal velocity component difference, by subtracting the mean velocity magnitude of the droplet-phase from the air-phase data, the resulting contour plot (see Figure 6.30(b)) resembles Figure 6.29(a).

The stream-traces based on the two mean velocity component differences are shown in Figure 6.30(a) that indicate practically the direction of the mean drag force acting on the droplets, which leads to the mixing of the discrete phase.

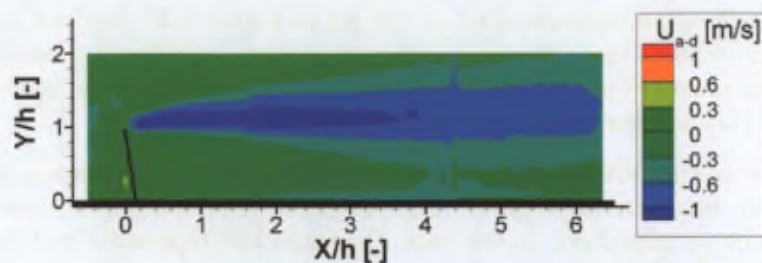
The turbulence intensities are shown in Figure 6.31. Since the transversal velocity component fluctuation of the droplet-phase is uniformly low (see Figure 6.24(c)), the pattern of the fluctuation difference (shown in Figure 6.31(b)) is similar to the pattern of the air-phase transversal fluctuation (see Figure 6.24(b)).

However, the difference of the mean longitudinal velocity component fluctuations (shown in Figure 6.31(a)) visualizes downstream the inhibitor tip both the slightly curved shear layer of the airflow and the high-fluctuation region of the droplet-phase (seen in Figure 6.25(c)) at the level of  $Y/h = 1$ . This latter is visible roughly up-to  $X/h = 4$ . It can be observed that these two areas are rather distinct spatially. Further downstream in the wake of the inhibitor, the longitudinal turbulence intensity component - similarly to the transversal component - shows a superior air-phase turbulence content.

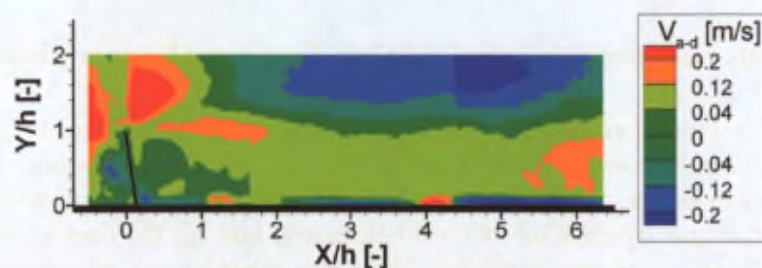
By subtracting the magnitudes of the corresponding fluctuation components of the droplet-phase from the air-phase (indicated in Figure 6.31(c)), all the above-described structures are appearing: the mixing layer of the droplet-phase is visible together with the air-phase shear layer, which is followed by the wake of the inhibitor.

---

<sup>4</sup>"air - droplets"

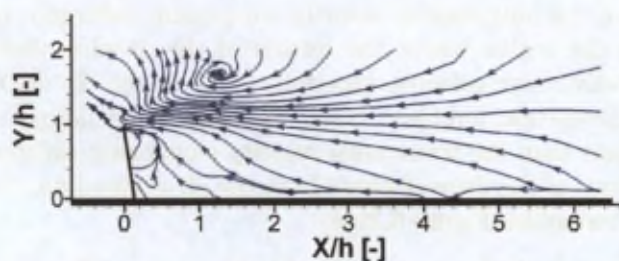


(a) Longitudinal velocity component.

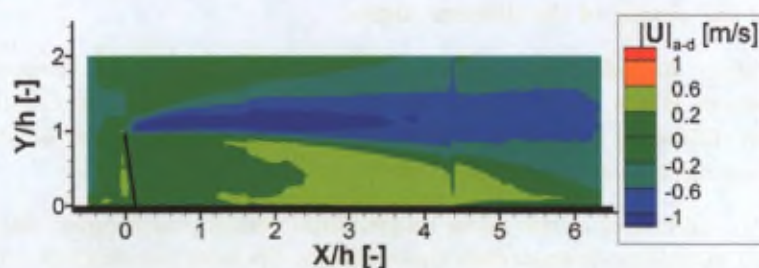


(b) Transversal velocity component.

FIGURE 6.29 – Velocity component differences (air-droplets).



(a) The stream-traces of the "flow-difference".



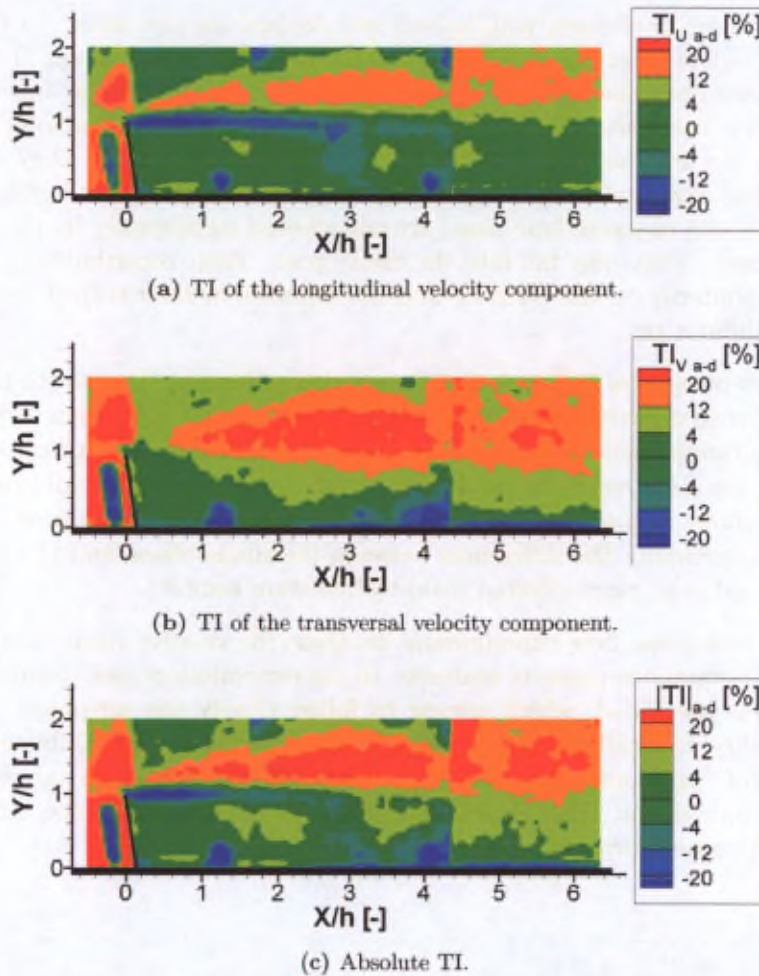
(b) Velocity magnitude.

FIGURE 6.30 – Velocity field differences (air-droplets).

## 6.5 Summary on the statistical flow field properties

To investigate the the flow behaviour, a statistical analysis is carried out using both experimental and numerical data.

The mean flow structures are analysed in details using a high-resolution single-phase flow PIV measurement data. In the absence of radial flow injection, a complex mean recirculation zone is

FIGURE 6.31 – *Turbulence intensity differences (air-droplets).*

present downstream the inhibitor and in the cavity. Furthermore, high velocity fluctuations are observed mainly in the wake of the inhibitor caused probably by the inhibitor shear layer and the shed vortices.

Using the experimental database single-phase flow simulations (performed by Lema et al. (2007)) are validated. A good agreement is found in terms of the properties of the mean flow structures. The inlet turbulence definition could be further improved, but due to the intrusive inhibitor the velocity fluctuation content of the simulations are matching reasonably well to the experimental pattern.

In two-phase flow configuration two simulations are performed by Lema et al. (2007). One with mono-dispersed droplets and one with poly-dispersed simulation modelling the experimental configuration used during the LeDaR experiments (chapter 5). Besides analysing the statistical flow quantities, the liquid accumulation inside the cavity is monitored as well. In the mono-dispersed configuration the mean air-phase structures appear to be highly modified, while the accumulation rate remains rather low. In contrary, the poly-dispersed droplets affect less the mean flow field, but result in a higher accumulation rate as a large quantity of smaller droplets are found to be entrapped in the recirculation zone of the cavity.

From these two-phase flow simulations the importance of the droplet size is found. Therefore,

new simulations are performed with halved and doubled droplet sizes. In both cases a higher accumulation rate is observed with respect to the nominal configuration. This database allows to dissociate two phenomena associated to the entrapment process in function of the droplet size. On the one hand, the smaller droplets (representing a short characteristic time) are able to respond to the fluctuations of the continuous-phase. Therefore, they are able to mix in the recirculation zone and be entrapped in the cavity. On the other hand, the large droplets (representing a long characteristic time) are not affected significantly by the airflow. Therefore, due to their inertia they may fall into the cavity pool. Their contribution to the accumulation rate depends primarily on the *OT2NT* and the direction of their trajectory, when they pass in front of the inhibitor tip.

Finally, two-phase flow PIV experiments are also performed. Due to the measurement conditions, the reference velocity had to be decreased (from 10 to 2 m/s) with respect to the nominal LeDaR configuration (and thus the CFD cases). Furthermore, the optical access allows to investigate only the main recirculation bubble region downstream the inhibitor. Nevertheless, the droplet-phase shows similar modification on the mean flow field than the numerical simulations. However, experimentally the differences between the single-phase and the two-phase cases are more pronounced (e.g. more affected main recirculation bubble).

Using the two-phase flow experimental database the relative mean motion of the droplet-phase and the continuous-phase is analysed. In the recirculation zone downstream the inhibitor smaller droplets are found, which appear to follow closely the air-phase (demonstrating the mixing capability of smaller droplet classes). However, near the inhibitor shear layer where large number of big droplets are located, a large velocity difference (above 1 m/s) is found, which decays very slowly. This shows once again the importance of the large droplets' inertia during the entrapment process.

## Chapter 7

# Instantaneous flow-field investigation

In the previous chapter the flow fields obtained from experiments and numerical investigations are described from statistical point of view (mean flow field, fluctuations, etc.). The goal of the present chapter is to analyse the same database, but focusing on instantaneous phenomena. Primarily, the vortical structures of the flow fields are identified and the evolution of their properties are investigated.

As it could be seen before, the two-phase PIV experiments are performed at a lower reference velocity compared to the nominal LeDaR configuration. Therefore, the discussion of the instantaneous results are divided in function of the velocity as well. The *nominal* section (7.2) includes the single-phase PIV experiment together with the corresponding numerical simulations, which is then followed by the two-phase PIV description (section 7.3).

### 7.1 The methodology of the vortex analysis

To identify the vortices in the available instantaneous flow fields, the VKI wavelet-based vortex detection algorithm is used (for details concerning the method, please refer to section A.2). At first, it is detecting the structures of high vorticity values by convoluting the *enstrophy-field* (square of the vorticity) with different scales of a *2D Marr* (Mexican-hat) *mother wavelet*. To discriminate between shear and rotating motions, the  $\lambda_2$  criterion of Jeong and Hussain (1995) is used. This coefficient is the second eigenvalue of the  $S^2 + \Omega^2$  tensor ( $S$  and  $\Omega$  being the symmetric and the anti-symmetric part of the velocity gradient tensor respectively), which simplifies to equation 7.1 in 2D. As it is shown by Jeong and Hussain (1995),  $\lambda_2$  always has negative value where the rotation is predominant, which is the case in the core of vortices. Therefore, the discrimination between shear and rotation can be made.

$$\lambda_2 = \left(\frac{du}{dx}\right)^2 + \left(\frac{du}{dy} \cdot \frac{dv}{dx}\right) \quad (7.1)$$

As Table 7.1 indicates, the nominal speed single-phase PIV experiments provide 1000 instantaneous samples in all of the FoVs. The single-phase and the poly-dispersed CFD cases provide 698 and 593 snapshots respectively. Finally, from the two-phase PIV experiments 1200 fields are considered both in single-phase flow and two-phase flow configurations.

To be able to identify the coherent structures with the existing tool, at first the various data

Table 7.1 – Database parameters for the vortex detection.

Case	# of samples per FoV	$\Delta$ [mm/cell]
Single-phase PIV	1000	0.6
Single-phase LES	698	2
Poly-disperse LES	593	2
Two-phase PIV		
Single-phase	1200	1.1
Two-phase	1200	1.1

sets (PIV and CFD) should represent a two-dimensional vector-field with equal spatial resolution. Otherwise, the vortex detection algorithm might be biased simply by the resolution difference. The typical field resolutions are also summarized in Table 7.1. From the PIV experiments the obtained vector-fields always have constant resolution of about the indicated value. However, the CFD simulations are performed on a hybrid type grid. Here, the reference  $\Delta = 2$  mm/cell is defined by the typical unstructured cell size in the wake area (in the middle of the domain).

At first, all the images of the 12 PIV FoVs (of the nominal speed investigation) are reprocessed using the parameters of the coarsest field (resulting 0.6 mm vector spacing).

To obtain similar 2D instantaneous fields from the numerical domain, the 3D LES data is transformed. From each stored time-step the hybrid data structure from the mid-span plane is extracted and interpolated to a rectangular isotropic grid, which has the same resolution ( $\Delta = 0.6$  mm/cell) as the corresponding measurements.

As it is mentioned above, the two-phase PIV results are not intended to be compared directly to the nominal speed experimental and CFD data. Therefore, in these fields (both in the single-phase and two-phase flow cases) the original lower resolution is kept ( $\Delta = 1.1$  mm/cell).

For the experimental database at nominal speed, all the 1000 instantaneous samples of all the FoVs are acquired at about 1 Hz. During the two-phase PIV measurements a frequency of about 3 Hz is used. These are sufficiently low frequencies to represent statistically independent flow fields. On the other hand, the single-phase numerical simulations provide 698 instantaneous fields (and the poly-dispersed case provides 593 fields) exported at a frequency of about 1.5 kHz (lower than the one associated with the time step), which does not allow real independence from a statistical point of view. Despite the fact that this limitation would need to be further broadened (by taking samples from longer time series), the methodology should still allow to highlight some aspects of the instantaneous flow nature. The statistical convergence of the numerical data will be further analysed in section 7.2.

In each field, the thresholds of the detection (for details concerning the detection thresholds, see section A.2.2) are set to twice the standard deviation of the vorticity and negative  $\lambda_2$  values respectively. Furthermore, a minimum Oseen likeness of  $Like \geq 0.5$  is defined.<sup>1</sup>

Similarly to the methodology of Özsoy et al. (2005), the analysis is carried out on a coarse  $40 \times 20$  rectangular grid, which is created to cover the whole domain (see Figure 7.1(a)). The number of vortices located in each cell of this grid are counted and their properties (e.g. core diameter, Oseen likeness, circulation, etc.) are averaged. Naturally, in the PIV database the FoVs are trimmed to avoid overlapping. In the vicinity of most of the boundaries the cells

<sup>1</sup>As mentioned in section A.2.2, the likeness coefficient (*Like*) should give an indication about the deformation of the identified vortical structures. It is defined by the ratio between the wavelet coefficient of the detected vortex and the wavelet coefficient of the ideal 2D Oseen vortex of the same size.

partially cover the walls as well. Furthermore, because of the particular shear e.g. at the curved nozzle lip, non-physical vortices centered to the solid surface are systematically detected. To avoid these ambiguities, the first cells next to the boundaries are not considered during the analysis (see the filled cells in Figure 7.1(a)). Furthermore, the cells upstream the inhibitor are also disregarded.

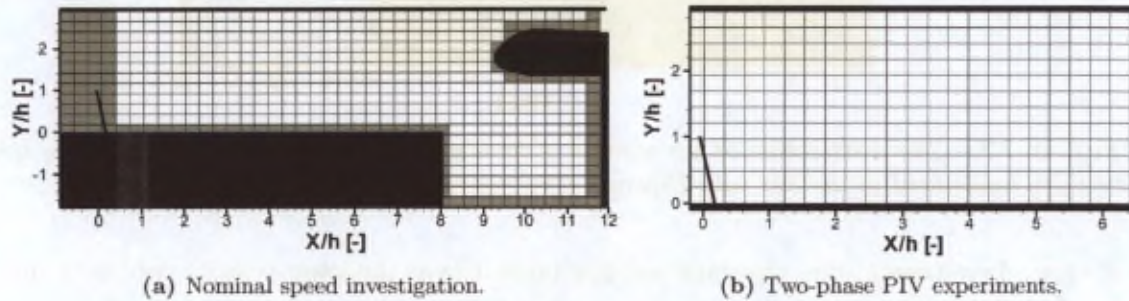


FIGURE 7.1 – *The vortex analysis domain.*

Concerning the two-phase PIV data, a similarly coarse grid is defined, where the vortex properties are locally averaged after detection. However, as the experiments do not cover the whole domain, a smaller grid of  $25 \times 12$  cells is created between the bottom wall and the splitting plate of the test section (see Figure 7.1(b)). Please note that the FoVs of the experiments do not cover the whole section. Therefore, in the presented results a band of constantly zero values will be visible in the vicinity of the splitting plate.

## 7.2 Nominal speed investigation

Within the nominal speed investigation the single-phase flow assessments are discussed separately (section 7.2.1) from the two-phase flow simulation (section 7.2.2). However, to allow an easier comparison, the poly-disperse case plots are already shown together with the single-phase figures.

Before the results on the vortical structures are presented, the statistical convergence of the time resolved numerical simulations is assessed. For this purpose the 593 instantaneous fields corresponding to the mid-span plane of the poly-dispersed case domain are taken into account.<sup>2</sup> The investigation is performed with the algorithm of Theunissen et al. (2007), which is a statistical analysis tool based on *Moving Block Bootstrapping*. It determines the first and second order momentum (i.e. mean and standard deviation) of a signal. The output furthermore contains the errors made in the momentum statistics at a given confidence level. Knowing the error, a rough estimate is given concerning the number of independent samples, which is to be evaluated in the present assessment. Currently the local longitudinal velocity component ( $U$ ) is analysed in each cell of the domain at a strict confidence level of 99%.

As Figure 7.2 shows, in the wake of the inhibitor and in the recirculation region (where the vortices are expected to be located) the number of independent samples of the time averaged data remains mostly below  $NI_U = 100$ , which corresponds to about 17% of the total samples. Values below  $NI_U = 20$  are visible as well in the low velocity region of the recirculation zone. Therefore, the numerical data is considered not being fully converged from the statistical point

<sup>2</sup>These are the same fields used for the vortex detection purposes as well (mentioned in section 7.1).

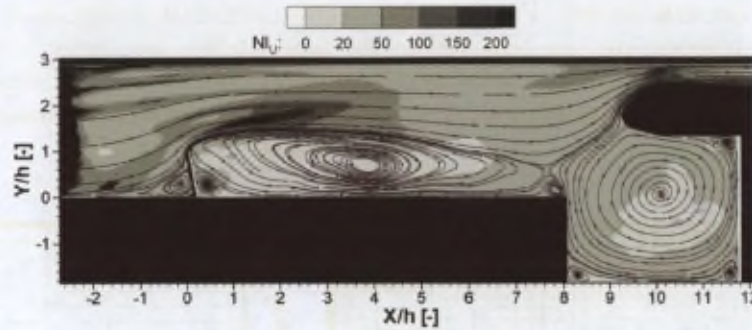


FIGURE 7.2 – The distribution of the number of locally independent samples considering the  $U$  velocity component of the 593 poly-dispersed CFD fields.

of view. As a consequence, the statistical flow properties at the lower velocity regions should be handled with care.

### 7.2.1 Single-phase flow configuration

The goal of the analysis of the vortex content of the CFD data of Lema et al. (2007) is twofold. On the one hand, one can be interested whether the time-resolved numerical simulations, which might be free of experimental artifacts (e.g. light reflections, experimental noise, droplet deposition in two-phase flow configuration, etc.) are able to provide an additional insight to the instantaneous structures. On the other hand, the present investigation verifies whether the vortex contents of the experimental and the numerical database are matching, validating the simulations on instantaneous basis.

Following the detection, first of all the total number of the identified vortices is analysed. As Table 7.2 shows, in the ensemble of the PIV fields about 3.7-times more vortical structures are extracted than in the corresponding simulations. The possible sources of this deviation are assessed a few paragraphs below.

Table 7.2 – Number of detected vortices (at nominal speed).

Case	Total # of vortices	# / sample
Single-phase PIV	199244	199.24
Single-phase LES	38051	54.51
Poly-disperse LES	34100	57.50

To visualize qualitatively which regions exhibit the lower total number of the detected vortices, all the structures of the nominal speed database are plotted in Figure 7.3. Quantitative comparison will be given later on. By comparing Figure 7.3(a) and 7.3(b), a global decrease can be observed without any particular areas that would have suffered more, except the free stream region. As it can be seen, in the PIV database a number of vortices are located above the shear layer of the inhibitor, while no vortices are found in the numerical field. This difference might also be the result of the incorrect inlet turbulence definition of the numerical domain, which is mentioned in section 6.2.2<sup>3</sup>.

Furthermore, in the areas with lower vortex concentration, one can trace clearly the path of

<sup>3</sup>random perturbation with no spatial nor temporal correlation

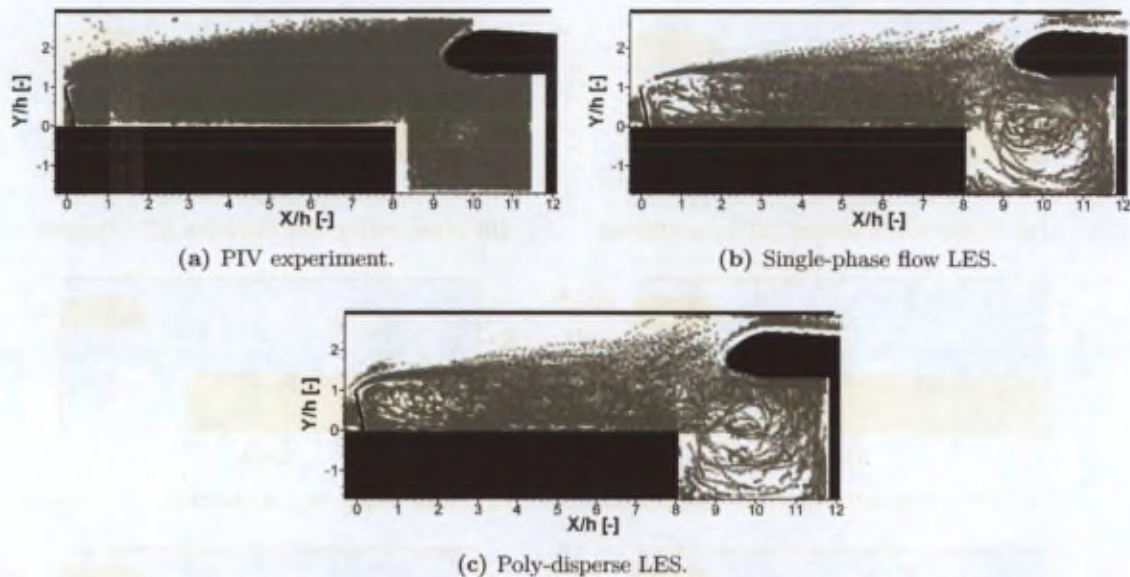


FIGURE 7.3 – Spatial vortex distribution map at the nominal reference velocity.

the vortices in Figure 7.3(b) and 7.3(c), which indicates once again the statistical dependence of the numerical samples, as mentioned above. Thus, especially in these regions (e.g. inside the cavity) the average vortex properties should be handled with care.

According to the vortex concentration maps (Figure 7.4(a) and Figure 7.4(c)) similar distributions can be observed experimentally and numerically. The coherent structures originate from the shear layer attached to the inhibitor tip and then they follow the streamlines of the flow. The region of  $0 < X/h < 2$  can be considered as the zone where the shear layer becomes unstable and creates vortices. At about  $2 < X/h < 4$ , the zone of high vortex concentration is spreading, while the total number of vortices counted crosswise in the region seems to remain constant.

In the zone  $4 < X/h < 8$  the vortices are mainly carried towards the nozzle. Some remain in the free stream flow region, others descend closer to the wall. The latter vortical structures may interact with the recirculating flow and thus may induce vortices at the wall, which are entrained towards the inhibitor. However, before reaching it, they probably dissipate below a detectable level, which can be seen from their decreasing number. At this point one should add that this recirculation is visible in the numerical simulation (in Figure 7.4(c)), while experimentally the vortices appear to dissipate quicker below the limit of detection.

To verify whether the vortices physically dissipate or only reach below a detectable level, the distribution of the Kolmogorov scale is estimated using  $\eta = \nu/RMS_U$ . As Figure 7.5 shows, the Kolmogorov scale ranges between  $\eta = 3$  and  $50 \mu\text{m}$ . In the regions, where vortices are detected, the values are limited to  $\eta < 15 \mu\text{m}$ . As it will be explained below, the core diameter of the smallest detected structures is about  $4 \cdot \Delta_{PIV} = 2.4 \text{ mm}$ . The two orders of magnitude difference between the Kolmogorov scale and the smallest detected vortices suggests that the vortices do not dissipate physically, when the local vortex concentration decreases. Instead, the available data is not able to resolve them.

In the area represented by the streamline that closes the cavity entrance between  $X/h = 8$  and the nozzle tip (around  $X/h = 9$ ,  $Y/h = 1.5$ ; see Figure 6.4), the number of vortices looks to be decreasing, as the free stream flow accelerates for a second time.

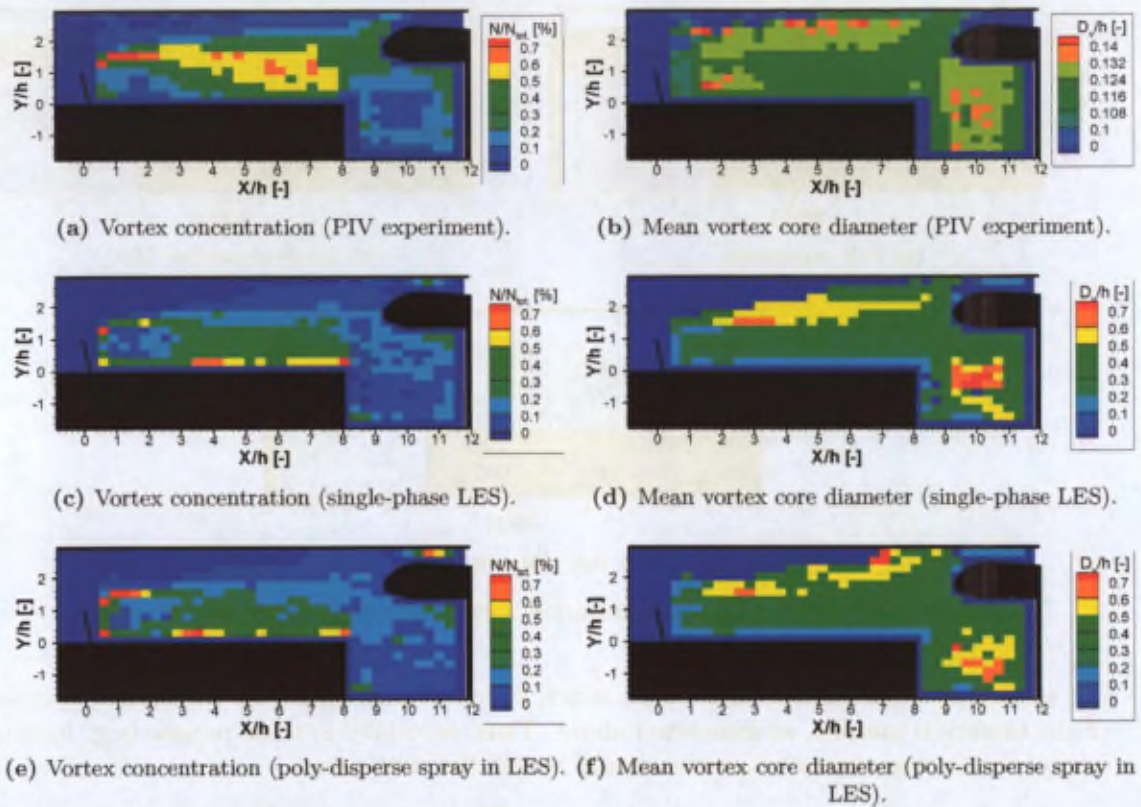


FIGURE 7.4 – Statistical properties of the identified coherent structures (concentration and vortex core diameter).

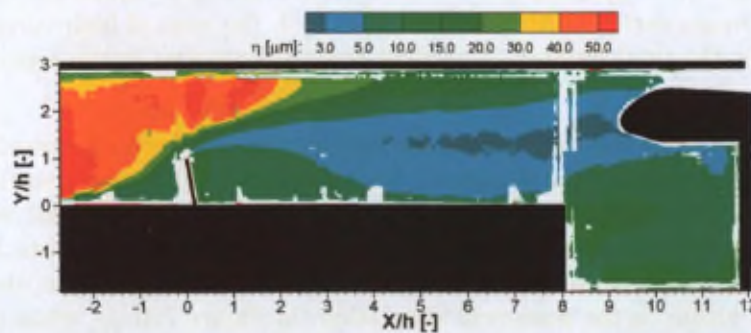


FIGURE 7.5 – The estimated Kolmogorov scale distribution using the nominal speed PIV measurement data.

Topologically, as it may be seen, in Figure 6.5(a) and 6.10(a) the mean stream-traces reveal a stagnation point near the nozzle tip (at about  $X/h = 9.3$ ,  $Y/h = 1.5$ , indicated in Figure 6.4). In an average sense the vortices are convected by following the streamlines, but the flow around this mean stagnation point is highly fluctuating as it is seen by the high levels of RMS values of both velocity components (refer to Figure 6.5(c)-6.5(d) and Figure 6.10(c)-6.10(d)). Reflecting this observation to the instantaneous point of view (Figure 7.4(a)), a large amount of vortices fly over the nozzle through the throat, but a large number of vortices enter in the cavity as well. It is worth noticing that these vortices interact also with the wall vorticity produced at the vicinity of the nozzle lip.

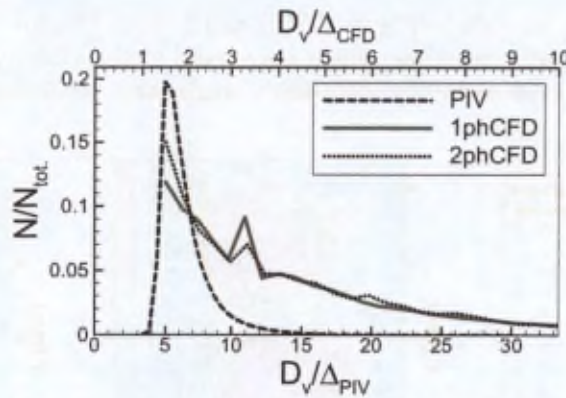


FIGURE 7.6 – Normalized vortex diameter distributions (Nominal speed cases).

However, following the streamlines of the flow, from the corner between the nozzle lip and the cavity bottom, the vortex production seems to weaken in the cavity both in the experimental and numerical data (Figure 7.4(a) and 7.4(c)). The existing structures are simply rotating with the flow and most of them disappear before turning once and reaching again the entrance of the cavity.

Furthermore, disregarding the shear phenomena (e.g. inhibitor shear layer, boundary layers), in an average sense a good agreement is found between the areas of high vortex concentration (Figure 7.4(a)) and the areas of high velocity fluctuation (e.g. Figure 6.5(c)). This confirms that the fluctuations of the main flow are linked with the passage of vortices.

Concerning the mean size of the vortices, a similar pattern can be seen between the experimental case (see Figure 7.4(b)) and the numerical data (shown in Figure 7.4(d)). However, one should notice that the ranges of the core sizes are considerably different.

This might be the result of the considerably lower numerical spatial resolution. While the PIV measurements have a constant high resolution (about  $\Delta_{PIV} = 0.6$  mm), the numerical grid is refined close to the walls<sup>4</sup>, but rather coarse unstructured cells (typically of the order of  $\Delta_{CFD} = 2$  mm, but cells larger than 4 mm also exist) are applied farther away from the boundaries. Furthermore, in case of a vortical structure, which has the size of a cell, the LES simulation relies on the sub-grid model, which is essentially dissipating all the small events. Although the numerical data is interpolated to a rectangular grid that has the same resolution as the experimental grid, the unresolved details of the flow can not be retrieved. As a result, the large quantity of small vortices identified experimentally could not be extracted numerically and thus the range of the mean size distribution shifts towards smaller diameters in the experiments. The core diameter populations normalized by the original grid sizes are indicated in Figure 7.6. The abscissa magnifications represent equal physical dimensions. As it can be seen, the detection algorithm has a cut-off core diameter, as no vortices are obtained with  $D_v < 4\Delta_{PIV}$ . The smallest numerical vortices have a diameter of  $D_v = 5\Delta_{PIV}$ , which corresponds to about  $D_v = 1.5\Delta_{CFD}$ .

To verify, whether the roots of the core diameter mismatch are in the resolution difference, 450 image pairs of FoV#4 of the PIV experiments (Figure 6.2) are processed at lower resolution, with a final vector spacing of  $\Delta_{PIV} = 1.95$  mm. In Figure 7.7(a) a cut-off core diameter of about  $D_v = 7.5$  mm can be observed, which corresponds approximately to 4-times the coarse vector spacing. The resulting core distribution shifts towards considerably higher diameters. The main

<sup>4</sup>The smallest cell size is about  $\Delta_{CFD} = 0.04$  mm.

reason of the shift can be seen in Figure 7.7(b) and 7.7(c). The low resolution velocity field is not able to describe small structures, which may travel in the vicinity of each other. Therefore, the wavelet algorithm systematically identifies a single large structures at these locations.

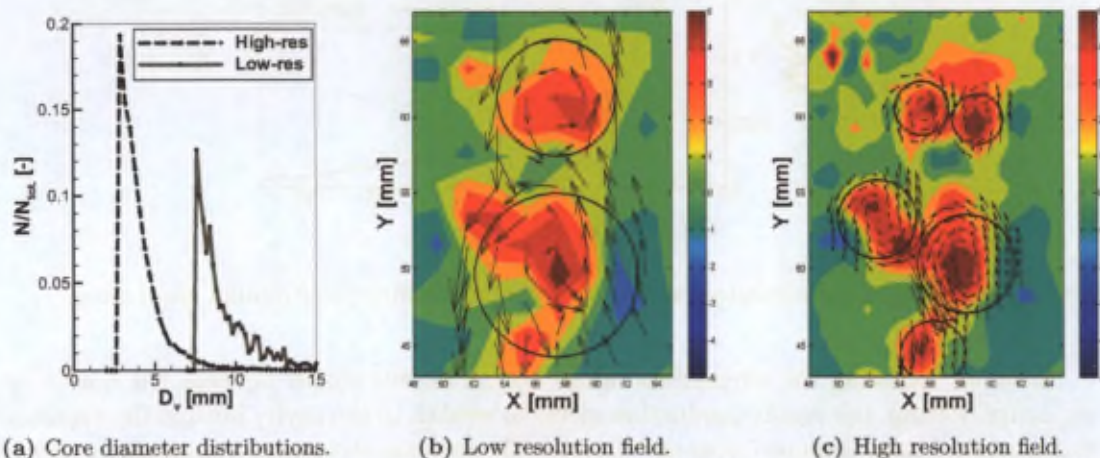


FIGURE 7.7 – The effect of the flow field resolution on the vortex detection.

Although the low resolution CFD data ( $\Delta_{CFD} = 2$  mm) is interpolated to a high-resolution grid ( $\Delta_{PIV} = 0.6$  mm, corresponding to the PIV measurements) the flow fields are only over-sampled, but they do not contain any further detail of the vortical structures. Therefore, either a simulation at a finer mesh or a PIV analysis at a similarly coarse resolution should be performed to obtain a more fair comparison between the vortex content of the experimental and numerical data. In the present case, the experimental vortices are considered to be better resolved, while the numerical database still allows a quasi qualitative comparison.

Another aspect related to the study of Foucat and Stanislas (2002) that might bias the vortex size distribution is the experimental noise of the PIV measurements, which might be amplified by higher order derivatives during the wavelet detection (Vollmers (2001)). As the experimental data are not filtered, the noise might distort the contours of the vortical structures, which might lead to biased core size detection with the wavelet analysis. However, by comparing the derivatives on the present fields using second order and third order schemes<sup>5</sup>, no significant difference can be observed on the related quantities.

A third reason might originate from the turbulence content of the numerical model. As one can see e.g. in Figure 7.4(d), large vortices are created in the wake of the separating inhibitor flow. As the turbulence levels are underestimated in the simulations up-to about  $X/h \leq 4.5$  (explained in section 6.2.2), the vortices may grow with almost no interaction with other turbulent structures. This could contribute to larger vortex production in the numerical domain as well.

In both of the plots (Figure 7.4(b)) and 7.4(d)), starting from the tip of the inhibitor the growth of the vortices is clear. From about  $X/h = 2$  the test section could be divided into two parts: on the one hand, the structures transported at higher  $Y/h$  locations (typically  $Y/h > 1.4$ ) are able to maintain their larger diameter probably due to the energy transfer from the free stream flow; on the other hand, at lower  $Y/h$  locations the mean vortex core diameter decreases, which could be due to the interaction between the vortices and the flow of the recirculation region. The interaction may also induce the production of smaller structures. As it will be

<sup>5</sup>during the vortex detection in the present data set third order Richardson scheme is applied

shown later, in the same region (about  $Y/h < 1.4$ ) a large number of counter-rotating vortices are present, which cannot originate from the inhibitor shear layer. Thus, these structures should be produced in the main recirculation region and therefore they may have a small diameter, which decreases the local mean core size. Longitudinally, this divided zone extends until about  $X/h = 8$ . Downstream from here, the core size of the larger vortices decreases as well roughly to the level of the vortices of the recirculation region.

During the interaction with nozzle head, the vortex properties may decrease below a detectable limit probably due to strong deformation, as Figure 7.4(a) and 7.4(c) show a gradually decreasing vortex concentration in the nozzle throat. On the cavity side of the nozzle lip the concentration also decreases. However, the mean vortex core diameter appears to be increasing especially in the very low velocity central region of the rotating cavity flow. One has to add that in Figure 7.4(d) the spots of minimum vortex core diameter is simply the result of no detected vortical structures in the corresponding cells (see Figure 7.3(b) as well).

In the followings the vortex deformation is assessed, which is characterized by the shape factor *Like* (Oseen likeness). The deformation of the detected vortices is compared to the ideal Oseen vortex and the matching is expressed on a scale of  $[0, 1]$ , 1 being the ideal vortex (for details, please refer to section A.2.2). As previously mentioned, structures with a coefficient  $Like < 0.5$  are rejected during the wavelet analysis.

The mean Oseen likeness distribution of the experiments (Figure 7.8(a)) shows a generally high value (of around  $Like = 0.8$ ) in the field with a rather small amount of deviation. As the majority of the identified PIV vortices have a relatively small diameter, the lower amount of distortion associated with the higher values of likeness is understandable.

In the recirculation region ( $X/h \leq 8$ ) the lowest shape factors are located in the wake of the inhibitor (Figure 7.8(a) and 7.8(b)), where the largest vortex concentration is observed (Figure 7.4(a)). This is probably due to the strong three-dimensional behaviour, which characterizes the wake region (pointed out by Lema et al. (2006)). As the vortex detection is two-dimensional, it can only give an indication about the in-plane projection of the vortices. If a vortex is not oriented normal to the mid-span plane, in function of its inclination angle the resulting Oseen likeness coefficient will be lower. Therefore, the decrease in likeness may be an indication of the turbulent flow behaviour.

In the free stream flow area a lower vortex distortion is visible (see Figure 7.8(a)). However, the Oseen likeness presents a larger amount of fluctuation, which is probably the result of the locally lower number of detected coherent structures and therefore the lack of statistical convergence. As the main flow passes through the vena contracta, it remains less disturbed (e.g. no significant shear is present), which may explain a smaller vortex distortion.

At the bottom part of the recirculation region, close to the sidewall of the test section a consistently high Oseen likeness can be seen. This area (about  $X/h \geq 3$ ,  $Y/h \leq 0.8$ ) corresponds to a low mean velocity seeded with smaller vortices at a lower concentration. These could result in a lower amount of deformation. As these vortices may be transported further upstream ( $X/h < 3$ ), the area of lower flow velocity and lower fluctuation values broadens (see Figure 6.5). Although a decreasing number of coherent structures are detected, their core size is increasing, while they keep a shape which is closer to an ideal Oseen vortex.

The area of the cavity entrance is probably highly affected by the local measurement quality (Figure 6.3), because vertically organized areas with suddenly lower Oseen likeness appear between about  $8 < X/h < 9$ . Although the recirculation region is more complex to be able to judge, but no sudden change is expected in the free stream. The locally low SN may have

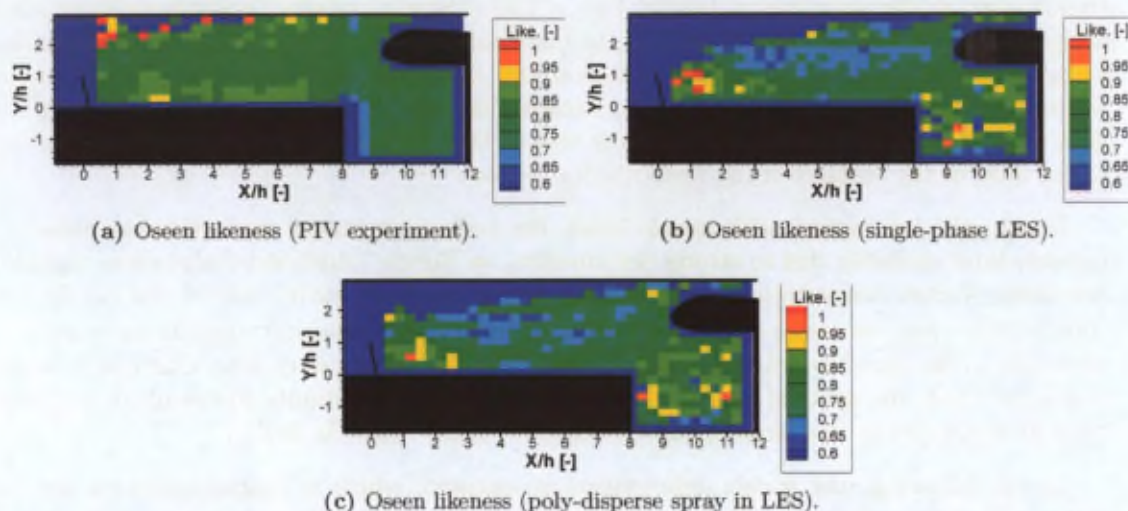


FIGURE 7.8 – Statistical properties of the identified coherent structures (Oseen likeness).

biased the vortex distortion in the same band inside the cavity and even at  $X/h > 11$  as well. However, in the centre area of the cavity the relative vortex deformation variations along the transversal axis should be unaffected by the measurement quality, as the SN is roughly constant in that direction, which represents the orientation of the laser-sheet.

In the band of about  $9 < X/h < 11$  a rather uniform Oseen likeness can be seen. As the flow of the mean recirculation bubble of the cavity transports the vortices, although the number of the vortices is decreasing, their distortion seems to be constant. Nevertheless, an increase of deformation (decrease of likeness) is apparent in the centre of this mean structure, which is represented by relatively larger vortices.

By comparing the experimental Oseen likeness distribution (Figure 7.8(a)) to the numerical case (Figure 7.8(b)), qualitatively a similar pattern can be seen. However, in this latter plot the transversally oriented areas of lower Oseen likeness coefficients are not visible in the area of  $8 < X/h < 9$ , which also suggests that the above-mentioned behaviour is related to the lower local measurement quality (lower SN in the PIV data).

Although Figure 7.8(b) represents a larger local fluctuation of the distortion coefficient (certainly due to the lack of statistical convergence), it exhibits a larger dynamics as well. For instance, compared to the experiments, the numerical data contains considerably lower and higher values in the inhibitor wake. However, the same local increasing Oseen likeness tendency can be observed in the free stream and close to the sidewall of the test section as well. Furthermore, the previously described locally higher distortion level appears also in the centre of the cavity. At the periphery of the cavity, drawing any conclusion would be difficult, as the appearing pattern is the result of a low number of passing vortices.

In the detection algorithm, among the properties of the detected coherent structures the circulation ( $\Gamma$ ) is defined by the integral of the vorticity over the in-plane vortex surface. The circulation may have a positive or a negative sign depending on the direction of the rotational speed vector (the sense of rotation). In the present fields the negative values represent clockwise rotation, the positive values represent counter-clockwise rotation. Therefore, instead of simply averaging the circulation, it is divided into two quantities: its sign (*Sign*, which can have a value of -1 or +1 at each vortex) and its magnitude ( $|\Gamma|$ ). During the post-processing both of these quantities are averaged and the obtained plots are analysed.

The average rotational sign distribution of the PIV fields is shown in Figure 7.9(a). Since *Sign* can only have a value of -1 or +1, during the averaging one can get in each cell an indication of the preferential direction of rotation on the  $[-1, 1]$  scale. For example, an average value of *Sign* = -0.2 means that in the given cell 60% of the vortices are turning clockwise and 40% counter-clockwise.

Looking at the experimental database (Figure 7.9(a)), the field can be divided into four regions according to the sign of the preferential rotational direction (please follow Figure 6.4): the wake of the inhibitor, the cavity, the area around the cavity entrance corner and finally, the downstream corner of the inhibitor.

The primary area is the wake of the inhibitor, which is initiated by the shear layer attached to the inhibitor tip. As the vortices are formed from the shear layer induced by the high-speed free stream flow, all these primary vortical structures rotate clockwise (indicated by the value lower than -0.8).<sup>6</sup> As some of these vortices lift up to the free stream flow (to about  $Y/h > 2$ ), the mean sign of the rotation remains below -0.6, which suggests no significant interaction with each other, with the inlet turbulence, or with the splitting plate. Please note that the few counter-clockwise rotating vortices detected at  $X/h < 4$  and  $Y/h > 2$  are probably vortices which already existed in the flow upstream the inhibitor.

Those of the shed coherent structures, which tend to follow better the mean stream-traces of the flow might interact with each other due to the rather high local vortex concentration and they might interact with the reversed flow passing close to the sidewall of the test section. As a result, counter-clockwise rotating vortices might be created. Their number almost reaches the number of the clockwise vortices at  $Y/h < 0.7$ .

The second largest region of Figure 7.9(a) is the cavity, where the majority of the vortices turn again clockwise, which matches the rotational direction of the mean recirculation bubble of the cavity. Therefore, it appears that the eventual production of new vortices from the nozzle lip interaction (mentioned earlier) does not have an important effect on the main vortex content in the cavity farther from the boundaries, but the main flow rotation is predominant.

As indicated earlier, by the time the cavity flow turns once and approaches again the corner at the cavity entrance ( $X/h \cong 8$ ,  $Y/h = 0$ ), most of the vortices are probably dissipating below a detectable level, as their number is decreasing rapidly. However, starting from the corner opposite to the nozzle lip ( $X/h \cong 8$ ,  $Y/h = -1.8$ ) new, mainly counter-clockwise turning vortices seem to be born near the boundary due to the flow-wall interaction. Furthermore, at the cavity entrance corner a small secondary shear layer is induced by the cavity flow (visible in Figure 6.5(a)), which may also produce additional vortical structures rotating counter-clockwise.

The fourth region that can be elaborated is the area of the downstream corner of the inhibitor, where a mean counter-rotating structure resides which is driven by the main recirculation bubble (see Figure 6.5(a)). Therefore, at this location probably the same swirling structure is identified instantaneously. Although its location might shift slightly from the interaction with the flow of the main recirculation bubble, its presence is rather consistent, which is shown by the local *Sign* > 0.8 value and the vortex concentration map (Figure 7.4(a)) as well.

Comparing the experimental results (Figure 7.9(a)) to the numerical data (Figure 7.9(c)), once again a pattern representing similar features can be seen. Like in the previously mentioned properties, the lack of statistical convergence is also visible. Furthermore, probably due to the different numerical inlet turbulence definition (random perturbation with neither spatial, nor temporal correlation) no vortices can be seen that would originate from upstream the inhibitor.

<sup>6</sup>In the shear layer values lower than -0.98 are present.

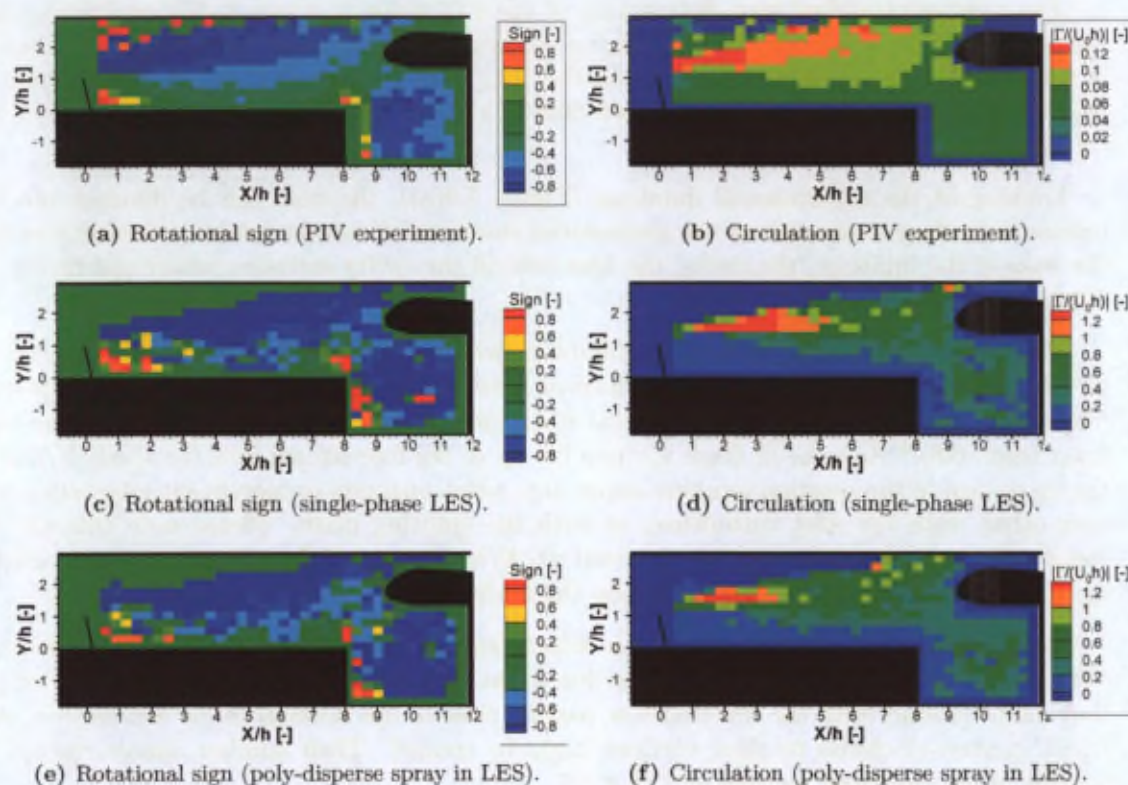


FIGURE 7.9 – Statistical properties of the identified coherent structures (*Sign of rotation and circulation magnitude*).

Consequently, a very homogeneous vortex rotational direction ( $Sign < -0.8$ ) appears along an imaginary straight line between the obstacle tip and the nozzle throat. Furthermore, the negative *Sign* values in the cavity and the positive values along the above-mentioned boundaries (the cavity entrance corner and the downstream corner of the inhibitor) are also more pronounced by the numerical vortices. It is more difficult to find regions, where opposite rotational signs would coexist statistically.

To analyse the magnitude of the circulation (the strength of the vortices), at first the experimental database is considered (the normalized plot is shown in Figure 7.9(b)). The maximum circulation magnitude value is observed at the main location of their production (at the inhibitor shear layer). Lower values in multiple neighbouring cells can only be seen just below the shear layer and in the free stream, at  $X/h < 1$ .

As the strongest coherent structures are transported downstream from the inhibitor shear layer, they are spreading and probably interacting with each other and with the flow, possibly through pairing, breakup, or even creation of new vortices, which leads to the gradual dissipation of their energy. As they arrive at the nozzle head, the vortices still possess about 2/3 of their initial strength. However, as meanwhile the average vortex diameter is considerably decreasing, the vorticity (and thus the angular velocity) of the vortices should increase, which might be induced by the free stream flow.

No other significantly high energy vortex is generated in the cavity or at the downstream corner of the obstacle. So, the flow rotation in the cavity and the secondary recirculation bubble just downstream the inhibitor appear to be secondary mechanisms with respect to the inhibitor

shear layer.

By analysing the strength of the coherent structures of the numerical simulations (see Figure 7.9(d)), first of all about an order of magnitude higher peak values can be observed. Furthermore, similarly to the transversal velocity component fluctuations of the flow (Figure 6.10(d)), but at a slightly higher  $Y/h$  region, the mean circulation magnitude in the wake appears to decrease until about  $X/h = 6.5$ , where it slightly increases again. However, due to the rather low number of local samples this observation might not be representative. In any case, the mean circulation appears to decrease at a higher rate than what is observed experimentally. Furthermore, a clear increase of vortex strength is visible in the centre region of the cavity, which might be due to the local core diameter increase and the lack of less energetic structures, which are not able to enter in the centre of the mean recirculation bubble of the cavity.

As the necessary data is available, the turbulence cascade of the flow is attempted to be estimated by using the energies of the vortices (similar to Schram (2003)). Although, relating it to the accumulation process is far from being obvious, it is part of the characteristics of the vortices, which are transporting the droplets. Therefore, the normalized energy computed from the circulation is plotted in function of a normalized wave number  $((D_v/h)^{-1})$ , which is based on the vortex core diameter (see e.g. Figure 7.10(a)). The energy spectrum of a homogeneous isotropic turbulent flow could exhibit an energy decay with a slope of  $-5/3$ . The actual values corresponding to the various data sets are indicated in Table 7.3.

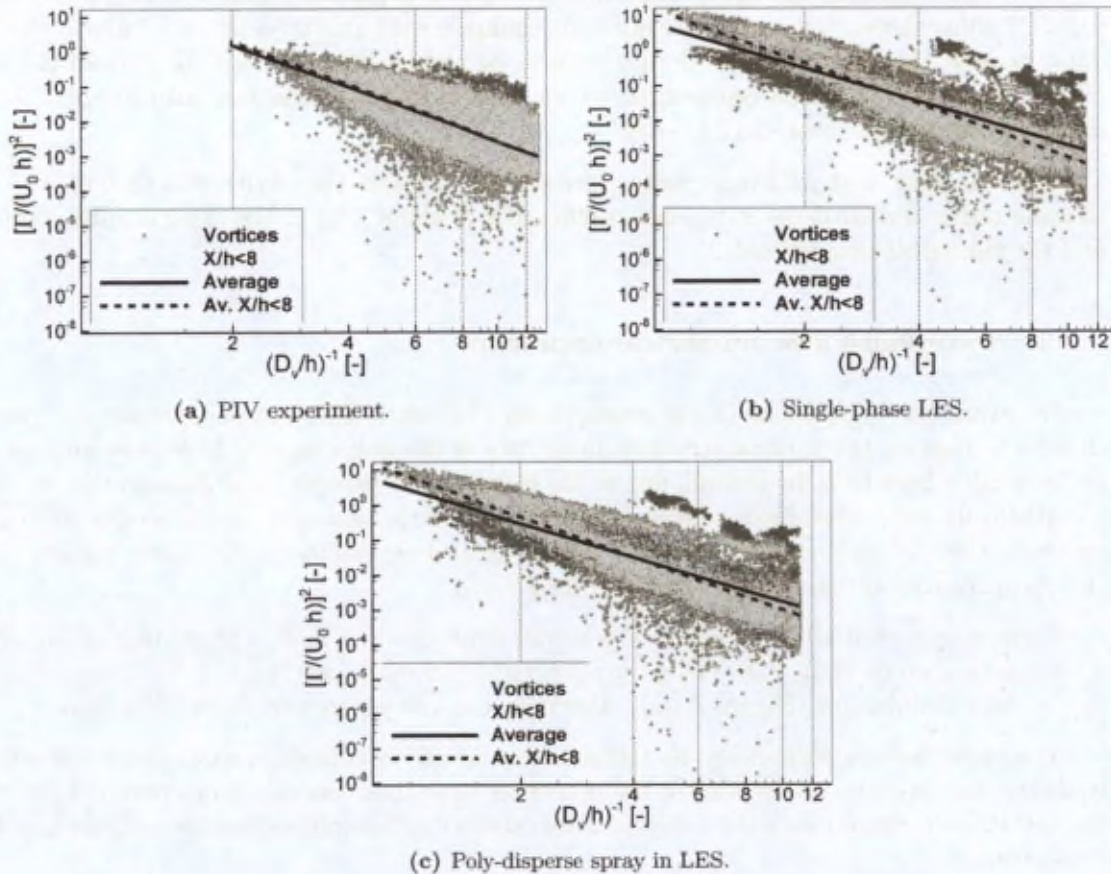


FIGURE 7.10 – Turbulence spectrum estimation.

As Figure 7.10(a) shows, the spectrum of the experimental vortices is quite homogeneously

distributed with a rather steep decaying slope of -3.97. However, looking at the spectrum of the numerical data (Figure 7.10(b)), the most important difference is that on the left hand side of the plot, two lobes are visible representing equally large vortices with an energy difference of about an order of magnitude. The overall decay slope is -3.17 in the CFD data.

In the average core diameter distribution of the LES vortices (Figure 7.4(d)) large structures appear in the wake of the inhibitor and in the centre of the cavity. In order to distinguish the two lobes, the vortices of the recirculation region ( $X/h < 8$ ) are highlighted. In two-phase flow condition these vortical structures should be responsible for the droplets mixing and hence for the droplet entrapment process. The light-gray filled points of Figure 7.10 highlight that these vortices are the more energetic ones and the second lobe should correspond to the cavity centre.

Table 7.3 – *Estimated turbulence dissipation rate (at nominal speed).*

Case	Dissipation coef.	Dissipation coef.
	(entire field)	( $X/h < 8$ )
Single-phase PIV	-3.97	-4.09
Single-phase LES	-3.17	-3.88
Poly-disperse LES	-3.19	-3.79

As the vortical structures located upstream the cavity are expected to have a larger influence on the droplets mixing, the decay slope of this region is separately indicated in Table 7.3. As Figure 7.10(a) shows, the decay rate does not change considerably (-4.09 vs. -3.97) in the PIV data, because the cavity vortices do not seem to be highly different from the ones of the wake region. However, the slope represented by the numerical structures (see also Figure 7.10(b)) changes considerably from -3.17 to -3.88.

Thus, in spite of the different vortex characteristics inside the cavity, the zone of  $X/h < 8$  shows a rather similar decay rate (with a difference of about 5%) in the experimental database and the numerical simulations.

## 7.2.2 Two-phase flow numerical approach

Following the comparison of the single-phase PIV and CFD vortex contents, the present chapter focuses on the vortical structure properties of the poly-disperse LES case with respect to the single-phase LES. In general, due to the fact that the present CFD data do not represent a statistically fully converged solution, the explanation focuses only on the major differences visible in the various vortex properties. This is applied especially in the cavity region, where the vortex concentration is even lower (Figure 7.4(c)).

Examining first of all the number of detected structures per field, a slight increase of about 5.5% can be seen in Table 7.2. The vortex concentration map (see Figure 7.4(e)) resembles the single-phase simulations (Figure 7.4(c)). However, one can notice some clear differences.

The shear layer attached to the inhibitor tip seems to contain more vortical structures. However, this may be an artifact of the detection algorithm, because from about  $X/h = 1.5$  the vortex concentrations of the two-phase case shows similar values than the single-phase flow configuration.

Further downstream, in the recirculation zone a longitudinal shift can be seen in terms of the zones containing larger number of vortices. The coherent structures of the recirculation zone using the poly-disperse spray clearly appear to shift upstream with respect to the single-phase

flow configuration. It suggests that the coherent structures descend earlier closer to the wall and interact with the recirculation zone. It indicates that the liquid droplets might push the vortices closer to the bottom wall, which is in good agreement with the statistical flow field observations (section 6.3.2 and 6.4.2), where the main recirculation became flatter. Consequently, the vortices, which are transported towards the free stream region also appear to be more limited in terms of mean transversal ( $Y/h$ ) location.

In the mean vortex core diameters, a similar growth is visible in the shear layer in the presence of the droplets and in single-phase flow configuration (see Figures 7.4(f) and 7.4(d)). However, in the wake the spreading of the large vortices is more limited in the two-phase flow case. Even a core diameter decrease can be observed from about  $X/h = 3.5$ .

The size decrease in the presence of the dispersed phase is in agreement with the results of a mixing layer investigated by Miller (2001), where the vortices appear also to be more distorted in the presence of particles or droplets. A larger degree of distortion is reported by Wallner and Meiburg (1999) as well. However, by comparing Figure 7.8(b) and 7.8(c), no clear decrease of the Oseen likeness parameter (which would mean a larger amount of vortex deformation) can be stated.

No clear difference in terms of preferential rotational direction can be seen either (shown in Figure 7.9(c) and 7.9(e)).

However, the poly-disperse droplets seem to modify the strength of the vortices (see Figure 7.9(d) and 7.9(f)). Inside the wake lower mean circulation magnitudes can be observed, which might be the direct effect of the decreasing vortex diameter in the presence of the droplet-phase.

To verify whether the rotating motion of the vortices changes due to the droplets, a non-dimensional rotational speed is calculated. As the rotation also equals to the integral of the tangential velocity along the vortex periphery, the dimensionless rotational speed can be obtained from the normalized circulation magnitude and the normalized core diameter using equation 7.2.

$$\omega_v = \frac{\left| \frac{\Gamma}{U_0 h} \right|}{\frac{\pi}{2} \left( \frac{D_v}{h} \right)^2} \quad (7.2)$$

As it can be seen in Figure 7.11, in the presence of the droplets, the mean rotational speed of the vortices also decreases slightly. Therefore, the weakening of the vortical structures is a combination of shrinking and slower rotation.

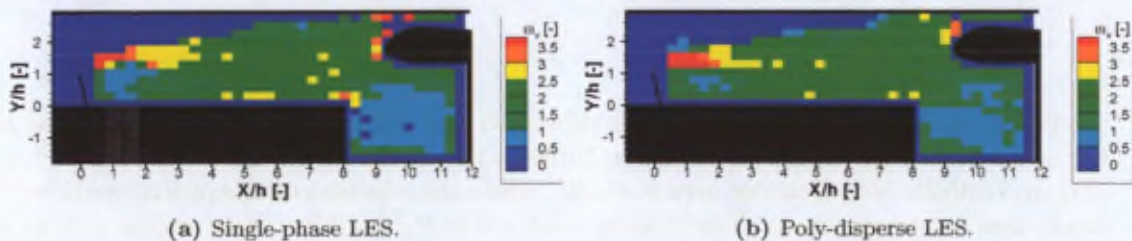


FIGURE 7.11 – Normalized angular velocity distribution.

Comparing Figure 7.10(b) and 7.10(c), the turbulence spectra appear to be similar consid-

ering either the whole field or the region of  $X/h < 8$ . As Table 7.3 shows, the single-phase and two-phase decay slopes give rather close values. As the few identified vortices in the centre of the cavity are smaller in the presence of the poly-disperse droplets (Figure 7.4(f)), the lobe corresponding to these structures in Figure 7.10(c) becomes less distinct as well.

Finally, one should notice that as far as the statistical convergence of the mean quantities allows to judge, the observed differences between the single-phase and two-phase flow cases are rather modest. This behaviour might be correct, but it might originate also from the way the solver models the Lagrangian phase. In order to save a considerable amount of computational time, the droplets are not tracked individually. Instead, packets of droplets of the same diameter are created, which are called *parcels* or *super-particles*. Each parcel carries several physical droplets. This number can reach above 20000 in case of smaller droplets (Lema et al. (2007)). When they are tracked, the parcels behave as a single droplet. It is only at the accumulation, where their real mass is retrieved. Therefore, the simulations might represent correct droplet mass fraction, but the volume fraction is considerably lower than it is physically, which could limit the amplitude of the modelled interaction between the two phases.

### 7.3 Two-phase PIV investigation

The phenomena controlling the evolution of the properties of the vortices in single-phase flow condition are detailed in section 7.2.1. Therefore, similarly to section 7.2.2, the description of the vortical structures of the two-phase PIV experiments is focusing on the effect of the droplet-phase. Note that the reference velocity for these experiments is  $U_0 = 2$  m/s. The two-phase PIV data are therefore not comparable to the results shown in section 7.2.1. However, they are compared to other single-phase experiments performed exactly for the same conditions as the two-phase flow measurements but without operating the spray. As Table 7.1 summarizes, 1200 samples are analysed for each flow configuration.

Analysing first of all the total number of detected vortices, Table 7.4 shows about 30% less vortical structures in the two-phase flow configuration. This tendency is the contrary of the numerical tendency, where a slight increase is experienced. As Figure 7.12 indicates, the vortex core size distribution presents very high values near the detectable limit of about  $D_v = 4\Delta_{PIV}$  (during the two-phase PIV investigation  $\Delta_{PIV} = 1.1$  mm). Thus, probably a considerable amount of structures shrank below that limit, which may lead to a lower total number of identified vortical structures.

Table 7.4 – Two-phase PIV vortex detection results.

Case	Total # of vortices	# / sample	Dissipation coef.
Single-phase	17720	14.77	-3.70
Two-phase	12398	10.33	-3.73

The spatial vortex distribution of the two-phase case (Figure 7.13(b)) shows that the number of detected vortices decreases quasi uniformly with respect to the single-phase configuration (Figure 7.13(a)). No particular area is visible, where the relative concentration would be drastically lower than elsewhere. Nevertheless, each cell in the inhibitor wake region represents at least 100 vortices. Therefore, the mean vortex properties should be statistically representative.

Concerning the pattern, the vortices seem to be pushed closer to the sidewall of the test section, as it is also observed in the mean flow pattern (Figure 6.21(b)) and in the numerical

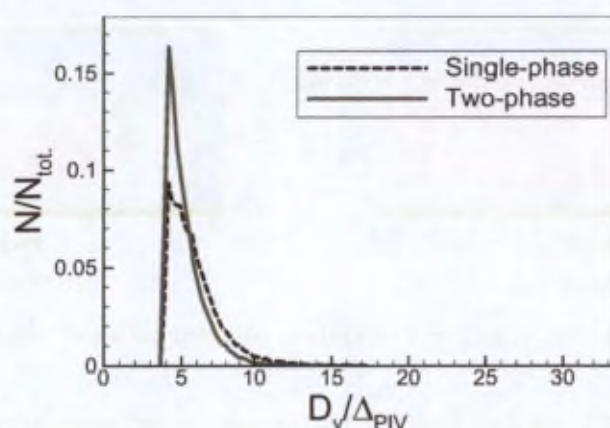


FIGURE 7.12 – Normalized vortex diameter distributions (two-phase PIV).

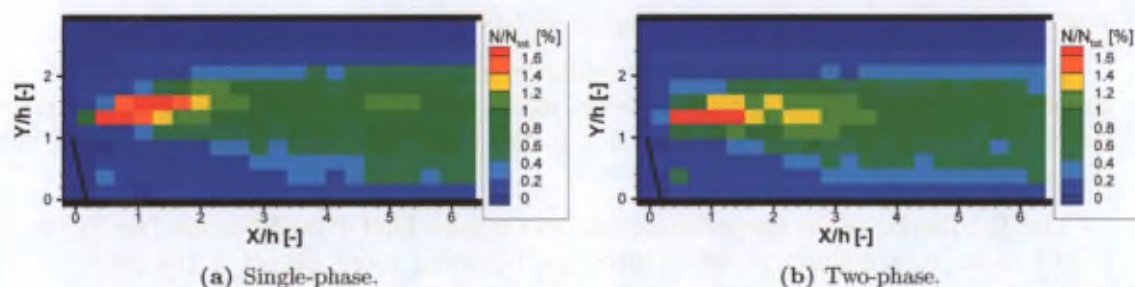


FIGURE 7.13 – Vortex concentration distribution obtained with the two-phase PIV experiments.

data. Consequently, the shear layer, where the vortices are generated is flatter and even in the spreading wake, a lower amount of vortical structures appears at  $Y/h > 2$ . The spreading of the wake appears to be quicker as well. By  $X/h = 3$  it seems to be established; from this location a rather constant transversal concentration distribution is visible.<sup>7</sup>

Furthermore, in the region close to the shear layer (about  $1 < X/h < 4$ ,  $0.8 < Y/h < 2$ ) a slightly larger local vortex concentration can be seen in the two-phase flow case. The vortices appear to spread more transversally. However, by  $X/h = 4$  these tendencies reverse. The structures start to dissipate below a detectable limit and their overall number is slightly decreasing, while in single-phase flow condition their number looks to increase slightly.

Without the droplets the vortices are spreading transversally from the shear layer up to  $X/h = 6$ . In the presence of the liquid-phase, the areas seeded with more vortices can be found gradually farther from the sidewall, beyond  $X/h > 4$ .

The differences in the plots representing the mean core diameter distribution are even more apparent (Figure 7.14). First of all, one should notice that the vortices are slightly larger than in the previously observed nominal speed experimental investigation (Figure 7.4(b)), which is in agreement with the coarser velocity field.<sup>8</sup>

<sup>7</sup>The transversal distribution does not change considerably in function of the longitudinal position.

<sup>8</sup>In section 7.2.1 the effect of resolution is assessed. It is shown that by decreasing the resolution, larger vortices may be identified at locations, where small structures are transported in the vicinity of each other. Furthermore, simply the increase of the detectable limit (which remains  $D_v = 4\Delta$ ) shifts the mean core diameter towards larger values as well.

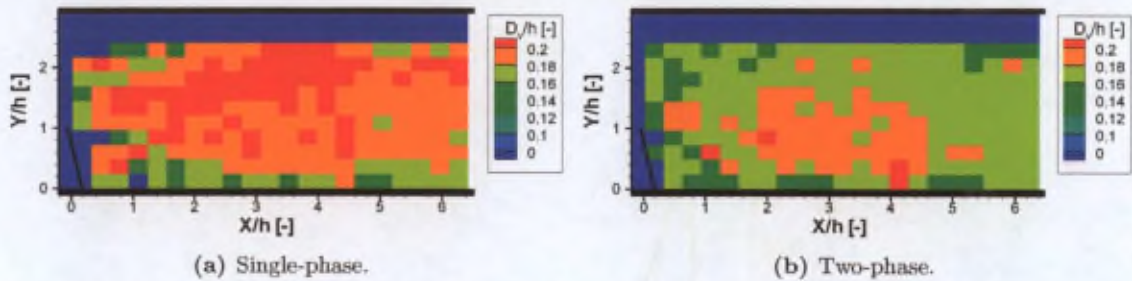


FIGURE 7.14 – Mean core diameter distribution obtained with the two-phase PIV experiments.

As one could expect based on Figure 7.12, the mean vortex cores appear to shrink in the two-phase flow configuration (Figure 7.14(a)) with respect to the single-phase case (Figure 7.14(b)) throughout the field. A slight change can be observed at the location of the mean recirculation centre (approximately at  $1.8 < X/h < 4.2$ ,  $Y/h < 1.2$ ). In the inhibitor wake region, the diameter of the structures appear to drop by 10 to 20%.

Even the downstream corner of the inhibitor is no exception, where the secondary mean structure can be found. It is found already in the statistical results that this mean rotating structure became considerably smaller due to the more restricted main recirculation bubble (Figure 6.21(b)).

The distribution of the Oseen likeness shows the same kind of modification (see Figure 7.13) as the mean core diameter: the vortices are becoming more distorted (by about  $Like = 0.05$  to  $0.1$ ) in the main part of the field, except in the centre area of the main recirculation bubble, where the Oseen likeness decrease is limited to about  $Like = 0.05$ .

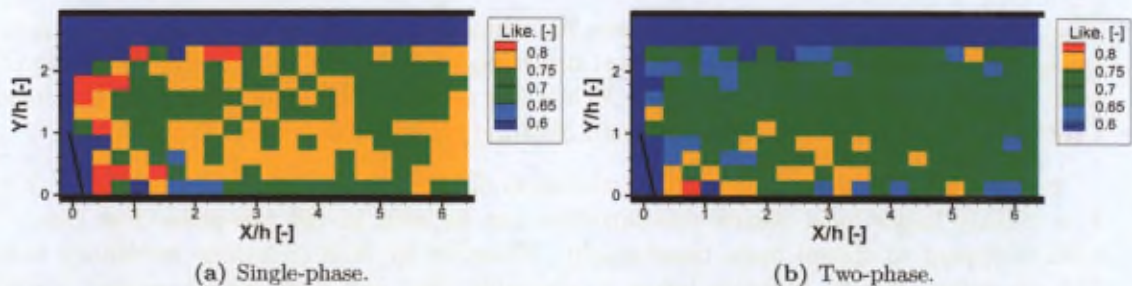


FIGURE 7.15 – Oseen likeness distribution obtained with the two-phase PIV experiments.

Therefore, these results suggest that the injected liquid droplets prevent the developing vortices from an increased core diameter maybe by limiting the flapping of the shear layer or through other mechanisms. Furthermore, due to its discrete distribution, the dispersed phase may distort the vortices as well starting from their creation. As mentioned in section 7.2.2, this tendency is in good agreement with Miller (2001); Wallner and Meiburg (1999). Hence, the combination of these effects may put a considerable number of vortices below the limit of detectability ( $D_v \cong 4\Delta_{PIV}$  and  $Like = 0.5$  respectively), which could explain the 30% drop in the total number of vortices.

Furthermore, one should notice that if the vortices were only more distorted, but exhibiting the same overall diameter, the detection algorithm might be also biased, when determining the core diameter. Therefore, the vorticity peak of each vortex centre is extracted and averaged as well. This property is independent of the detection algorithm as it is computed directly

from the velocity field. Looking at the wake region in Figure 7.16(a), the vortices appear to be more energetic in single-phase flow configuration compared to the two-phase flow case, which is shown in Figure 7.16(b). Therefore, the presence of the droplet-phase appears to damp the shed vortices.

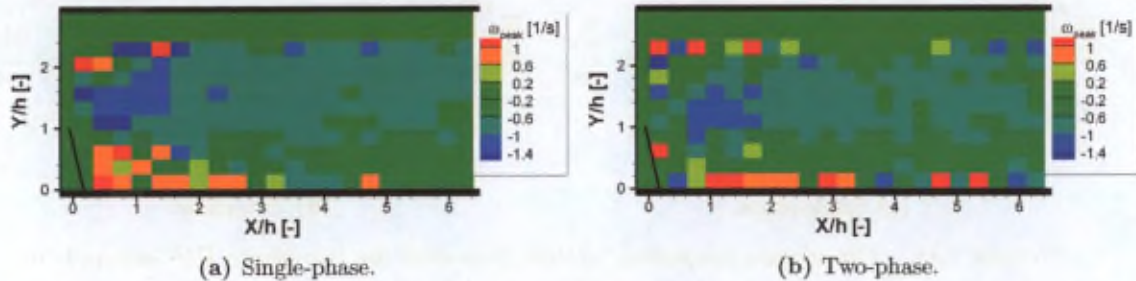


FIGURE 7.16 – Vorticity peak distribution obtained with the two-phase PIV experiments.

In the followings the quantities derived from the circulation are analysed in the same way as in section 7.2.2. At first, the average direction of rotation is shown in Figure 7.17. In both configurations, the few incoming vortices of the free stream flow (about  $X/h < 1.5$ ,  $Y/h > 1.5$ ) are rotating in arbitrary directions. However, the ones created by the shear layer turn clockwise. Some of the vortical structures, are probably affected by the free stream flow and gradually lift up. They define this preferential direction even up-to  $X/h = 6$  in single-phase flow configuration. However, in the two-phase flow condition the vortices of the inhibitor wake are more divided. A consistent negative rotational sign ( $Sign \leq -0.8$ ) can be seen only up-to about  $X/h = 4$ . Almost everywhere else in the wake and in the recirculation region, one can observe about 10% higher number of local counter-clockwise rotating vortical structures. On the one hand, it may suggest the generation of a relatively larger number of vortices due to the interaction with the reversed flow area or with other vortical structures. On the other hand, it may signify a higher rate of vortex dissipation below a detectable limit among the vortices originating from the inhibitor shear layer.

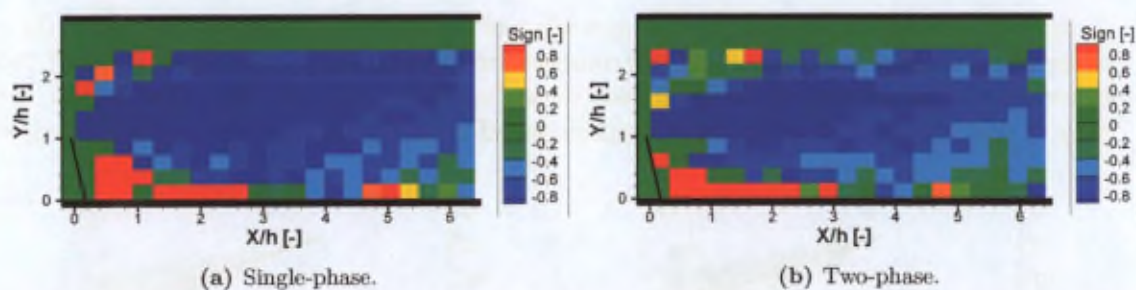


FIGURE 7.17 – Preferential direction of rotation with the two-phase PIV experiments.

Close to the sidewall and at the downstream corner of the inhibitor, where counter-clockwise rotation is predominant, no significant change can be observed. However, one should note that in these regions the number of vortices is lower. Nevertheless, one can see the shrinking of the area of the secondary mean rotating structure once again.

Figure 7.18 also visualizes the wake of the inhibitor represented by the larger circulation magnitude values. In two-phase flow condition the strongest instantaneous structures are transported at a lower  $Y/h$  location, as it is expected according to the previous observations. Furthermore, the two-phase vortices appear to be about 15% weaker than the vortical structures in

the single-phase flow configurations, which is consistent with the mean core diameter decrease mentioned above.

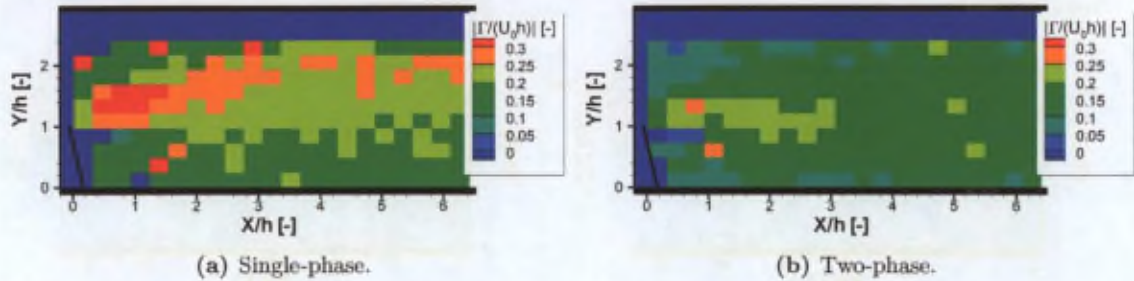


FIGURE 7.18 – Circulation magnitude distribution with the two-phase PIV experiments.

Figure 7.16 already showed a weaker vorticity peak in the centre of the vortices. However, the mean normalized rotational speed distribution is also determined by using equation 7.2. Figure 7.17 demonstrates that although the mean rotational speed values are slightly lower in the two-phase flow configuration (see Figure 7.19(a) vs. 7.19(b)), the magnitudes are quite similar.

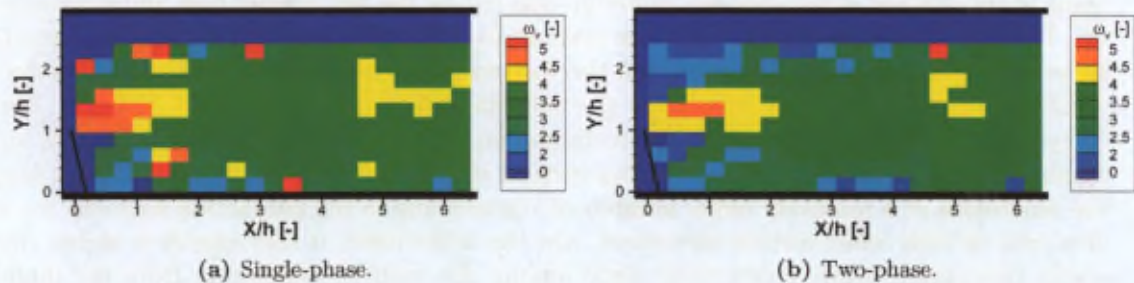


FIGURE 7.19 – Normalized angular velocity distribution with the two-phase PIV experiments.

In the turbulence spectrum, a larger spreading of the data points can be observed in the two-phase flow configuration (Figure 7.20(b)) compared to the single-phase flow case (Figure 7.20(a)). However, the corresponding decay slopes (shown in Table 7.4) give very close values, which suggest that the droplets do not have a significant effect on the decay of the turbulent processes.

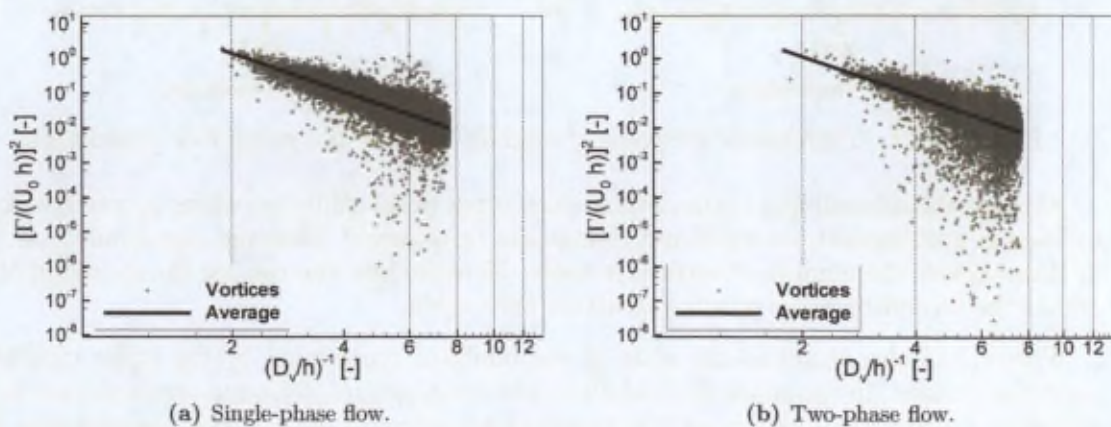


FIGURE 7.20 – Turbulence spectrum estimation.

Furthermore, the obtained decay rates of the current experiments are lower in magnitude than the ones obtained in the corresponding area ( $X/h < 8$ ) during the nominal speed investigation (see Table 7.3).

## 7.4 Summary on the instantaneous flow behaviour

To investigate the instantaneous flow behaviour, the vortical structures are detected in the snapshots of all the databases and their properties are analysed.

The most energetic vortices are generated by the shear layer attached to the inhibitor tip. As they are transported by the flow further downstream, they may interact with each other, the free stream and the recirculation region and thus their energy is mainly dissipating.

Comparing all the presented experimental and numerical databases, one of the main differences is the consistently smaller mean experimental vortex size. Multiple possibilities are mentioned. The most probable reason is the coarse numerical grid, which simply does not resolve the smaller vortices.

Unfortunately, the numerical database does not provide sufficient statistically independent samples, which prevents a detailed comparison of the single-phase and two-phase flow cases.

Using the two-phase PIV technique more pronounced effects are revealed due to the presence of the droplet-phase (noticed already in the statistical properties) in spite of the quasi lower volume fraction compared to the poly-dispersed LES computations. Differences can be discovered practically in all of the vortex properties. In general, in the presence of the droplets, the air-phase vortices show a damped energy content, which could be observed in all the related variables.

Considering that the droplets require a certain time to respond to the flow motion (due to their longer characteristic time), their mixing with the flow of the recirculation zone should begin farther upstream from the nozzle. As it will be explained in section 8.2, in the entrainment process of the smaller droplet classes the energetic vortices of the inhibitor wake play an important role.

Published by the University of Chicago Press, 5 East Lake Street, Chicago, Illinois 60607  
Printed in the United States of America

THE UNIVERSITY OF CHICAGO PRESS

1995

THE UNIVERSITY OF CHICAGO PRESS

## Chapter 8

# The understanding of the current accumulation process

In chapter 5 the tendencies of the liquid accumulation are determined, where the importance of the inhibitor height and the *obstacle tip to nozzle tip distance* (OT2NT) are identified. To understand better the flow mechanisms of the present configuration, PIV campaigns and numerical simulations are performed both in single-phase and two-phase flow configurations. The obtained statistical flow quantities are presented in chapter 6 and the vortex properties are discussed in chapter 7.

The current chapter's aims are to synthesize the main observations and describe the current understanding of the accumulation process. As it will be shown, in the presence of the droplet-phase, liquid can accumulate in the cavity through two main mechanisms:

- droplet entrapment;
- dripping.

Following the above-mentioned flow field investigations, the main aspects of the entrapment process are described in section 8.2. However, the present databases do not provide sufficient information about the dripping phenomenon. It could only be observed during the LeDaR investigation. So far, it has been neglected (both in the present study and elsewhere), but its main aspects are attempted to be explained and explored in section 8.1.

### 8.1 The dripping process

As it was described in section 5.1, liquid accumulates on the upstream surface of the inhibitor and without the liquid extraction system a considerable amount of water falls directly in the cavity and disturbs the LeDaR measurements. Although, the suction system reduces it considerably, dripping still occurs from the inhibitor.

As mentioned in section 6.3.2, the poly-disperse droplets result in a CFD predicted entrapment rate of about 0.7% of the injected mass, while in the corresponding nominal configuration of the LeDaR measurements approximately 8% is observed. The difference, which is about an order of magnitude is not believed to be numerical error. Instead, the contribution of the residual experimental dripping is assessed.

Supplementary visualization experiments are carried out to understand the contribution of dripping to the accumulation in the 2D-like facility (section 8.1.1) and additional simulations are performed in the framework of this research work to assess its importance in the presence of radial flow injection (section 8.1.2).

### 8.1.1 Dripping visualization

During the LeDaR image recording large drops of water are dripping from the downstream surface of the inhibitor (see section 5.1). The inhibitor is inclined by  $10^\circ$  against the gravity and a liquid extraction system is installed to evacuate a major quantity of depositing liquid from the upstream corner of the inhibitor. Thus, the number of drops falling in the cavity is considerably lower. However, it can be still observed occasionally in the recordings.

To explore the dripping, a new experimental campaign is initiated. The goal is to visualize the falling drops and give a rough estimation of their contribution to the accumulation.

The investigation is performed in the nominal configuration of the LeDaR experiments ( $h = 33.5$  mm,  $U_0 = 10$  m/s, LeDaR spray device). To quantify the dripping, the Phantom v7.1 high-speed CMOS camera is used at  $640 \times 480$  pixels<sup>2</sup> resolution with a  $f = 50$  mm AF Nikkor lens at  $f\# = 1.8$  to obtain the shallowest possible *depth-of-field* (DoF). The camera is positioned according to Figure 8.1(b) to visualize the whole width (200 mm) of the test section.

The illumination is provided by a 1 kW halogenous photographic lamp, which is placed about 1 m from the lateral wall of the test section. The bulb has about  $\varnothing 10$  mm diameter and 100 mm length. Its length is oriented vertically (aligned with the flow). On the test section wall a black paper frame is mounted with a slit opening to limit the illuminated volume (see Figure 8.1). The arrangement ensures a quasi collimated lighting in the path of the drops, while most of the test section walls remain darker. This is essential to obtain an optical access through the fully wet boundaries, while the spray is operating.

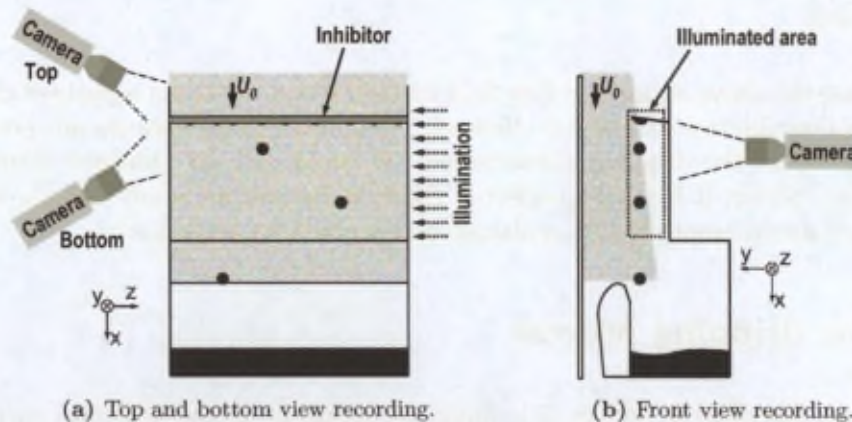


FIGURE 8.1 - *Dripping visualization arrangement.*

While the set-up is operating, the high-speed camera acquires series of 2296 images at frequencies of [100, 200, 300] fps with [9.9, 3, 3.3] ms exposure times respectively (similar to Figure 8.2(a)) to test the influence of the sampling rate. However, no importance of the recording frequency is found. Thus, the various cases are not differentiated during the analysis.

In the images the typical droplet diameter is measured by counting the number of pixels across their image at the moment when the minuscus of the departing drop vanishes. This gives

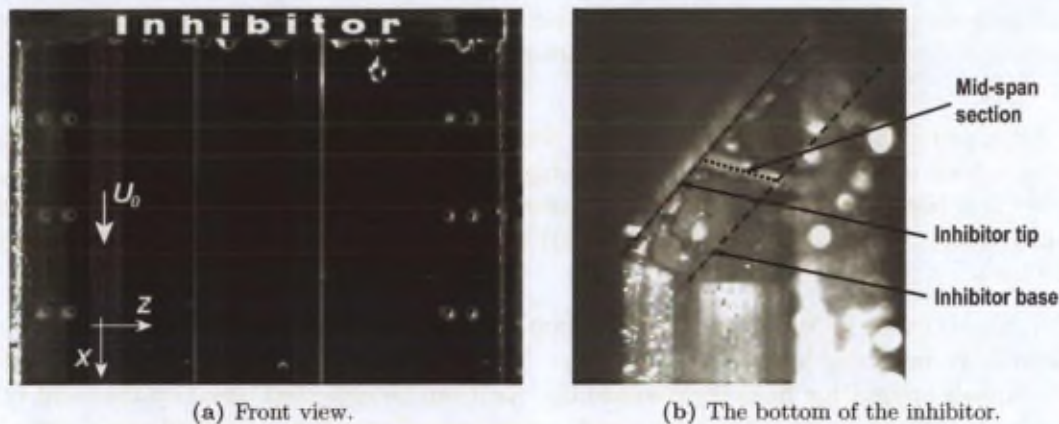


FIGURE 8.2 – Sample frames of the high-speed camera visualization of the dripping phenomenon.

an average value of  $d_p = 25$  pixels that corresponds to about  $d_p = 8$  mm. From  $d_p$  the droplet volume is calculated by assuming spherical shape. Finally, the dripping frequency is determined from the time series by counting the number of drops during the acquisitions. This gives an average value of  $f_d = 6.8$  Hz. As a result, the residual dripping contribution to the accumulation is about 6.1% of the injected water.

To determine the amount of liquid extracted by the suction system from the upstream face of the inhibitor, the nominal LeDaR configuration is further assessed. Using the same parameters, three tests are performed, for which the liquid accumulation in the cavities and the total extracted water volume are measured separately. As a result, in the cavity an accumulation rate (entrapment+dripping) of 9.2% is obtained, while 14.5% of the total sprayed water is extracted by the suction system from the inhibitors, which gives a total of 23.7%.

In the numerical simulations using the poly-dispersed droplets, 0.7% entrapment rate is obtained and 19.1% of the injected liquid accumulates on the inhibitor (Lema et al. (2007)). Hence, a sum of 19.8% water deposits on the inhibitor and in the cavity. This measure seems to be reasonably close to the 23.7% found experimentally. However, when considering that the dripping contributes with 6.1% to the experimental accumulation, the entrapment mass represents 3.1% of the total sprayed water mass, which is 4.4-times more important than the numerical entrapment rate.

Although the dripping drops represent an important mass, between them and the continuous-phase no coupling is assumed. On the one hand, the drops are far too large to be noticeably influenced by the lower-velocity flow of the recirculation region. On the other hand, the dripping frequency is quite low and span-wise dispersed (occurs all along the inhibitor), which suggests that on statistical basis this liquid does not modify the air-phase noticeably.

Considering the large drop diameter ( $d_p = 8$  mm) the stability of the drops is assessed. In the high-speed camera images no breakup is observed up-to about  $X = 150$  mm = 4.5h. However, further downstream no recording is available to observe the drop behaviour. A conservative estimation is performed by neglecting the drag force. The impact velocity of the drop at the cavity bottom (about  $X = 400$  mm  $\cong$  12h from the inhibitor) is computed. Due to gravity it accelerates to  $U_d = 2.8$  m/s. While the drop traverses the recirculation zone, it may cross the zone representing the highest velocity reverse flow ( $U_f \cong -5$  m/s, see Figure 6.5(b)). To follow

the conservative estimation, the Weber number<sup>1</sup> is computed using  $U = U_d - U_f = 7.8$  m/s. The resulting  $We = 6.67$  shows that the drops are stable and should not break up before arriving to the cavity.

Attempting to gather more information about the liquid behaviour on the inhibitor, further visualizations are performed. At first, the high-speed camera is positioned to the side of the test section (see Figure 8.1(a)) in order to record images of the downstream face of the inhibitor (called *bottom view*, similar to Figure 8.2(b)) and of the upstream face of the inhibitor (called *top view*).

In the bottom view (Figure 8.2(b)) drop seeds are visible, which are located at about  $1/2$  to  $2/3h$  from the base of the inhibitor. The drop seeds are fed with water through liquid channels originating from the obstacle tip. As it can be expected based on the local velocity magnitudes (Figure 6.5(b)) the high-speed camera recordings show no considerable disturbance of the seed surfaces due to the airflow. The low disturbance allows the drop seeds to grow until they reach a critical mass and fall in the cavity. This explains the rather uniform drop sizes observed in the *front view* acquisitions (Figure 8.2(a)).

The images of the high-speed camera do not reveal any temporally resolvable event on the upstream face of the inhibitor (*top view*). Therefore, to achieve better image quality, two PCO SensiCam PIV cameras are used with  $f = 35$  mm AF Nikkor lenses. The two cameras record images ( $640 \times 480$  pixels<sup>2</sup> resolution) simultaneously at about 3 Hz. One of them is acquiring the top view and the second one the front view (see the arrangements in Figure 8.1(a) and 8.1(b) respectively). To realize the shallowest possible DoF, the widest aperture is chosen ( $f\# = 2$ ). As the top camera is facing the illumination, very large reflections appear on the entire surface of the inhibitor, which hide all the details of the surface. The cameras are commonly triggered and therefore they apply the same exposure time ( $t_{exp} = 1.2$  ms). To attenuate the light in general, the top camera is equipped with an SP-500 short-pass filter and to reduce the amount of reflection, it is fitted with a linear polarizer filter as well, which is rotated to its most effectively attenuating position. In this arrangement similar acquisitions are obtained with the two CCD cameras (Figure 8.3).

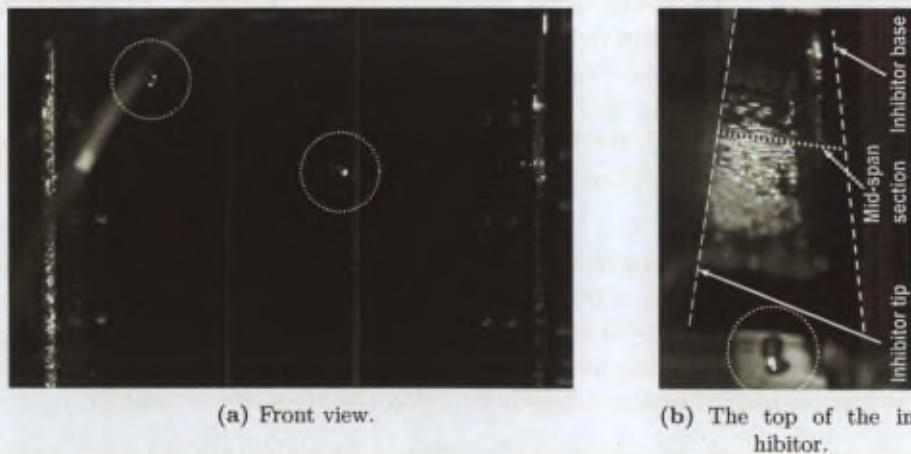


FIGURE 8.3 – Sample images of the CCD camera visualization of the dripping phenomenon.

Besides investigating the top of the inhibitor, the simultaneous acquisition allows to determine occasionally the distance between the dripping drops and the sidewall of the test section.

$${}^1We = \frac{\rho_f U^2 d_p}{\sigma}$$

The image pair of Figure 8.3 shows a unique instant, where two drops are visible simultaneously, which represent different distances from the inhibitor. They visualize well that the airflow has indeed small influence transversally on the drop path.

As Figure 8.3(b) shows, while the spray is operating, a continuous liquid film can be observed on the inhibitor. Even with the high-speed camera (up-to 4000 fps) no temporal correlation can be observed on the visible surface irregularities. Therefore, the appearing waves are assumed to be caused primarily by the impacting water droplets, which is confirmed by the first image recorded after the last droplet is seen in the test section when closing the spray (Figure 8.4(a)). The absolutely still surface suggests a very thin liquid thickness. Unfortunately, with this visualization it cannot be quantified. The impact of the flow field can be observed in Figure 8.4(b) that is acquired about 7.7 s after Figure 8.4(a). Here, the inhibitor is already dry at its tip and close to its base, but still wet in the middle area.

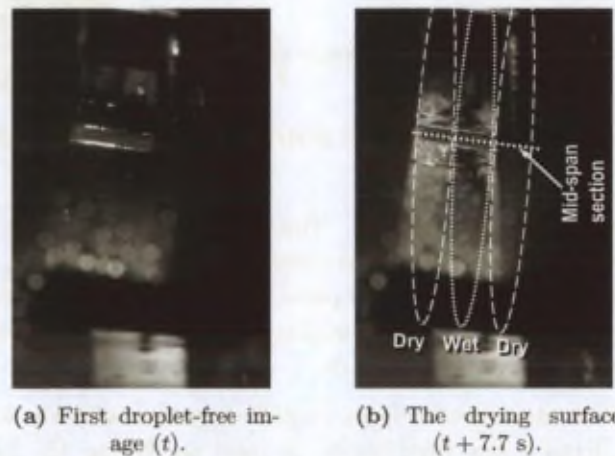


FIGURE 8.4 – Sample images of the upstream surface of the inhibitor with closed spray.

The stream-traces of Figure 6.5(a) and 6.10(a) reveal a stagnation point in the middle of the upstream face of the inhibitor. From the stagnation point towards the inhibitor tip the flow accelerates, which might direct the liquid film towards the tip, where the water remains attached to the surface and flows to the downstream surface. As mentioned above, at the downstream face of the inhibitor no significant air forces act, which allows the liquid to accumulate with the continuous supply from the upstream surface forming drop seeds and thus producing the dripping phenomenon.

### 8.1.2 Liquid deposition with radial flow injection

In the present model the liquid deposition on the inhibitor provides an important contribution to the liquid accumulation in the cavity through the dripping phenomenon. As mentioned above, the deposition rate on the inhibitor is of the order of 20%. Therefore, one may ask, whether the contribution of the dripping phenomenon in a real SRM could be important. Within the present PhD thesis only a brief assessment is performed based on new numerical simulations to determine the ratio of the droplet deposition on the inhibitor and the entrapment in the cavity using two simple cases with (quasi) radial flow injection.

At first, the 3D grid of Lema et al. (2007) representing the current nominal configuration is taken. The surface of the quasi axial injection is replaced by a wall and the whole sidewall of the test section (in the plane  $Y/h = 0$ ) is defined to be the injection. The rest of the geometry

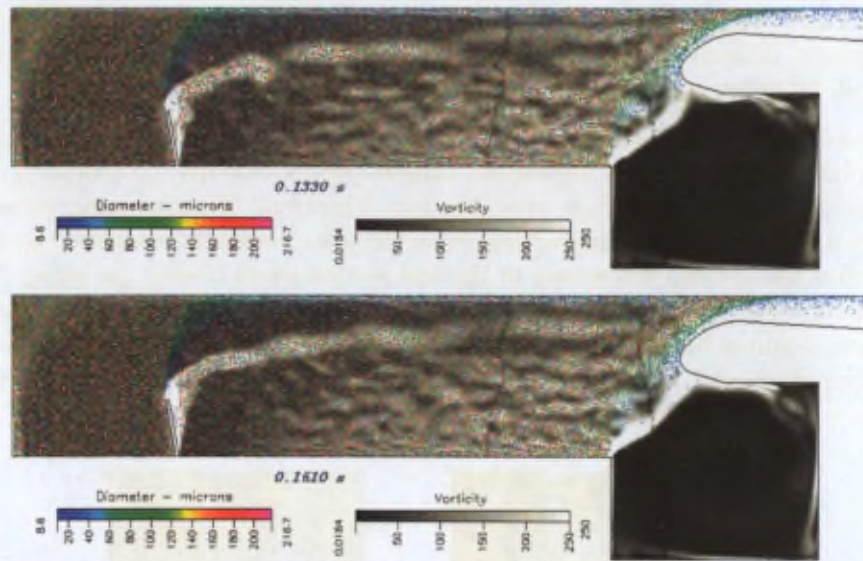


FIGURE 8.5 – Instantaneous droplet distributions with quasi radial flow injection.

and therefore the grid itself is unchanged. The quasi radial flow inlet is normal to the wall at a magnitude of  $V = 2.129$  m/s. It is perturbed by 1.5% turbulence, which is a typical value when the flow is injected through a porous plate (Anthoine (2000)). The mean injection velocity ensures the same air mass injection as the axial configuration, which means that the bulk velocity just upstream the nozzle tip is  $U_0 = 10$  m/s.

The droplet-phase is also injected quasi radially together with the air. The same total water mass flow-rate and droplet size distribution is used as during the poly-dispersed simulation (section 6.3.2). Hence, the Stokes number ( $St$ ) and the volume fraction ( $\alpha_p$ ) are unchanged.

Instantaneous droplet distributions are shown in Figure 8.5. Above the inhibitor the gradient which is visible in the droplet size distribution suggests that the larger droplets are unable to follow the flow as it turns around the obstacle and they probably hit the top wall (modelling the splitting plate).

The contour plot representing the vorticity visualizes the shear layer attached to the inhibitor tip, which leads to vortex shedding. The shed vortices are passing close to the splitting plate. Thus, when they arrive at the nozzle, they do not interact with the nozzle tip and therefore no larger droplets are carried into the cavity. There, only a few very small droplets are visible. They might be entrained by the interaction between the nozzle head and the flapping shear layer that closes the cavity entrance.

The liquid mass deposition rate is calculated both on the inhibitor and in the cavity during 6 flow-throughs (FTs). On the inhibitor 3.4% of the injected water is observed. This value is 5.6-times lower than in the axial-injection case. As explained in section 6.3.3, the droplets have a long characteristic time, which limits their response to the air-phase motion. Therefore, when they move towards the obstacle, especially the larger droplets tend to impact on it, while the flow is passing around the inhibitor. In the radial injection case the projection of the inhibitor on the injecting surface ( $\sim \sin(10^\circ)h$ ) is considerably smaller than the inhibitor projection on the axial injection surface ( $\sim \cos(10^\circ)h$ ). Therefore, by assuming no droplet deviation after the injection, in the quasi radial configuration proportionally lower<sup>2</sup> accumulation rate can be

<sup>2</sup>with a factor of about  $\sin(10^\circ)/\cos(10^\circ) = \tan(10^\circ)$ , where  $10^\circ$  is the inclination angle of the inhibitor with

expected.

As mentioned above, only a few small droplets are observed instantaneously in the cavity. Consequently, the average entrapment rate is 0.07%, an order of magnitude lower compared to the quasi axial injection.

This simulation demonstrates the importance of the vortex-nozzle interaction. As the vortices together with the droplets are transported through the throat, the entrapment drops by an order of magnitude in this special configuration. As mentioned above, the deposition on the inhibitor decreases considerably as well, which would suggest a lower amount of dripping. The ratio between the inhibitor deposition (3.4%) and the cavity entrapment (0.07%) is 48.6 (Table 8.1). The same ratio with axial injection using the poly-dispersed droplet distribution is 27.3. Therefore, the relative importance of the dripping increased by injecting the flow quasi radially in the same domain.

Modelling the flow downstream an inhibitor, Lema (2005) showed the irrelevance of two-dimensional simulations on statistical basis in similar situations. However, to have a rough idea about the accumulation rate on the inhibitor in an axisymmetric geometry with radial injection, a new 2D axisymmetric LES simulation is performed. In this case the geometry of the present 2D-like model is abandoned. Instead, a more realistic geometry, the nominal configuration of the 1/30 scale cold-gas EAP model of Anthoine (2000) (introduced in section 1.3.1.5) is meshed using 85497 cells.

As shown in Figure 1.11(b), the inhibitor is not inclined in any direction. The internal diameter of the channel is  $D = \varnothing 76$  mm and the passage at the inhibitor is  $d = \varnothing 58$  mm (please follow Figure 1.11(b)). The nozzle throat is  $o = \varnothing 30$  mm and no needle is considered. The injection velocity (using air) is normal to the cylindrical wall. Its magnitude ( $V = 0.30$  m/s) ensures a bulk flow velocity of 10 m/s just upstream the nozzle head. Therefore, a similar Mach number is modelled like during the nominal speed investigation (see section 2.3.2.1). At the inlet 1.5% turbulence intensity is prescribed, which corresponds to the characterization of Anthoine (2000).

The droplet size distribution of the poly-dispersed 3D model (shown in section 6.3) is taken as a reference. However, to keep the Stokes number constant, the diameters corresponding to every class are divided by 1.6 (similarly to the halved distribution shown in Figure 6.17). The flow-rate of water is set to  $\dot{Q}_m = 1.10 \cdot 10^{-3}$  kg/(s · rad), which keeps the volume fraction constant.

An instantaneous vorticity plot of the whole field can be seen in Figure 8.6(a), which visualizes the characteristic vortex shedding phenomenon. A close-up view of the inhibitor region including the instantaneous droplets' locations (Figure 8.6(b)) reveals the blockage of the straight obstacle. From the inhibitor tip the shear layer of the air-phase and the quasi shear layer of the droplets are distinguishable. However, while in the 2D-like test section with two-phase PIV (section 6.4.4) the quasi shear layer of the droplets is observed closer to the obstacle base, in the present simulation it is on the opposite side of the air shear layer (i.e. in the free stream region). As the air shear layer always follows the curvature of the vena contracta, when the droplets are injected radially, their initial momentum and their time lag (due to their long characteristic time) do not allow them to enter in the shear layer with the air-phase. Thus the droplets of the S2 segment are initially separated from the shed vortices. However, as it can be seen in the plot, the developing vortical structures start to entrain the smaller droplets from the free stream region. Furthermore, in the centre of the shed vortical structures only middle-class and large

particles (originating from the S3 segment) can be found, which are characterized by a longer relaxation time. The smaller droplets (which have a correspondingly shorter characteristic time) respond quicker to the flow. Therefore, due to the local rotation of the forming vortices, the smaller droplets can be found in the periphery of the vortical structures.

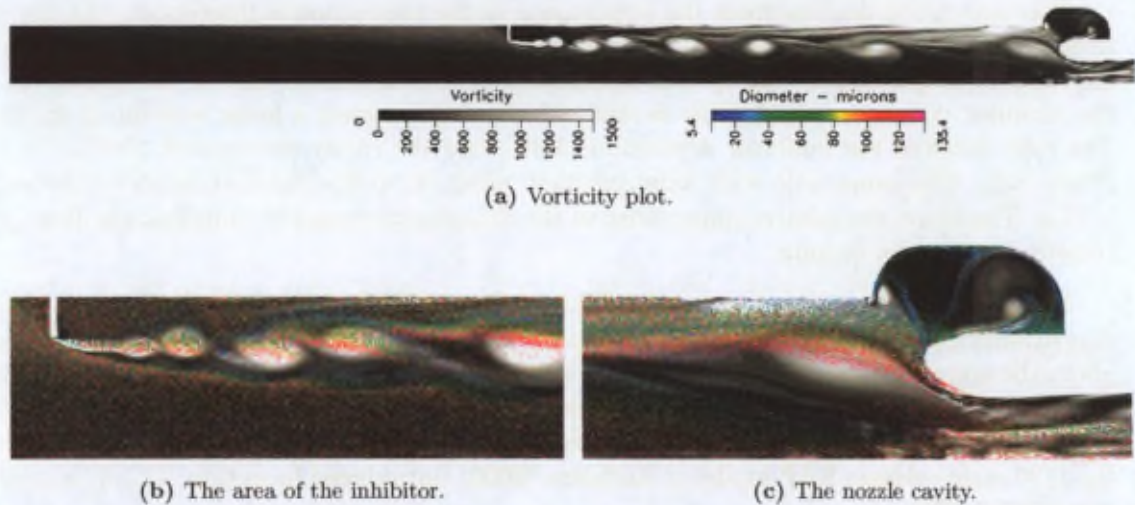


FIGURE 8.6 – Instantaneous droplet distributions with radial flow injection in the axisymmetric domain (A common legend, shown in Figure 8.6(a) is applicable to all the sub-figures).

Further downstream, close to the nozzle (Figure 8.6(c)) only the largest droplets reside in the centre region of the vortices, while the smaller ones are encircling the vortical structures. This corresponds well to the observations of e.g. Godfroy and Guéry (1997). Consequently, as the vortices interact with the nozzle head, packets of droplets of smaller classes are transported in the cavity. Most of them are entrapped and contribute to the accumulation. In the cavity two counter-rotating structures can be seen, which appear to be stable in time considering both their location and size.

Due to the inertia of the larger droplets, they tend to cross the highly fluctuating flow region and are transported by the free stream flow close to the axis of the model. Therefore, most of them exit through the throat or impinge on the convergent part of the nozzle<sup>3</sup>. Only few large particles are observed inside the cavity. Thus, their contribution is low to the liquid entrapment process.

The depositing liquid mass in the axisymmetric case is also computed on the inhibitor and in the cavity during 1.4 FTs. In the cavity an entrapment rate of 5.9% resulted, which is about 8.4-times higher than in the original quasi-axial simulation using the poly-dispersed droplet distribution (section 6.3.2). On the straight inhibitor a deposition rate of 1.4% is observed, which is about 13.3-times lower than in the quasi axial poly-dispersed case.

The liquid deposition on the inhibitor is about 1/4 of the amount of the entrapped droplets in the cavity (Table 8.1). Although, this ratio is considerably lower than the one observed with the rectangular 2D-like geometry, the potential of dripping is still quite large. Therefore, this aspect should be further investigated preferably with 3D simulation on the real geometry with flexible inhibitor ring. If the importance of dripping is confirmed, the liquid behaviour on the inhibitor should also be assessed.

<sup>3</sup>between the nozzle tip and the throat

Table 8.1 – *The importance of dripping*

Case	Dripping [%]	Entrapment [%]	$\frac{\text{Dripping}}{\text{Entrapment}}$
Poly-dispersed	19.1	0.7	27.3
Quasi radial	3.4	0.07	48.6
Axisymmetric radial	1.4	5.9	0.24

## 8.2 The entrapment process

The process, by which liquid droplets travelling in the continuous-phase are finally entrained in the stagnation area modelling the nozzle cavity to contribute to the liquid accumulation is called presently *entrapment*.

As it can be seen from the previous chapters and section 8.1.2, the flow fluctuations within the inhibitor wake might have a major influence on the entrapment. However, based on the size (and therefore the characteristic time) of the droplets, their path may or may not be governed by the continuous-phase. Accordingly, the entrapment can be divided into two mechanisms:

- inertia-driven transport;
- vortex-driven transport (mixing).

As demonstrated in section 6.3.3, since the large droplets have a characteristic time ( $\tau_p$ ) that is considerably longer than the one of the flow ( $\tau_f$ ), their response to the higher frequency fluctuations associated e.g. with the passage of vortical structures is strongly limited. Therefore, they tend to behave according to their initial momentum, which is defined by the developed upstream flow and probably by gravity as well. As they pass in front of the inhibitor tip, they might be slightly deviated by the curved main flow acceleration in the vena contracta (see Figure 6.21(c) and 6.15(a)), but due to their inertia they do not respond to the fluctuations that are present in the wake of the inhibitor.

Consequently, the tendency of the large droplets for being entrapped is defined by their velocity vector, when they pass above the inhibitor tip, their transversal distance from the inhibitor tip at the same moment, and the *obstacle tip to nozzle tip distance* (OT2NT).

On the other hand, the small droplets have a shorter characteristic time, which is closer to the one of the flow. Although they are not tracers, they tend to respond to the flow fluctuations, which allows the continuous-phase to guide them.

A shear layer is attached to the inhibitor. Due to its unstable behaviour, vortices are generated, which are transported by the main flow towards the nozzle. They may follow the mean streamlines of the flow, enter the main recirculation region downstream the obstacle or lift up to the free stream flow, as explained in chapter 7. In either case, droplets encircle the vortical structures. The smaller droplets remain on the periphery of the vortices and they are thus transported. This behaviour can be seen numerically (see Figure 6.15(a)) and reported e.g. by Godfroy and Guéry (1997); Miller (2001). Figure 8.7 indicates two instantaneous images of the droplet-phase, where the circles indicate the location of the vortical structures of the air-phase extracted from the corresponding tracer acquisitions. These examples also show a lower local droplet concentration in the vicinity of the vortices and a higher concentration encircling the vortex core regions, which finally enhances the mixing of droplets.

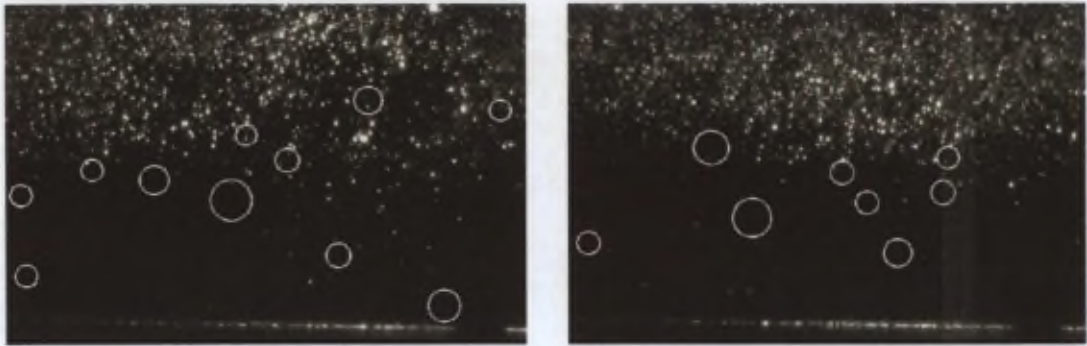


FIGURE 8.7 – Instantaneous vortex-droplet distribution in FoV#2 of the two-phase PIV investigation.

On statistical basis the mixing behaviour induced by vortices can be demonstrated by comparing the typical vortex locations and the mean droplet concentration. Figure 8.8(a) shows once again the droplet concentration map of the two-phase PIV experiments. In the figure the area corresponding to transversal concentration gradient can be identified (between the high concentration free stream and the minimum concentration near-sidewall region). Focusing on the same area in Figure 8.8(b), a high vortex concentration can be observed.

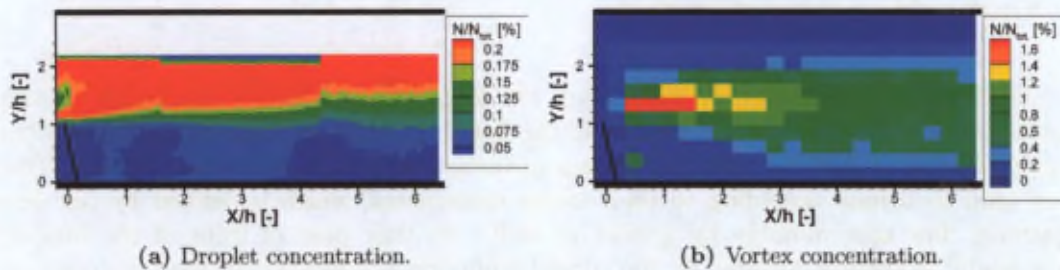


FIGURE 8.8 – Statistical vortex-droplet distribution in the two-phase PIV investigation.

As shown in Figure 7.4(a), the vortices are interacting with the nozzle tip. Then, some are deviated towards the throat, the others enter the cavity. All of them are carrying smaller droplets, which thus may enter in the cavity with the latter structures. Most of these droplets hit one wall of the cavity, and contribute to the accumulation.

### 8.3 Summary on the accumulation process

In the present chapter at first the dripping phenomenon is further assessed to better understand its importance on the liquid accumulation in the cavity. As it is shown, in the present configuration the dripping is the main contributor with respect to the droplet entrapment.

By performing complementary simulations, the potential of dripping is investigated. The obtained results suggest that this process is less important in a more realistic motor configuration (with radial injection and in axisymmetric geometry).

Furthermore, the entrapment process is analysed, which represents the accumulation induced by the interaction between the continuous-phase and the droplet-phase. The smaller droplets are found to be transported by the vortices into the cavity. The air-phase has less effect on the

path of the larger droplets, which may fall into the cavity due to their inertia. Finally, these two mechanisms give the total quantity of the entrapped liquid.



## Chapter 9

# Conclusions and future perspectives

### 9.1 Conclusions

The first stage of spacecrafts (e.g. Ariane 5, Vega, Shuttle) generally consists of *solid propellant rocket motors* (SRM). These are typically operating during the first part of the lift-off providing most of the thrust to accelerate the vehicle. On the one hand, to shorten the overall length, the nozzle is submerged in the last segment of solid propellant. This means that the convergent, the sonic throat and a part of the divergent are surrounded by solid propellant. This integration allows the orientation of the nozzle to provide adaptation of the rocket trajectory during the launch. During the combustion, the regression of the solid propellant surrounding the nozzle integration part leads to the formation of a cavity around the nozzle lip. On the other hand, the propellant combustion generates liquefied alumina droplets coming from chemical reaction of the aluminum composing the propellant grain. The alumina droplets being carried away by the hot burnt gases are flowing towards the nozzle. Meanwhile the droplets may interact with the internal flow. As a consequence, some of the droplets are entrapped in the cavity instead of being exhausted through the throat. The accumulation of the droplets in the cavity generates an alumina puddle, also called slag. This slag reduces the performance of the solid propellant motor due to its dead weight absence of impulse generation, sloshing, etc. In case of the EAP of Ariane 5 the mass of the accumulated droplets can reach up to 2 tons by the end of the launch in each motor.

The aim of the present study is to characterize the slag accumulation process in a simplified model of the MPS P230 solid rocket motors of the Ariane 5 launcher using primarily optical experimental techniques. Therefore, at first a 2D-like cold-gas model is defined and built, which represents the main geometrical features of the real motor (presence of an inhibitor, a nozzle and a cavity) and allows to approximate non-dimensional parameters of the internal two-phase flow (e.g. Stokes number, volume fraction). The model is attached to a wind-tunnel that provides quasi-axial flow (air) injection. A water spray device in the stagnation chamber realizes the models of the alumina droplets, which are accumulating in the aft-end cavity of the motor. The planar transparent walls of the test section give an optical access to observe various flow events.

To be able to carry out an experimental investigation, at first the available measurement techniques had to be adapted to the two-phase flow condition of the facility. The related conclusions are described in section 9.2. A parametric liquid accumulation assessment is performed experimentally in the model to identify the most influential parameters of the slag deposition. In the followings, the flow field is analysed experimentally, which is supported by numerical simulations to understand the main driving forces of the accumulation process. The obtained

databases and achievements are concluded in section 9.3.

## 9.2 Conclusions on the measurement techniques

During the project mainly two optical experimental techniques are used: *Level Detection and Recording* (LeDaR) and *Particle Image Velocimetry* (PIV).

With LeDaR liquid free surfaces can be detected in a plane, which makes it a good candidate for the parametric study of the accumulation rate tendencies in the cavity. However, it requires clear imaging of the investigated surface. While the spray is operating, the wetting of the wall and the frequent dripping deteriorate the measurement quality. Therefore, the inhibitor is inclined and fitted with a liquid extraction system, the cavity wall is treated and the optical properties of the acquisition system are optimized to minimize the effect of the disturbances. The processing algorithm is also redeveloped and more robust detection filters are implemented. Thus, the adapted LeDaR technique has been significantly improved to be capable of delivering good quality information in harsh condition.

The PIV technique is used to determine the velocity field of the flow in the mid-span plane of the test section. The flow velocity is obtained with the help of tracer particles through image analysis. However, in two-phase flow configuration the acquisitions contain both tracer and droplet images, which the cross-correlation algorithm cannot distinguish. As a result, the droplets would bias the air-phase velocity measurement. Thus, the images of the two phases have to be separated. Several methods are proposed and evaluated to separate the images of the two phases either optically or through image processing. Finally, the UV technique is chosen and developed within the frame of the present research work. It is based on a laser producing green and UV light pulses simultaneously. The two wavelengths excite different fluorescent dyes, which emit light at distinct wavelengths. Therefore, using a pair of synchronized cameras equipped with proper optical filters, the images of the two phases can be separated simultaneously and purely optically. During the development its applicability is verified and its performance is demonstrated. Once principally operational, it still needed to be adapted to the wet environment of the test section. It required the development of a dynamic background subtraction algorithm, frequent cleaning and wall treatment during the test campaigns.

## 9.3 Conclusions on the slag accumulation process

At first a parametric study is performed with the adapted LeDaR technique using the available configurations of the facility to identify the most influential parameters of the liquid accumulation process.

As a result, the primary importance of the *obstacle tip to nozzle tip distance* ( $OT2NT$ ) is pointed out. This parameter includes the inhibitor height ( $h$ ) and the nozzle throat opening<sup>1</sup> ( $o$ ).  $OT2NT$  indicates how much a droplet passing just at the inhibitor tip should deviate transversally to leave through the nozzle and not to be entrapped in the cavity. The cavity width ( $w$ ) and the reference flow velocity ( $U_0$ ) are considered to have a secondary role during the accumulation. The inhibitor position ( $L_i$ ) and the *obstacle-to-nozzle ratio* ( $O2NR$ ) do not have a significant influence in the present model.

With the attempt to understand better the mechanisms driving the accumulation process,

---

<sup>1</sup>or nozzle head location

the flow field of the nominal LeDaR configuration is studied. The main mean flow topology is characterized in single-phase flow configuration using the PIV technique. The area of interest (the mid-span plane from the inhibitor until the nozzle throat and the cavity) is divided into 12 FoVs<sup>2</sup>, which provide high resolution and good local measurement quality. In the absence of quasi radial flow injection through the sidewall a recirculation region is observed in the mean flow fields downstream the inhibitor and inside the cavity. The velocity fluctuation plots visualize the inhibitor shear layer and the wake of the inhibitor, which represent high fluctuation values and suggest the shedding of vortical structures.

The nominal configuration is modelled numerically by Lema et al. (2007) with 3D LES simulations both in single-phase and two-phase flow configuration. Using the above-mentioned experimental flow field, the numerical data are successfully validated in terms of the statistical flow quantities. In the two-phase flow simulations with poly-dispersed droplet size distribution the Lagrangian phase does not appear to influence outstandingly the mean flow quantities. Concerning the accumulation, primarily small particles are observed in the cavity, which suggests the importance of the droplet size on the droplet entrapment process. Therefore, based on the poly-dispersed case two new simulations are performed: one with doubled and one with halved droplet size distribution at a constant liquid mass fraction. In both cases the amount of accumulation (obtained with a mass counter user subroutine) became higher than with the nominal distribution. It reveals that the small droplets are carried by the air and therefore they may mix easily in the recirculation zone and finally be entrapped in the cavity. On the other hand, the large droplets are not able to follow the air motion. Therefore, in function of the *OT2NT*, due to their inertia they may also be entrapped in large quantities in the cavity.

The area of interest between the inhibitor and the cavity entrance is also measured in two-phase flow configuration using the developed two-phase PIV technique. Unfortunately, the experiments had to be performed at a reduced reference velocity in the nominal geometry. In order to attempt to keep the non-dimensional parameters unchanged, for this campaign a different spray device is used. In terms of the statistical flow quantities a decrease is observed in the main recirculation bubble size and a damping is seen in the transversal velocity component fluctuation levels in two-phase flow configuration with respect to the single-phase flow case. The noticed droplet effects are similar to those of the numerical simulations. Additionally, the motion of the droplet-phase is analysed and compared to the simultaneous mean air-phase motion (using the experimental data). In the wake of the inhibitor a significant mean velocity difference is discovered between the air-phase and the droplet-phase (locally represented by large droplets). It shows that due to the associated long characteristic time, the droplets are not able to adapt their velocity to the locally low air velocity.

To investigate the droplets' mixing mechanism, the instantaneous flow structure properties are analysed. The vortices are detected using the various databases (experimental and numerical, single-phase and two-phase flow configuration) with a wavelet-analysis based algorithm. Comparing the vortical structures of the numerical and the experimental databases, consistently smaller core diameters are observed experimentally. As discussed, this might be caused by the locally coarse 3D hybrid numerical mesh in the wake area. The analysis shows that the vortices are mainly created by the inhibitor shear layer and are populated primarily in the wake of the inhibitor, where their energy is gradually dissipated. Vortices are also found in the cavity centre representing locally higher energy, but in low number. The comparison between single-phase and two-phase cases (relying mainly on the two-phase PIV data) shows the damping effect of the droplets on the vortices. As mentioned in the previous paragraph, the droplets are not able to respond to the changes of the air-phase motion. However, they represent a considerable

---

<sup>2</sup>fields-of-view

volume fraction, which allows them to act on the continuous-phase and damp the fluctuations. Thus, the vortices may become weaker. As observed also from the statistical flow quantities, the two-phase PIV experiments give more pronounced modification on the vortical structure properties than the poly-dispersed numerical simulation compared to the corresponding single-phase configuration.

The energetic vortices of the inhibitor wake are found to drive the mixing phenomenon. As the smaller droplets are able to respond to the flow fluctuations, they encircle the vortices and are thus entrained in the recirculation zone or during the vortex-nozzle interaction they are probably entrapped directly in the cavity.

Another mechanism of the droplet entrapment is related to the large droplets, which are not responding considerably to the flow fluctuations. In function of the  $OT2NT$  due to their initial inertia (at the inhibitor tip) they may fall directly into the cavity.

Besides the entrapment mechanisms a new phenomenon is identified. As the droplets are injected upstream the inhibitor, a large liquid quantity is depositing on it, which finally produces dripping drops. In the experimental model the dripping has an important contribution to the total accumulation. Preliminary numerical simulations suggest that its importance may be lower in case of radially injected flow, but its contribution could be still significant during the accumulation process.

According to the present understanding the entrapment mechanisms and the dripping phenomenon together give the total amount of liquid accumulation in the nozzle cavity.

## 9.4 Future perspectives

Through an experimental and numerical single-phase and two-phase flow investigation the present research pointed out the main phenomena acting during the slag accumulation process in a simplified cold-gas model.

To complete the current database, numerical simulations should be performed in the conditions of the two-phase flow PIV experiments. Therefore, the numerical tools could be validated directly in the presence of droplets.

Related to the slag accumulation process most importantly the potential of the dripping phenomenon should be further assessed. The influence of the radial injection should be investigated preferably in a representative axisymmetric geometry with a proper flexible inhibitor ring between the S2 and the S3 segments. The deformed shape of this obstacle might have a large impact on the characteristics of the liquid deposition (drop seed formation location and drop size) and therefore on the amount of dripping.

In the present study axially injected flow configuration is investigated, which can be considered as the contribution of the S2 segment of the motor to the accumulation process. Therefore, the effect of the S3 segment should also be incorporated. Namely, the interaction between the injected droplets and the vortices passing just above the injection surface should be assessed. As the droplet injection through a porous medium appears to be challenging, the corresponding study might not be realizable through cold-gas experiments.

Concerning the entrapment process, the transport mechanism of the various droplet classes should be quantified. Their response to the typical vortices of the EAP configuration over the length between the inhibitor and the nozzle tip should be described. Such a quantitative

droplet-vortex interaction model would enable to elaborate the vortex and the inertia driven mechanisms and the eventual hybrid phenomena. Thus, the entrapment rate could be better estimated during future motor design and analysis.

Finally, the currently developed two-phase PIV method is applicable to assess any kind of two-way coupled gaseous fluid in the presence of liquid droplets. Although the wetting of the boundaries are complicating the experiments and the image processing, with a limited amount of droplets on the windows the technique is still operational.



# Bibliography

- (2000, March). Ariane 5 user's manual (issue 3, revision 0). Issued and approved by Arianespace, by Mugnier, D.
- (2002, May). Internal aerodynamics in solid rocket propulsion. In *RTO AVT/VKI Special Course, edited by Anthoine, J. and Kuentzmann, P.* von Karman Institute, Rhode-Saint-Genèse, Belgium.
- (2004, November). Ariane 5 user's manual (issue 4, revision 0). Issued and approved by Arianespace, by Perez, E.
- Adrian, R. J. and C. S. Yao (1983, September). Development of pulsed laser velocimetry (plv) for measurement of turbulent flow. In *Proceedings of the 8<sup>th</sup> Symposium on Turbulence*.
- Anthoine, J. (2000, October). *Experimental and Numerical Study of Aeroacoustic Phenomena in Large Solid Propellant Boosters*. Ph. D. thesis, von Karman Institute for Fluid Dynamics; Université Libre de Bruxelles.
- Anthoine, J., J.-M. Buchlin, and A. Hirschberg (2002). Effect of nozzle cavity on resonance in large SRM: theoretical modeling. *Journal of Propulsion and Power* 18(2), 304-311.
- Beckstead, M. W. (1977). A model for solid propellant combustion. In *Proceedings of the 14<sup>th</sup> Jannaf Combustion Meeting*.
- Boëdec, T. and S. Simoëns (2001). Instantaneous and simultaneous planar velocity field measurements of two phases for turbulent mixing of high pressure sprays. *Experiments in Fluids* 31, 506-518.
- Boraas, S. (1990, May). SRM/RSRM slag motion study. Thiokol TWR-50405.
- Bouchez, D., L. Zimmer, and M. L. Riethmuller (2000, August). Optical detection and characterisation of interfaces. In *Proceedings of the 9<sup>th</sup> International Symposium on Flow Visualization*.
- Brackmann, U. (2000). *Lambdachrome® Laser Dyes*.
- Cesco, N. (1997, Novembre). *Étude et modélisation de l'écoulement diphasique à l'intérieur des propulseurs à poudre*. Ph. D. thesis, École Nationale Supérieure de l'Aéronautique et de l'Espace, Toulouse, France.
- Cesco, N., L. Dumas, A. Hulin, T. Pevergne, and Y. Fabignon (1997, July). Stochastic models to the investigation of slag accumulation in a large solid rocket motor. AIAA Paper 97-3118. In 33rd AIAA/ASME/SAE/ASEE Joint Propulsion Conference & Exhibit, July 6-9, 1997, Seattle (WA), USA.
- Cohen, N. S. (1983). A pocket model for aluminum agglomeration in composite propellants. *AIAA Journal* 21(5), 720-725.

- Delfour, A., J.-P. Lafforgue, M. Prévost, and P. Tarrin (1998, March). Répartition granulométrique dans une section droite du jet d'un propulseur LP2. In *3<sup>ème</sup> Colloque R&T à l'ENSMA, 25-27 March 1998*. Poitiers, France.
- Dias Pereira, M. I. (1999). *Bubble formation at a multiple orifice plate submerged in quiescent liquid*. Ph. D. thesis, von Karman Institute for Fluid Dynamics; Université Libre de Bruxelles.
- Dias Pereira, M. I. and M. L. Riethmuller (1998). PIV in two-phase flows: simultaneous bubble sizing and liquid velocity measurements. In *Proceedings of the Ninth International Symposium on Applications of Laser Techniques to Fluid Mechanics*. Lisbon, Portugal.
- Dotson, K. W., J. W. Murdock, and D. K. Kamimoto (1999). Launch vehicle dynamic and control effects from solid rocket motor slag ejection. *Journal of Propulsion and Power* 15(3), 468-475.
- Driscoll, K. D., V. Sick, and C. Gray (2003). Simultaneous air/fuel-phase PIV measurements in a dense fuel spray. *Experiments in Fluids* 35, 112-115.
- Dupays, J. (2002, October). Two-phase unsteady flow in solid rocket motors. *Aerospace Science and Technology* 6(6), 413-422.
- Dupays, J., Y. Fabignon, O. Orlandi, and J.-F. Trubert (2000, June). Combustion of aluminium particles in solid rocket motors. In *Proceedings of the ODAS 2000, ONERA/DLR Aerospace Symposium*. Berlin, Germany.
- Duterque, J. (1996, May). Experimental studies of aluminum agglomeration in solid rocket motors. In *Proceedings of the 4<sup>th</sup> International Symposium on Special Topics in Chemical Propulsion, 27-31 May 1996*. Stockholm, Sweden.
- Duterque, J. and D. Lambert (1998, March). Synthèse des travaux sur l'agglomération de l'aluminium dans le propergol du MPS P230. In *3<sup>ème</sup> Colloque R&T à l'ENSMA, 25-27 March 1998*. Poitiers, France.
- Elghobashi, S. E. (1994). Predicting particle-laden turbulent flows. *Applied Scientific Research* 52, 309-329.
- Fabignon, Y., J. Dupays, G. Avalon, F. Vuillot, N. Lupoglazoff, G. Casalis, and M. Prévost (2003). Instabilities and pressure oscillations in solid rocket motors. *Aerospace Science and Technology* 7(3), 191-200.
- Fabignon, Y., J.-F. Guéry, F. Godfroy, P. Le Helley, J. Hylkema, L. Jacques, G. Lavergne, and P. Villedieu (2000, November). Slag accumulation in large segmented solid motors with a submerged nozzle. In *2<sup>nd</sup> European Conference on Launcher Technology, 21-24 November 2000*. Rome, Italy.
- Fabignon, Y., P. Kuentzmann, F. Vuillot, M. Prévost, R. Bec, T. Robert, and P. Marion Duval (2000, November). A survey of french research and technology program on the internal aerodynamics of segmented solid motors. In *2<sup>nd</sup> European Conference on Launcher Technology, 21-24 November 2000*. Rome, Italy.
- Farge, M. (1992). *Wavelet transforms and their applications to turbulence.*, Volume 24 of *Annual Review of Fluid Mechanics*, pp. 395-457. Annual Reviews Inc.
- Farge, M., K. Schneider, and N. Kevlahan (1998). Coherent structures eduction in wavelet-forced two-dimensional turbulent flows. In *Proceedings of the IUTAM Symposium in Dynamics of Slender Vortices (E. Krause and K. Gersten, editors)*. Kluwer Academic Publishers.

- Figliola, R. S. and B. D. E. (1991). *Theory and Design for Mechanical Measurements*. John Wiley and Sons.
- Foucat, J. M. and M. Stanislas (2002). Some considerations on the accuracy and frequency response of some derivative filters applied to particle image velocimetry vector fields. *Measurement Science and Technology* 13, 1058–1071.
- Frederick, R. A. (1990, September). DS-8 slag accumulation analysis. Sverdrup/AEDC Memo 90-294.
- Geisler, R. L. (2002). A global view of the use of aluminum fuel in solid rocket motors. In *Proceedings of the 38<sup>th</sup> AIAA/ASME/SAE/ASEE Joint Propulsion Conference and Exhibit*. Indianapolis, Indiana: AIAA Paper 2002-3748.
- Godfroy, F. and J.-F. Guéry (1997, July). Unsteady eulerian flow analysis of solid rocket motor slag. AIAA Paper 97-2859. In 33rd AIAA/ASME/SAE/ASEE Joint Propulsion Conference & Exhibit, July 6–9, 1997, Seattle (WA), USA.
- Gore, R. A. and C. T. Crowe (1989). Effect of particle size on modulating turbulent intensity. *International Journal of Multiphase Flow* 15(2), 279–285.
- Grünfeld, G., H. Finke, J. Bartelheimer, and S. Krüger (2000). Probing the velocity fields of gas and liquid phase simultaneously in a two-phase flow. *Experiments in Fluids* 29, 322–330.
- Guéry, J.-F., G. Avalon, F. Vuillot, F. Plourde, J. Anthoine, and B. Platet (2000, November). Use of cold flow experiments in the ASSM program - lessons and results. In *2<sup>nd</sup> European Conference on Launcher Technology, 21-24 November 2000*. Rome, Italy.
- Gui, L., S. T. Wereley, and Y. H. Kim (2003). Advances and application of the digital mask technique in particle image velocimetry experiments. *Measurement Science and Technology* 14, 1820–1828.
- Isakowitz, S. J., J. P. Hopkins Jr., and J. B. Hopkins (1999). *International reference guide to space launch systems*. American Institute of Aeronautics and Astronautics.
- Jackson, T. L., F. Najjar, and J. Buckmaster (2005, September-October). New aluminum agglomeration models and their use in solid-propellant-rocket simulations. *Journal of Propulsion and Power* 21(5), 925–936.
- Jeong, J. and F. Hussain (1995, February). On the identification of a vortex. *Journal of Fluid Mechanics* 285, 69–94.
- Johnston, W. A., J. W. Murdock, S. Koshigoe, and P. T. Than (1994, June). Slag accumulation in the Titan SRMU. AIAA Paper 94-3279.
- Khalitov, D. A. and E. K. Longmire (2002). Simultaneous two-phase PIV by two-parameter phase discrimination. *Experiments in Fluids* 32, 252–268.
- Kosiwczuk, W. (2006, July). *Mesure simultanée des vitesses des gouttes et du gaz en mélange diphasique par PIV et fluorescence*. Ph. D. thesis, Université de Rouen.
- Kosiwczuk, W., A. Cessou, B. Lecordier, and M. Trinité (2003, September). Simultaneous velocity field measurements in two-phase flows for turbulent mixing of sprays by means of two-phase PIV. In *5<sup>th</sup> International Symposium on Particle Image Velocimetry*. Busan, Korea: Paper 3229.

- Kosiwczuk, W., A. Cessou, M. Trinité, and B. Lecordier (2005, September). Simultaneous velocity field measurements in two-phase flows for turbulent mixing of sprays by means of two-phase PIV. *Experiments in Fluids* 39(5), 895–908.
- Kovalev, O. B. (2002). Motor and plume particle size prediction in solid-propellant rocket motor. *Journal of Propulsion and Power* 18(6), 1199–1210.
- Laboureur, D. (2007, June). Experimental and numerical investigation of Taylor flow. VKI Project report 2007-14.
- Law, C. K. (1973). A simplified theoretical model for the vapor phase combustion of metal particles. *Combustion Sciences and Technology* 7, 197–212.
- Le Helley, P., S. Coste, and T. Pevergne (2000, November). Influence of the unsteady flow on the alumina flux impinging the nozzle and the aft dome of the Ariane 5 booster. In *2<sup>nd</sup> European Conference on Launcher Technology, 21-24 November 2000*. Rome, Italy.
- Legrand, B., L. Catoire, C. Chauveau, and I. Gökalp (2000, November). Combustion of levitated aluminum in CO<sub>2</sub>/HCl mixture. In *2<sup>nd</sup> European Conference on Launcher Technology, 21-24 November 2000*. Rome, Italy.
- Lema, M. R. (2005, February). Numerical study of the entrapment and accumulation of droplets in solid rocket motors (SRM). Spanish Trainee Program Report EWP-2275.
- Lema, M. R., P. Rambaud, and J. Anthoine (2005, October). Entrapment and accumulation of droplets in stagnant areas - "numerical study - part 1". VKI Contract report 2005-50.
- Lema, M. R., P. Rambaud, and J. Anthoine (2007, September). Entrapment and accumulation of droplets in stagnant areas - "numerical study - part 2". VKI Contract report 2006-33.
- Lema, M. R., P. Rambaud, J. Anthoine, and J. Steelant (2006). Assessment of slag accumulation in solid rocket boosters: Part III, two-phase flow CFD. In *Proceedings of the 42<sup>nd</sup> AIAA/ASME/SAE/ASEE Joint Propulsion Conference and Exhibit*. Sacramento (CA): AIAA Paper 2006-4431.
- Lindken, R. and W. Merzkirch (2002). A novel PIV technique for measurements in multiphase flows and its application to two-phase bubbly flows. *Experiments in Fluids* 33, 814–825.
- Lupoglazoff, N. and F. Vuillot (1996, January). Parietal vortex shedding as a cause of instability for long solid propellant motors. Numerical simulations and comparisons with firing tests. AIAA Paper 96-0761.
- Lupoglazoff, N., F. Vuillot, J. Dupays, and Y. Fabignon (2000, November). Numerical simulations of the unsteady flow inside Ariane 5 P230 SRM booster with burning aluminum particles. In *2<sup>nd</sup> European Conference on Launcher Technology, 21-24 November 2000*. Rome, Italy.
- Melcher, J. C., H. Krier, and R. L. Burton (2002). Burning aluminum particles inside a laboratory-scale solid rocket motor. *Journal of Propulsion and Power* 18(3), 631–640.
- Meyer, R. X. (1992). In-flight formation of slag in spinning solid propellant rocket motors. *Journal of Propulsion and Power* 8(1), 45–50.
- Meyer, R. X. (1996). Coning instability of spacecraft during periods of thrust. *Journal of Propulsion and Power* 33(6), 781–788.

- Miller, R. S. (2001). Effects of nonreacting solid particle and liquid droplet loading on an exothermic reacting mixing layer. *Physics of Fluids* 13(11), 3303–3320.
- Moraitis, C. S. (1987, June). Particle image displacement velocimetry: application to high-speed flows and development of processing techniques. VKI Project report 1987-16.
- Myrillas, K. (2006, June). VOF computation of the deformation of a liquid surface. VKI Project report 2006-24.
- Najjar, F. M., A. Haselbacher, S. Balachandar, and R. D. Moser (2006, July). Simulations of droplet nozzle impact and slag accumulation in the RSRM. AIAA Paper 2006-4588. In 42<sup>nd</sup> AIAA/ASME/SAE/ASEE Joint Propulsion Conference & Exhibit, July 09–12, 2006, Sacramento (CA), USA.
- Nogueira, S., R. G. Sousa, A. M. F. R. Pinto, M. L. Riethmuller, and J. B. L. M. Campos (2004). Simultaneous PIV and pulsed shadow technique in slug flow: a solution for optical problems. *Experiments in Fluids* 35, 598–609.
- Orlandi, O. and Y. Fabignon (2000, November). Numerical simulation of a single aluminum particle in a propellant gas. In 2<sup>nd</sup> European Conference on Launcher Technology, 21-24 November 2000. Rome, Italy.
- Özsoy, E., P. Rambaud, A. Stitou, and M. L. Riethmuller (2005). Vortex characteristics in laminar cavity flow at very low mach number. *Experiments in Fluids* 38, 133–145.
- Peveigne, T. and P. Le Helley (1998, March). Simulation numérique des impacts de particules et du dépôt dans le MPS P230. In 3<sup>ème</sup> Colloque R&T à l'ENSMA, 25-27 March 1998. Poitiers, France.
- Planquart, P., M. L. Riethmuller, A. Joly, and J. M. Detry (2002). Real time optical detection and characterisation of water model free surfaces - application to the study of mold. In *Proceedings of the 4th European Continuous Casting Conference*. Birmingham, United Kingdom.
- Pope, A. (1947). *Wind tunnel testing*. Wiley.
- Régert, T. (2004, June). Experimental investigation of the effect of droplets on coherent structures over an open, rectangular cavity. VKI Project report 2004-16.
- Repellin, O. (1999, June). Experimental characterisation of vortical structures with aeroacoustic effects. VKI Project report 1999-28.
- Rottenkolber, G., J. Gindele, J. Raposo, K. Dullenkopf, W. Hentschel, S. Wittig, U. Spicher, and W. Merzkirch (1999). Spray analysis of gasoline direct injector by means of two phase PIV. In *Proceedings of the 3<sup>rd</sup> Workshop on PIV*. University of California, Santa Barbara.
- Rottenkolber, G., J. Gindele, J. Raposo, K. Dullenkopf, W. Hentschel, S. Wittig, U. Spicher, and W. Merzkirch (2002). Spray analysis of a gasoline direct injector by means of two-phase PIV. *Experiments in Fluids* 32, 710–721.
- Salita, M. (1995, January-February). Deficiencies and requirements in modeling of slag generation in solid rocket motors. *Journal of Propulsion and Power* 11(1), 10–23.
- Salita, M., R. Smith-Kent, M. Golafshani, H.-T. Loh, R. Abel, and D. Pratt (1990, September). Prediction of slag accumulation in SICBM static and flight motors. Thiokol TWR-40259.

- Sambamurthi, J. K. (1996).  $\text{Al}_2\text{O}_3$  collection and sizing from solid rocket motor plumes. *Journal of Propulsion and Power* 12(3), 598–604.
- Sarou-Kanian, V., B. Glorieux, B. Legrand, J. C. Rifflet, F. Millot, and I. Gökalp (2000, November). High temperature properties of liquid Al and  $\text{Al}_2\text{O}_3$  from contactless methods. In *2<sup>nd</sup> European Conference on Launcher Technology, 21-24 November 2000*. Rome, Italy.
- Scarano, F. (2000, March). *Particle Image Velocimetry Development and Application; Investigation of Coherent Structures in Turbulent Flows*. Ph. D. thesis, Università degli Studi di Napoli.
- Scarano, F. and M. L. Riethmuller (1999a). Advances in iterative multigrid PIV image processing. *Experiments in Fluids* 29, S51–S60.
- Scarano, F. and M. L. Riethmuller (1999b). Iterative multigrid approach in PIV image processing with discrete window offset. *Experiments in Fluids* 26, 513–523.
- Schram, C., P. Rambaud, and M. L. Riethmuller (2004). Wavelet based eddy structure eduction from a backward facing step flow investigated using particle image velocimetry. *Experiments in Fluids* 36, 233–245.
- Schram, C. F. (2003, January). *Aeroacoustics of Subsonic Jets: Prediction of the Sound Produced by Vortex Pairing Based on Particle Image Velocimetry*. Ph. D. thesis, Technische Universiteit Eindhoven.
- Stubos, A. K., C. Benocci, E. Palli, G. K. Stoubos, and D. Olivari (1999). Aerodynamically generated acoustic resonance in a pipe with annular flow restrictors. *Journal of Fluids and Structures* 13(6), 755–778.
- Suda, J. M. (2000, June). Experimental investigation on turbulence modification by particles in shear layer flow using 1-6 twin-jet wind tunnel. VKI Project report 2000-20.
- Telara, M., F. Paglia, F. Stella, and M. Giangi (2006a). Pressure oscillations in P230 SRM: numerical simulation. In *Proceedings of the 42<sup>nd</sup> AIAA/ASME/SAE/ASEE Joint Propulsion Conference and Exhibit*. Sacramento, CA (USA).
- Telara, M., F. Paglia, F. Stella, and M. Giangi (2006b). Ariane 5 P230 SRM frontal thermal protection evolution: numerical simulation. In *Proceedings of the 42<sup>nd</sup> AIAA/ASME/SAE/ASEE Joint Propulsion Conference and Exhibit*. Sacramento, CA (USA).
- Theunissen, R., A. Di Sante, M. L. Riethmuller, and R. A. Van den Braembussche (2007). Confidence estimation using dependent circular block bootstrapping: application to the statistical analysis of PIV measurements. *Experiments in Fluids*, DOI 10.1007/s00348-007-0418-8.
- Tóth, B. and J. Anthoine (2003, November). Entrapment and accumulation of droplets in stagnant areas: Experimental simulation and assessment of measurement techniques. VKI Contract report 2004-10.
- Tóth, B. and J. Anthoine (2004, November). Entrapment and accumulation of droplets in stagnant areas - "design of a generic set-up" and "preliminary investigation with PIV-PTV-LeDaR". VKI Contract report 2005-08.
- Tóth, B., M. R. Lema, J. Anthoine, and J. Steelant (2006). Assessment of slag accumulation in solid rocket boosters: Part II, two-phase flow experiments. In *Proceedings of the 42<sup>nd</sup> AIAA/ASME/SAE/ASEE Joint Propulsion Conference and Exhibit*. Sacramento (CA): AIAA Paper 2006-4430.

- Tóth, B., M. R. Lema, J. Steelant, J. Anthoine, and P. Rambaud (2005). Assessment of slag accumulation in solid rocket boosters: Part I, single-phase. In *Proceedings of the 41<sup>st</sup> AIAA/ASME/SAE/ASEE Joint Propulsion Conference and Exhibit*. Tucson (AZ): AIAA Paper 2005-4489.
- Towers, D. P., C. E. Towers, C. H. Buckberry, and M. Reeves (1999). A colour PIV system employing fluorescent particles for two-phase flow measurements. *Measurement Science and Technology* 10, 824-830.
- Traineau, J. C., P. Kuentzmann, M. Prévost, P. Tarrin, and A. Delfour (1992, July). Particle size distribution measurements in a subscale motor for the Ariane 5 solid rocket booster. AIAA Paper 92-3049.
- Traineau, J. C., M. Prévost, F. Vuillot, P. Le Breton, J. Cuny, N. Preioni, and R. Bec (1997, July). A subscale test program to assess the vortex shedding driven instabilities in segmented solid motors. AIAA Paper 97-3247.
- Tran, N. (2004, June). Slag accumulation in a stagnant area. VKI Project report 2004-23.
- Trubert, J. F. (2000, November). Agglomeration and combustion of aluminum particles in solid rocket motors. In *2<sup>nd</sup> European Conference on Launcher Technology, 21-24 November 2000*. Rome, Italy.
- Vardelle, M., C. Escure, P. Fauchais, B. Platet, and G. Lavergne (2000, November). Impact of alumina droplets on cold and hot surfaces. In *2<sup>nd</sup> European Conference on Launcher Technology, 21-24 November 2000*. Rome, Italy.
- Villedieu, P., J. Hylkema, G. Lavergne, B. Platet, Y. Fabignon, M. Vardelle, J.-F. Guéry, F. Godfroy, P. Le Helley, and L. Jacques (2000, November). Slag accumulation in solid propellant rocket motors with a submerged nozzle. In *2<sup>nd</sup> European Conference on Launcher Technology, 21-24 November 2000*. Rome, Italy.
- Vollmers, H. (2001). Detection of vortices and quantitative evaluation of their main parameters from experimental velocity data. *Measurement Science and Technology* 12, 1199-1207.
- Vuillot, F. (1995, July-August). Vortex-shedding phenomena in solid rocket motors. *Journal of Propulsion and Power* 11(4), 626-639.
- Wallner, E. and E. Meiburg (1999). Numerical simulations of two-way coupled particle laden mixing layers. In *Proceedings of the Third International Workshop on Vortex Flows and Related Numerical Methods*.
- Wirzberger, H., Y. Macales, and S. Yaniv (2005, July). Prediction of slag formation in a solid rocket motor. AIAA Paper 2005-4488. In *41<sup>st</sup> AIAA/ASME/SAE/ASEE Joint Propulsion Conference & Exhibit, July 10-13, 2005, Tucson (AZ), USA*.
- Wirzberger, H. and S. Yaniv (2005, July). Prediction of erosion in a solid rocket motor by alumina particles. AIAA Paper 2005-4496. In *41<sup>st</sup> AIAA/ASME/SAE/ASEE Joint Propulsion Conference & Exhibit, July 10-13, 2005, Tucson (AZ), USA*.
- Zaleski, S. and D. Gueyffier (1998, March). Simulation de l'impact de gouttes sur des films liquides. In *3<sup>ème</sup> Colloque R&T à l'ENSMa, 25-27 March 1998*. Poitiers, France.

THE HISTORY OF THE UNITED STATES OF AMERICA

CHAPTER I  
THE DISCOVERY OF AMERICA  
The first discovery of America was made by Christopher Columbus in 1492. He sailed from Spain and reached the island of San Salvador in the West Indies. This was the beginning of the European discovery of the New World.

CHAPTER II  
THE EARLY SETTLEMENTS  
The first permanent European settlement in North America was founded by the Pilgrims in 1620. They came to the Massachusetts coast and established the town of Plymouth.

CHAPTER III  
THE GROWTH OF THE COLONIES  
The colonies grew rapidly in the 17th and 18th centuries. They became more independent of England and developed their own laws and customs.

CHAPTER IV  
THE REVOLUTIONARY WAR  
The Revolutionary War began in 1775 and ended in 1783. The American colonies fought for their independence from Great Britain and won.

CHAPTER V  
THE CONSTITUTION  
The Constitution was written in 1787 and became the supreme law of the United States. It established the three branches of government: the executive, the legislative, and the judicial.

CHAPTER VI  
THE WESTERN EXPANSION  
The United States expanded westward in the 18th and 19th centuries. This was done through the Louisiana Purchase and the acquisition of new territories.

CHAPTER VII  
THE CIVIL WAR  
The Civil War was fought between 1861 and 1865. It was a conflict between the Union and the Confederate States of America over the issue of slavery.

CHAPTER VIII  
THE RECONSTRUCTION PERIOD  
The Reconstruction Period followed the Civil War. It was a time when the Southern States were brought back into the Union and the rights of African Americans were being restored.

CHAPTER IX  
THE GROWTH OF THE UNITED STATES  
The United States continued to grow in the 19th century. It became a world power and its influence spread across the globe.

CHAPTER X  
THE 20TH CENTURY  
The 20th century was a time of great change for the United States. It saw the rise of the industrial revolution, the growth of the middle class, and the emergence of the United States as a superpower.

CHAPTER XI  
THE PRESENT  
The United States today is a democratic nation with a strong economy and a rich cultural heritage. It continues to play a leading role in the world.

CHAPTER XII  
CONCLUSION  
The history of the United States is a story of courage, sacrifice, and the pursuit of the American dream. It is a story that continues to inspire and guide us today.

## Appendices

Alphabetic

## Appendix A

# The existing experimental tools

### A.1 The PIV technique

As its name shows, with the *Particle Image Velocimetry* (PIV) technique one can determine the velocity field of a flow with the help of particle images.

The conventional arrangement during a PIV measurement is shown in Figure A.1.

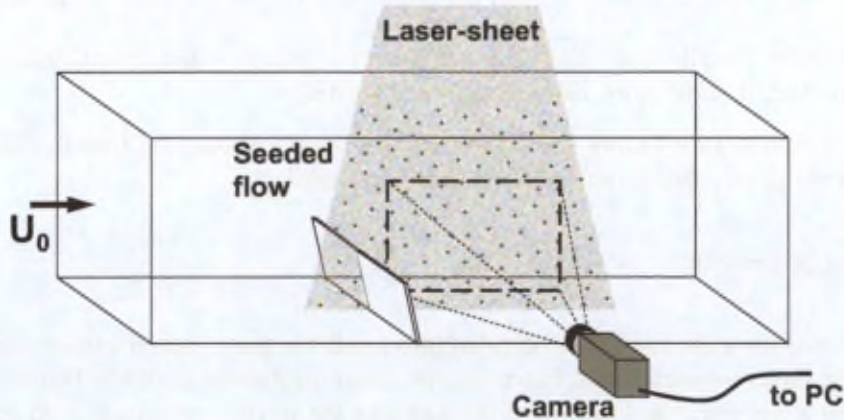


FIGURE A.1 – A conventional PIV arrangement.

Small particles (tracers) are suspended in the fluid. These particles are small enough to follow the flow accurately. A thin light sheet produced by a laser source illuminates the plane of interest. Two successive images are acquired with a camera from the light scattered by the tracers located inside the laser-sheet. The two exposures are separated by a short time interval - called *separation time* ( $\Delta t$ ) -, during which the tracers are moving with the flow. According to their displacement ( $\Delta \vec{r}$ ) and the time interval the velocity can be calculated as:

$$\bar{v} = \frac{\Delta \vec{r}}{\Delta t} \tag{A.1}$$

In practice, the in-plane components of  $\Delta \vec{r}$  ( $r_x, r_y$ ) of equation A.1 can be determined by image processing (using cross-correlation). Thus, the two-dimensional, two-component velocity field of the flow can be determined by the classical PIV technique.

In the followings, the main aspects of the above-mentioned elements are discussed briefly:

- Tracers:

Particles seeded into a flow field act as small tracers allowing the visualization of the movement of the flow in time. On the one hand, the particles must be sufficiently large and efficient in light scattering; they must be detectable by the imaging system. This depends on the recording optics and the illumination source as well. On the other hand, the tracers must be small enough to follow accurately the fluid motion (they should represent  $St \ll 1$ ). Measuring air, generally oil particles of the order of  $1 \mu m$  are used. Finally, the concentration of the particles must be sufficiently high in order to obtain a good correlation of the images and determine the displacement.

- Illumination:

The flow is illuminated by a plane of light (laser) with finite thickness (usually about 1 mm). The light plane should not have variable thickness, because it might cause failure if the flow has substantial gradients across the thickness.

The shape of the light sheet should be smooth. The central plane should really be a planar surface.

The intensity distribution inside the laser-sheet is not very significant during PIV measurements. However, it should not have significant variations.

Even at high velocity flows the images of the tracers should be frozen. Therefore, during measurements in air, double-pulsed YAG lasers are used.

- Image processing:

At first, the recorded images are divided into smaller regions, called *windows* (see Figure A.2). Then, using the cross-correlation function, the mean displacement of the tracer images is determined in each window: the location of the largest peak in the correlation-field gives directly the local motion.<sup>1</sup> Thus, one can obtain the displacement-field of the flow. Knowing the magnification factor of the camera and the separation time ( $\Delta t$ ), the computation of the velocity field is straightforward.

Supposing that the light intensity in the first window,  $a$  is given by the function  $W_a(x, y)$  and that of the second window,  $b$  by  $W_b(x, y)$ . If the intensity distribution of the tracer images is denoted by  $I(x, y)$  it is possible to write:

$$W_a(x, y) = I(x, y) \tag{A.2}$$

$$W_b(x, y) = I(x + \Delta x, y + \Delta y) = I(x, y) \otimes \delta(x - \Delta x, y - \Delta y) \tag{A.3}$$

<sup>1</sup>The maximum value of the cross-correlation of two functions gives a shift ( $\delta$ ). Shifting the first function by this amount, results in a superposition of the two functions.

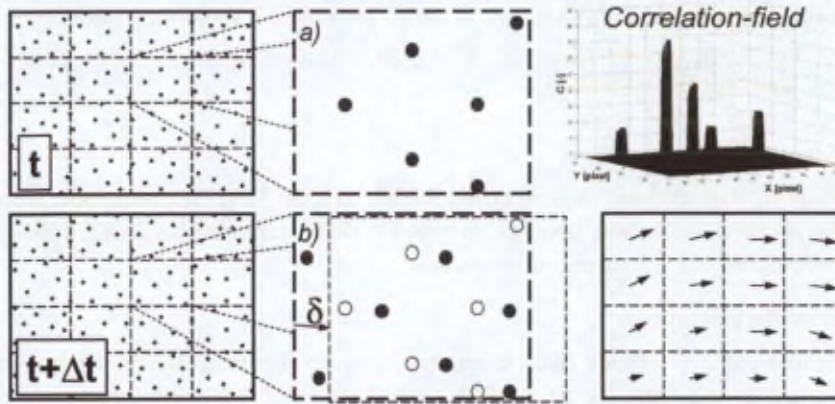


FIGURE A.2 – A conventional PIV arrangement.

Supposing that the first image is simply translated by  $(\Delta x, \Delta y)$ , the convolution with the Dirac function acts as the translation operator.

The cross-correlation of the two functions has to be computed now by its definition:

$$W_a(x, y) \circ W_b(x, y) = C(x, y) \quad (\text{A.4})$$

Applying Fourier transformation can also help in this purpose to facilitate digital processing:

$$F(W_a(x, y) \circ W_b(x, y)) = F(W_a(x, y))F(W_b(x, y))^* \quad (\text{A.5})$$

$$\Rightarrow W_a(x, y) \circ W_b(x, y) = F^{-1}(F(W_a(x, y))F(W_b(x, y))^*) \quad (\text{A.6})$$

- Digital processing:

The size of the interrogation windows ( $W_s$ ) depends on the number of particles and the maximum displacement of the particles in the window. It is suggested that the window must be at least four times as large as the maximum displacement of the particles to obtain the maximum probability that the particle pairs from each exposure will be present inside the corresponding window. It is also suggested, that the maximum displacement normal to the plane should be maximum 30% of the light sheet thickness in order to preserve a large number of the particle pairs in both recordings.

Reducing the time interval causes smaller displacements. In this case the spatial resolution of the flow properties will be better using smaller window sizes, but the accuracy will be worse. The number of particles per window also reduces; since the correlation technique is dependent on the particles, it may make the result noise-dependent.

To increase the measurement density overlapping of the interrogation windows is applied. Determining the overlapping carefully is very important. If it is small, the velocity field will be under-sampled. If it is too high, the velocity field will be over-sampled.

The implemented particularities of *WiDIM* (which software was used during the data processing) are described below. More detailed description is given by the author, Scarano (2000); Scarano and Riethmuller (1999b;a).

1. Iterative processing

In *WiDIM*, the analysis is performed iteratively. At first, a prediction is made by applying all the above-mentioned processing rules. Then, the results can be refined step-by-step, always relying on the previous iteration.

2. Window displacement

There are some particles, which escape from the corresponding region in the second image. That is why the location of the windows in the second image are defined based on the displacement of the previous iteration. In this case it is no matter how large is the displacement to window size ratio, the *signal to noise ratio*<sup>2</sup> will be maximized in the correlation map.

3. Multigrid

Once the windows are "following" the displacement of the tracer images, the window size is not limited anymore by the particle motion. Thus, in order to increase the spatial resolution, the interrogation windows are made finer at each step of the iterative process.

4. Correction of erroneous vectors

For different reasons, there are invalid vectors. They arise from:

- weak local seeding concentration;
- reflections near boundaries;
- laser-sheet misalignment;
- strong out-of-plane motion of the flow.

In *WiDIM*, an automatic erroneous vector detection is performed (based on the SN and a median threshold) and interpolation is applied to compute the displacements at these places.

5. Window distortion

The cross-correlation technique assumed that the particle displacement is uniform in the windows but in reality it is not the case. The quality and the accuracy of the correlation highly depend on the velocity gradient in the correlation windows. Therefore, in the last iteration the windows of the second (*b*) image are distorted according to the local velocity gradient. Thus, combined with the window displacement, the correlation technique can achieve good measurement in high gradient flow field.

6. Sub-pixel interpolation of the correlation function

The cross-correlation function described above (and shown in Figure A.2) gives discrete values of the correlation peak locations. For instance, in a  $32 \times 32$  pixels<sup>2</sup> window there are 1024 possible discrete places of the correlation peak (velocity vector). To obtain a continuous description of the correlation function, the following interpolations are implemented:

- centroid or centre of mass method
- gaussian curve fitting method
- Whittaker's reconstruction filter method

<sup>2</sup>SN, the ratio of the amplitude of the largest- and the second largest peaks in the correlation-field

## A.2 The wavelet analysis based vortex detection

### A.2.1 The detection algorithm

Before entering into the details of the detection principle, a definition of the vortical structures needs to be established. In the present investigation two-dimensional velocity fields are considered (PIV data and the mid-span plane of 3D simulations). Therefore, during the analysis only two-dimensional slices of structures are taken into account. The vortices are defined to be distinct regions exhibiting energetic uniform rotation around a centre point, which can be advected with a certain transport velocity. Accordingly, the rotating structures are assumed to have an axis of rotation normal to the plane of investigation.

To detect the vortices of the available instantaneous flow fields, the continuous wavelet transformation algorithm of Schram et al. (2004) is used, which is based on the method of Farge (1992); Farge et al. (1998).

The  $n$ -dimensional wavelet transform of the function  $f$  is obtained by:

$$\tilde{f}(a, \mathbf{b}) = \langle \Psi_{a, \mathbf{b}} | f \rangle = \int_{\mathbb{R}^n} f(\mathbf{x}) \Psi_{a, \mathbf{b}}^*(\mathbf{x}) d^n \mathbf{x} \quad (\text{A.7})$$

where  $\Psi_{a, \mathbf{b}}$  represents the wavelet family function, which contains the wave-like *mother wavelet* ( $\Psi(\mathbf{x})$ ) at various scales ( $a$ ) and translation ( $\mathbf{b}$ ):

$$\Psi_{a, \mathbf{b}}(\mathbf{x}) = a^{-n/2} \Psi\left(\frac{\mathbf{x} - \mathbf{b}}{a}\right) \quad (\text{A.8})$$

In the continuous wavelet transform the ( $a$ ) and ( $\mathbf{b}$ ) parameters vary continuously between  $[0, \infty]$  and  $[-\infty, \infty]$  respectively.

The mother wavelet function satisfies the admissibility condition, which implies that it has to have a zero mean value. Furthermore, it should have a similar shape to the pattern to be extracted.

The vortices are assumed to have a 2D distribution close to the classical Oseen vortex, which exhibits a Gaussian vorticity pattern. The detection is performed on the *enstrophy-field* (square of the vorticity) to increase the signal-to-noise ratio of the coherent structures with respect to the background noise. Therefore, the 2D *Marr* (Mexican-hat) mother wavelet (see equation A.9 and Figure A.3) is implemented, which has a Gaussian central peak surrounded by negative valued annulus to ensure the zero mean.

$$\Psi_{x, y} = (2 - x^2 - y^2) e^{-\frac{x^2 + y^2}{2}} \quad (\text{A.9})$$

The described detection method identifies all sort of structures, which are represented by high vorticity values (i.e. vortical structures, shear). To discriminate between the shear-like motion and rotation, the algorithm relies on the  $\lambda_2$  criterion of Jeong and Hussain (1995). The  $\lambda_2$  coefficient is the second eigenvalue of the  $S^2 + \Omega^2$  tensor ( $S$  and  $\Omega$  being the symmetric

and the anti-symmetric part of the velocity gradient tensor respectively<sup>3</sup>), which simplifies to equation A.10 in 2D. As it is shown by Jeong and Hussain (1995),  $\lambda_2$  always has a negative value where the rotation is predominant, which is the case in the core of vortices. Therefore the discrimination between shear and rotation can be made.

$$\lambda_2 = \left(\frac{du}{dx}\right)^2 + \left(\frac{du}{dy} \cdot \frac{dv}{dx}\right) \quad (\text{A.10})$$

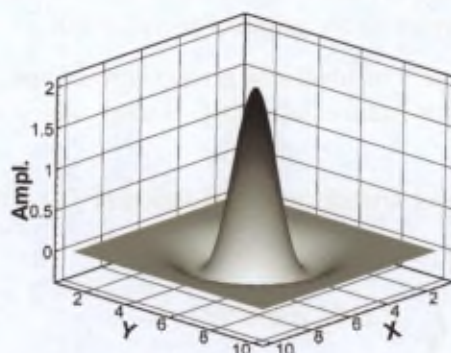


FIGURE A.3 – The 2D Marr mother wavelet.

### A.2.2 The detection criteria

To be able to decide whether an identified structure is an acceptable vortex, the algorithm relies on a set of user-defined thresholds.

At first, thresholds are required on the minimum acceptable vorticity peak and on the maximum  $\lambda_2$  peak. As explained in section A.2.1  $\lambda_2$  is negative in the vortex cores. Therefore, the threshold represents the maximum acceptable value in the centre of the vortical structure. In the present investigation these thresholds are determined according to Schram (2003). Using all the instantaneous flow fields of each FoV<sup>4</sup> the standard deviation of vorticity and of the negative  $\lambda_2$  values are determined in the area of interest. The threshold of both variables is defined to be twice its standard deviation.

The algorithm determines the diameter of the vortices by choosing the scale of the mother wavelet, which is fitting the best with the enstrophy field (provides the highest wavelet coefficient) at the location of the vortex. However, the scales are defined in a user-defined interval ( $[D_{vmin}, D_{vmax}]$ ), which limits the range of the resulting core sizes. If  $D_{vmin} = 0$  and  $D_{vmax} = \infty$  is imposed (also in the present investigation), the algorithm defines automatically the scales in function of the size of the field maximizing the range of core sizes.

An indicator of the vortex deformation (*Like*) is defined by the ratio between the wavelet coefficient of the detected vortex and the wavelet coefficient of the ideal 2D Oseen vortex of the same size. Therefore, it can range between  $Like = [0, 1]$ . In the algorithm a threshold is defined (currently  $Like = 0.5$  is used) below which the vortex is rejected to keep uniformly rotating structures.

<sup>3</sup> $S = \frac{1}{2} (\nabla v + (\nabla v)^T)$  and  $\Omega = \frac{1}{2} (\nabla v - (\nabla v)^T)$

<sup>4</sup>Field-of-View

If the parameters of a detected structure satisfies all these criteria, it is accepted and considered as a vortex.



## Appendix B

# The design and characterization of the experimental facility

The current chapter is describing step-by-step the design of the main parameters of the experimental model from the choice of the facility, the definition of the main dimensions and finally the verification of the internal flow uniformity as well.

### B.1 Choosing the wind-tunnel

At the von Karman Institute (VKI), initially the so-called L-6 vertical twin-jet wind tunnel served for two-phase flow (air + water droplets) investigations. However, non-uniformities are encountered with the inlet velocity profile in its test section (see Tóth and Anthoine (2003) for further details). Therefore, the applicability of another tunnel is assessed. The subject of the assessment became very quickly the VKI L-11 wind-tunnel for its known uniformity, stability and convenient dimensions.

However, it has to be mentioned that the L-6 wind-tunnel was also used in order to gain experience and assess the applicability of certain optical measurement techniques (LeDaR and PIV). These investigations are explained by Tóth and Anthoine (2003) and Tóth and Anthoine (2004).

#### B.1.1 General considerations and the Blockage effect

The VKI L-11 wind-tunnel (see Figure B.1) is based on a square design. Its cross section is square from the diffuser to the test section. For this reason, symmetric inlet conditions are expected. Furthermore, the flow inlet is expected to be more uniform as well. The cross section of the wind-tunnel at the end of the contraction is  $200 \times 200 \text{ mm}^2$ . Thus, the cross section of the original test section is  $200 \times 200 \text{ mm}^2$  as well.

Originally, the wind-tunnel is supplied by a blower, which is attached directly with a flexible (rubber) joint. Nominally, the blower is capable of achieving about 15 m/s flow velocity in the test section. This velocity would be acceptable for the final measurements. However, this should be produced by having the inhibitors and the nozzle model installed as well. Since these pieces of equipment produce a considerable pressure drop, their blockage effect should be taken into account, when the maximum performance of the blower is measured.

During the investigation of the highest achievable velocity, only the largest blockage is modelled, which in practice is imposed by the nozzle throat.

As the dimensions of the model of the nozzle are not known yet, several blockage elements are created for the existing test section (with  $200 \times 200 \text{ mm}^2$  cross-section) in order to assess the pressure drop. These elements are aluminium sheets, which can be attached to the end of the existing test section. In the aluminium sheets different opening geometries and opening areas are created. The different shapes (square and two-dimensional) are summarized in Table B.1.

In Table B.1 the passage ratio ( $PR$ ) is defined by dividing the open section by the original section of the wind-tunnel  $200 \times 200 \text{ mm}^2$ .

The  $PR$  of the square (80 mm) and the 2D (31 mm) plates corresponds approximately to the passage ratio of the real nozzle in the Ariane 5 EAP (see details later in B.2.2.2).

First of all, the effect of changing the blockage shape (square vs. 2D) and the passage ratio is investigated. Therefore, the blockage elements are mounted at the outlet of the test section of the wind-tunnel (see the square element in Figure B.3) one after the other. The flow velocity inside the test section is set to 2 m/s (measured by a turbine meter) in each case. In this condition, the pressure difference between the stagnation chamber of the wind-tunnel and the ambient is measured by a Betz-type water column manometer.

The 2D blockages, which have 25 and 80 mm openings are mounted in an asymmetric way as well in order to represent higher passage ratios. In practice, the 2D blockage consists of two aluminium plates, which are fixed to the exit of the wind-tunnel in such a way that a horizontal opening remains in the center of the section (see the sketches in Table B.1 as well). Producing the asymmetric blockage in the present case means that only one of the blocking plates is mounted.

The results of the pressure drop measurements can be seen in Figure B.2. It is experienced that a small difference between the square and the 2D shape exists by having approximately the same blockage ratio (square 80 mm and 2D 31 mm). The pressure drop associated with the square configuration resulted in being slightly larger. However, the difference is negligible in the present case. For this reason, in the further tests only the square plate is used, which allows an easier repeatability of the tests.

In the followings, the maximum velocity and thus the maximum flow-rate in the test section is determined by using the originally installed blower of the wind-tunnel with the square blockage element attached to the end of the test section (see Figure B.3). The free stream velocity of the flow inside the test section is still measured by a turbine meter.

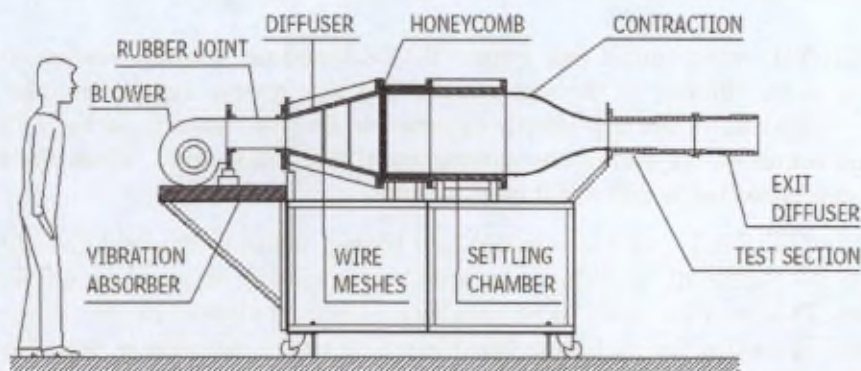


FIGURE B.1 - The initial arrangement of the VKI L-11 wind-tunnel.

Table B.1 – Blockage geometries for the speed tests

Opening type	Opening section [mm <sup>2</sup> ]	PR [-]	Schematic
No blockage	200×200	1	
Square (80 mm)	80×80	0.156	
2D (31 mm)	31×200	0.151	
2D (25 mm)	25×200	0.122	
2D (80 mm)	80×200	0.390	
2D (25 mm) asymmetric	112.5×200	0.561	
2D (80 mm) asymmetric	140×200	0.695	

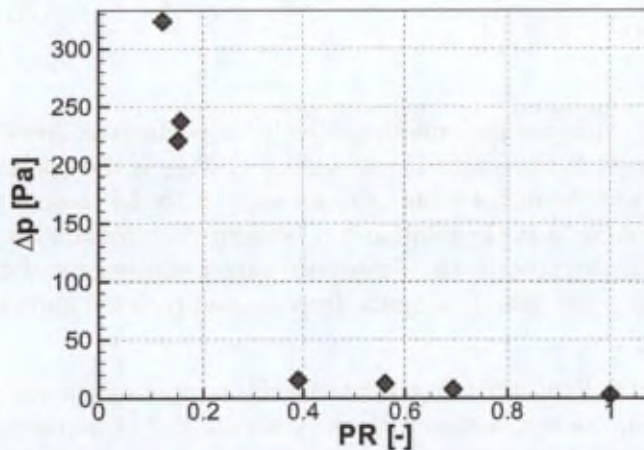


FIGURE B.2 – Effect of using different blockages.

It turns out that using a blockage of about 84.4%, the maximum velocity the blower can provide in the test section is around 2.61 m/s. This corresponds to a flow-rate of about 385 m<sup>3</sup>/h. The pressure drop is measured simultaneously with a Betz-type water column manometer. The manometer is measuring the pressure difference between the stagnation chamber of the wind-tunnel and the ambient. The main source of the pressure drop is considered to be the blockage itself. Therefore, the dynamic pressure of the flow is neglected at this stage. At the maximum performance (2.61 m/s) of the fan the pressure drop is about 395 Pa (see also Figure B.4).

The obtained maximum flow velocity in the test section is not sufficient for the later mea-



FIGURE B.3 – The square blockage installed on the test section of the wind-tunnel.

surements. Therefore, the blower should be exchanged by another one, which is able to provide a flow velocity above 10 m/s with the present blockage.

According to the principles of the orifice flowmeters (Figliola and E. (1991)), it is known (see equation (B.1)) that the pressure drop is proportional to the square of the flow-rate.

$$\dot{Q}_V = c_d A_2 \sqrt{\frac{2\Delta p}{\rho \left[1 - \left(\frac{A_2}{A_1}\right)^2\right]}} \Rightarrow \Delta p = \frac{1}{2} \rho \dot{Q}_V^2 \frac{1}{c_d^2 A_2^2} \left[1 - \left(\frac{A_2}{A_1}\right)^2\right] \quad (\text{B.1})$$

In equation (B.1)  $\Delta p$  is the pressure drop;  $\dot{Q}_V$  is the volumetric flow-rate;  $c_d$  is the so-called discharge coefficient;  $A_1$  is the original cross-section and  $A_2$  is the opening of the orifice plate. Based on the analogy of the orifice plate, one can apply it to the present problem regarding the blocking plates. Knowing that the relationship between the pressure drop and the flow-rate is second order, one can extrapolate the already existing measurement data to higher flow-rates (see Figure B.4). Thus, the desired pressure drop can be predicted and the required blower can be selected.

As it is illustrated in Figure B.4, in order to be able to operate the wind-tunnel above 10 m/s free stream velocity in the test section with the given amount of blockage, a blower is required, which is able to provide about 2000 m<sup>3</sup>/h flow-rate against about 10 kPa pressure drop.

The final selected blower operates with 96 kW power and according to its characteristics, it is able to provide the desired conditions by having its working point still below the pumping curve. Thus, the air supply is continuous without fluctuations.

Once the suitable blower is selected, it is installed to the wind-tunnel. Since the new blower has a considerably bigger size than the original, it cannot be mounted directly on the wind-tunnel. Instead, the blower supplies the tunnel through a tubing system (see Figure B.5).

Connecting the new blower to the wind-tunnel, the previously described speed tests are repeated including the pressure drop measurements. These results are also indicated in Figure B.4. Unfortunately, the Betz-type manometer cannot measure higher pressures than 600 mmH<sub>2</sub>O (about 5.9 kPa). Otherwise, the available new measurement points fit well with the extrapola-

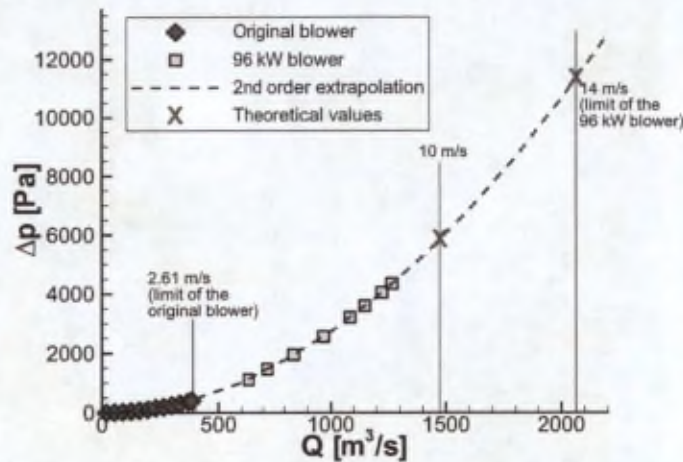


FIGURE B.4 – Speed test with the new blower of the L-11 wind-tunnel and with the square blockage.

tion. The real maximum performance of the blower is not reached in order to save the engine; therefore the maximum velocity is approximated to be at least 14 m/s. However, the blower can be used in long term at 10-11 m/s, which is already acceptable.

Later, the expected pressure drop was verified at 10 m/s using a calibrated pressure transducer. The resulting 5923 Pa confirms the prediction as well.

### B.1.2 Uniformity test with the original test section

In its final configuration the wind-tunnel will be installed in vertical position (the flow is going towards the ground) at the place of the VKI L-6 wind-tunnel. The available space at this location above the wind-tunnel is strongly limited. Therefore, the tubing system of the air supply should have a 90° curvature just before the diffuser of the stagnation chamber. However, in this configuration it is not guaranteed that this curvature has no effect on the uniformity of the flow inside the test section. Thus before installing the wind-tunnel to its place, the flow uniformity at the inlet of the test section has to be verified.

For this reason, the supplying tube is aligned in the position, which is expected to be its final configuration (indicated in Figure B.5) and one plane of the original test section of the tunnel is fully characterized (from the flow uniformity point of view) with hot-wire. The selected cross section is located 80 mm downstream the convergent part of the stagnation chamber.

In order to verify the uniformity of the flow with the single hot-wire (installed on a 1D displacement system), the mean velocity profiles are measured at six different locations. The arrangement of the profiles is shown in Figure B.6. Three horizontal and three vertical profiles are taken. Two profiles represent the symmetry axes and the four remaining profiles are chosen to be in the vicinity of the four sidewalls of the test section.

The flow velocity is set to about 12 m/s. The velocity is verified continuously by a hot-sphere, which is installed downstream the hot-wire.

The frequency response of the hot-wire is in each measurement case higher than 9.5 kHz. The signal of the hot-wire is filtered at  $f_f = 0.75$  kHz and amplified with a gain of  $A = 5$ . The sampling frequency of the acquisition system is set to  $f_s = 2$  kHz and at each measurement

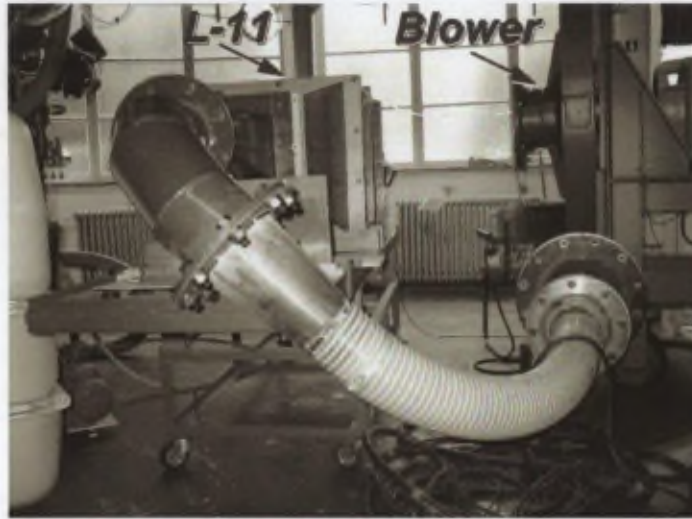


FIGURE B.5 - The tubing between the blower and the wind-tunnel.

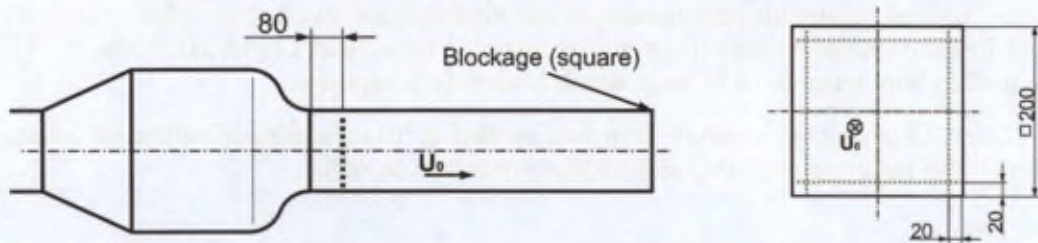


FIGURE B.6 - Preliminary flow inlet uniformity characterization location.

position  $N_s = 15000$  samples are recorded.

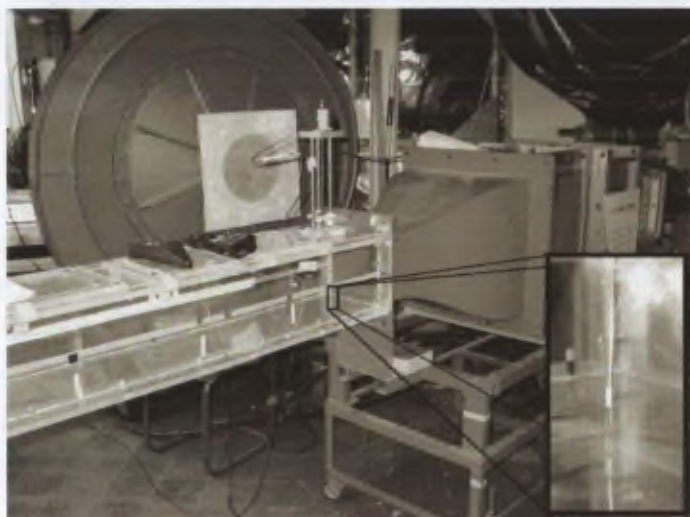
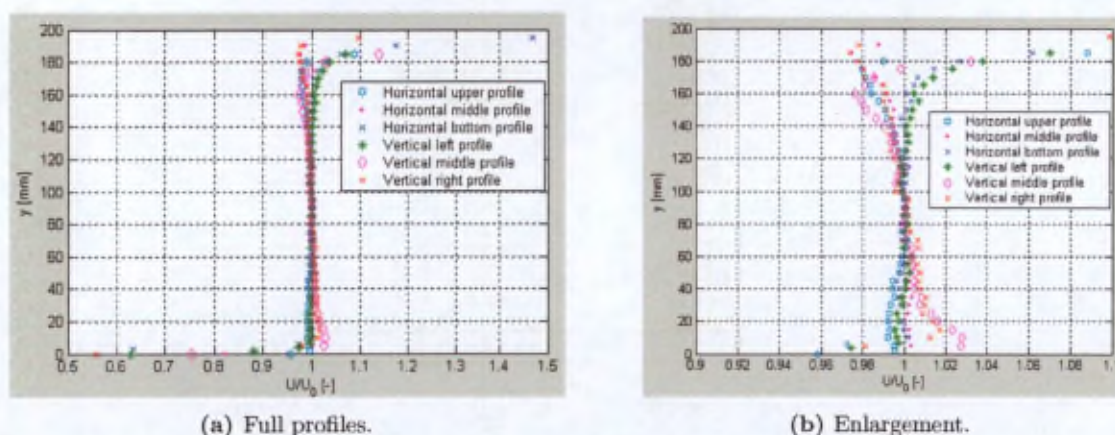
Based on these samples, the mean stream-wise velocity is determined at each measurement point. Each profile is normalized by the actual free stream velocity. The actual free stream velocity is determined by averaging the mean velocity values that correspond to  $40 < y < 160$  mm.

The resulting normalized mean velocity profiles are shown in Figure B.8(a). In the figure all the profiles are plotted in one graph to be able to see the deviations from each other, which would show the non-uniformity of the flow.

The profiles taken at different positions show a good agreement in general. The top of the profiles ( $y > 170$  mm) shows an acceleration of the flow, which is certainly not representing the mean stream-wise movement of the flow. This effect is most probably due to the presence of the holes (about 10 mm in diameter) through which the hot-wire is penetrating the test section. Through these holes rapid air evacuation is observed due to the large pressure drop caused by the blockage (for this reason, during the measurements the holes out of use are blocked).

Furthermore, most of the profiles show a slight deceleration in the mean velocity by the increasing  $y$  position. However, this deceleration is around 3-4 %, which could be simply caused by the blockage effect of the shaft of the hot-wire.

In Figure B.8(b) one can see the deviations of the velocity profiles from each other. The figure shows a zoom-in to the region  $0.9 < U/U_0 < 1.1$ . It is clear that the deviations are mainly

FIGURE B.7 – *The applied hot-wire.*FIGURE B.8 – *Mean velocity profiles of the inlet uniformity characterization.*

below  $\pm 2\%$ , which is considered to be acceptable (Pope (1947)).

Performing all the above-mentioned tests and considering the results, it is decided that the VKI L-11 wind-tunnel is applicable for the planned measurements. Thus, the design of the final configuration can be started.

## B.2 Facility design and adaptations

Finally, as the L-11 wind-tunnel is selected to be the basis of the final facility, it is installed in the place of the L-6 wind-tunnel in vertical position and to design a new test section for the present purposes. This is shown in Figure B.9.

### B.2.1 The wind-tunnel

The platform is two-storey. Mainly, the wind-tunnel itself - the stagnation chamber and part of the convergent - is located upstairs. On the top one can see the tube, through which the air is supplied. It is designed to be in the same position as it is arranged during the first characterization of the facility (see B.1.2).

The sprays, which generate the liquid-phase during the measurements are going to be installed just upstream the convergent part of the stagnation chamber. One of the walls of the stagnation chamber includes a plexiglass window. Through this window the operation of the spray could be monitored.

The test section is going to be located downstairs attached to the end of the convergent module.

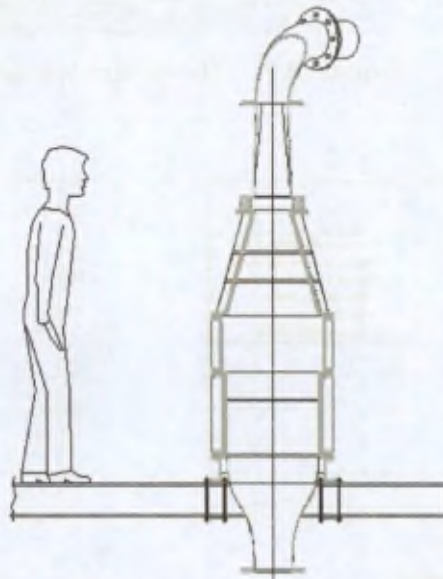


FIGURE B.9 - *The L-11 wind-tunnel installed vertically.*

Before the wind-tunnel is fixed in its final position, it is disassembled in order to inspect and clean its interior. Once it is disassembled, all the wooden surfaces (all the walls, except for the plexiglass) are lacqued in order to make them water-repellent. Otherwise, operating the water sprays, the water would shortly damage the structure.

After all the treatments, the wind-tunnel is finally mounted to its place, mainly according to the design.

### B.2.2 The test section

As it has been mentioned before, the test section is directly attached to the end of the convergent part of the L-11 wind-tunnel.

The test section itself represents the main characteristics of the solid propellant motor (P230/MPS) of the Ariane 5 spacecraft. The test section should model in the best possible way the main features of the motor, when 50 % of the propellant is burnt. However, there are four important differences compared to the real situation:

- The present tests are cold-gas simulations. Therefore, the measurements are carried out at ambient temperature, without any chemical reaction;
- The flow is axial;
- The Mach number of the real case ( $M = 0.1$ ) is not respected (having approximately  $M = 0.04$ ). In any case, the sonic condition at the nozzle is not modelled;
- The real motor is axisymmetric, while the model is two-dimensional.

In spite of the differences, the main internal geometrical characteristics should be respected. On the one hand, in the real case (see also a schematic in Figure 2.1(c)) there is an inhibitor (thermal insulation) between the second and the third stage, which defines the main structure of the internal flow and first of all, this inhibitor is responsible for the vortex formation in the flow. On the other hand, the presence of the nozzle is important, since the generated vortices are impinging on the nozzle head. Therefore, depending on the interaction between the vortices and the nozzle, the accumulation of the liquid in the cavity next to the nozzle could be strongly influenced.

As a consequence, in order to understand the main parameters of the liquid accumulation, one has to model the presence of the inhibitor between the second and the third segments and the nozzle (with the cavity).

From now, within this section (only in section B.2.2.1 and B.2.2.2), the term "test section" stands for the test section of the wind-tunnel, including the inhibitor, but excluding the nozzle. This is made in order to be able to explain the design in a more simple way.

### B.2.2.1 The test section geometry

Basically the final section of the convergent part of the L-11 wind-tunnel defines the dimension of the test section. Therefore, it should be  $200 \times 200 \text{ mm}^2$ . Since the test section has a square concept, one has the possibility to use it in the square configuration. However, by installing a splitting plate in the middle of the test section a 2D concept can be created easily (see Figure B.10(a)). The geometry of the set-up can be symmetric, which equalizes the pressure drops on either side. On the other hand, in the square design all the elements (obstacle, nozzle, cavity) should be square.

During the design, as it was mentioned before, one of the goals is to create a model, which represents in the best possible way the characteristics of the real motor. For this reason, at the design, the section ratios (e.g. the  $PR$  of the inhibitor) should be respected in order to have similar flow-pattern. However, considering the inhibitor, if the section ratios are respected with the real, axisymmetric motor, the obstacle height in the model should be relatively higher. However, if the inhibitor height is higher, the path of the vortices will be farther from the sidewall, which by itself may modify their properties. Furthermore, the presence of the splitting plate (which does not exist in the real case) may have an influence on the flow as well.

As a consequence, the square concept is more favourable, since in this case one can respect the section ratios with the real motor, while the distance ratios are similar as well. In addition, in the square model no splitting plate is needed. On the other hand, using the square configuration, one should verify that there are no considerable corner and three-dimensional effects appearing in the flow.

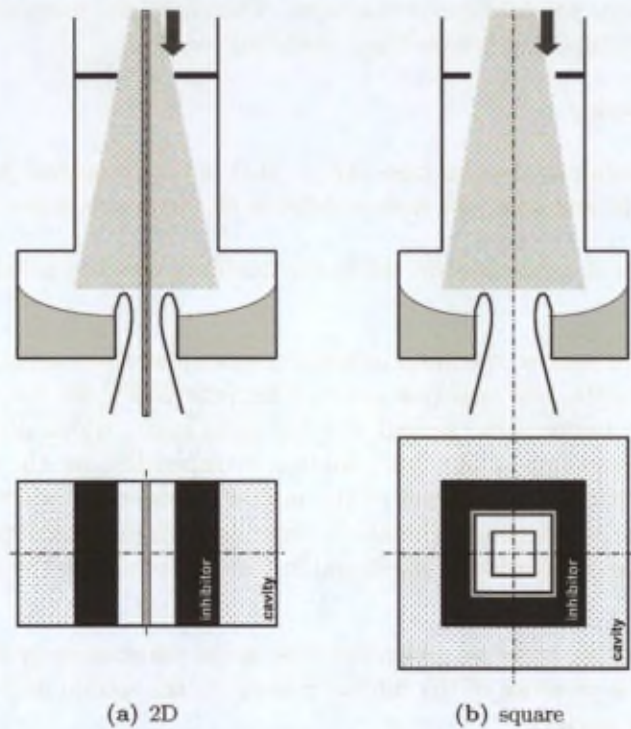


FIGURE B.10 - Test section concepts.

Therefore, at the present state, both designs are kept in mind and the very first task is to perform some tests to be able to decide between the two configurations.

**B.2.2.1.1 The sidewalls of the test section** Since optical measurement techniques would be used, the walls of the test section should provide optical access. Therefore, it should be made of plexiglass, since it is easier to machine than glass.

However, performing PIV measurements with a YAG Laser, the high-energy light is dangerous for the plexiglass. Due to the impurities of plexiglass, the light heats up the material, which starts locally boiling and forms small (up to 1 mm) bubbles. Since these bubbles scatter the light, the light intensity distribution in the laser-sheet inside the test section would not be uniform. In order to avoid this effect, in the wall of the wind tunnel, where the Laser enters, a glass window is designed in the plexiglass frame. Therefore, the Laser light can enter the section through the glass window, which is more robust against the high-energy light. This wall is called to be the front of the test section.

Performing PIV measurements close to walls is always difficult mainly because of light reflections from the wall. These reflections have an effect on the images even in the regions of the flow field, where they reduce the performances of the cross-correlation. That is why the surface, close to which measurements are carried out, should be treated carefully. The best solution in case of plane areas is to make them mirror-like surfaces. In this case, as the light of the laser-sheet hits the surface, it is reflected back in itself. Thus, besides reducing the side reflections, the light energy inside the laser sheet could be almost doubled as well. To realize the mirror-like surface of one of the walls of the wind-tunnel, the easiest solution is to apply polished metal. Therefore, the wall of the test section opposite to the glass windowed wall is made of stainless steel and its surface along its centre is polished. This wall is called to be the back of the test section.

According to the experiences that are gained during the preliminary assessment of the LeDaR measurement technique (see section 3.2.1) and the two-phase PIV measurement technique, it seems that plexiglass is not well suited as being the material of the sidewalls. Due to water deposition, the optical access to the test section dramatically reduces during the measurements. In addition, the surface of the plexiglass cannot be treated to be water-repellent. For this reason, according to the original design, the side surfaces of the test section are covered in the interior by a thin (1 mm thick) glass film, which is glued to the plexiglass along its border.

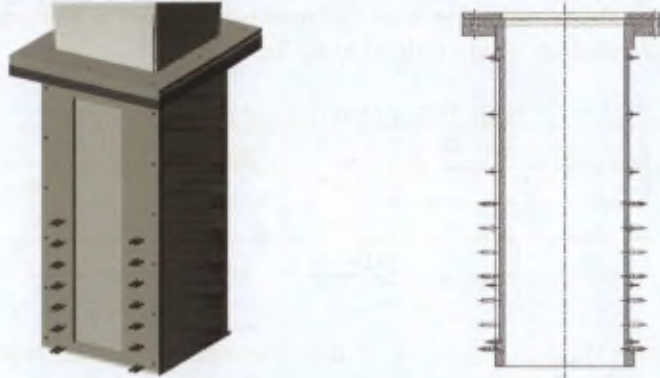


FIGURE B.11 – *The main walls of the test section.*

The final design of the walls of the test section can be seen in Figure B.11. The front wall can be easily recognized by the glass window. The identification of the rest of the walls is then straightforward. Finally, including the glass films on the sidewalls, the internal dimension of the first test section in practice became  $199 \times 197 \text{ mm}^2$  (the distance between the front and the back surface is 199 mm).

**B.2.2.1.2 Inhibitors** At the state of the design of the facility, before making the decision between the two-dimensional and the square test section, the design of the inhibitors has not been finalized yet. However, obstacles are designed for both of the geometries.

The test section is designed in a way that the inhibitors can be fixed through the front and the back walls (see the pairs of small sticks in the 3D drawing in Figure B.11). Since the glass film is glued to the sidewalls, through them no fixation is possible.

This limitation is true for the splitting plate as well. Therefore, the splitting plate has to be also fixed to the front and the back walls, which can only be realized by applying additional plexiglass sheets placed onto the sidewalls. The concept can be seen in Figure B.12, which is the top-view of the two-dimensional configuration. The additional plates are hatched.



FIGURE B.12 – *The position of the additional plates to fix the splitting plate.*

These additional plates are covered by a glass film (1 mm thick) as well. Therefore, in the two-dimensional case the cross section of the test section is further reduced to  $199 \times 183 \text{ mm}^2$ , where

the 4 mm thick splitting plate is not taken into account. Naturally, in the square configuration the section is not modified ( $199 \times 197 \text{ mm}^2$ ).

To determine the dimensions of the first generation inhibitors, a previous study of Anthoine (2000) is kept in mind. Within that project the acoustic coupling is studied experimentally inside the motor, using a 1/30 scaled axisymmetric model with either axial or radial flow injection. The model is a scaled representation of the geometry of the real motor, when half of the propellant is burnt. The first inhibitors of the L-11 facility are designed to respect the same section ratios (same  $PR$ ) as for the three main obstacles that can be installed in the axisymmetric model. The calculated inhibitor heights ( $h$ ) are indicated in Table B.2.

Table B.2 - Determined inhibitor sizes

$h_{axisymmetric}$ [mm]	$PR$ [-]	$h_{square}$ [mm]	$h_{2D}$ [mm]
9	0.582	24	41
7	0.666	18	27
4	0.801	11	13

The obstacle with  $h_{axisymmetric} = 9 \text{ mm}$  corresponds to the real case. Therefore, this inhibitor is considered to be nominal during the tests related to the design of the facility. The definitive nominal inhibitor size will be chosen in section B.4.

In the final measurements the applied obstacles are going to be inclined as it is justified in section 5.1.

Regarding the position of the obstacle, this parameter can also be changed later during the measurements. According to the present design of the L-11 facility, the shortest possible distance between the inhibitor and the tip of the nozzle can be  $L_i = 70 \text{ mm}$ . The maximum position is designed to be  $L_i = 310 \text{ mm}$ . In between, the available positions are spaced by 40 mm. This can cover the  $O2NRs^1$  between 1.7 and 23.8 in the two-dimensional case (calculating with the inhibitors of Table B.2) and between 2.9 and 28.2 in the square case.

### B.2.2.2 The cavity geometry

Due to the fact that the final decision between the square and the two-dimensional concept is not made at the present status, the final nozzle and the cavity geometry is not available.

However, it is already known that the nominal geometry of the nozzle and the cavity should represent the geometry of the real case. Defining the width of the cavity, the section ratios with respect to the test section should be considered. In addition, modification of the cavity geometry (e.g. the volume of the cavity) should be possible on the final set-up.

In practice, the modification of the cavity geometry is very difficult in the square case. That is why it is decided that for each configuration a new cavity (the nozzle and the cavity are considered to be one unit) is built. In the two-dimensional case the cavity can be designed in a way that the modification of its geometry can be realized on the same piece.

In Figure B.13 the cavity corresponding to the square concept can be seen, as it is positioned to its place.

During preliminary measurements with the L-6 wind-tunnel, when the liquid accumulation is studied, a balance is used to determine the weight of the accumulated liquid and compare it to

<sup>1</sup>Obstacle-to-Nozzle Ratio,  $O2NR = L_i/h$

the LeDaR measurements (for further details on these tests, please refer to Tóth and Anthoine (2004) and Tran (2004)). The possibility of performing balance measurements should be kept in the L-11 wind-tunnel as well. However, this necessitates that the cavity is not fixed, nor attached to the test section. Instead, a small (maximum 1 mm) gap is left between the two. This gap should be small enough so as not to have considerable leakage. Therefore, in both (square and 2D) cases, the cavity is not planned to be fixed to the test section but put on a balance system. When the balance measurement is not needed, the cavity can be supported by a table, which has an opening to allow the flow to leave the test section through the nozzle. In this case, the gap between the test section and the cavity can be closed.

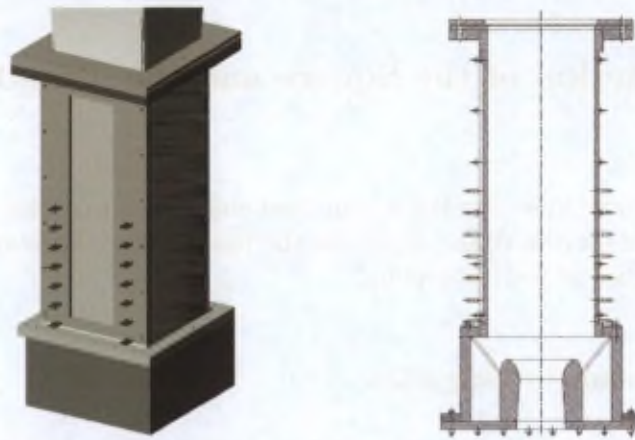


FIGURE B.13 – *The cavity at its position in the square configuration.*

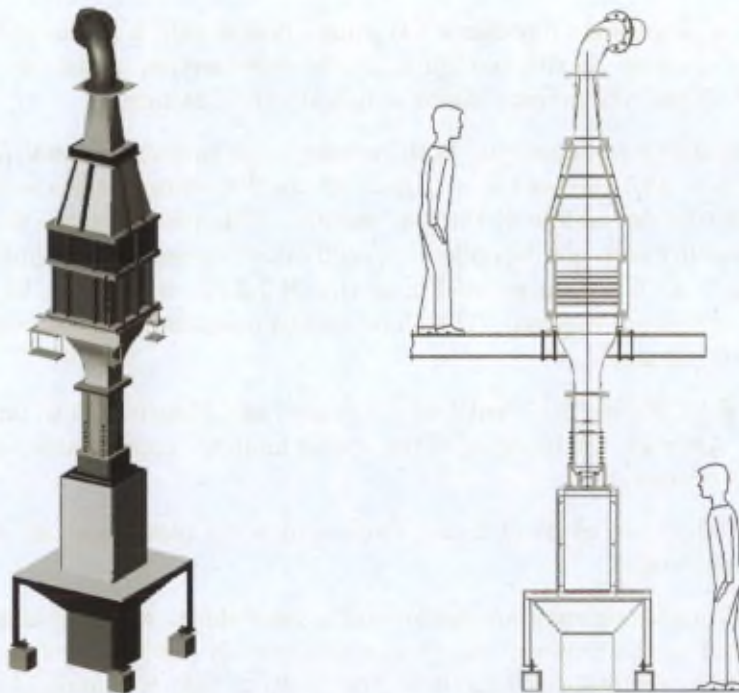


FIGURE B.14 – *The cavity at its position in the square configuration.*

As it was mentioned earlier, during the design of the cavity and the nozzle, no sonic condition is expected at the nozzle.

Finally, Figure B.14 shows the design of the whole assembled facility including the wind-tunnel and the test section with the cavity. The various gray levels of the three-dimensional drawing represent different pieces, but not necessarily different materials.

Below the cavity its special support can be seen. This support is holding the cavity, when no balance measurements are made. Below the support the suction system can be installed. This is required for the PIV measurements.

The spray, which produces the droplets of the second phase, can be installed in the stagnation chamber of the wind-tunnel. Its location is not indicated in these drawings.

### **B.3 Investigation of the Square and the Two-dimensional concept**

As it was introduced in section B.2.2.1, the first objective is to decide between the square and the two-dimensional concept of the design for the final facility. Therefore, a PIV experimental campaign is performed in the test section.

#### **B.3.1 The in-plane investigation**

During the PIV measurements, three configurations are compared. In this case, apart from the inhibitor, nothing else is installed in the test section (tests without the cavity). Every investigated obstacle is fixed about 303 mm downstream the beginning of the test section.

One of the arrangements represents the square design with a square inhibitor, which has a  $150 \times 150 \text{ mm}^2$  opening. In this configuration the cross-section of the test section is therefore  $199 \times 197 \text{ mm}^2$ . Thus, the average inhibitor height is  $h = 24 \text{ mm}$ .

The two remaining arrangements both represent the two-dimensional (2D) design with inhibitor sizes of  $h = 33.5 \text{ mm}$  and  $h = 41 \text{ mm}$ . In the 2D configurations a 4 mm thick splitting plate is mounted in the middle of the test section. This plate ensures that the flows behind the opposite inhibitors are not dependent on each other (prevents the coupling between the two vortex shedding). As it was mentioned in section B.2.2.1.2, in order to fix the splitting plate, two additional plates are required. Therefore, in this case, the cross-section of the test section reduces to  $199 \times 183 \text{ mm}^2$ .

See Figure B.10, Figure B.11 (without the cavity) and Figure B.15 to understand better the configurations. After all, the blockage of the square inhibitor corresponds to the blockage of the 41 mm high 2D obstacle.

All the inhibitors are made of 2 mm thick aluminium plates and all of them are straight (normal to the sidewalls).

At first, PIV measurements are made with a laser-sheet, which is aligned with the mean flow and adjusted to the center of the test section (see the dashed lines in Figure B.15). This laser-sheet position corresponds exactly to the position that is planned to use in the future. However, in the present experiments, the FoV of the camera covers the whole cross-section of the wind-tunnel. During the measurements the symmetry and the stability of the flow are investigated.

The free stream velocity of the flow is  $U_0 = 10 \text{ m/s}$ . With each configuration 1000 image pairs

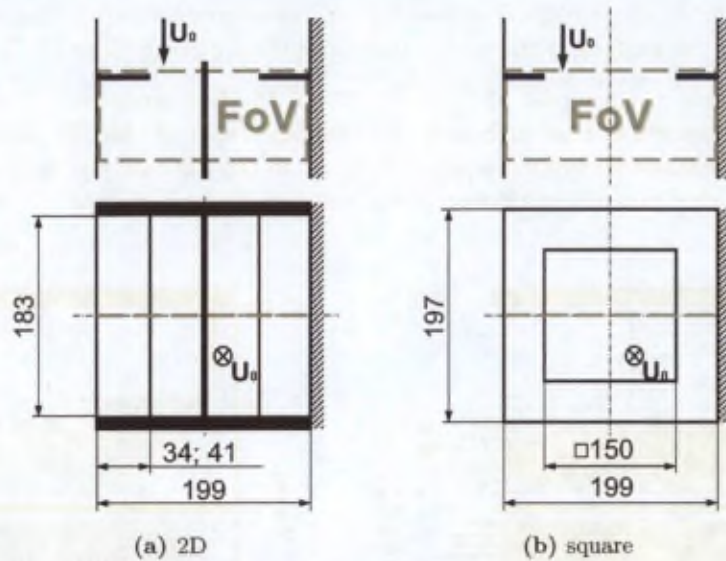


FIGURE B.15 – Test section configurations.

are recorded to calculate the mean flow field. During the data processing, the initial window size is  $72 \times 72$  pixel<sup>2</sup>. Two window refinement steps and finally 50 % of window overlapping are applied. As a result, the spacing between the velocity vectors is  $9 \times 9$  pixel<sup>2</sup> ( $1.4 \times 1.4$  mm<sup>2</sup>).

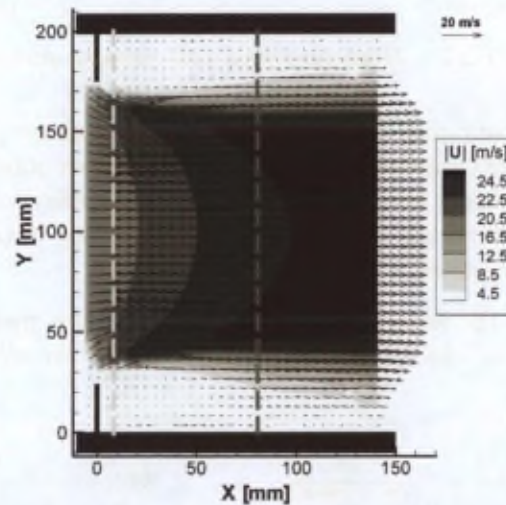


FIGURE B.16 – Mean flow field (square configuration; in-plane).

The mean flow field corresponding to each arrangement can be seen in Figure B.16 and Figure B.17. The contour plots of the figures show the mean velocity magnitude. Furthermore, the mean velocity vectors are indicated as well.

Based on the contour plot of Figure B.16, it can be seen that in mean, the velocity magnitudes show a very symmetric distribution. The maximum velocity at the vena contracta is just above 24.8 m/s.

In the 2D-case results (Figure B.17(a) and Figure B.17(b)), close to the splitting plate unexpected, large velocity magnitude variations can be seen. However, they appear only because

the image quality in these regions is low due to image quality issues (from the glue that fixes the glass film to the surface of the plates that hold the splitting plate).

Looking at the contour plot of Figure B.17(a), the flow appears to be rather symmetric. However, it is important that although the blockage ratio of the 2D obstacle ( $h = 41$  mm) equals to the blockage effect of the square inhibitor, in the 2D case the flow acceleration appears to be larger. In this case the maximum mean velocity reaches 28 m/s.

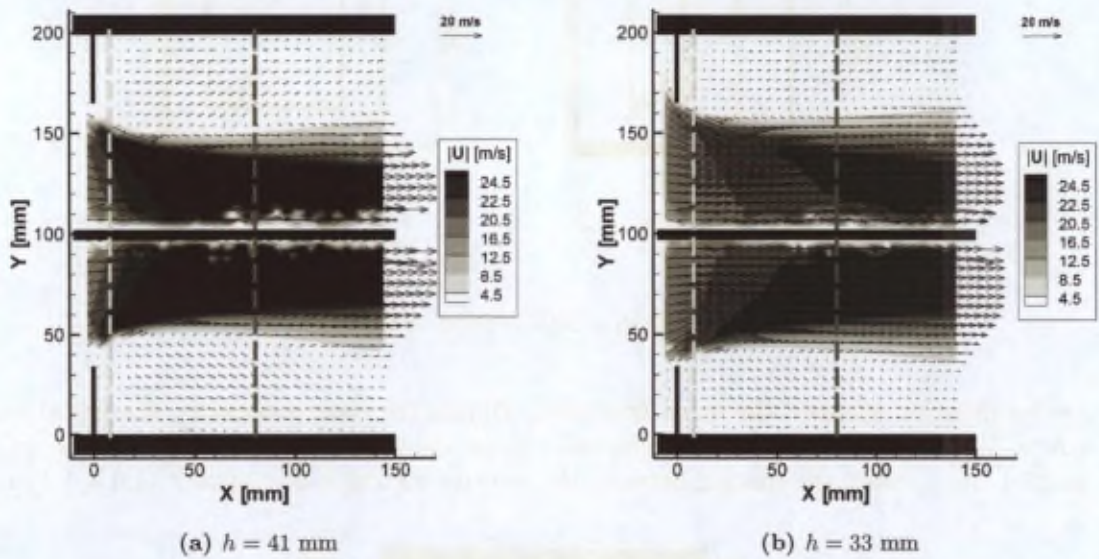


FIGURE B.17 - Mean flow field (2D configurations; in-plane).

Considering the contour plot of Figure B.17(b), one can see that using the  $h = 33$  mm obstacle - which represents smaller blockage than the square inhibitor -, the maximum mean velocity of the accelerated flow is closer to the value that is observed with the square obstacle (it is just below 24.5 m/s). However, in this case the distribution of the velocity magnitude values does not seem to be very symmetric.

In order to quantify the asymmetry of the mean velocity magnitude with the latter configuration, profiles of the velocity magnitude information are extracted at  $X = 8$  mm and  $X = 80$  mm.

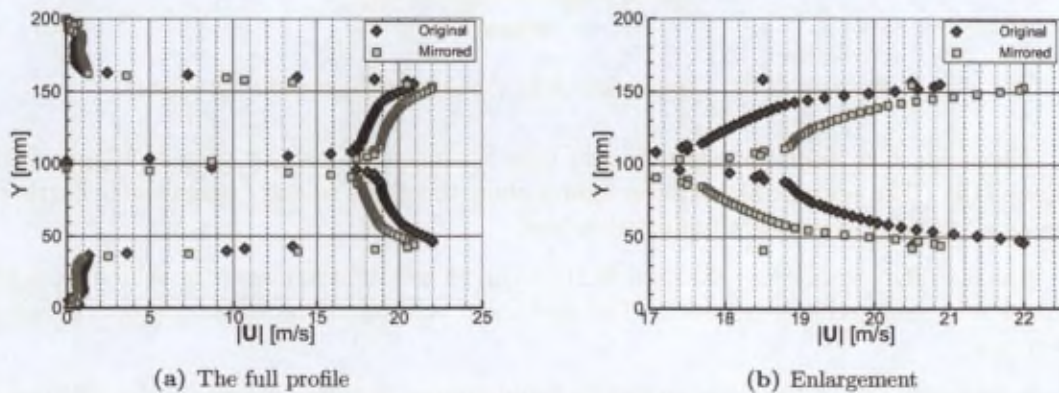


FIGURE B.18 - Velocity magnitude at  $X = 8$  mm.

The profile from the position  $X = 8$  mm is shown in Figure B.18. In the figure the points called "Original" represent the profile. However, in order to be able to see easier the difference, the profile is mirrored and plotted in the same graph under the name of "Mirrored". Furthermore, Figure B.18(a) the left plot shows the whole profile and Figure B.18(b) shows a zoom-in to the region of the maximum velocity values.

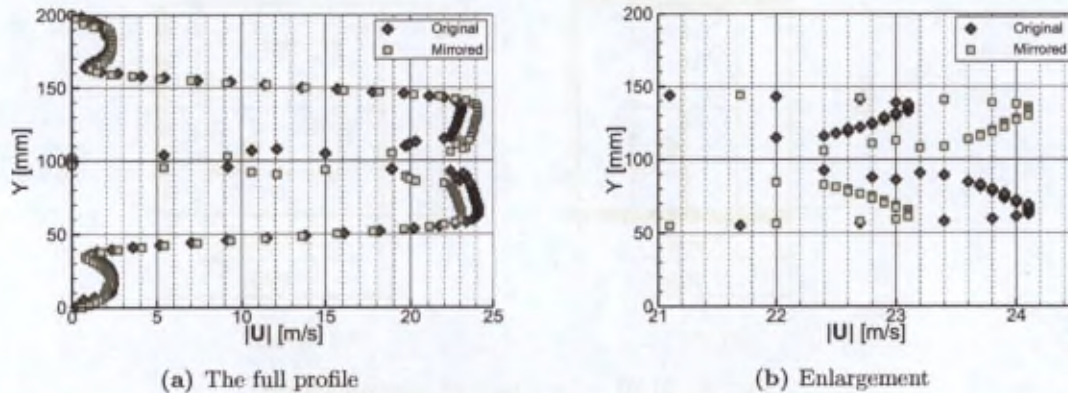


FIGURE B.19 – Velocity magnitude at  $X = 80$  mm.

In Figure B.19 the profile from the position  $X = 80$  mm is presented in the same way as Figure B.18. Based on the two figures, it is clear that in the mean velocity magnitude a difference of about 1 m/s can be observed as asymmetry. Comparing this value to the maximum values, a ratio of about 4.5% or  $\pm 2.3\%$  can be found. Although, this amount is still acceptable, it should be verified later, with the final obstacles especially, when the nozzle is also installed.

However, observing a considerable difference in the mean velocities, when different geometry (square and 2D) inhibitors are applied, the flow acceleration will be studied later more deeply (in B.4). Considering the two-dimensional configuration, one should find out, what is the relationship between respecting section ratios and respecting dimension ratios. The section ratio means the blockage (or passage) ratio. The dimension ratio means the ratio between the height of the obstacle and the total height of the test section.

### B.3.2 The out-of-plane investigation

Using the PIV technique, the flow in the *out-of-plane* (in the plane normal to the mean flow direction) is investigated downstream the inhibitors (see Figure B.20). However, during the out-of-plane cases only one of the 2D obstacles ( $h = 33.5$  mm) is investigated beside the square inhibitor. The free stream velocity of the flow is again  $U_0 = 10$  m/s.

The difference of the present measurements with respect to the in-plane investigation is that in the present case the laser-sheet is horizontal, perpendicular to the main flow direction. Using both inhibitors, two laser-sheet positions are investigated. The sheet is placed at  $X = 8$  and 80 mm downstream each obstacle. These positions are indicated in Figure B.20(a) and Figure B.20(b) by the dashed lines.

Since the camera has to be perpendicular to the laser-sheet during the conventional (2-dimensional, 2-component) PIV measurement, it is placed below the wind-tunnel. In order to prevent the optics of the camera to be contaminated by the oil seeding, a plexiglass shield is placed above it, which has to be cleaned frequently. The plexiglass is fixed to a support, which is independent from the camera. Therefore, the camera is protected from the aerodynamic forces

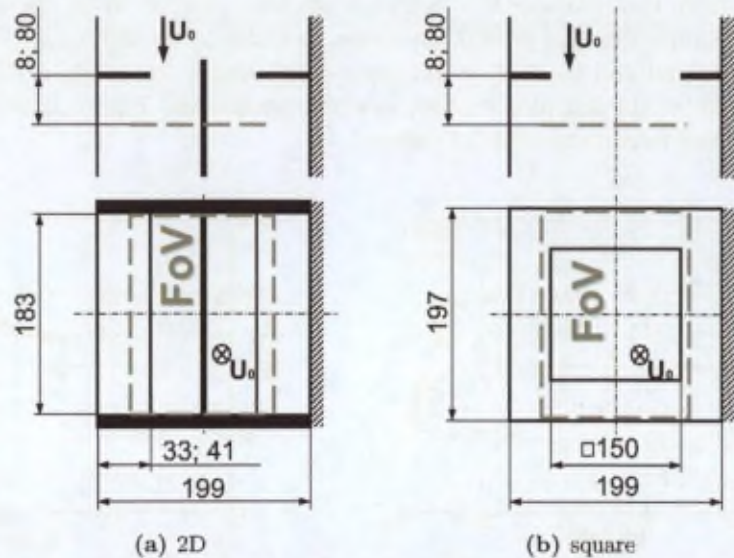


FIGURE B.20 – Test section configurations.

as well. Otherwise, the exhaust flow of the test section would continuously move the camera and the FoV would not be constant.

With each configuration 1000 image pairs are recorded to calculate the mean flow field. During the data processing, the initial window size is  $80 \times 80$  pixels<sup>2</sup>. Two window refinement steps and finally 50% of window overlapping are applied. As a result, the spacing between the velocity vectors is  $10 \times 10$  pixels<sup>2</sup> ( $\sim 1.6 \times 1.6$  mm<sup>2</sup>).

In order to reduce the ambiguities, each measurement is performed using one FoV (one position) of the camera. Therefore, the whole cross-section of the test section has to be illuminated by the laser-sheet. At this point the polished back surface became undoubtedly handy. Thanks to it, even in the areas that are shadowed by the frame of the glass window in the front wall of the test section it is possible to obtain some results. Although, the signal-to-noise-ratio is lower, mostly it is still acceptable.

Due to the harsh measurement conditions, before the results, the mean *signal-to-noise ratio*  $SN_{mean}$  distribution is shown in Figure B.21 corresponding to every measurement configuration. Later, using these figures, one can judge the physical content and the reliability of the results.

The results of the measurements are shown in Figure B.22 and Figure B.23(b). In each figure the walls are indicated. The red dashed line in the centre stands for the position of the in-plane measurement.

At  $X = 8$  mm far from the inhibitor the flow is strongly dominated by the obstacle. That is why in terms of the mean quantities no 3D effect was observed. Thus, in Figure B.22(a) and Figure B.22(b) the contour plot represents the mean  $V$  velocity component (aligned with the  $Y$ -axis), which is common with the in-plane component of the regular measurements.

Looking at the mean  $V$  component, the symmetry of the flow acceleration can be seen, which appears to be symmetric both in the two-dimensional (Figure B.22(b)) and the square (Figure B.22(a)) case. If the flow acceleration were asymmetric, then farther downstream more important 3D effects could be expected.

At  $X = 80$  mm far from the inhibitor the effect of the obstacle is less dominant and the

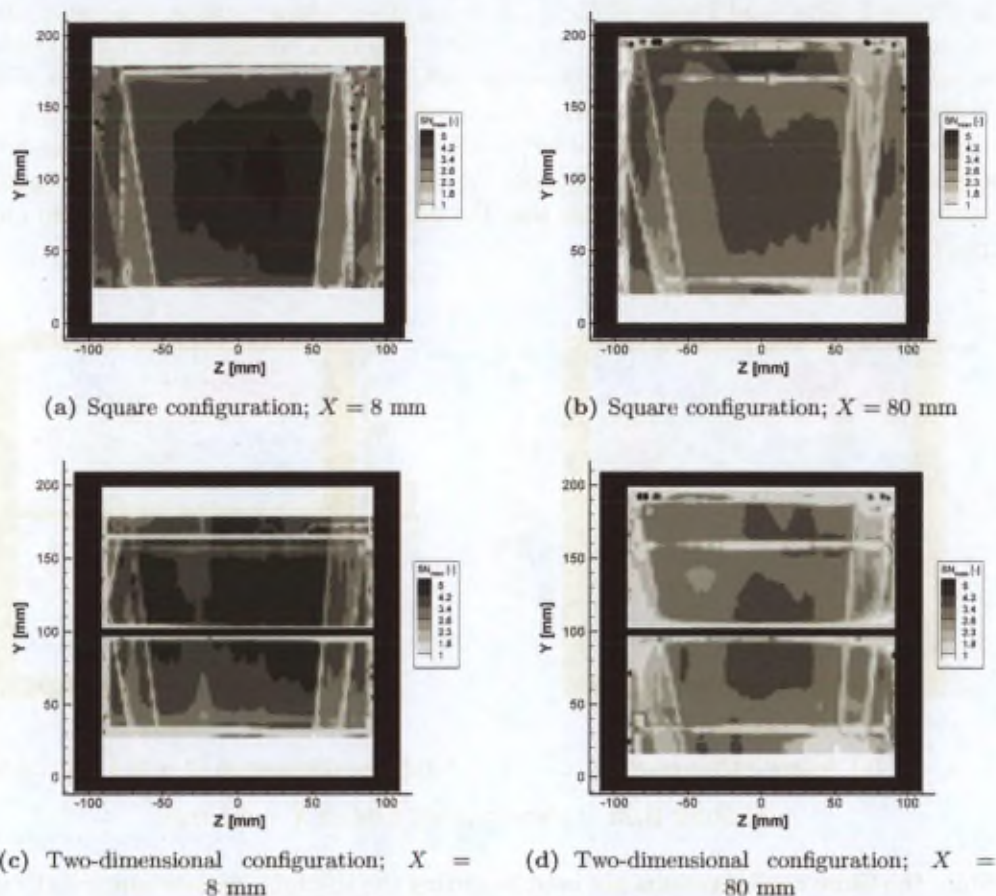
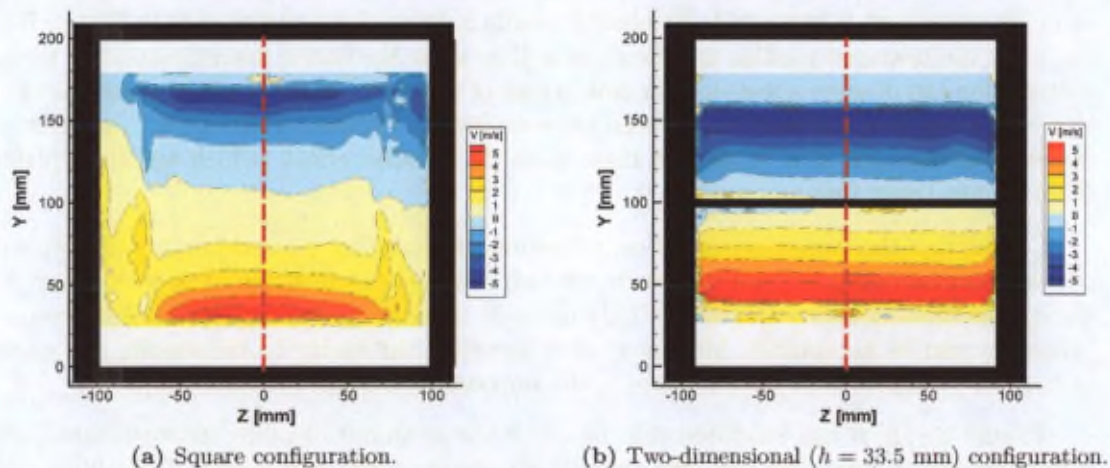


FIGURE B.21 – Measurement quality in the perpendicular planes.

FIGURE B.22 – Mean velocity field at  $X = 8$  mm.

3D structures of the flow already establish. Therefore, in Figure B.23(a) and Figure B.23(b) the mean  $W$  velocity component (aligned with the  $Z$ -axis) is shown in the contour plot. In the regular PIV measurement this component is the out-of-plane component, which cannot be measured.

In Figure B.23(a) and Figure B.23(b) the mean out-of-plane motion, the mean 3D effect on the regular measurements can be seen directly. In the square configuration (see Figure B.23(a)) an out-of-plane motion of 0.2 to 0.4 m/s can be seen in the middle region of the test section along the centre line. With respect to the free stream velocity upstream the inhibitor ( $U_0 = 10$  m/s) this cross-flow is less than 4%. Regarding the 2D case (Figure B.23(b)), this cross-flow is more important in some regions. It even exceeds 8%, but considering the  $SN_{mean}$  (Figure B.21) in the corresponding region, it is probable that the measured magnitude of the mean cross-flow is not physical.

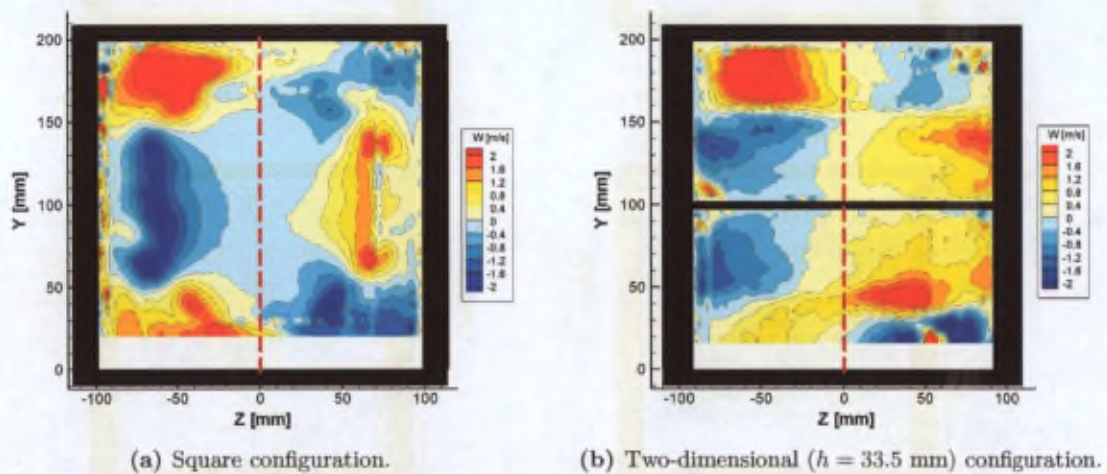


FIGURE B.23 – Mean velocity field at  $X = 80$  mm.

Since the same configurations are used as during the in-plane measurements, the discovered symmetry problem (see Figure B.18 and Figure B.19) can be investigated again focusing to the 2D  $h = 33.5$  mm high obstacle. During the two measurements the  $V$  velocity component is common. Therefore, along the line, which is common in the two measurement planes, the  $V$  velocity component is extracted. Its absolute value is determined and plotted in Figure B.24. In the plots the mirrored profiles are shown as well to allow the easier determination of the asymmetry. One can observe a less smooth plot in case of the out-of-plane measurement. However, in this case a better symmetry can be seen between  $0 < Y < 45$  mm, while a high amplitude peak appears between  $100 < Y < 150$ . In these plots the parallax effect (which will be explained in B.5.1) is not taken into account.

Considering the two-dimensional configuration, the splitting plate separates the two sides of the wind-tunnel. Therefore, the flow in the two sides cannot interact with each other. Since, during the measurements the flow of only one side is investigated, the observed degree of non-symmetry can be acceptable. Moreover, after installing the cavity to the set-up, the symmetry of the flow is expected to improve due to the imposed additional pressure drop.

To sum up all, it can be stated that based on the mean out-of-plane measurements, the two configurations (square and two-dimensional) are similar. The symmetry of the flow could be accepted and no outstanding mean 3D effect is discovered.

### B.3.3 Deciding between the square and the two-dimensional design

In order to be able to decide between the square and the two-dimensional configurations, the measurement data are further analysed.

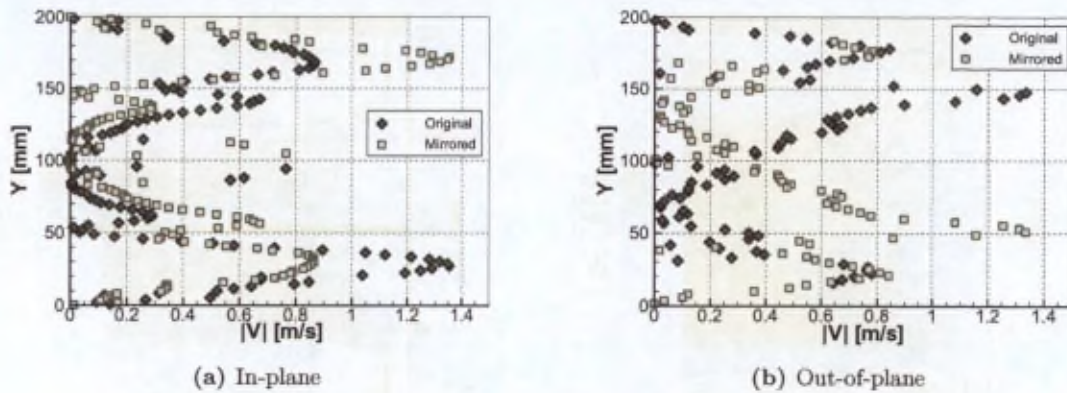


FIGURE B.24 –  $|V|$  profiles at  $X = 80$  mm (2D inhibitor;  $h = 33.5$  mm).

The contour plots of Figure B.25(a) and Figure B.25(b) show the velocity magnitude in the square and the two-dimensional (using the  $h = 33.5$  mm 2D obstacle) case respectively.

As it was discussed earlier, the velocity magnitudes are slightly higher in the square case, but they are still similar with these geometries. Some non-symmetry can also be seen in the two-dimensional (2D) case, which is now neglected according to the previous agreement.

In the figures the streamlines of the flow are indicated as well. Looking at the 2D configuration (Figure B.25(b)), the mean flow structures between  $0 < Y < 50$  mm and  $150 < Y < 200$  mm, they show a good symmetry. In both sides, a big recirculating structure extends from the tip of the obstacles. Their center seems to be close to the edge of the present fields of view. In earlier (see the report of Tóth and Anthoine (2003)) obstacle-flow measurement (with  $U_0 = 2.33$  m/s and  $BR = 27\%$ , while currently  $U_0 = 10$  (m/s) and  $BR = 34.4\%$ ) the center of the main recirculating region resulted to be  $3.65 \cdot h$  (where  $h$  is the obstacle height). In the present case ( $h = 33.5$  mm) this distance corresponds to 122.3 mm.

In addition, in the 2D measurements (Figure B.25(b)) the secondary circulating structure also appears just downstream the obstacles. Although, these structures cannot be characterized due to the low resolution of the measurements, their appearance is already welcome.

Looking at the streamlines of the flow representing the square configuration (Figure B.25(a)), the above-mentioned structures cannot be identified. The mean in-plane flow field shows strong three-dimensionality. Sources and drains are visible. The mean structures are not well defined either. Between  $0 < Y < 50$  mm two small circulating structures seem to appear, while between  $150 < Y < 200$  mm only a larger structure is visible. After all, there is no similar mean recirculation in the flow field that would be similar to any earlier 2D studies downstream an inhibitor.

Regardless of the above-mentioned observations, the data were further investigated in order to discover differences in the instantaneous fields as well. However, not individual samples are studied, but quantities are defined, which could represent instantaneous behaviour.

At first, the distribution of the absolute value of vorticity is computed in each instantaneous velocity field using equation B.2.

$$|\omega| = \left| \frac{dv}{dx} - \frac{du}{dy} \right| \quad (\text{B.2})$$

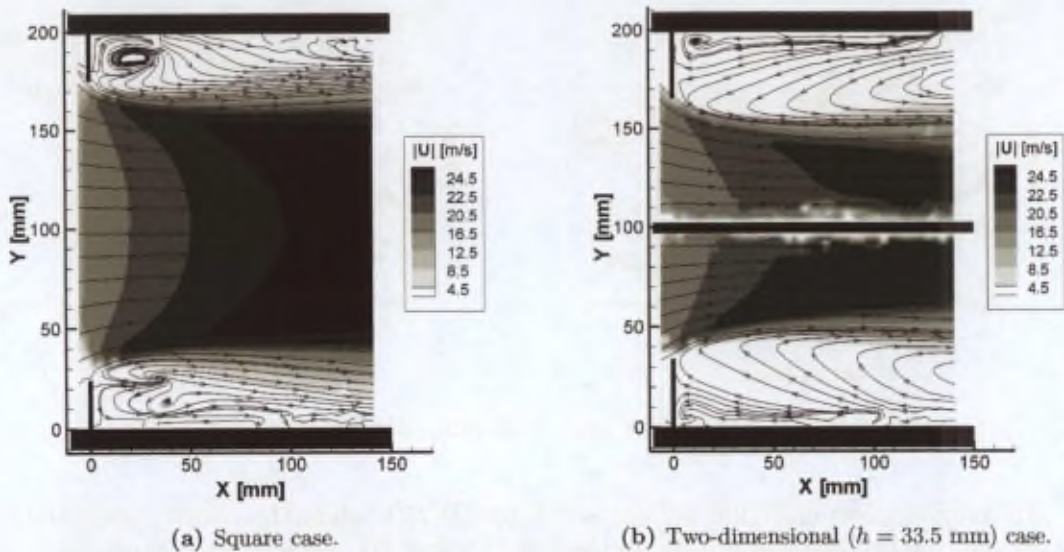


FIGURE B.25 – Velocity magnitude and streamlines.

Then, this quantity is averaged in each spatial location over the 1000 recorded fields. With this method in terms of mean, one can still see the regions, which have a vorticity value different from zero with a higher probability in the instantaneous fields. The result can be seen in the contour plot of Figure B.26(a) (square case) and Figure B.26(b) (2D case).

Based on these figures, the two configurations show a good agreement. No significant difference can be found. The large values in Figure B.26(b) in the vicinity of the splitting plate are not considered, since they are due to the low local image quality and lack of visual access.

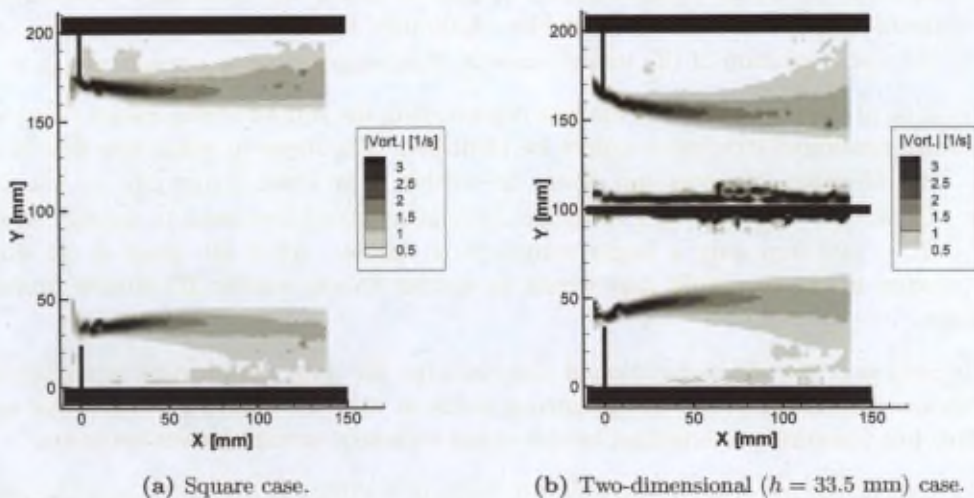


FIGURE B.26 – Absolute vorticity plot.

Finally, one more quantity, "Neg. $\lambda$ " is defined based on  $\lambda_2$ . A criterion, based on  $\lambda_2$  is used e.g. in the VKI wavelet-analysis algorithm, which is detecting vortices in flow fields. The

definition (assuming 2D flow) is shown in equation B.3.

$$\lambda_2 = \left( \frac{du}{dx} \right)^2 + \left( \frac{du}{dy} \cdot \frac{dv}{dx} \right) \quad (\text{B.3})$$

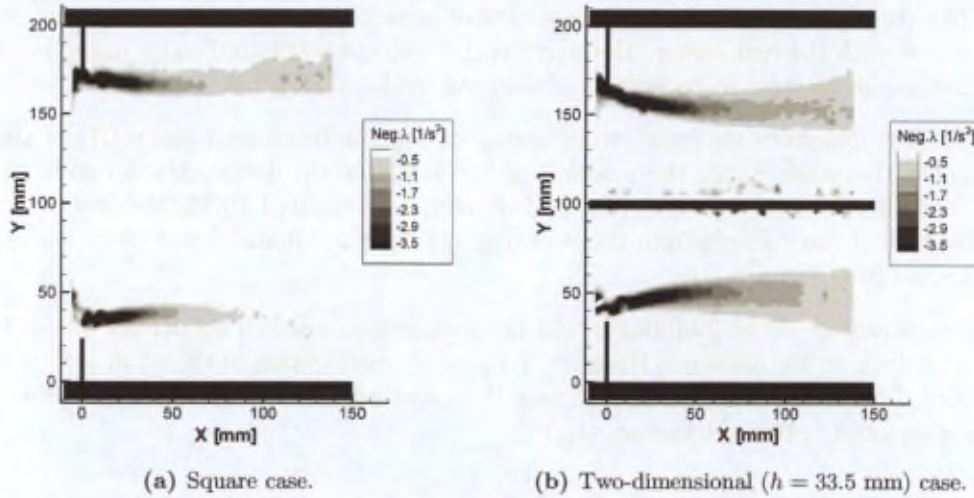


FIGURE B.27 – Negative Lambda distribution.

The regions with negative  $\lambda_2$  value represent regions, where the rotation of the flow is stronger, so it indicates vortex-like structures. From  $\lambda_2$ , the mean "Neg. $\lambda$ " field is defined by equation B.4.

$$Neg.\lambda = \sum_{Fields} \begin{pmatrix} 0 & \text{if } \lambda_2 \geq 0 \\ \lambda_2 & \text{if } \lambda_2 < 0 \end{pmatrix} \quad (\text{B.4})$$

Thus, this quantity should indicate in each field the regions, where vortices, or vortex-like structures appear in the instantaneous fields. The more negative this value is, the higher the probability is that at a given position vortices exist. Therefore, it should show the path of the vortices. The result can be seen in the contour plot of Figure B.27(a) (square case) and Figure B.27(b) (2D case).

One can observe more significant differences between the "Neg. $\lambda$ " plots, than between the  $|\omega|$  plots previously. In the square case (Figure B.27(a)) "Neg. $\lambda$ " is closer to zero, than in the 2D case (Figure B.27(b)). In addition, the square configuration is far less symmetric, than the 2D configuration.

Concisely, it can be seen, that looking either at the mean flow structures, or at the instantaneous structures (vortices), the square configuration performs far worse, than the 2D configuration. The reason is probably the large three-dimensional effect appearing with the square obstacle. Therefore, it is suggested to apply a 2D configuration for the later investigation.

Furthermore, during this investigation, the glass layer of the sidewall was found to be very limiting due to its fragility and due to the optical distortions of its glue. In addition, it made the splitting plate mount complicated. Since first of all numerous single-phase experiments are

to be done, the sidewalls of the test section were remanufactured using only plexiglass, where the - plexiglass - splitting plate can be fixed directly to the sidewalls with screws. This new test section has again a dimension of  $200 \times 200 \text{ mm}^2$ .

#### B.4 About the importance of the splitting plate

With the square design the model could have respected both the "distance" and section ratio similarities with the real motor. However, as this concept was found to be inapplicable, at least the flow dynamics were to be kept similar in the model, if possible.

The flow dynamics depends on the one hand on the blockage ratio ( $BR$ ) of the inhibitor itself. On the other hand, the position of the inhibitor tip defines the location of the shear layer and therefore the location of the shed vortices compared to the sidewall. Furthermore, the distance of the vortices from the wall may influence the dynamics of the vortical structures (Anthoine (2000)).

The parameter of the inhibitor height ( $h$ ) is straightforward. This defines the location of the inhibitor tip from the sidewall. However, keeping the test section of the wind tunnel unchanged, the  $BR$  of the inhibitor (see also Figure B.28 and equation B.5) can be modified by using different splitting plate thicknesses ( $t_{sp}$ ).

$$BR = \frac{h}{H} \quad (\text{B.5})$$

Therefore, a study is initiated in order to investigate that in function of different splitting plate thicknesses and inhibitor heights, how the main flow characteristics change.

For the study, seven different configurations are defined (please, see the first four columns of Table B.3). The first configuration does not contain any splitting plate guiding the flow.

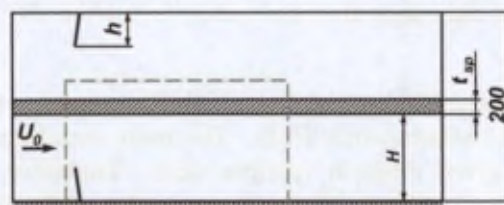


FIGURE B.28 - Mean flow field (square configuration; in-plane).

In the followings, configurations are chosen, which represent large  $BR$  ( $h = 41 \text{ mm}$  with  $t_{sp} = 57 \text{ mm}$ ;  $BR = 0.58$ ), small  $BR$  ( $h = 13.5 \text{ mm}$  with  $t_{sp} = 5 \text{ mm}$ ;  $BR = 0.14$ ) and intermediate blockages. The intermediate configurations are defined in order to realize similar blockage ratios ( $0.33 \approx 0.35$  and  $0.42 = 0.42$ ) at different inhibitor heights (by compensating with  $t_{sp}$ ).

The whole investigation is carried out at  $U_0 = 10 \text{ m/s}$  using the Particle Image Velocimetry (PIV) measurement technique. The fields-of-view (FoVs) of the camera include entirely one side of the test section. However, they always includes a part of the test section from the opposite side of the splitting plate in order to be able to verify qualitatively the flow symmetry. Furthermore, in each FoV 1000 image pairs are recorded from which statistical quantities can be obtained. Finally, the spatial resolution of the experiments is around  $1.1 \times 1.1 \text{ mm}^2$

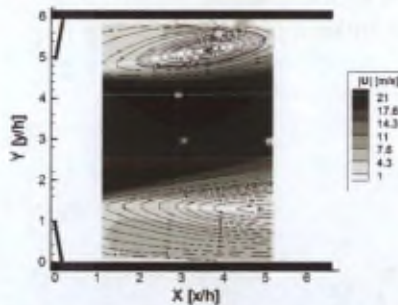
Table B.3 – The flow acceleration over the inhibitors

Config.	$h$ [mm]	$t_{sp}$ [mm]	$BR$ [-]	$\overline{U}_{max}$ [m/s]	$\frac{X\overline{U}_{max}}{h}$ [-]	$\frac{Y\overline{U}_{max}}{h}$ [-]	$c_{vc}$ [-]
(0)	33.5	0	0.34	21.94	2.91	4.08	0.687
(1)	13.5	5	0.14	14.25	3.82	2.91	0.815
(2)	23.5	57	0.33	19.94	3.35	2.30	0.750
(3)	33.5	5	0.35	21.43	3.52	2.33	0.713
(4)	33.5	40	0.42	24.57	2.48	1.99	0.703
(5)	41	5	0.42	25.54	3.06	2.11	0.678
(6)	41	57	0.58	34.27	1.94	1.59	0.691

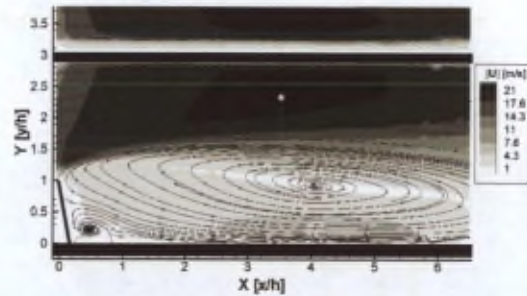
### B.4.1 The mean flow fields

From the PIV experiments, most importantly the whole-field mean velocity distributions can be obtained (some examples are shown in Figure B.29).

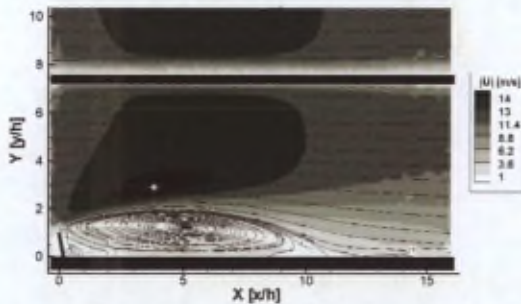
First of all, in the configurations that imply a splitting plate, a good flow symmetry is found. However, in the configuration without the splitting plate, the flow symmetry is very poor (the result is shown in Figure B.29(a)). This observation reassures the necessity of the splitting plate in the test section in the two-dimensional inhibitor arrangement.



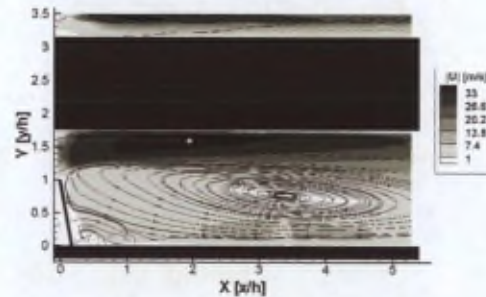
(a) Without splitting plate,  $h = 33.5$  mm (Config. (0)).



(b)  $t_{sp} = 5$  mm and  $h = 33.5$  mm (Config. (3)).



(c)  $t_{sp} = 5$  mm and  $h = 13.5$  mm (Config. (1)).



(d)  $t_{sp} = 41$  mm and  $h = 57$  mm (Config. (6)).

FIGURE B.29 – Resulting mean flow fields.

In general, the flow downstream an emerging fence (e.g. the inhibitor) separates from the tip of the obstacle and further accelerates, creating a contraction, also called *vena contracta*. Therefore, as it confirmed by the present results, the highest velocity magnitudes can be found

well downstream the inhibitor. The magnitude of the flow acceleration can be described by equation B.6. This depends on the undisturbed free stream velocity,  $U_0$ , the passage ratio ( $PR = S_p/S$ ) and the so-called *vena contracta coefficient* ( $c_{vc}$ ). The value of  $c_{vc}$  varies depending on the geometry of the blockage.

The investigation of the obtained flow fields is started by the magnitude of the flow acceleration. In each mean flow field the location of the maximum velocity is identified (see the marks in Figure B.29) and its magnitude and co-ordinates are recorded (see columns 5 to 7 of Table B.3).

The evolution of the maximum mean velocity co-ordinates is shown in Figure B.30. It is clear that by increasing the blockage ( $BR$ ), the flow accelerates faster downstream from the tip of the inhibitor and reaches its maximum magnitude at smaller  $X/h$  locations. Furthermore, the regions with the highest velocity magnitude appear at smaller  $Y/h$  locations as well. This shows the increasing influence of the splitting plate.

Configuration (1) ( $h = 13.5$  mm;  $t = 5$  mm) represents a case, where the flow is almost not effected by the presence of the splitting plate (as if  $H \rightarrow \infty$ ). Here, the flow is capable of forming a more curved *vena contracta*.

In contrary, configuration (6) ( $h = 41$  mm;  $t = 57$  mm) represents a case, where the flow is highly restricted by the inhibitor ( $H \rightarrow h$ ). Here, the inhibitor acts more similarly to the nozzle of a simple subsonic jet, where the flow reaches its highest velocity at the nozzle throat. Therefore, as the  $BR$  increases, the longitudinal location of the highest velocity approaches the inhibitor tip. Similarly, as the flow is more restricted, it is not capable of forming an ideal *vena contracta* shape and therefore the transversal location of the maximum velocity becomes closer to the inhibitor tip and even more pronouncedly to the splitting plate as well (see Figure B.29).

$$U_{jet} = \frac{1}{c_{vc}} \frac{S}{S_p} U_0 \quad (B.6)$$

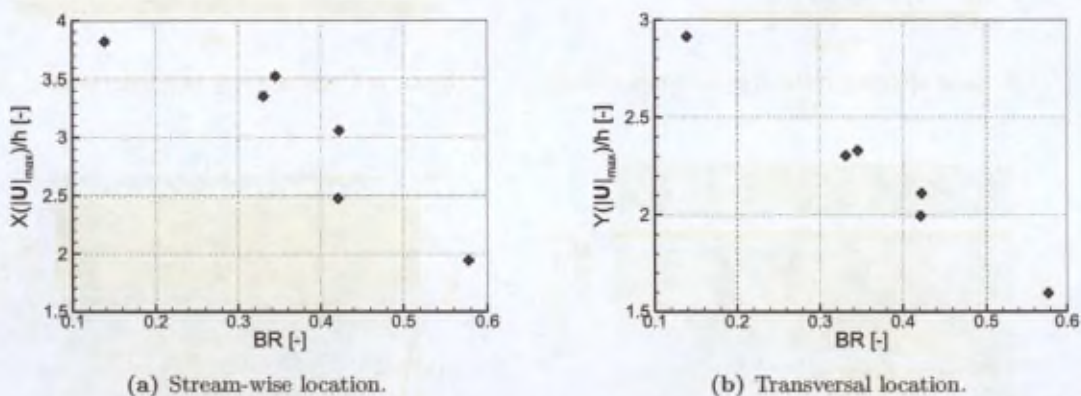


FIGURE B.30 - The location of the maximum velocity.

During the axial-flow investigation of the axisymmetric 1/30 scale SRM model, Anthoine (2000) found the highest flow velocity magnitudes at around  $x/h = 3$  to 4.5. From this point of view, most of the present configurations perform similarly.

Considering the amplitude of the velocity, the maxima vary between about 1.4 and  $3.4U_0$ , while Anthoine (2000) found about  $2.6U_0$  in the axisymmetric model. From this point of view, configuration (5) gives the closest performance.

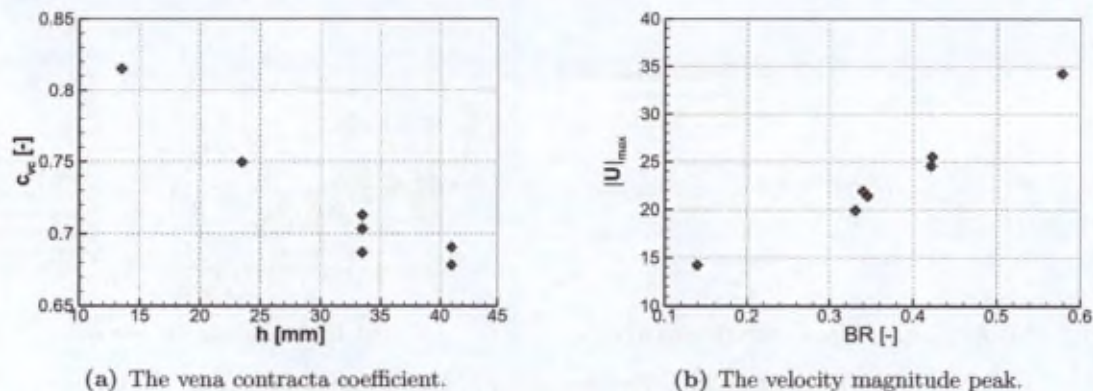


FIGURE B.31 – Flow acceleration in the vena contracta.

Taking the velocity maxima as  $U_{jet}$ , from equation B.6  $c_{vc}$  can be obtained in each case. Here, Anthoine (2000) found  $c_{vc} = 0.68$  with the axisymmetric geometry with acoustic resonance. As it can be seen in the last column of table B.3 and in figure B.31, this value can also be modelled the best with configuration (5) ( $t_{sp} = 41$  mm;  $h = 5$  mm) in the present 2D geometry.

#### B.4.2 The vortical structures

Besides the mean flow field downstream the inhibitor, one should keep in mind the vortices and if possible, respect their behaviour as well. Therefore, in each case (except configuration (0)) the vortical structures are identified in all of the instantaneous flow fields using the wavelet-based vortex detection algorithm.

Later, a statistical analysis (similar to the one applied by Repellin (1999) and Anthoine (2000)) is performed. The field-of-view is divided into equal longitudinal zones, where each zone covers  $x = 1h$  distance downstream the inhibitor. Within every zone the different properties of the vortices are averaged.

At this stage, first of all the location of the vortices are investigated in order to see their mean path. From the PIV measurements performed by Anthoine (2000) the mean path of the vortices is known in the axisymmetric configuration (with axial flow injection).

The comparison can be seen in Figure B.32. The path of the vortices of Anthoine (2000) matches the best with configuration (3) (representing  $t_{sp} = 5$  mm and  $h = 33.5$  mm).

Configuration (5) (with  $h = 41$  mm), which was favoured previously (in B.4.1) from the flow acceleration point of view, performs very similarly. However, determining the physical location of the vortices, it turns out that  $Y_{mean} = 1.20$  to  $1.40h = 0.510$  to  $0.589H$ , which means that the vortices are closer to the splitting plate than to the sidewall. Therefore, the wall effect of the artificial splitting plate may act on them stronger and inversely than the sidewall. In the same time, using  $h = 33.5$  mm, in mean the vortices appear to be located around the centre of the test section, but mostly closer to the sidewall ( $Y_{mean} = 1.18$  to  $1.47h = 0.405$  to  $0.505H$ ).

Since the main objective of these experiments was to analyse the acceleration of the mean flow and therefore a considerably large field-of-view was applied, the measurement quality does not allow a reliable comparison of further vortex properties.

Therefore, in the end,  $t_{sp} = 5$  mm and  $h = 33.5$  mm are chosen to represent the nominal

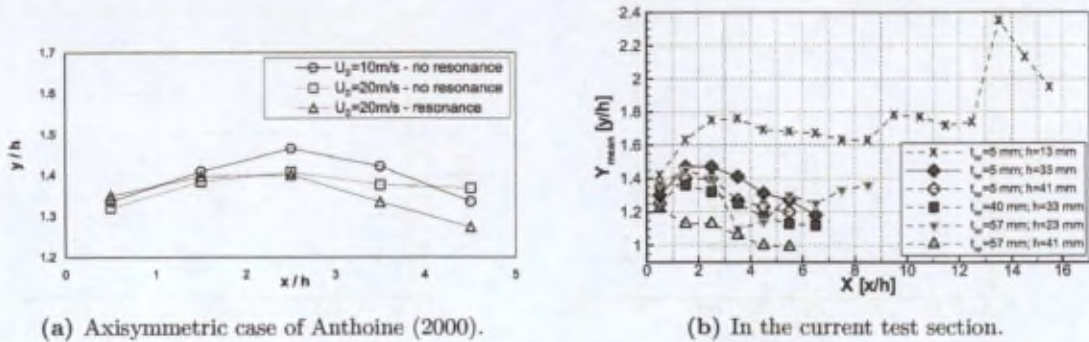


FIGURE B.32 – The evolution of mean vortex location.

condition.

## B.5 L-11 flow uniformity confirmation tests

As soon as the L-11 wind-tunnel was installed vertically, a preliminary characterization took place using several laser-sheet positions with PIV. These experiments are not shown here; they are described by Tóth and Anthoine (2004). However, when the main parameters of the test section are fixed, a shorter characterization took place still with the PIV technique, but this time only in two planes. Since these tests are performed in the final nominal condition, only these tests are described here.

Furthermore, this section shows an investigation of the flow symmetry of the two-dimensional test section as well.

### B.5.1 Inlet uniformity

As the inlet uniformity verification PIV measurements are performed at the top of the test section, just downstream the end of the convergent part of the tunnel. These tests are performed with the empty test section in the two-dimensional configuration. It means that according to the plans for the future measurements, a 5 mm splitting plate (see also Figure B.33) is installed at the mid-width of the test section. The plate originates from the end of the convergent part of the wind-tunnel. The inhibitors and the model of the nozzle with the cavities are not installed. On the one hand, this allows optical access in flow direction (from the bottom of the test section). On the other hand, with this characterization, the worst condition is analysed. By installing the inhibitors and the nozzle model, the downstream pressure drop is increasing, due to which the uniformity of the inlet flow is expected to be improved (according to Pope (1947)).

Altogether two PIV measurement planes are defined (for easier understanding see Figure B.33). The first (in-plane) is located at the mid-span of the test section aligned with the mean flow direction. In practice, this is the plane of the future measurements. The second plane (perpendicular plane) is normal to the mean flow direction and covers almost the whole test section. Both of them are located in the inlet part of the test section: the in-plane flow field extends from about 40 to 120 mm from the end of the convergent part of the wind-tunnel; the perpendicular plane is located at 109 mm from the end of the same convergent.

From the in-plane test the variation of the flow velocity or its non-uniformity can be discov-

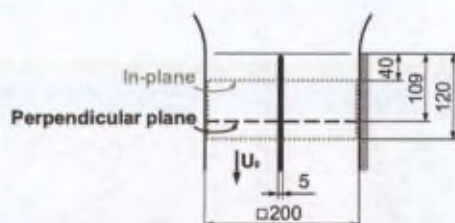


FIGURE B.33 – PIV measurement planes.

ered. Using the perpendicular plane, non-uniformities and flow anomalies can be discovered in the whole cross section of the test section. However, in the second plane, the magnitude of the mean flow velocity cannot be measured.

During the uniformity confirmation tests, the free stream velocity of the airflow is  $U_0 = 10$  m/s. This is the velocity that is used during most of the previous tests and this would be used in most of the later experiments as well. With both laser-sheet configurations 1000 image pairs are recorded. This database serves for the determination of the mean flow field.

In Figure B.34 the mean (the mean over 1000 image pairs) flow field corresponding to the in-plane measurement can be seen. Figure B.35 shows the mean flow field in the perpendicular plane. The contour plot of the figures stands for the mean *signal-to-noise ratio* ( $SN$ ) distribution. In the regions of the contours where  $SN_{mean} < 2.2$ , the measurement has low quality and the obtained velocity vector should not be considered to be physical.

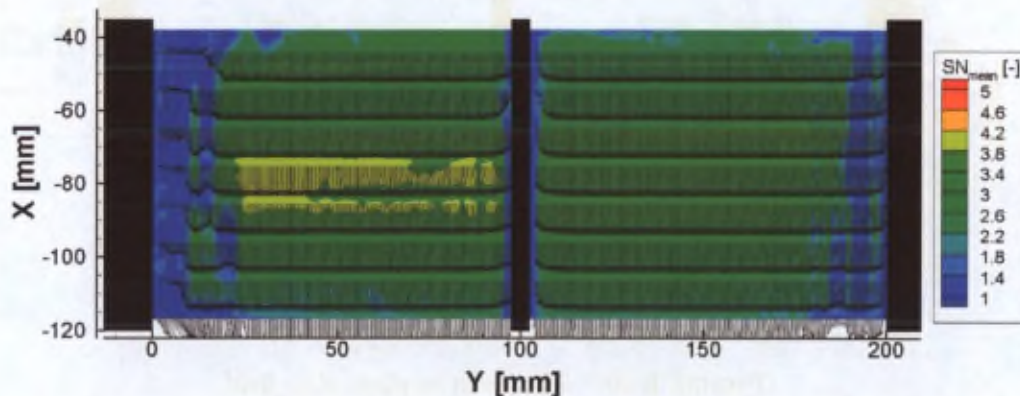


FIGURE B.34 – The mean in-plane signal-to-noise ratio distribution.

In the reliable measurement region of the in-plane case (Figure B.34) the velocity vectors show a uniform distribution. Furthermore, plotting the non-dimensional velocity amplitude (see Figure B.36), the non-uniformity is limited to about  $\pm 0.8\%$  of the free stream velocity ( $U_0 = 10$  m/s).

Regarding the perpendicular plane (Figure B.35), the velocity vectors are pointing radially outwards from the centre of the plot. Looking at the non-dimensional velocity magnitudes (see Figure B.37) one could conclude that the flow is accelerating towards the sidewalls of the wind-tunnel. However, this conclusion would not be correct, because it is only the consequence of the parallax effect during the image recording.

Generally, it is assumed that the measured displacement is lying in the plane of the laser-sheet. More precisely, in the plane that is perpendicular to the optical axis of the camera.

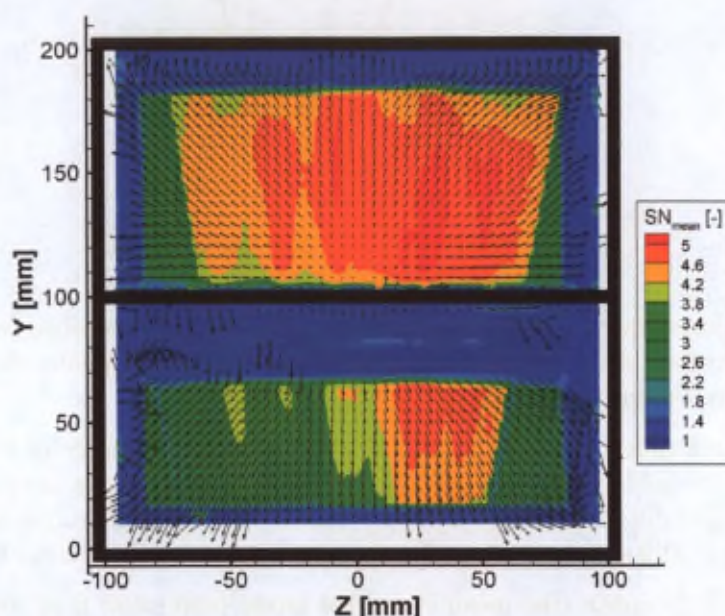


FIGURE B.35 – The mean perpendicular plane signal-to-noise ratio distribution.

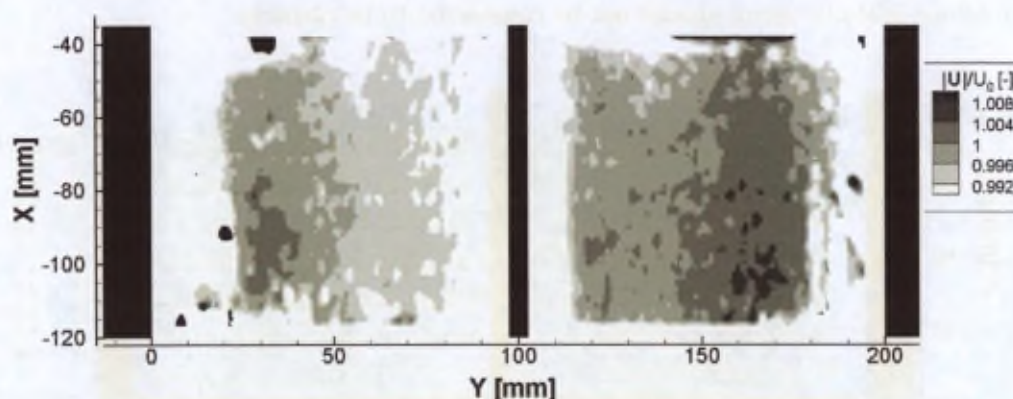


FIGURE B.36 – The mean in-plane flow field.

However, this is not exactly true either. In practice, each velocity vector that one can see in the PIV plots is lying in a plane that is locally normal to the line drawn between the centre of the optics of the camera and the local measurement position (see Figure B.38). This is due to the fact that the camera has a non-zero viewing angle (except by using telecentric lenses). Thus, each point of the measurement plane is seen under a different viewing angle.

Therefore, if the flow has a strong out-of-plane motion (in the present case the mean flow has 10 m/s velocity perpendicular to the laser-sheet), this out-of plane component causes a considerable impact on the measurement. In the present case, zero velocity components should be seen in the mean flow field if a lens with zero viewing angles (a telecentric lens) was used. However, the applied optical system had a conical field of view. Therefore, in the optical axis (in the centre of the image) the measured velocity should be zero and the rest of the vectors should point outwards in radial direction and have increasing amplitude according to the sine of the local viewing angle.

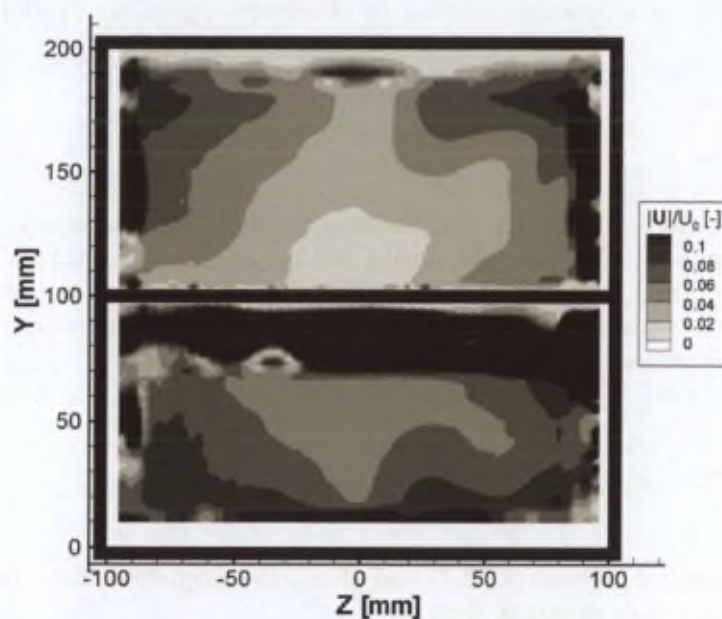


FIGURE B.37 – The mean perpendicular plane flow field.

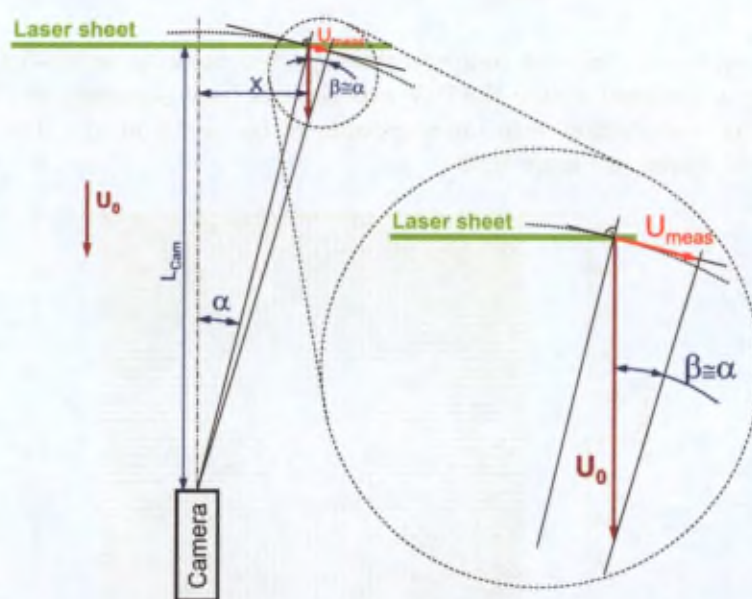


FIGURE B.38 – The projection of the measured velocity vector.

In order to calculate the synthetic parallax effect, first of all, the flow is assumed to have a uniform  $U_0 = 10$  m/s velocity distribution; the velocity vectors pointing towards the camera parallel to its optical axis. The schematic in Figure B.38 shows the geometrical arrangement and the acquisition of the artificial displacement  $U_{meas}$  in case of an out-of-plane displacement of  $U_0$  in a given location.

Accordingly, the local viewing angle can be obtained easily using relationship (B.7).

$$\tan \alpha = \frac{X}{L_{Cam}} \Rightarrow \alpha = \arctan \frac{X}{L_{Cam}} \quad (\text{B.7})$$

During the actual experiments, the distance between the laser-sheet and the camera is  $L_{Cam} = 1227$  mm. At  $U_0 = 10$  m/s, during the  $\Delta t = 120 \mu\text{s}$  separation time that is used for the image recording, the flow is displacing by about 1.2 mm towards the camera. This 1.2 mm is negligible with respect to  $L_{Cam}$  and therefore one can assume that  $\beta \approx \alpha$ . Thus, the artificial displacement can be described by relationship (B.8).

$$\sin \beta = \frac{U_{meas}}{U_0} \approx \sin \alpha \Rightarrow U_{meas} \approx U_0 \sin \alpha \quad (\text{B.8})$$

Finally, combining relationship (B.7) and (B.8), the displacement to be measured can be estimated with the simple equation (B.9).

$$U_{meas} \approx U_0 \sin \left( \arctan \frac{X}{L_{Cam}} \right) \quad (\text{B.9})$$

Using this equation, one can compute the expected velocity vector-field in each location, where a vector is obtained during the PIV experiments (still assuming an ideally uniform out-of-plane velocity distribution with an amplitude of  $U_0 = 10$  m/s). The resulting artificial vector-field is indicated in Figure B.39.

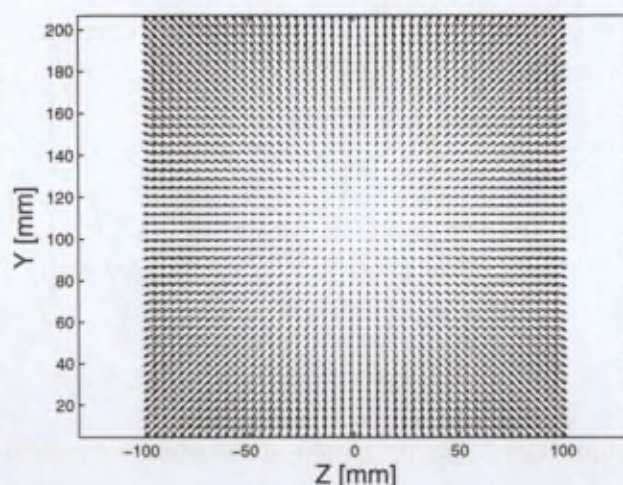


FIGURE B.39 – The parallax effect on a uniform flow.

Since the co-ordinate system, the grid of the synthetic field and the actual measurements (see Figure B.37) are identical, the artificial field can be simply subtracted from the mean experimental field in order to eliminate the parallax effect of the out-of-plane component and expose the pure in-plane component of the displacements. The final result is presented in Figure B.40.

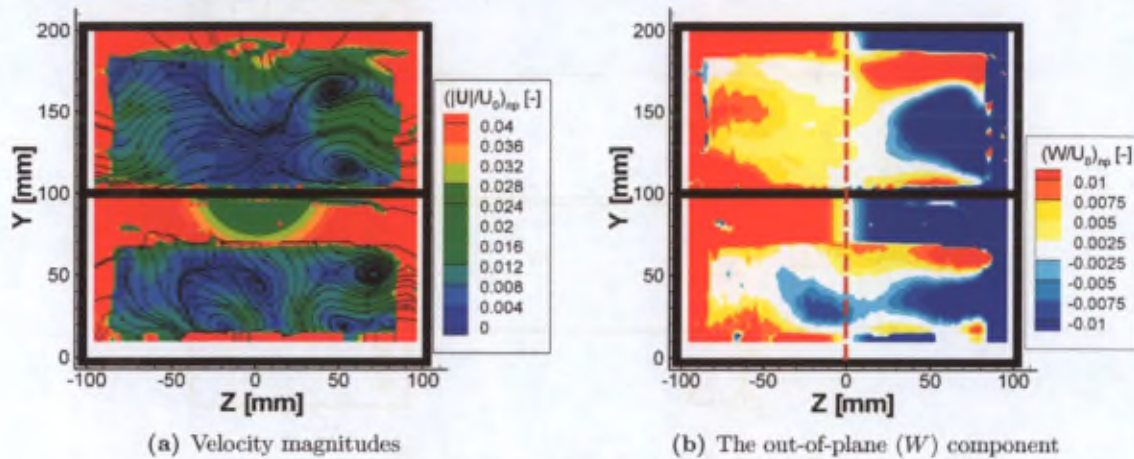


FIGURE B.40 – The measured mean flow field by correcting the parallax effect.

The non-zero flow field shows that the mean inlet flow of the test section is not ideally uniform. One can observe several rotating structures, drains and sources with the help of the streamlines (in Figure B.40(a)). The most important rotating structures are located at  $Z > 15$  mm in both sides of the test section.

However, considering the future experiments, which would be performed in the plane of  $Z = 0$  mm (indicated by the dashed line in Figure B.40(b)), the future mean out-of-plane velocity component ( $W$ ) is shown in Figure B.40(b). As it is visible, in the mid-span of the test section the mean out-of-plane motion remains well below 1% of  $U_0$  (mostly, it remains below 0.5%), which is indeed acceptable.

### B.5.2 Flow symmetry

By defining the present symmetric 2D-like test section (divided by a splitting plate), one should be sure that the flow field is symmetric as well. If it is the case, one could perform measurements at any of the sides depending on which one has easier access.

Having one more look at Figure B.36 it is visible that the flow inside the empty test section is symmetric. The non-symmetry appears to be within about 0.8% of the free stream velocity. However, installing all the blockage elements (inhibitor and nozzle), the situation may change.

To find out, how the flow behaves in the final configuration, PIV measurements are carried out with a nominal geometry (see Figure B.41). During this test the  $h = 33.5$  mm inhibitor is fixed 310 mm (roughly "9h") far from the nozzle tip. At the bottom of the  $w = 107$  mm wide cavity a 30 mm thick plexiglas sheet is placed to model the accumulated liquid. The nozzle throat has an opening of  $o = 15.5$  mm. The free stream velocity of the airflow is  $U_0 = 10$  m/s.

Using the three indicated (rectangles with "Inlet", "Cavity1" and "Cavity2" in Figure B.41) Fields of View (FoVs), PIV measurements are performed. Note that due to illumination constraints "Cavity2" FoV is smaller than "Cavity1". At each location 1000 image pairs are recorded and the mean flow properties are determined. With the large FoV (Inlet) upstream the inhibitors, the incoming flow symmetry can be validated; with the two remaining FoVs in the cavities (Cavity1 and Cavity2), the symmetry in a complex flow region can be verified.

Regarding the incoming flow measurements, the results are shown in Figure B.42. In each

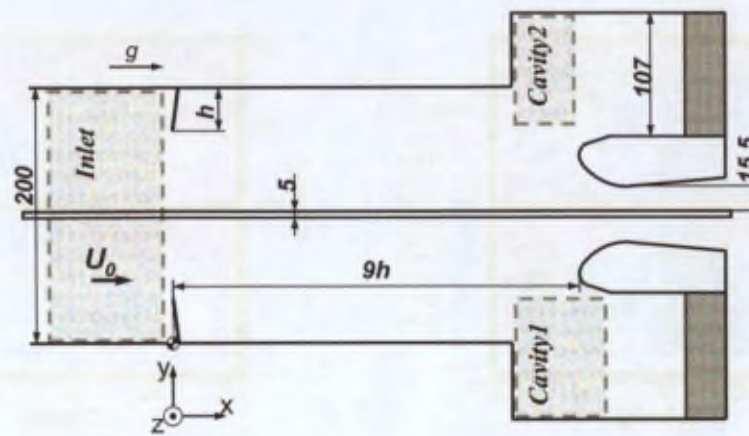


FIGURE B.41 - Symmetry verification geometry.

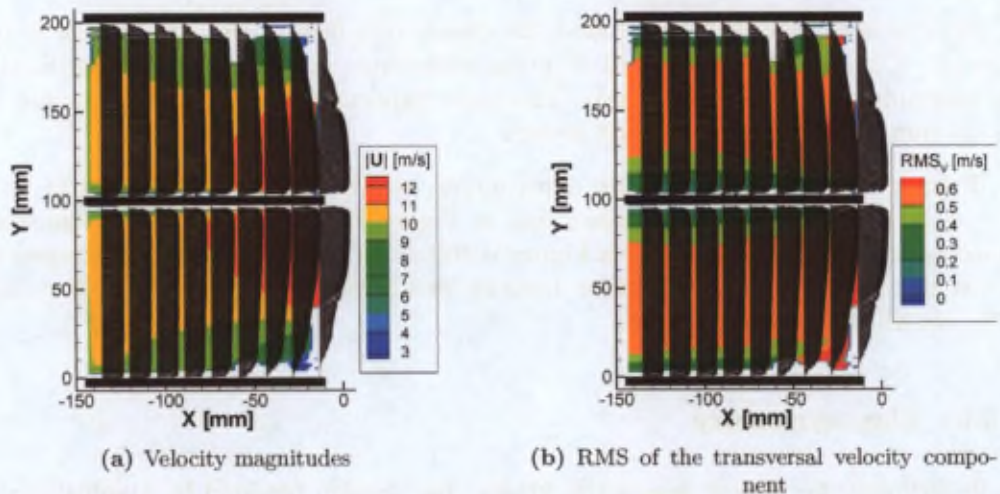


FIGURE B.42 - The incoming flow.

plot the two sides of the wind-tunnel (separated by the splitting plate) are shown in the arrangement defined by Figure B.41. The white areas of the contours show regions, where the measurement quality is not acceptable based on the  $SN_{mean}$ .

The longitudinal velocity values are extracted at  $x = -93.2\text{mm}$  from the tip of the inhibitor. Based on the plot (shown in Figure B.43), in the side of lower  $Y$  values of the tunnel 2% higher local velocity components are found, which means  $\pm 1\%$  deviation. This discrepancy is slightly larger than the one observed during the inlet uniformity verification ( $\pm 0.8\%$ ). However, this difference could also be due to a slight non-symmetry of the internal geometry (blockage of the inhibitor and/or the nozzle) and it is considered to be still acceptable.

Considering the fluctuation of the transversal velocity component of the airflow (shown in Figure B.42(b) and Figure B.44), a good symmetry is found. The unusually high RMS values are due to the presence of the spray support system in the stagnation chamber of the wind-tunnel (which is described in 2.3.2.2). By removing the support, the velocity fluctuation values would show the usual distribution, where the larger values can be found close to the walls (this was seen during earlier preliminary measurements).

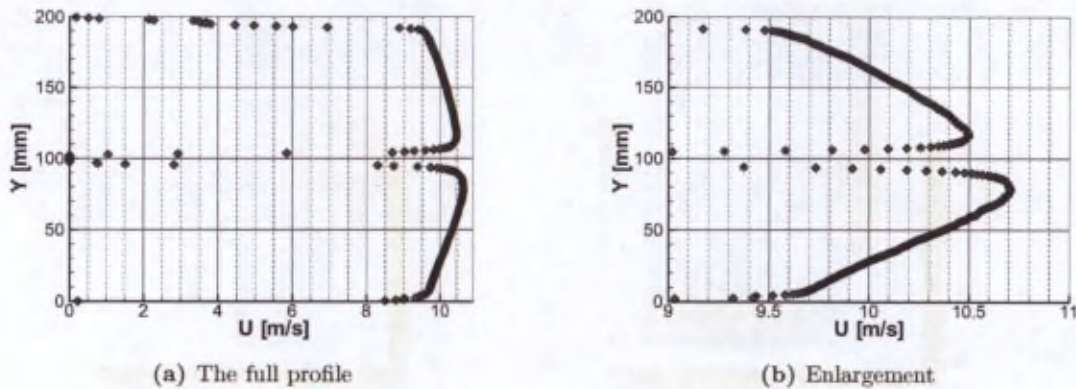


FIGURE B.43 – Longitudinal velocity component evolution at  $x = -93.2\text{mm}$ .

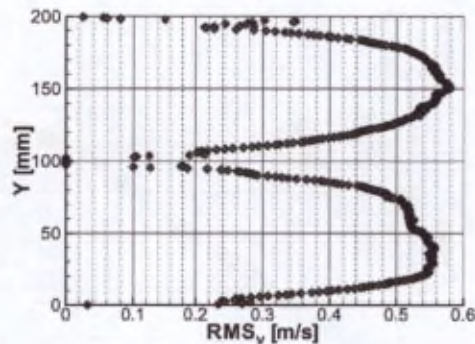


FIGURE B.44 – The fluctuation of the longitudinal velocity component at  $x = -93.2\text{mm}$ .

Regarding the symmetry confirmation in the region of the cavity, the velocity amplitude distribution is shown in Figure B.45. The plots corresponding to *Cavity2* are transformed into the common co-ordinate system that is applied to the *Cavity1* measurements as well. Similarly to the previous measurements, the white areas stand for unacceptable measurement qualities.

Focusing on the velocity magnitudes, the difference between the two measurements are negligible. In the profile (Figure B.46) of the longitudinal velocity component (extracted at  $x = 300\text{mm}$ ) the agreement is more pronounced.

Finally, Figure B.47 shows the fluctuation of the transversal velocity component in the region of the cavity. Investigating the plots, the maximum difference between the velocity fluctuations is found to be around  $0.22\text{ m/s}$  (see also the extracted profile in Figure B.48 as well), which could be accepted. Furthermore, this local deviation could originate mainly from the uncertainty of the PIV measurements as well.

Summarizing the flow inlet and symmetry verifications, one can see that the facility complies with all the current requirements. Therefore, the present wind-tunnel configuration is considered to be the final setting and represent the nominal configuration.

### B.5.3 Measuring the reference flow velocity

As mentioned in section 2.4, the reference flow velocity is measured with a Validyne pressure transducer by measuring the pressure difference between the stagnation chamber and the test

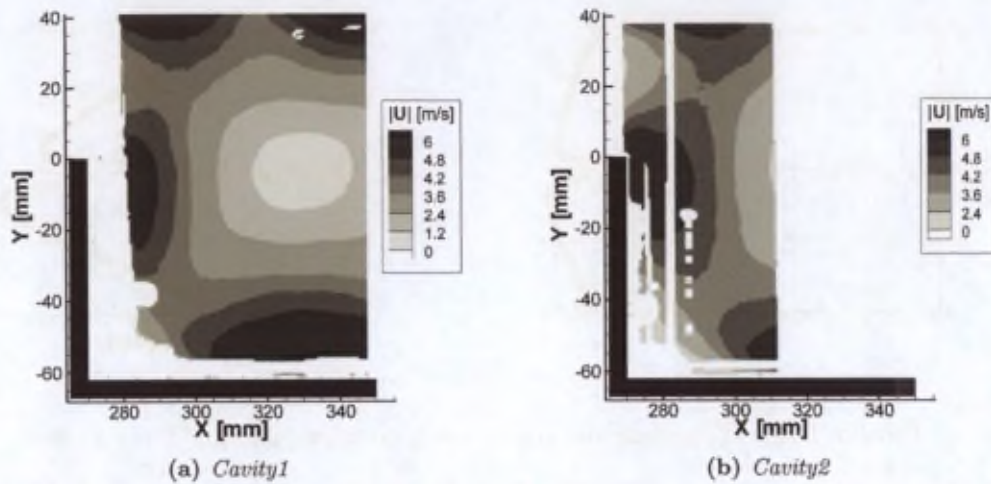


FIGURE B.45 – Velocity magnitude comparison inside the cavity.

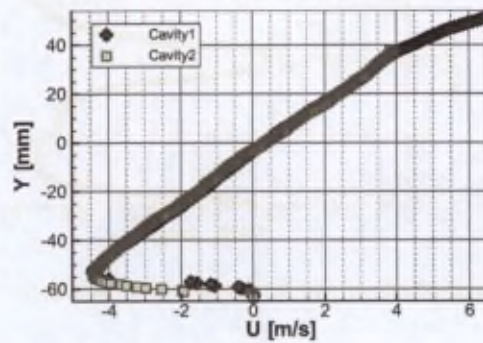


FIGURE B.46 – Longitudinal velocity component evolution in the cavity at  $x = 300\text{mm}$ .

section. The pressure transducer arrangement is shown in Figure B.49.

In order to obtain the pressure information from the voltage signal, the transducer is calibrated with a water column manometer. Then, to compute the flow velocity, the Bernoulli equation and the continuity equation are used:

$$\frac{U_0^2}{2} = \frac{\Delta p}{\rho_{air}} + \frac{U_s^2}{2} \quad (\text{B.10})$$

$$U_0 \cdot S = U_s \cdot S_s \quad (\text{B.11})$$

where  $U_0$  and  $U_s$  are the velocity magnitudes in the test section and in the stagnation chamber respectively,  $\Delta p$  is the pressure difference measured by the transducer,  $S$  and  $S_s$  are the cross sections of the test section and the stagnation chamber respectively. Therefore, from

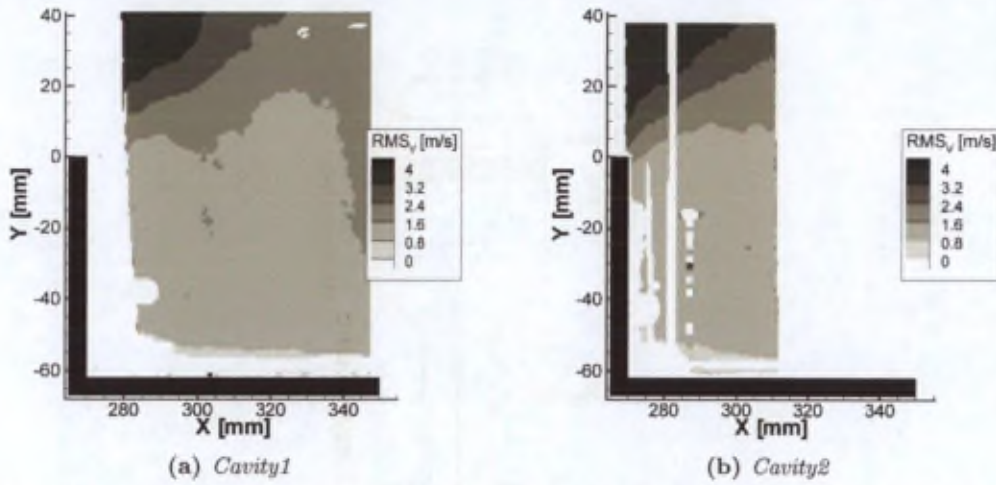


FIGURE B.47 – Comparing the transversal velocity component fluctuation inside the cavity.

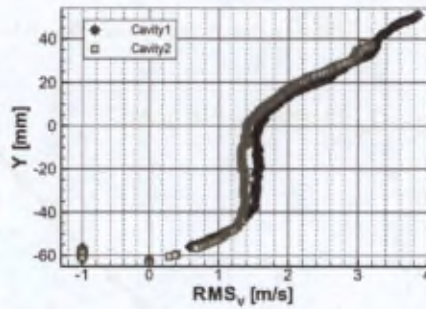


FIGURE B.48 – The fluctuation of the longitudinal velocity component in the cavity at  $x = 300\text{mm}$ .

equation B.10 and equation B.11 the flow velocity is

$$U_0 = \sqrt{\frac{2 \cdot \Delta p}{\rho_{air} \cdot \left(1 - \left(\frac{S}{S_e}\right)^2\right)}} \tag{B.12}$$

In equation B.12 always the actual air density is used depending on the ambient conditions:

$$\rho_{air} = \left(0.0004646 \cdot \left(P - 4990221.6 \cdot RH \cdot e^{-5315.56/T}\right)\right) / T \tag{B.13}$$

where  $P$  is the barometric pressure in [mmHg],  $T$  is the air temperature in [K] and  $RH$  is the relative humidity in [%].

Therefore, a direct relationship can be drawn between the voltage signal of the pressure transducer and the actual reference flow velocity. An example is shown in Figure B.50.

However, during two-phase experiments the generated water droplets often block the pressure tap of the test section. Therefore, the stability of the flow velocity cannot be monitored through

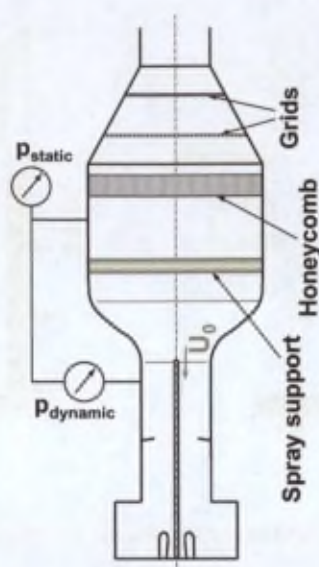


FIGURE B.49 - The pressure transducers of the wind-tunnel.

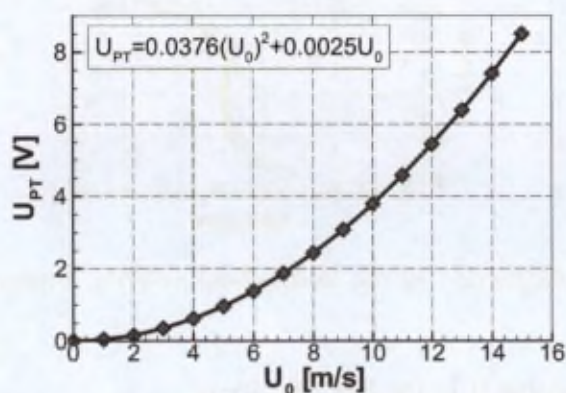


FIGURE B.50 - Typical Validyne calibration curve.

the dynamic pressure. Therefore, a second pressure transducer is installed (shown in Figure B.49 as well), from which the static pressure evolution of the stagnation chamber can be followed using an acquisition computer.

